Charles University, Faculty of Mathematics and Physics
Astronomical Institute

PhD Thesis

Yarkovsky effect and the Dynamics of the Solar System

Miroslav Brož

supervisor: Doc. RNDr. **David Vokrouhlický**, DrSc.

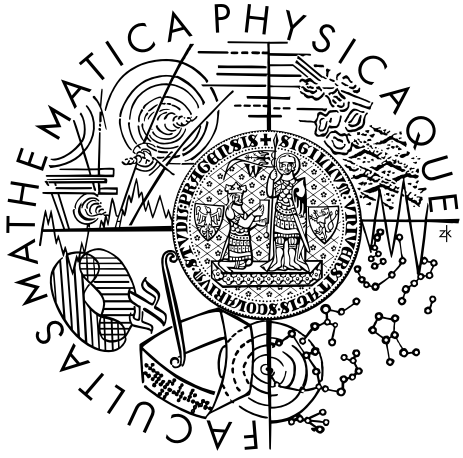

Prague, 2006

Acknowledgements

I would like to thank to the supervisor of my PhD Thesis Doc. RNDr. David Vokrouhlický, DrSc., to my colleagues David Nesvorný, Alessandro Morbidelli, Bill Bottke, David Čapek, Josef Ďurech, co-authors I had honour to collaborate with and also to my wife Míša and son Rostík.

The work of MB was supported by the Grant Agency of the Czech Republic by grant 205/05/2737 and by the Observatory and Planetarium in Hradec Králové.

Brož, Miroslav

Yarkovsky effect and the dynamics of the Solar System

(celestial mechanics, asteroids, Yarkovsky effect)

Contents

1 Introduction

The Solar System has been a domain of important discoveries, which have helped us to justify and verify basic laws of physics. The kinematics of planetary motion, described by Johannes Kepler (1571–1630) at the beginning of the 17$^{\text{th}}$ century, and the corresponding dynamics, unveiled by Isaac Newton (1642–1727) at the end of the 17$^{\text{th}}$ century, are the best known examples.

For a long time, the Newtonian gravitational attraction have been though to be the only driving force affecting the motion of celestial bodies. On the other hand, Kepler already speculated about some kind of *repulsive* force, because he knew the tails of comets are directed away from the Sun. In the first half of the 19$^{\text{th}}$ century, Johann Friedrich Bessel (1784–1846) noted the gases emanating from the cometary surfaces might possibly change the orbits of comets.

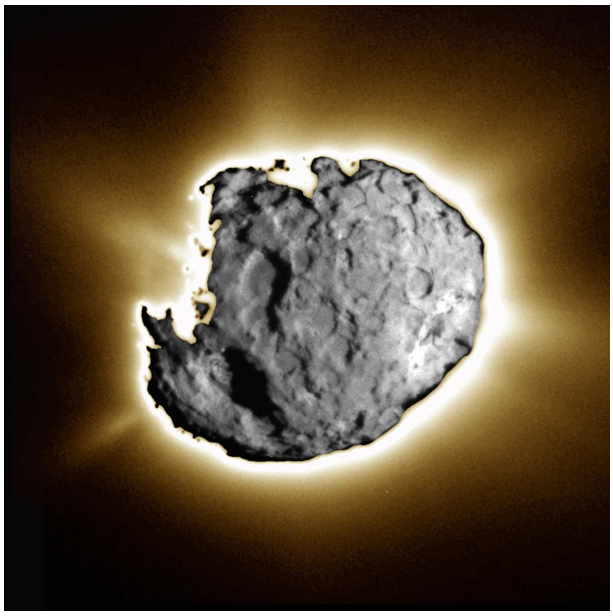

Figure 1: A composite image of the comet Wild 2 taken by the Stardust spacecraft on January 2$^{\text{nd}}$ 2004. The short exposure snapshot depicts the surface topography and the long exposure shows clearly several active jets. The nucleus is approximately 5 kilometres in diameter. From *Stardust, JPL, NASA*.

The precise observations of Solar System objects in the 20$^{\text{th}}$ century allowed us not only to verify the current theory of gravitaton, the General Theory of Relativity, but also to recognise the role of electromagnetic force, which substantially affects the dynamics, escpecially of the small objects.

We can distinguish a number of 'modes', how the electromagnetic field interacts with the matter in the Solar System. We describe this complex interaction in terms of cometary jets, radiation pressure, the Poynting-Robertson effect, the Yarkovsky/YORP effect, the Lorentz force, etc. Such division is very useful, because every mode is usually important only for bodies in a particular size-range or with special surface properties. (For example, the Poynting-Robertson drag affects mainly micrometer dust particles; the jets form on the surface consisting of volatile materials.)

We see an increasing interest in the non-gravitational phenomenon called the *Yarkovsky/YORP effect* during the last 15 years. This is motivated by many observations of small asteroids (and their groups), which properties can be elegantly interpreted with help of the Yarkovsky effect — an electromagnetic recoil force arising due to anisotropic thermal emission from the surface of a celestial body. The implications of this phenomenon on the evolution of small Solar System bodies are the main topic of this thesis.

1.1 Contents and structure of the thesis

We present a brief historical overview of non-gravitational phenomena observed in the Solar System (Section 2.1). It is followed by a state-of-the-art review of the non-gravitational forces acting on small bodies (Section 2.2); hereinafter, we focus on the Yarkovsky/YORP effect. The mathematical formulation of the Yarkovsky/YORP effect and the analytical and numerical methods of its calculation are recalled in Section 2.3.

The major part of the thesis is a detailed description of models we developed to describe the long-term evolution of meteoroids and main-belt asteroids, which reside in both unstable and stable regions. We study transport mechanisms of putative meteoroids from (6) Hebe, (170) Maria and (8) Flora parent bodies to Mars- and Earth-crossing orbits (Section 2.3.4), the case of the asteroid (2953) Vysheslavia (Section 4), the asteroidal population in the 2/1 mean motion resonance with Jupiter (Section 4.5) and the Eos and Agnia asteroid families (Sections 6 and 7). The objects under study or mentioned in the reviews are depicted in Figure 2.

Finally, we describe a by-product of our research: an on-line catalogue of proper orbital elements (Section 9.1), we present numerical tests of a new integrator (Section 9.2) and we reprint a 'lost' publication by I.O. Yarkovsky (Section 9.3).

All major sections start with an abstract, summarizing the main motivation and aim of the following work. We also list the refereed articles, where the results were already published.

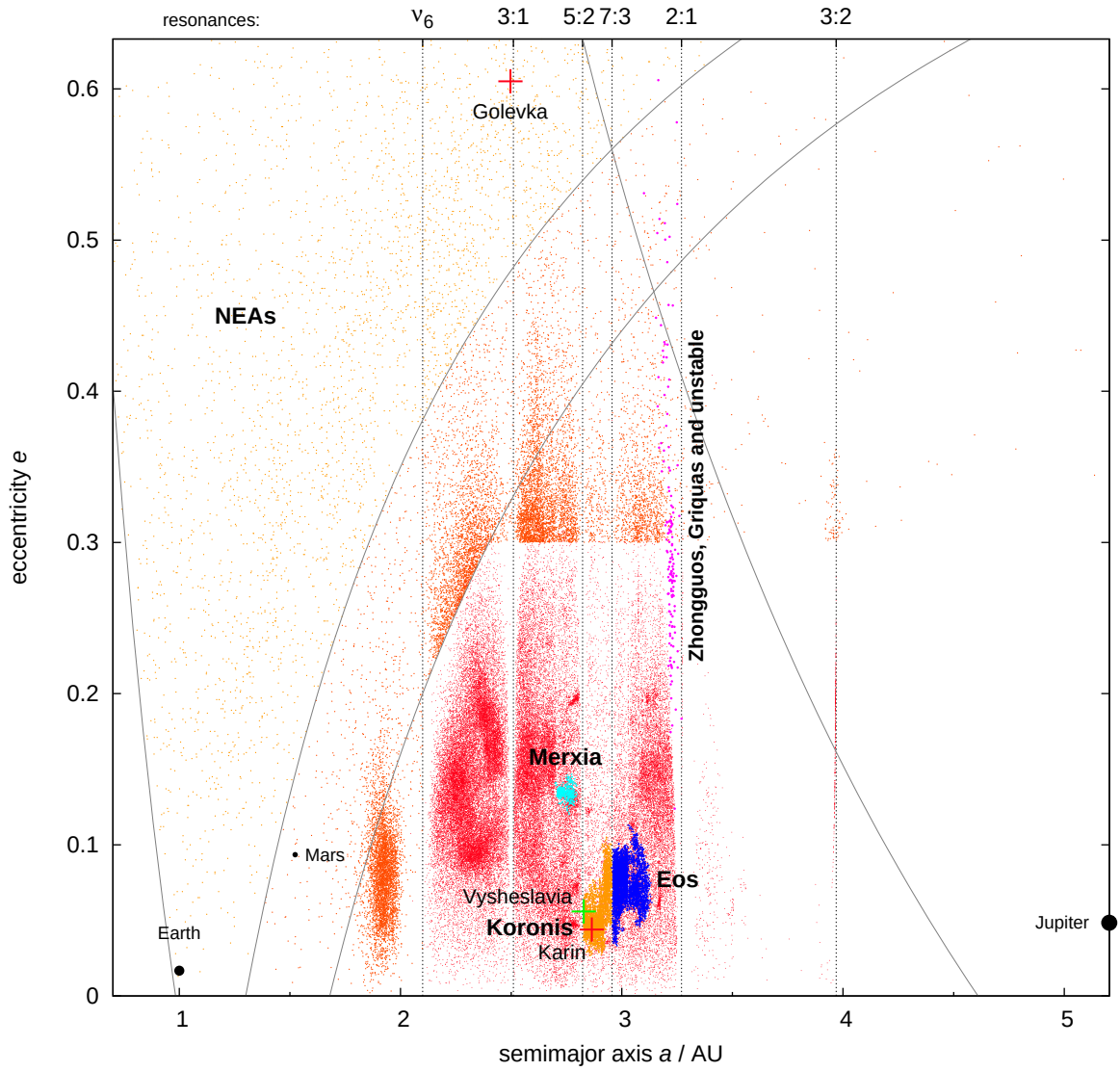

Figure 2: The contents of the thesis displayed as a the semimajor axis vs. eccentricity plot, with the Main Asteroid Belt (red) and the near-Earth space (yellow). Positions of the objects studied (or reviewed) in this thesis are enhanced and labelled: the asteroid (2953) Vysheslavia, the Zhongguos, Griquas and the unstable asteroids in the 2/1 mean motion resonance with Jupiter, the Eos, Koronis and Merxia families, the Karin cluster, and the near-Earth asteroid (6489) Golevka. The curves enclose the region of planet-crossing orbits (they are defined by $Q = q_{\mathrm{Earth}}$, $q < 1.3$ AU, $q < Q_{\mathrm{Mars}}$, $Q > q_{\mathrm{Jupiter}}$, where q's denote perihelia and Q's aphelia).

2 Non-gravitational forces in the Solar System

2.1 A brief history of non-gravitational phenomena

We present a historical 'timeline' of important discoveries connected with non-gravitational phenomena here. The list is sorted by the year of discovery and it is supplemented by several figures, explaining briefly the non-gravitational effects, which we do not discuss elsewhere in the thesis. Most of the data were taken from *Wikipedia*.

1540 Peter Apian (1495–1552) recognised cometary tails are directed away from the Sun.

1619 Johannes Kepler (1571–1630) suggested the Sun exerts a repulsive force on the cometary particles.

1835 Friedrich Wilhelm Bessel (1784–1846) noted, that the orbit of the Halley's comet might change unpredictably due to jets.

1873 James Clerk Maxwell (1831–1839) deduced the existence of a light pressure from his electromagnetic theory.

1884 Otto Boeddicker (1853–1937) measured, that the minimum of the Moon's thermal emission takes place later than the minimum of the Moon's visible light during a total lunar eclipse, what is caused by the thermal inertia of Moon's material.

1888 Ivan Osipovich Yarkovsky (1844–1902) described the non-gravitational effect now called the Yarkovsky effect (even thought in a different context we use it today; see Section 2.1.1).

1899 Pyotr Nikolaevich Lebedev (1866–1912) measured the direct effect of the radiation pressure in a laboratory.

1903 John Henry Poynting (1852–1914) suggested dust particles and even centimetre meteoroids can fall onto the Sun due to a drag force, because the light pressure is decreased behind a moving particle.

1937 Howard Percy Robertson (1903–1961) calculated the radiative drag using an appropriate relativistic theory; now it is called the *Poynting-Robertson drag* (Figure 4).

1950 Fred Lawrence Whipple (1906–2004) defined rocket effect acting on comets due to the sublimation of gases from their surfaces.

1951 Ernst Julius Öpik (1893–1985) described the force arising due to the anisotropic thermal emission, when the surface is heated by the absorption of solar radiation; he noted the original idea in Yarkovsky's pamphlet (see Section 9.3).

1952 Vladimir Vyacheslavovich Radzievskii (1911–2003) described the same effect independently.

1987 The small variations in motion of the LAGEOS artificial satellite were succesfully explained using a Yarkovsky effect theory (Rubincam (1987); Figure 5 and Table 1).

1995 D.P. Rubincam introduced a seasonal variant of the Yarkovsky effect in asteroidal dynamics (Rubincam (1995)).

1998 Paolo Farinella (1953–2000) and others pointed out the importance of the Yarkovsky effect on meteoroids and small asteroids.

2000 D.P. Rubincam calculated Yarkovsky-O'Keefe-Radzievskii-Paddack (YORP) effect, which is able to change rotational states of small asteroids (Rubincam (2000)).

2003 The Yarkovsky effect was measured for the first time on an asteroid (6489) Golevka (Chesley *et al.* (2003)).

Figure 3: Some of the people involved in the explorations of non-gravitational forces. From the left: P. Apian, J. Kepler, F.W. Bessel, J.C. Maxwell, P.N. Lebedev, J.H. Poynting, F.L. Whipple, E.J. Öpik, P. Farinella. From *Wikipedia*.

See Section 2.2 for a review of recent developments in the theory and observation of non-gravitational phenomena.

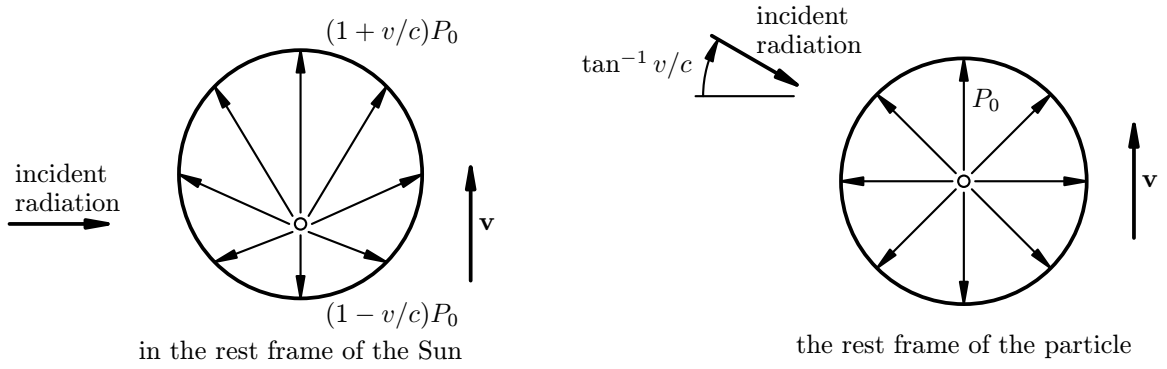

Figure 4: Poynting-Robertson drag depicted in the two reference frames: the rest frame of the Sun and the co-moving frame of the particle. In the first case, the particle scatters more radiation (momentum) forward, due to its non-zero velocity and the corresponding Doppler shift. In the second case, the scattering is isotropic, but the solar radiation is affected by the relativistic abberation and impings the particle preferentially from the front. Both views are equivalent. The particle decelerates, spirals towards the Sun and its orbit becomes circular (i.e., the semimajor axis and eccentricity decrease). Adapted from Burns *et al.* (1979). The relevant timescale of the orbital decay can be estimated as $\tau_{\rm d} = 7 \times 10^6 \,{\rm y} \left(\frac{\varrho}{\rm g/cm^3}\right) \left(\frac{R}{\rm cm}\right) \left(\frac{r}{\rm AU}\right)^2$ (from Bertotti, Farinella & Vokrouhlický (2003)).

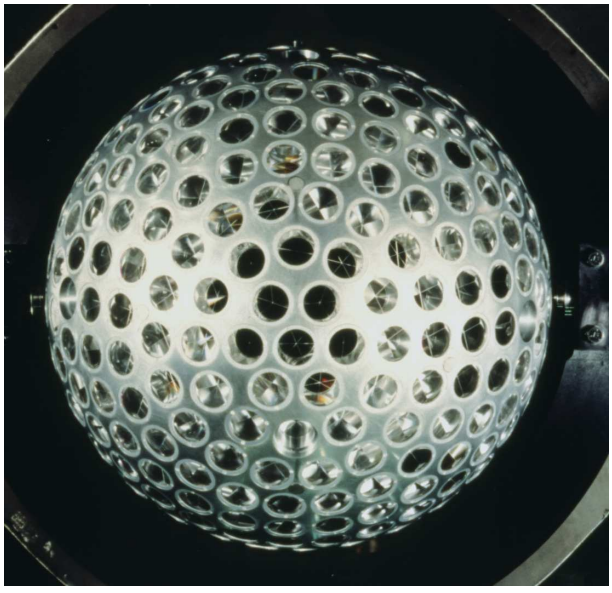

Figure 5: The LAGEOS geodynamical satellite — a sphere with a radius 30 cm and mass 410 kg, covered by 426 retro-reflectors, which make it suitable for the laser tracking by Earth-based observatories. It orbits 5,900 km above the Earth. See also Table 1. From Bertotti, Farinella & Vokrouhlický (2003).

Table 1: Accelerations a of the LAGEOS satellite in $\mathrm{m}\cdot\mathrm{s}^{-2}$ and their fractional uncertainities σ_a/a. LAGEOS is probably the best studied object, for which a very tiny accelerations were detected. The observational limit of the laser-tracking technique is of the order $10^{-12}\,\mathrm{m}\cdot\mathrm{s}^{-2}$. The values below (sorted by their magnitude) are the instantaneous accelerations; some of them might accumulate on the long term (e.g., the Yarkovsky/YORP effect) but the rest produce quasi-periodic oscillations only (e.g, the tidal effects). The radiation effects acting on the LAGEOS have two important sources: the Sun and the Earth. Of course, different spacecrafts have different values of the accelerations: the objects at low Earth orbits typically have many orders of magnitude larger atmospheric drag than LAGEOS; the interplanetery spacecrafts equipped with radio thermoelectric generators, like Cassini, produce additional anisotropic infrared radiation and the corresponding acceleration is of the order $10^{-9}\,\mathrm{m}\cdot\mathrm{s}^{-2}$. Kinematic tides, the polar wobble and length of the day changes are not real accelerations acting on the spacecraft, they only affect the positions of the observing stations. If we do not take them into account directly, we can see these effects as apparent accelerations in the measured signal. Adapted from Bertotti, Farinella & Vokrouhlický (2003).

origin	a $(\mathrm{m}\cdot\mathrm{s}^{-2})$	σ_a/a
Earth's monopole	2.65	2×10^{-9}
Earth's oblatness	0.001	7×10^{-8}
geopotential $\ell, m = 2$	5.8×10^{-6}	3×10^{-5}
Moon	2.1×10^{-6}	10^{-7}
apparent accelerations due to polar wobble and δ(LOD)	upto 10^{-6}	
Sun	9.6×10^{-7}	4×10^{-10}
$\ell, m = 6$	8.8×10^{-8}	7×10^{-4}
dynamic solid tide	3.7×10^{-8}	0.002
kinematic solid tide	5.8×10^{-9}	0.03
dynamic oceanic tide	3.7×10^{-9}	0.1
solar radiation pressure	3.2×10^{-9}	0.02
kinematic ocean loading	10^{-9}	0.2
relativistic effects	9.5×10^{-10}	2×10^{-9}
Earth albedo	3.4×10^{-10}	1
Venus	1.3×10^{-10}	3×10^{-7}
Yarkovsky/YORP effect	5×10^{-11}	0.1
$\ell, m = 18$	6.9×10^{-12}	4×10^{-2}
reference system due to non-rigid Earth	3.5×10^{-12}	0.1
atmospheric drag	1×10^{-12}	0.3–1
Poynting-Robertson effect	10^{-13}	0.1
micrometeorite impacts	10^{-13}	
photoelectric effect due to UV $\odot$ radiation and $\oplus$ ionosphere	$< 10^{-13}$	

Figure 6: Ivan Osipovich Yarkovsky. From Beekman (2006).

2.1.1 Ivan Osipovich Yarkovsky

The Yarkovsky effect is called after Ivan Osipovich Yarkovsky (Figure 6), a person mostly unknown to present-day scientists. Only a very recent publication by Beekman (2006) unveiled some information about his life and work. This is the reason, why we include an excerpt here. We also reprint Yarkovsky's 'lost' publication in Section 9.3.

Ivan Osipovich Yarkovsky was born on 24 May 1844 in Osveya, Vitebsk province, Russia (now Belorussia). He was of Polish nationality. After the death of his parents, he attended military school in Moscow and served in army for several years. Then he succesfully studied in the Institute of Practical Technology in St Petersburg and became a civil engineer in 1872.

He worked for Russian railway companies, but he was also interested in many other technologies as well — manned aviation, ship design, rotary press, etc. He eventually became a president of the Russian Technological Society in 1889.

In his spare time, Yarkovsky studied physical sciences. He tried to find a unified theory of the matter, radiation and gravity and, similarly to other scientists of that time, he though about the ether as an immaterial medium, which enables interactions between separated objects.

His book *Kinetic theory of universal gravitation in relation to the formation of the chemical elements* was published in French in 1888 (Figure 7). He endorsed the theory of the steady expansion of the Earth by the absorption and condensation of the ether. He attributed the 0.1 mm difference found in the length the metre (which was defined as a part of the Earth's circumference) between the 1820 and 1880 measurements to this expansion. According to his ethereal theory of gravitation, the gravitational force could be 'screened' by matter. Yarkovsky even errorneously measured a decrease of solar gravitation during the total solar eclipse on 19 August 1887. Well, as we can see, he was mistaken mostly...

Nevertheless, this is the book, where Yarkovsky mentions the effect, now called after him. He thought, that the planets are decelerated by the ether, as they move along their orbits, but this is compensated by a Sun driven heat engine: the ether is compressed in front of the planet, the Sun heats the ether up as the planet rotates and the warmer ether expands in the back of the planet causing the necessary acceleration. (He tried to support this hypothesis by the observed motion of the great 1882 II comet.) In a modern context, we talk about the solar radiation, absorption, temperature distribution and thermal emission, but the basic priciple is the same.

Ivan Osipovich Yarkovsky died on 22 January 1902 in Heidelberg, Germany. His work fell into oblivion, but 'his' effect was rediscovered in 1950's by Öpik and Radzievskii.

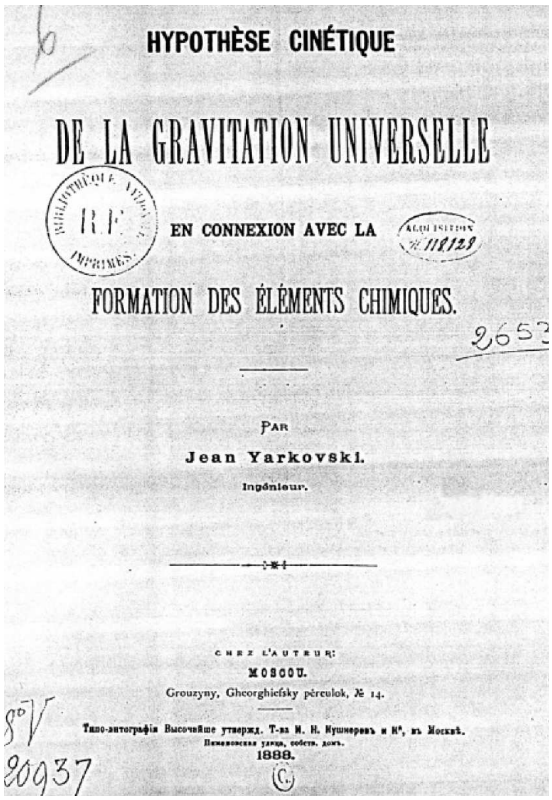

HYPOTHÈSE CINÉTIQUE

DE LA GRAVITATION UNIVERSELLE

EN CONNEXION AVEC LA

FORMATION DES ÉLÉMENTS CHIMIQUES.

PAR

Jean Yarkovski.

Ingénieur.

CHEZ L'AUTEUR:

MOSCOU.

Grouzyny, Gheorghievsky pèreulok, № 14.

1888.

Figure 7: The cover of Yarkovsky's book *Hypothése cinetique de la gravitation universelle en connection avec la formation des éléments chimiques*, where 'his' effect is mentioned for the first time. From Beekman (2006).

2.2 Non-gravitational forces acting on small bodies

The following section reviews recent advances in the studies of non-gravitational forces. It focuses on meteoroids and small asteroids in the 10 cm–10 km size range, for which the principal force and torque arise from an anisotropic thermal emission of the absorbed solar radiation energy. Related perturbations of the orbital and rotational motion are called the Yarkovsky and YORP effects. We demonstrate, that many independent observations, like the current population and size-distribution of near-Earth objects, the existence of unstable resonant asteroids or the structure of asteroid families, can be naturally interpreted in the framework of Yarkovsky/YORP models. This section is an extended version of the reviews published in Brož et al. (2006) and in the Triennal report 2003–2006 of the IAU Commission 7.

Current observations of small Solar System bodies provide many important constraints for dynamical studies. Laboratory analyses of collected meteorite samples, astrometric and photometric observations of small asteroids in the Earth's neighbourhood or relatively larger asteroids orbiting in the Main Asteroid Belt allowed us to recognise, during the last ten years, the importance of non-gravitational phenomena affecting their orbital evolution.

In this review, we are going to focus on small asteroidal bodies in the size-range from 10 cm up to 10 km, which do not exhibit any outgassing and cometary activity. The principal accelerations affecting the motion of these small bodies are listed in Table 2.

The largest non-gravitational accelerations caused by the interaction with the solar radiation field — like the Yarkovsky/YORP effect, the radiation pressure or the Poynting-Robertson drag — are, roughly speaking, 10 orders of magnitude weaker than solar gravity. At a first glimpse, they seem to be too subtle phenomena, but we have to take into account also the direction of the acceleration vector and the effect of its eventual long-term accumulation.

Of course, a small radial acceleration, not exceeding the solar gravity, does not have significant orbital effects (it only slightly decreases or increases the orbital velocity), while a transversal acceleration may cause a secular change of energy (and hence the semimajor axis of the orbit). Some types of accelerations also tend to average-out along the orbit, while others can accumulate over millions or even billions of years. If we take into the account these two issues, the Yarkovsky/YORP effect is by far the most important non-gravitational force in the size-range 10 cm to 10 km and, hereinafter, we will focus on the Yarkovsky/YORP only.

How much a body can change its orbit? What are the secular effects? Typically, the Yarkovsky/YORP force can push a 10-m meteoroid's semimajor axis by 0.1–0.2 AU, before being disrupted by a random collision with another body. Similarly, a small 1-km Main-Belt asteroid can move by 0.05 AU (within its collisional lifetime). These are certainly significant shifts, comparable to the distances between major resonances or to the sizes of asteroid families (i.e., the prominent concentrations of asteroids in the proper-element space). They give a hint that the Yarkovsky/YORP effect plays an important role in the evolution of small Solar System bodies.

We present a brief overview of Yarkovsky and YORP effects principles in Section 2.2.1 and the most direct observational evidences for these phenomena in Section 2.2.2. Section 2.2.3 is devoted to various unstable populations, which the Yarkovsky/YORP helps to sustain, and Section 2.2.4 to evolutionary processes shaping asteroid families.

2.2.1 The Yarkovsky/YORP effect principles

The basic principle of the Yarkovsky/YORP thermal effect is the absorption of solar radiation by a body and its anisotropic thermal reemission. The temperature differences on the surface, together with an

Table 2: The approximate values of radial and transversal accelerations affecting bodies in the size-range 10 cm to 10 km. The solar gravity is scaled to unity. For comparison, typical gravitational perturbations by planets and large asteroids are $GM_{\rm pl} \simeq 10^{-3}$ and $GM_{\rm ast} \lesssim 10^{-9}$.

acceleration	radial	transversal
gravity	$GM_\odot \simeq 1$	
Yarkovsky/YORP effect	10^{-7} to 10^{-11}	10^{-8} to 10^{-12}
radiation pressure	10^{-6} to 10^{-11}	
Poynting-Robertson drag		10^{-10} to 10^{-15}
solar wind, Lorentz force, plasma drag	$< 10^{-15}$	

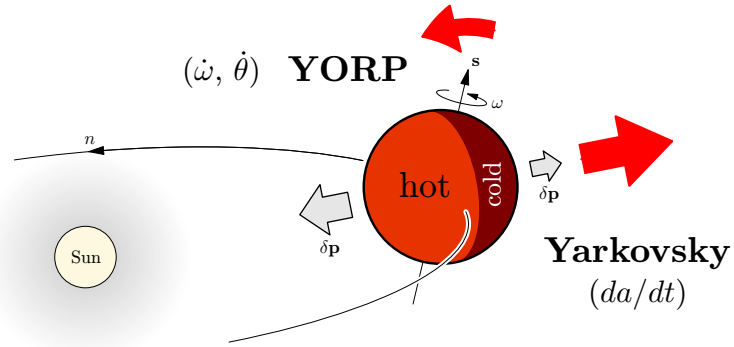

Figure 8: An illustration of the Yarkovsky/YORP effect principle. As an asteroid absorbs the solar radiation, its part facing the Sun becomes hotter than the reverse one. The infrared emission from the surface is then anisotropic, what gives rise to the Yarkovsky force, affecting the orbital motion of the asteroid, and the YORP torque, modifying the spin state.

uneven shape of the body, then lead to a recoil force and torque (Figure 8). (A detailed discussion on the mathematical theory describing the Yarkovsky/YORP effect can be found in Bottke *et al.* (2002b) and references therein.) Contrary to the direct radiation pressure and its relativistic counterpart, the Poynting-Robertson effect, the radiation is absorbed and thermally reprocessed here. Due to a finite thermal conductivity of the material, there is some "thermal lag" between the absorption and the emission. This is also the reason, why the Yarkovsky/YORP effect sensitively depends on the rotational state (obliquity γ and period P).

The Yarkovsky/YORP effect is negligible in case of very small and very large bodies: the upper limit for size D is a natural consequence of the fact, that the force is approximately proportional to the surface area (D^2), the mass $\propto D^3$ and thus the resulting acceleration $\propto 1/D$. The lower limit is given by the conduction of heat across the whole small body, which effectively diminishes temperature differences on the surface and the corresponding infrared emission is then almost isotropic.

In the next sections, we will need to know the principal secular effects of the force and torque on the orbital and rotational dynamics. The Yarkovsky force is related to the orbital dynamics (Rubincam 1995; Vokrouhlický 1998, 1999). Its diurnal variant, driven by the rotational frequency, dominates for bodies with low thermal conductivity (e.g., with regolith on the surface). It can either increase or decrease semimajor axis a and the change Δa is proportional to the cosine of the obliquity γ. In case of the seasonal variant, the changes of temperature on the surface are mainly driven by the orbital frequency. It is a usual situation for bodies with higher thermal conductivity (regolith-free surface). The semimajor axis a steadily decreases and $\Delta a \propto -\sin^2\gamma$.

The YORP torque (Rubincam 2000; Vokrouhlický & Čapek 2002) works for non-spherical bodies only. It has an asymptotic behaviour — it pushes the obliquity towards 0 or 180° and the rotation period towards 0 or ∞. (We note, however, that the behaviour of the YORP and collisional evolution close to these asymptotic spin states is poorly understood today and it will certainly be a subject of forthcoming studies.) Because of the dependence of the Yarkovsky force on the obliquity we can expect a complicated interplay between the Yarkovsky and YORP effects.

Of course all variants of the Yarkovsky forces and the YORP torque are produced by a single temperature distribution on the surface of the body — they are actually a single phenomenon. Nevertheless, we find the above division conceptually useful.

What do we need to calculate the Yarkovsky/YORP? To properly calculate the temperature distribution on the surface of an asteroid (and then straightforwardly the corresponding IR emission, force and torque) we need to know its orbit (i.e., the position of the radiation source), size and shape, spin axis orientation and period, mass, density of surface layers, albedo, thermal conductivity, capacity and IR emissivity of the material.

These are many a priori unknown parameters. In the "worst" case (and for vast majority of asteroids), we know only the orbit and broad-band photometry results (from which we can "guess" an approximate albedo, size and thermal parameters). How to overcome this lack of physical parameters? One possibility is to study only asteroids known very well, like (6489) Golevka (Figure 9). However, we can also use a collective dynamics approach — study whole groups of bodies (like asteroid families) and treat the unknown thermal parameters as statistical quantities, it means to select a reasonable probability distribution and

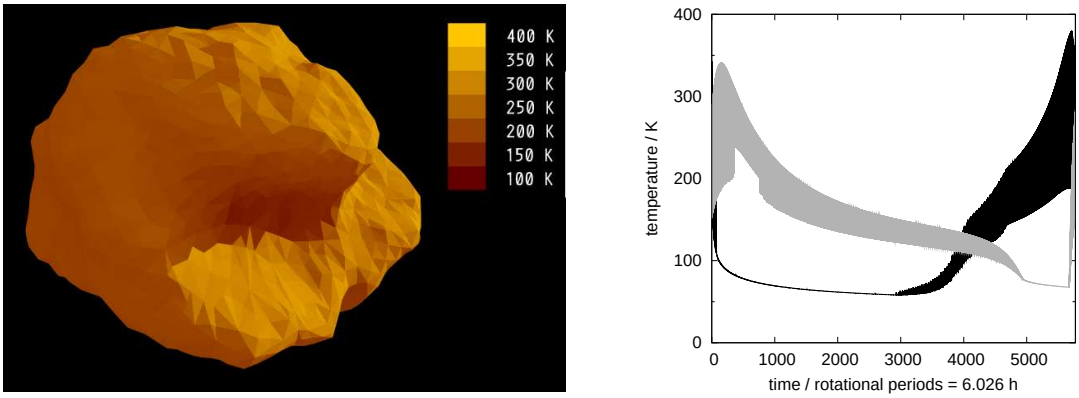

Figure 9: (Left) The temperature distribution on the surface of the asteroid (6489) Golevka, calculated by a numerical solution of the 1-dimensional heat diffusion equation, individually for all 4092 surface elements of the shape model. (Right) For two selected surface elements, located on roughly opposite sides of the body, we plot the time evolution of the temperature (the time is counted as the number of rotations and covers one complete orbit). Both seasonal and diurnal variations of the temperature, due to the changing distance from the Sun, illumination geometry and shadowing, are clearly visible. Adapted from Chesley *et al.* (2003).

assign them randomly to the individual bodies.

2.2.2 The Yarkovsky and YORP: direct observational evidence

Following a previous prediction by Vokrouhlický *et al.* (2000), Chesley *et al.* (2003) were the first to directly detect the non-gravitational semimajor axis drift due to the Yarkovsky effect. Vokrouhlický *et al.* (2000) computed the position of (6489) Golevka during its 2003 close approach to the Earth using all previous radar and optical astrometry data and two models of Golevka's motion: (i) purely gravitational only and (ii) with the Yarkovsky acceleration included (Figure 10).

The respective radar ranging to Golevka, reported by Chesley *et al.* (2003), confirmed the 15 km $O-C$ difference in the distance from the dish, what is outside 3-σ error interval of the purely gravitational model, but it fits very well with the Yarkovsky model. Because the latter involves a non-gravitational acceleration, they were also able to constrain the bulk density of Golevka to $2.7^{+0.4}_{-0.6}\,\mathrm{g/cm^3}$.

The current state-of-the-art model by Čapek & Vokrouhlický (2006) assumes Golevka consists of two layers: low conductivity surface and high conductivity core. It enables to put a lower limit for the surface thermal conductivity K, which should be at least 10^{-2} or $10^{-1}\,\mathrm{W/m/K}$, (i.e., substantially larger than the laboratory-measured conductivity of the lunar regolith $10^{-3}\,\mathrm{W/m/K}$). This is in a rough agreement with thermophysical models, which Delbó *et al.* (2003) use to interpret observed infrared fluxes coming from near-Earth asteroids. The average value of K for all observed NEA's seems to be of the same order.

Unfortunately, we do not have any direct measurement of the YORP effect yet. However, a strong evidence of the ongoing YORP evolution comes from the analysis of a group of Koronis-family asteroids, which has a bimodal obliquity distribution (Slivan 2002; Slivan *et al.* 2003). The prograde group has periods 7.5–9.5 h, obliquities 42°–50° and even similar ecliptic longitudes of the poles within 40°. The values for the retrograde group are $P < 5\,\mathrm{h}$ or $> 13\,\mathrm{h}$ and $\gamma \in (154°, 169°)$ (Figure 11). This observational result was very surprising, because collisions should produce a random distribution of rotational states, surely not the bimodal.

Vokrouhlický *et al.* (2003) thus constructed a model of spin state evolution, which included solar torques and the YORP thermal torque. Let's take the prograde-rotating asteroids as an example (Figure 12). They analysed the evolution of asteroids, which initially had periods $P = 4$–$5\,\mathrm{h}$ and obliquities γ evenly distributed in the interval $(0°, 90°)$. They found the evolution is firstly driven by the YORP effect toward an asymptotic state (γ decreases and P increases). After some 1 Gy, when the precession rate reaches the value $\simeq 26\,''/\mathrm{y}$, the spin is captured in the s_6 spin-orbit resonance and it pushes γ to $\sim 50°$, P to $\sim 8\,\mathrm{h}$ and also forces the spin axes to be really parallel in space. Around the time 2.5 Gy, what is an approximate age of the Koronis family, the match of the model with the observations is perfect. Similarly, it is possible to explain the existence of the retrograde-rotating group; there is no significant spin-orbit resonance in this case and the spin axes of the retrograde-rotating asteroids are let to evolve freely toward the YORP asymptotic states.

Generally, thermal torques seem to be more important than collisions for asteroids smaller than 40 km,

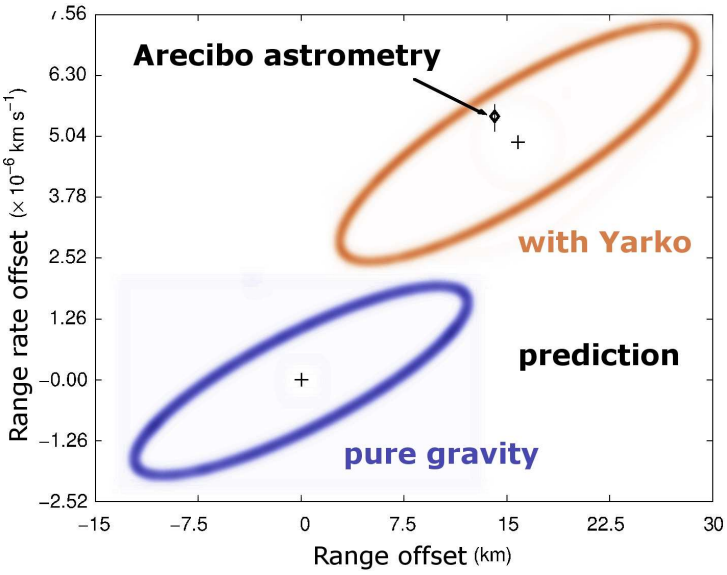

Figure 10: Range vs. range rate (i.e., the quantities measured by radar) for the close approach of (6489) Golevka in May 2003. The predictions of the two theoretical models of Golevka's motion, purely gravitational and with Yarkovsky, are plotted with their 90 % confidence ellipses. The astrometric observation by the Arecibo radar is denoted by the black symbol and arrow. Adapted from Chesley *et al.* (2003).

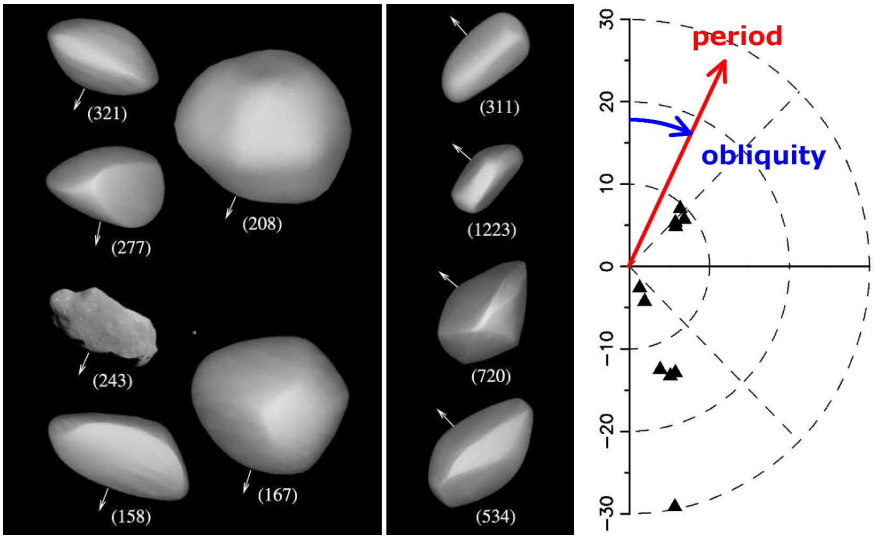

Figure 11: Shape models and spin vectors of 11 Koronis family asteroids (left) and a polar plot period vs. obliquity for the same group (right). Adapted from Slivan *et al.* (2003).

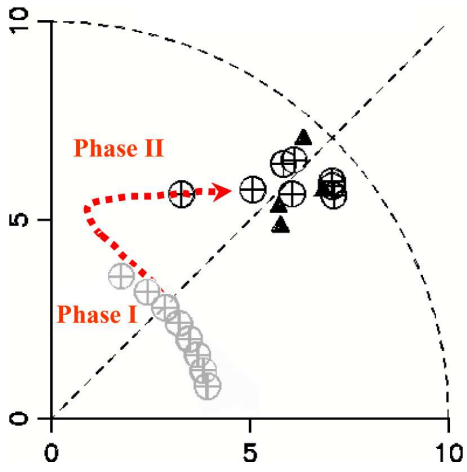

Figure 12: Period vs. obliquity polar plot depicting Slivan's prograde-rotating group. The observed asteroids are denoted by triangles, the initial state of the numerical model by gray circles and the final state after 2.5 Gy by black circles. The dashed line with an arrow shows an evolutionary path and two phases: (i) the YORP driven (Phase I) and (ii) the resonance capture (Phase II). Adapted from Vokrouhlický *et al.* (2003).

because today we can still clearly see the traces of the YORP-driven evolution and the collisions have not been able to randomise the spin states during several past Gy.

2.2.3 Delivery into unstable regions

Various unstable populations, like meteoroids hitting the Earth, near-Earth asteroids, or Main-Belt asteroids located inside major mean motion resonances, have dynamical lifetimes shorter than the age of the Solar System and provide a nice opportunity for dynamicists to look for sources and transport mechanisms.

Meteorite transport from the Main Belt. Meteorite transport from the Main Belt is the eldest application of the Yarkovsky effect (Öpik 1951; Peterson 1976; Farinella *et al.* 1998; Vokrouhlický & Farinella 2000; Bottke *et al.* 2000). The meteorites reach the Earth in two stages: (i) a Yarkovsky-driven change of the semimajor axis spanning ~ 10 My, and (ii) a capture in a powerful gravitational resonance, which increases eccentricity of the orbit up to 1 in a mere ~ 1 My (Figure 13). Approximately 1 % of meteoroids then collide with the Earth (and can be found as meteorites), but most of them fall directly to the Sun.

The main motivation for the introduction of the above Yarkovsky model were the observed cosmic ray exposure (CRE) ages of meteorites, which measure, how long time the meteorite spent in the interplanetary space as a small fragment. The model naturally explains that (i) the CRE ages are much longer than resonance residence times alone; (ii) there is a strong dependence of the CRE's on the material — namely the CRE's of iron meteorites are 10× longer than of stones; (iii) the most stony meteorites have the CRE's of the order 10 My (see Figure 14). The Yarkovsky drift is able to supply meteoroids from a wide range of parent bodies (not only from the vicinity of resonances); it is effective enough to explain the observed meteorite flux of the order 3×10^5 kg/y. Moreover, petrologic and mineralogical studies (Burbine *et al.* 2002) show the number of parent bodies of iron meteorites is larger than of stones. This is because hard irons are more resistant to collisions, their total semimajor-axis drift (within the collisional lifetime) is larger and thus they can effectively sample larger volume of the Main Asteroid Belt.

Delivery of near-Earth asteroids from the Main Belt. Observations of the near-Earth asteroids provide two important constraints: (i) the cumulative distribution of their absolute magnitudes has a slope $\gamma = 0.35$ ($N(<H) \sim 10^{\gamma H}$ in the magnitude range 15.5 to 18; Figure 15), and (ii) their removal rate by planetary scattering is ~ 200 bodies larger than 1 km per My.

Morbidelli & Vokrouhlický (2003) assumed the same basic scenario as for meteorites and constructed a Yarkovsky/YORP model of the transport from the Main Asteroid Belt (this source has the slope $\gamma = 0.26$, again in the interval $H \in (15.5, 18)$ mag). Their model yield a flux of 150–200 bodies (> 1 km) into the main J3/1 and ν_6 resonances (which then quickly became NEA's) and the slope of the resulting model

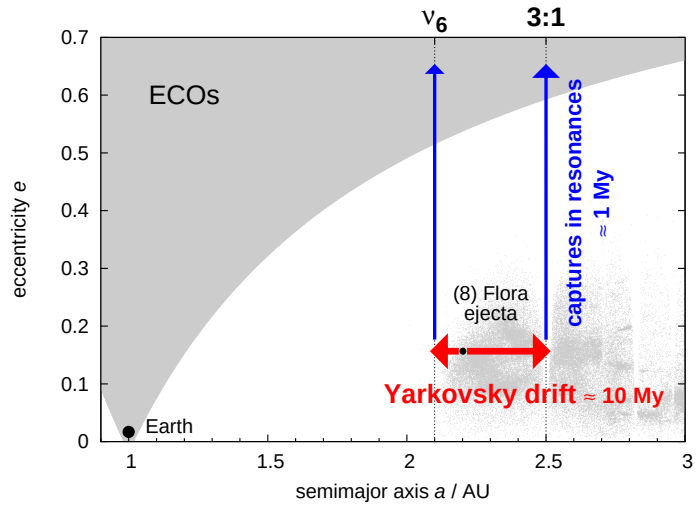

Figure 13: A schematic semimajor axis vs. eccentricity plot of the Yarkovsky-enabled model for the meteorite transport from the Main Belt. In the first stage, spanning typically ~ 10 My, the Yarkovsky effect pushes the semimajor axes of meteoroids toward principal gravitational resonances (like ν_6 secular resonance with Saturn and 3/1 mean motion resonance with Jupiter). In the second stage, the resonances pump the eccentricities quickly and thus in ~ 1 My the orbit reaches Earth-crossing space.

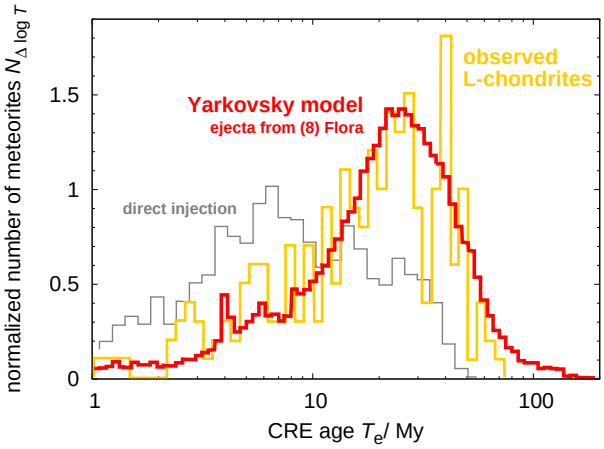

Figure 14: The observed distribution of cosmic ray exposure ages of L-chondrites (thick gray line), compared with the model distribution of Yarkovsky-driven ejecta from (8) Flora (bold line) and with an old model (thin gray line), which assumed only a direct injection of fragments into resonances. The non-random peaks on the observed CRE distribution, which were not possible to fit within a steady-state model, are most probably stochastic events, i.e., large craterings or disruptions, which produced many fragments at once. Adapted from Vokrouhlický & Farinella (2000).

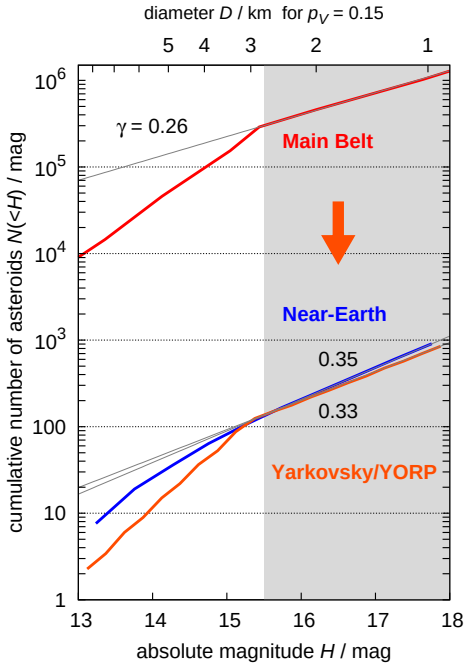

Figure 15: Cumulative distribution of absolute magnitudes H for the three populations: observed Main-Belt asteroids, observed near-Earth asteroids and the Yarkovsky/YORP model population, which assumes transport from the Main Belt to the near-Earth space. The slopes γ of the distributions ($N(<H) \sim 10^{\gamma H}$) were all fitted in the interval $H \in (15.5, 18)$ mag. Adapted from Morbidelli & Vokrouhlický (2003).

NEA population is $\gamma = 0.33$. So, the Yarkovsky/YORP effect is efficient enough to keep the current NEA population in steady state and it also explains, why the observed slope of NEA's is moderately shallower than that of MBA's.

Resonant populations resupplied from the Main Belt. Low-order mean motion resonances with Jupiter usually harbour small populations of objects with dynamically unstable orbits (and sometimes also stable ones). We consider here the J7/3 resonance at approximately 2.96 AU heliocentric distance and the J2/1 resonance at approximately 3.25 AU as two examples, which were previously studied in some detail.

There are 22 observed unstable asteroids in the J7/3 resonance. Tsiganis *et al.* (2003) proved, that the Yarkovsky drift may keep the resonant population in steady state, as it pushes members of the neighbouring Koronis and Eos families towards the resonance. An independent confirmation, that the resonant bodies are truly related to the families is the observed confinement of inclinations — the mean inclinations of the two resonant groups, 2° and 10° respectively, correspond to the mean inclinations of the Koronis and the Eos family (Figure 16).

The J2/1 resonance harbours some 150 asteroids and 50 of them are on dynamically unstable orbits. Brož *et al.* (2005b) simulated the evolution of neighbouring Main-Belt asteroids pushed by the Yarkovsky effect towards the J2/1 resonance. They verified this flux of Main-Belt bodies keeps the unstable resonant population in steady state. Moreover, the orbital evolutionary tracks of the Main-Belt asteroids, their dynamical lifetimes inside the J2/1 resonance and also size distribution are consistent with the actual observed unstable resonant asteroids. A few observed unstable objects, which escape from the J2/1 in less then 2 My, are most probably inactive Jupiter-Family comets.

The long-lived asteroids, confined to stable island of the J2/1 resonance, cannot be explained within the Yarkovsky model and the problem of their origin remains open.

2.2.4 Processes shaping asteroid families

Asteroid families are prominent clusters of asteroids, which are located close to each other in the space of proper elements a_p, e_p and $\sin I_p$ and usually also exhibit some spectral similarities. Families are thought to be remnants of large collisions producing fragments, which then has been evolving due to the Yarkovsky/YORP effect, gravitational resonances and further secondary collisions. The primary collisions

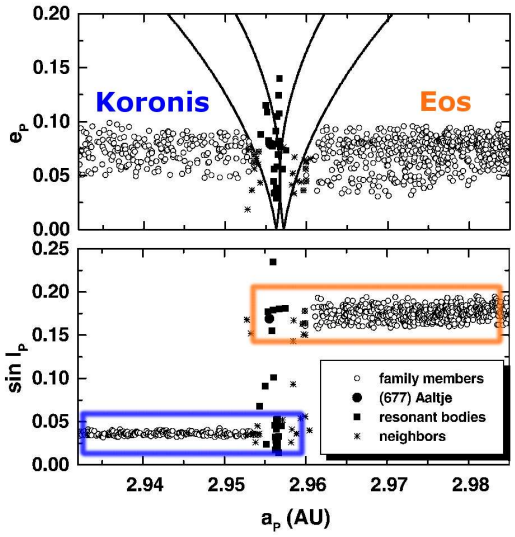

Figure 16: Proper semimajor axis vs. proper eccentricity and inclination in the surroundings of 7/3 mean motion resonance with Jupiter. The resonant asteroids and two adjacent asteroid families, the Koronis and Eos, are plotted. From Tsiganis *et al.* (2003).

can scale from large catastrophic disruptions of parent bodies to smaller cratering events (Michel *et al.* 2001, Durda *et al.* 2006). Typical velocities, which fragments gain with respect to the parent body, are of the order of a few tens of m/s.

Bottke *et al.* (2001) and Vokrouhlický *et al.* (2006a) demonstrated the post-impact evolution of asteroid families using two examples: the Koronis and the Eos family. They reported three general processes, how the Yarkovsky drift together with gravitational resonances can dramatically affect the overall shape of the families, i.e., the distribution of their members in the space of proper orbital elements. We can call these processes "bracketing", "crossing" and "trapping".

At first, notice the shape of the Eos family (Figure 17): it is sharply cut at a low value of proper semimajor axis a_p, there is a evident paucity of asteroids, especially the bigger ones, at large-a_p's and the family is also somewhat distorted or elongated towards low-a_p, low-e_p and low-$\sin I_p$. These observed features nicely coincide with analytically computed borders of resonances, namely with the 7/3 mean motion resonance with Jupiter at 2.955 AU, the J9/4 resonance at 3.03 AU and the $z_1 = g - g_6 + s - s_6$ secular resonance.

We explain the observations this way: initially, just after the parent body disruption, the family was more compact; asteroids drifting due to the Yarkovsky/YORP effect towards smaller semimajor axis meet the powerful J7/3 resonance, which scatters their eccentricities and inclinations, or pumps them up to planet crossing orbits, and consequently no family members are visible behind. The J7/3 resonance thus brackets the Eos family (Figure 17, left).

The asteroids drifting in the opposite direction, towards larger semimajor axis, meet the weaker J9/4 resonance. Some of them are able to cross it, but the remaining are scattered. This crossing explains, why there is less asteroids behind the J9/4, and why the paucity is size-dependent — the smaller asteroids drift faster and typically cross the J9/4 resonance at low eccentricity and inclination (Figure 17, left).

Many Eos-family members are trapped in the z_1 secular resonance; they drift in semimajor axis by the Yarkovsky effect and they are also forced to follow the libration centre of the resonance, which position, however, depends on all three orbital elements a_p, e_p and $\sin I_p$. Thus, not only the semimajor axis changes, but also eccentricity and inclination and the stream of asteroids forms at small values of a_p, e_p and $\sin I_p$, i.e., the elongated shape of the family (Figure 17, right).

In case of the Koronis family the situation is slightly different. This family is split in two parts, each of which has a different mean value of proper e_p (but the same mean $\sin I_p$). Their division correlates with the position of the secular resonance $g + 2g_5 - 3g_6$. A detailed study shows that, unlike in the Eos case, long-lasting captures in this resonance are not possible and drifting orbits necessarily jump over it. During this process their e_p is always lifted by ~ 0.025, right the observed difference between the mean e_p values of the two parts of the Koronis family (Figure 18). Because the resonance does not involve s-frequencies, the inclinations are not affected at all.

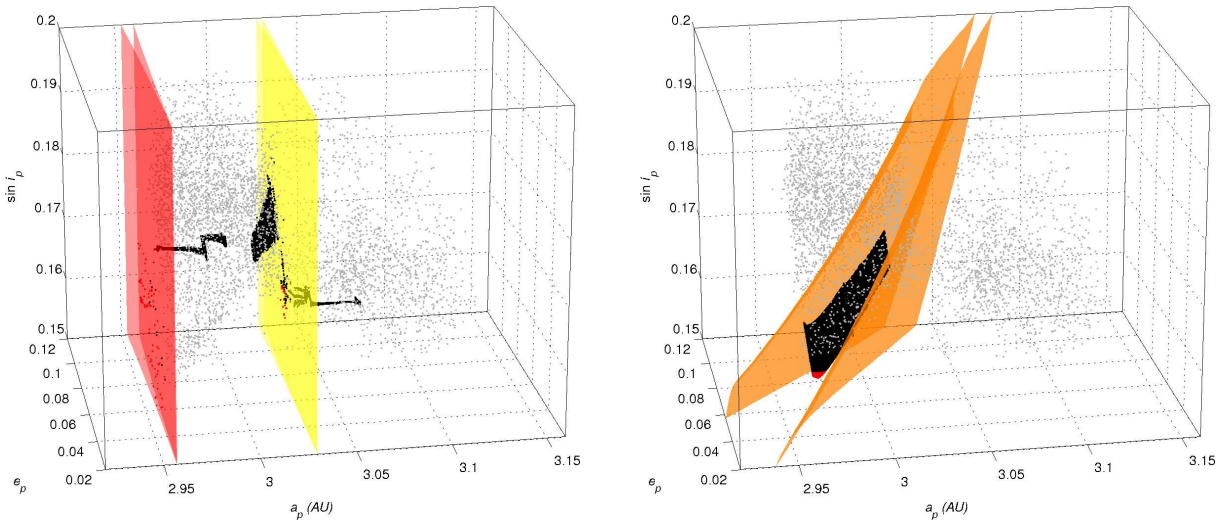

Figure 17: The Eos family in the 3-dimensional space of proper elements a_p, e_p and $\sin I_p$. The three resonances, J7/3 and J9/4 (left) and z_1 (right) are plotted together with examples of bodies drifting by the Yarkovsky effect and interacting with these resonances. Adapted from Vokrouhlický *et al.* (2006a).

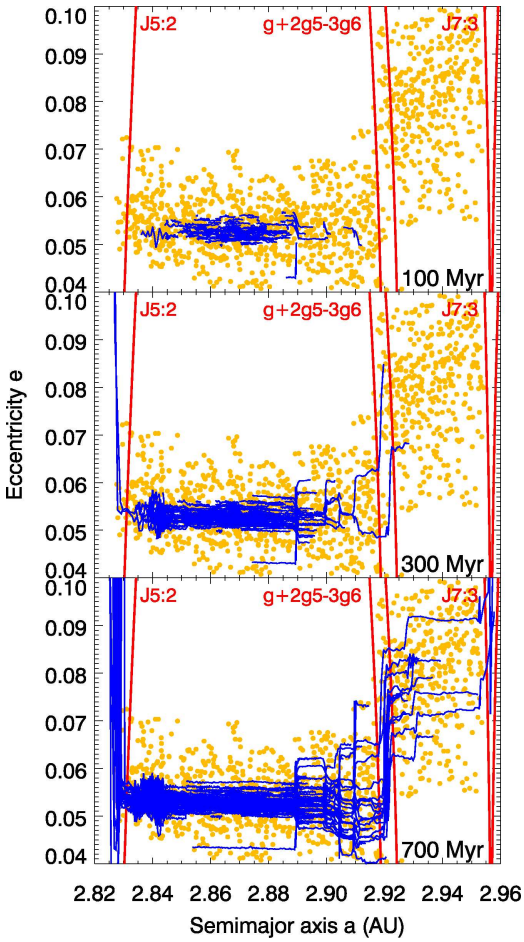

Figure 18: The Yarkovsky-driven evolution of 210 model asteroids (blue lines), placed initially close to (158) Koronis, as compared to the observed Koronis family asteroids (yellow dots). The interaction with the $g + 2g_5 - 3g_6$ secular resonance is clearly visible as a jump in eccentricities close to 2.92 AU. The Koronis family is also bracketed by the strong J5/2 and J7/3 mean motion resonances. The time span of this simulation is 700 My (less then the probably age of the family). From Bottke *et al.* (2001).

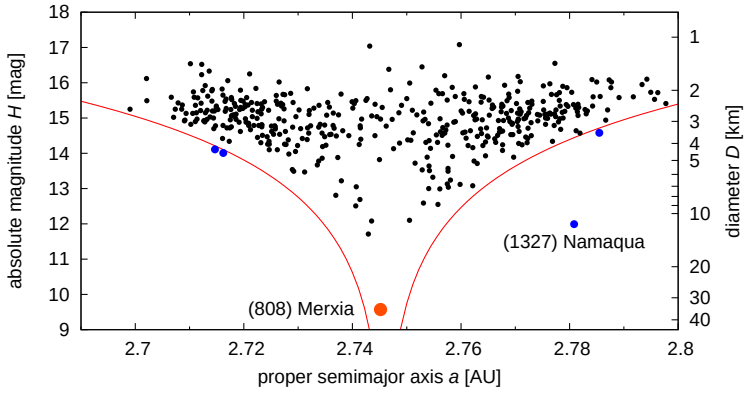

Figure 19: The Merxia family members (identified by the HCM method at the cut-off velocity 80 m/s) in the semimajor axis–absolute magnitude plot. The gray dots outside the 'V'-shape are probable interlopers.

To conclude, if one assumes an initially compact impact-generated family (with a reasonable ejection velocity field compatible with hydrocode models), and takes into account the above evolutionary processes, it is possible to understand the currently observed extent of the family and its overall shape.

"Eared" families and their age determination by the analysis of the (a, H) distribution. The age of an asteroid family, i.e., the time of the collision which generated the family, is a very important parameter, not only for dynamical studies, but also for physical ones, space-weathering models, etc. One indication of the family age seems to be a typical 'V'-shape, which many families exhibit in the proper semimajor axis a_p–absolute magnitude H plane; see Figure 19 for an example of the Merxia family. This shape is a natural consequence of two phenomena: (i) the initial impact, because smaller fragments (with higher H's) gain higher velocities with respect to the parent body and fall farther from the centre, and (ii) the Yarkovsky/YORP effect, because the smaller fragments drift faster in semimajor axis and subsequently move farther from the centre.

There are several outliers visible at the (a_p, H) plot, which do not fit to this scheme. Most probably, they are interlopers, which are not related to the Merxia family. Indeed, the big asteroid (1327) Namaqua is an X-type, which is spectrally incompatible with the S-type Merxia family asteroids.

The problem is, that we do not know the initial spread, just after the impact and we cannot calculate the age simply from the current extent of the family, since the Yarkovsky drift is only responsible for an unknown part of it. Luckily, there is more information hidden in the (a_p, H) plot — notice the depletion of small asteroids in the centre and the overdensity at extreme values of the semimajor axis. Sometimes we call this funny feature an "eared" family (Figure 19). Might this be a YORP effect fingerprint? The YORP effect tilts the spin axes of asteroids directly up or down what enhances the Yarkovsky semimajor-axis drift and can drive the smaller asteroids towards the edges of the family. Possibly, it can allow us to resolve the ambiguity and to determine the age more precisely.

To check it, Vokrouhlický *et al.* (2006b) constructed a family evolution model, which accounts for: (i) an isotropic ejection of fragments (and random periods P and obliquities γ at the beginning), (ii) the Yarkovsky drift, (iii) the YORP effect, and (iv) collisional reorientations. There are four free parameters in the model: (i) the initial velocity dispersion V of 5-km fragments (for a size D, $V(D) = V\frac{5\,\mathrm{km}}{D}$), (ii) the YORP "strength" c_{YORP} (iii) the family age T, and (iv) the surface thermal conductivity K.

They fit this model with observations using a 1-dimensional C-parameter, which is closely related to the semimajor axis a_p and the absolute magnitude H: $C = \Delta a_p / 10^{0.2H}$, where Δa_p is the distance from the family centre. The best fit for the Merxia family (Figure 20) yields the following results: the initial dispersion in semimajor axis was roughly one half of the currently observed one (what is in agreement with a statistical argument of Dell'Oro *et al.*, 2004); the initial velocity was small ($V = 24^{+6}_{-12}$ m/s), what is in agreement with impact models (Michel *et al.* 2001); the YORP effect is important ($c_{\mathrm{YORP}} = 0.6^{+1.4}_{-0.4}$); asteroids are probably covered with a low-conductivity layer ($K = 0.005$ W/m/K); and the family is of the young age ($T = 238^{+52}_{-23}$ My). See Table 3 for results concerning other asteroid families.

Up to now, the analysis of the Merxia family was done in the (a_p, H) plane only. We can, however, use also information hidden in the proper eccentricity e_p and inclination $\sin I_p$. The distribution of the Merxia members is clearly uneven in the (a_p, e_p) plane — the spread of e_p increases abruptly at $a_p \doteq 2.75$ AU. Vokrouhlický *et al.* (2006b) successfully explain it as a Yarkovsky transport across the three-body mean

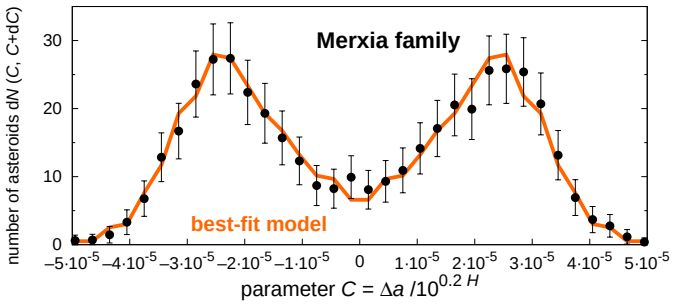

Figure 20: The distribution of the Merxia family members in the C-parameter and the comparison with the best fit model by Vokrouhlický *et al.* (2006b).

Table 3: List of asteroid families and their ages estimated by the method of Vokrouhlický *et al.* (2006b).

family	age/My	family	age/My
Agnia	100^{+30}_{-20}	Erigone	280^{+30}_{-50}
Astrid	180^{+80}_{-40}	Massalia	152^{+18}_{-18}
Eos	1300^{+150}_{-200}	Merxia	238^{-23}_{+52}

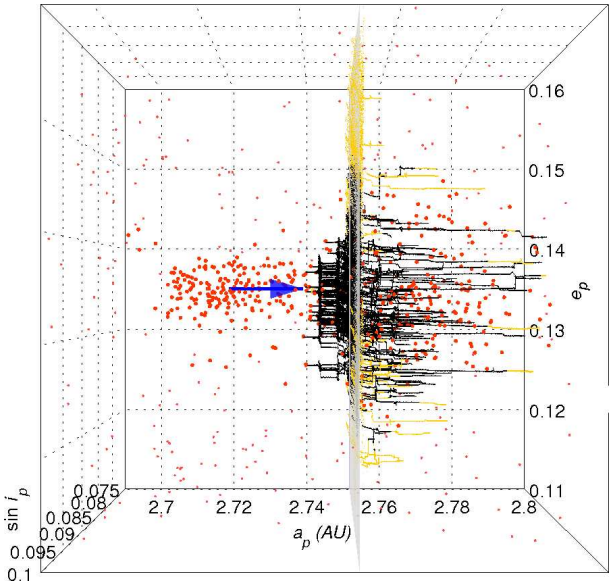

Figure 21: The observed Merxia family asteroids (big orange dots) in the $(a_p, e_p, \sin I_p)$ proper element space and simulated asteroids (black lines) drifting due to the Yarkovsky effect from the centre to larger semimajor axes (i.e., in the direction of the blue arrow). The 3J−1S−1 three-body resonance (which position is indicated by the gray plane at 2.752 AU) spreads the drifting bodies in eccentricity and inclination. The distribution of simulated asteroids behind the resonance then corresponds to the observed positions of the Merxia family members.

motion resonance with Jupiter and Saturn 3J−1S−1. It is actually an independent confirmation that the Yarkovsky semimajor-axis drift is calculated correctly, because the smaller spread of e_p before the resonance is increased by the resonance crossing and then matches the observed spread of the family members behind the resonance (Figure 21).

The chronology method mentioned in this section does not work for "too young" or "too old" families. The former have not had enough time to evolve by the Yarkovsky/YORP and to exhibit the "ears". The latter are much older than the typical time-scale of the YORP-driven evolution and the model does not account for the evolution of totally spun-up or spun-down asteroids.

Table 4: Young asteroid clusters exhibiting a clear convergence of longitudes of perihelia or longitudes of nodes (a sign of a collision, which produced the cluster). The ages were estimated by direct N-body integrations. Nesvorný *et al.* (2003) pointed out these three clusters are also associated with particular dust bands observed by IRAS (the clusters and the corresponding bands have very similar proper inclinations). The large amount of dust was most probably produced by the parent collision (and partially by a subsequent collisional cascade). Farley *et al.* (2006) provided a completely independent confirmation: The plot of ^{3}He abundance in marine sediments vs. their age exhibits a large peak around (8.2 ± 0.1) My. The light helium is thought to be of interplanetary origin and its excess can be attributed to the Veritas event.

cluster	age/My	IRAS dust band
Karin	(5.8 ± 0.2)	2.11°
Veritas	(8.3 ± 0.5)	9.38°
Iannini	< 5	probably J/K (12.11°)

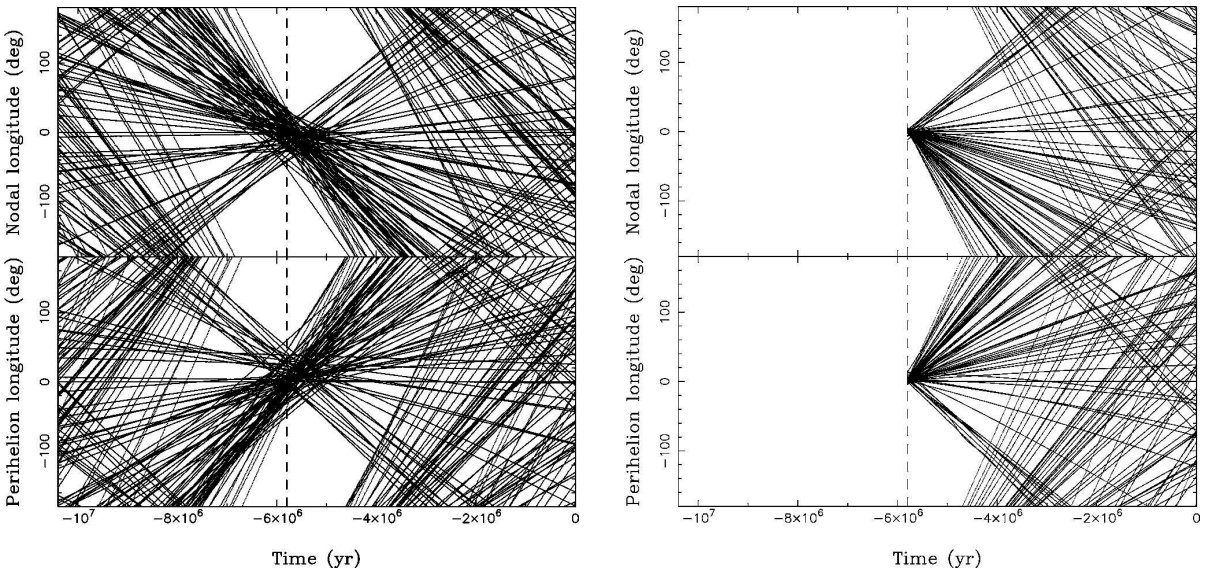

Figure 22: The orbits of the Karin cluster members on the plots longitude of perihelion and longitude of node vs. time. Left: without any non-gravitational forces (the dispersion of Ω and ϖ at the time -5.8 My is $\sim 40°$). Right: with the Yarkovsky semimajor axis drift included (the dispersions are $\sim 5°$ only). The current extent of the Karin cluster in semimajor axis is $\sim 10^{-2}$ AU (i.e., the Yarkovsky drift of the order 10^{-4} AU is clearly visible only in $\Omega(t)$, $\varpi(t)$ plots). From Nesvorný & Bottke (2004).

The youngest clusters and the measurement of the Yarkovsky effect. A few of the compact clusters, like Karin, Veritas or Iannini, exhibit a profound convergence of orbital nodes or perihelia, corresponding to the time of the disruption event; it can be revealed by direct backward N-body integrations. (Nesvorný *et al.* 2002, 2003). In case of the Karin cluster, the age determined this way was found to be 5.8 My (see also Table 4).

The precession rates of Ω and ϖ sensitively depend on the semimajor axis, which is in turn steadily affected by the Yarkovsky acceleration. Nesvorný & Bottke (2004) discovered, that the convergence of Karin orbits can be substantially improved, if they assume a particular value of the semimajor axis drift rate for each Karin member individually (the spread of Ω and ϖ at the impact time drops from 40° downto 5°, which is much more consistent with the observed spread of proper a, e, i, according to the Gauss equations; see Figure 22).

In other words, they were able to actually measure the drift rates $\frac{\mathrm{d}a}{\mathrm{d}t}$ of real asteroids; the only requirement was the better convergence of all orbits belonging to the Karin cluster. The most important conclusion, regarding non-gravitational forces, is that these measured drift rates are of the same magnitude as the theoretically calculated Yarkovsky effect drift rates and, moreover, they also exhibit a clear dependence on size (Figure 23). The model based on the Yarkovsky force also serves a testable prediction: obliquities of asteroids, which can be measured by future photometric observations.

Recently, Nesvorný *et al.* (2006c), Nesvorný & Vokrouhlický (2006) identified four clusters younger

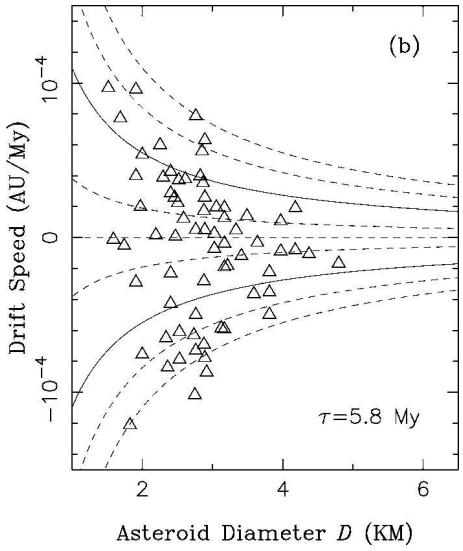

Figure 23: The semimajor axis drift rate $\frac{da}{dt}$ vs. size for the 70 Karin cluster asteroids. The drift values (triangles) plotted here are required for the orbits to have similar Ω's and ϖ's at the time -5.8 My (Figure 22). The diametres of asteroids were calculated from their absolute magnitudes, assuming the albedo 0.25. The curves represent theoretical Yarkovsky drift rates, calculated for different values of obliquity (ranging from 0° to 180°). Larger asteroids have smaller observed maximum drift rates, in agreenment with the Yarkovsky model. The position of the triangle with respect to the curves is essentially a prediction of asteroid obliquity. From Nesvorný & Bottke (2004).

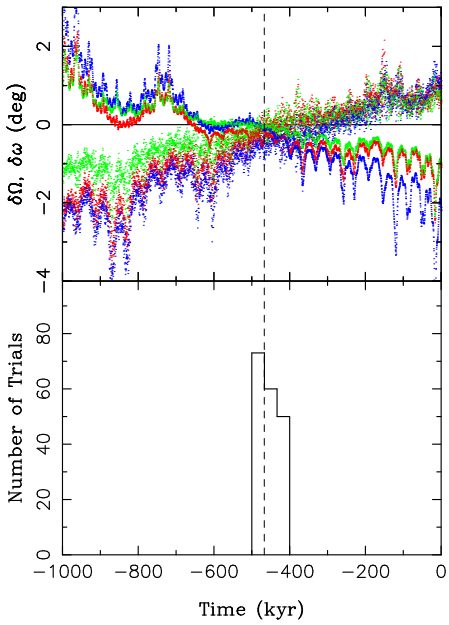

Figure 24: The convergence of Ω and ϖ angles for 3 members of the Datura cluster (relative to the asteroid (1262) Datura; the total number of known members is 7). There is a histogram of plausible ages (with the maximum mutual velocities $\delta V < 5$ m/s) determined from 10^6 various orbital histories. The trials differ due to the uncertainity in orbit determination and the a priori unknown magnitude of the Yarkovsky effect. The cluster formed most probably (450 ± 50) ky ago. From Nesvorný *et al.* (2006c).

than 1 My in the five dimensional space of *osculating* orbital elements (see Figure 24 for an example of the Datura cluster). Even on this short timescale, one have to take the Yarkovsky effect into account, in order to reach the convergence in the sixth element, the mean anomaly, too. The Yarkovsky semimajor axis drift spreads the mean anomaly by 360° in 200 ky only for 1–2 km asteroids (and the effect on Ω and ϖ is also not negligible).

2.2.5 Cometary bodies with outgassing

Cometary bodies are perturbed mainly by the Sun-driven sublimation of ices from the surface and the corresponding rocket effect. The detailed review of the cometary motion modeling was given by Yeomans *et al.* (2004).

The older four-parameter Extended Standard Model was superseded by the Rotating Jet Model, which assumes one or more jets emanating from a rotating nucleus; it can also account for orbit-to-orbit and seasonal changes of the outgassing activity. The jets activity is strongly supported by in-situ observations of cometary nuclei, performed by Deep Space 1, Stardust and Deep Impact spacecrafts (Soderblom *et al.* 2002, Sekanina *et al.* 2004, A'Hearn *et al.* 2005). Chesley & Yeomans (2005) applied the latter model to selected space mission targets. In some cases, it seems to be possible to deduce the physical parameters (i.e., the orientation of the spin axis and the positions of the jets) from astrometric data alone. On the other hand, models like Davidsson & Gutiérrez (2005) try to combine the non-gravitational changes of orbital elements with the nucleus rotational lightcurve and the water production rate.

2.2.6 Conclusions and future work

The non-gravitational forces, namely the Yarkovsky/YORP effect relevant for small asteroidal bodies in the size-range 10 cm to 10 km, are now inevitable ingredients of dynamical models. Today, there is a dozen of important applications of the Yarkovsky/YORP models; we mentioned some of them in this brief review.

The precise measurement of Golevka's non-gravitational drift was only a first step. Within the next decade, we expect a dozen of similar Yarkovsky detections by precise radar astrometry (Vokrouhlický *et al.* 2005c, 2005d) or future optical astrometry with GAIA.

Yarkovsky semimajor-axis drift of the order ~ 10 km per 10 years becomes crucial for an accurate orbit determination and even for estimates of an impact hazard (Giorgini *et al.* 2002). Especially, when the calculation of an impact probability depends on the fact, if the asteroid misses or hits a phase-space "keyhole", which is much smaller then the diameter of the Earth.

Further step forward might be a thorough combination of dynamical models with infrared observations of NEA's and their thermophysical models (Delbó *et al.* 2003) — they supply independent constraints (with different correlations) on Yarkovsky/YORP-related parameters, like the thermal conductivity.

We can await the first direct detection of the YORP effect in the forthcoming years, either from ground-based photometric measurements and corresponding lightcurve modelling, or from the space-borne mission Hayabusa, which now orbits the asteroid (25143) Itokawa (e.g.,Vokrouhlický *et al.* 2004).

The dynamical studies of asteroid families provide also predictions of physical properties and rotational states of individual asteroids, which can serve as good opportunities for further observational tests (similar to Vokrouhlický *et al.* (2005e) who photometrically observed (2953) Vysheslavia and confirmed its retrograde rotation predicted by Vokrouhlický *et al.* (2001)). For example, the small members of the families with intermediate ages (discussed in Section 2.2.4) should exhibit preferential values of obliquities due to the YORP torque and Yarkovsky drift: the asteroids located far from the family-centre at lower/larger values of semimajor axis should have retrograde/prograde rotations. The most suitable families for such survey seem to be the Massalia or the Erigone, located in the inner Main Belt, what makes them more easily observable.

An appealing project would be to determine systematically the ages of all asteroid families, including large and old ones. However, we have to face several obstacles: (i) we still lack the direct measurements of basic physical parameters (albedos, masses, shapes, spectra) for most family members and we cannot expect the situation dramatically improves in the next few years; (ii) a modelling of several subsequent YORP cycles have not been developed yet.

There is already a number of examples, how the YORP torque affects rotational states of asteroids (we discussed some in Sections 2.2.2 and 2.2.4). Moreover, there are further indications: (i) the distribution of rotational periods of all $\sim$1500 asteroids, we have lightcurves for, reveals an excess of very slow and very fast rotators (Pravec & Harris 2000); (ii) small NEA's have a non-Maxwellian distribution of periods; and (iii) there seems to exist a preference of retrograde-rotating asteroids among NEA's (La Spina *et al.* 2004), what is in concert with the positions of Main-Belt escape routes, fed by the obliquity-dependent Yarkovsky drift. A detailed model for a long-term YORP-driven period and obliquity evolution, concerning the entire Main-Belt and NEA's, does not exist yet. Also a possible YORP origin of binaries created by asteroid fission have not been studied in detail.

2.3 A mathematical formulation of the Yarkovsky/YORP effect

The goal of this section is to present, at first, a very simple analytical solution of the 1-dimensional heat diffusion equation, which allows us to quantitatively estimate the Yarkovsky acceleration. This solution, thougth being simple and clear, holds basic properties of the Yarkovsky effect, such as its dependence on material, the rotational or orbital frequency; we also discuss the dependence on size and obliquity. We follow the analysis by Bertotti, Farinella & Vokrouhlický (2003) here. There is a description of the spherically symmetric solution by Vokrouhlický (1998), Vokrouhlický & Farinella (1999) and Vokrouhlický (1999) in the second part, supplemented by notes on its implementation in the `swift_rmvsy` *numerical integrator package, which we usually use for numerical simulations involving the Yarkovsky effect.*

How do we calculate the Yarkovsky/YORP effect? In order to estimate the recoil force and momentum acting on an asteroid, which emits thermal radiation, we need to know, at first, the temperature distribution on its surface. A rough estimate of the mean *equilibrium* temperature $T_{\rm eq}$ can be obtained easily, if we assume the asteroid is in the thermal equilibrium:

$$\pi R^2(1-A)\frac{L_\odot}{4\pi r^2} = 4\pi R^2 \epsilon\sigma T_{\rm eq}^4\,, \tag{1}$$

where A denotes the Bond albedo, $L_\odot \doteq 3.83\times 10^{26}\,\mathrm{W}$ the solar radiation power, r the distance from the Sun, ϵ the infrared emissivity, σ the Stefan-Boltzmann constant (the radius R is not important). If we drop the number 4 from Eq. (1), we get the 'noon' subsolar temperature $T_\star = \sqrt{2}\,T_{\rm eq}$. For (2953) Vysheslavia (with $r \simeq a = 2.83\,\mathrm{AU}$ and $A \simeq 0.2$; discussed in Sec. 4) we have $T_{\rm eq} \doteq 160\,\mathrm{K}$ and $T_\star \doteq 220\,\mathrm{K}$.

Of course, a more realistic situation is more complicated — in order to find the temperature $T(\mathbf{r},t)$, as a function of the position $\mathbf{r}$ and time t, we have to solve a heat diffusion equation in the volume of the body:

$$\nabla\cdot(K\nabla T) = \rho C\frac{\partial T}{\partial t}\,, \tag{2}$$

with a boundary condition on the surface:

$$\left(K\frac{\partial T}{\partial r}\right)_{\rm surface} + \epsilon\sigma T^4 = (1-A)\,\boldsymbol{\mathcal{E}}(t)\cdot\mathbf{n}_\perp(\mathbf{r})\,, \tag{3}$$

where K denotes the thermal conductivity, ρ the density, C the specific thermal capacity and $\mathcal{E}(t)$ the time dependent radiation flux (with respect to the local normal; $\mathcal{E}(t)$ differs from 0 only when the scalar product $\boldsymbol{\mathcal{E}}\cdot\mathbf{n}$ is positive).

2.3.1 A 1-dimensional toy model.

To keep things as clear as possible, let us consider a 1-dimensional example: an half-space $x \geq 0$ of a homogeneous material irradiated by a periodic flux $\mathcal{E}(t) = \mathcal{E}_0 + \mathcal{E}_1\,\mathrm{e}^{\mathrm{i}2\pi f t}$, i.e., 'something like' alternating day and night. (Only the real part $\mathrm{Re}\{\mathcal{E}\} = \mathcal{E}_0 + \mathcal{E}_1\cos 2\pi f t$ is relevant.) We can imagine, this is a single thin 'column' of a big asteroid, with the surface element irradiated by the Sun, which changes its position on the sky. (The frequency f can characterise either the diurnal or the seasonal motion.) The heat diffusion equation (2) and the boundary condition (3) then read:

$$\chi\frac{\partial^2 T}{\partial x^2} = \frac{\partial T}{\partial t}\,, \tag{4}$$

$$-K\frac{\partial T}{\partial x} + \epsilon\sigma T^4 = (1-A)\mathcal{E}(t)\,, \tag{5}$$

where $\chi = \frac{K}{\rho C}$ is the thermal diffusivity of the material. In general, we want to find the temperature $T(x,t)$ as a function of the depth and time.

Because $\mathcal{E}(t)$ is a harmonic function, we 'guess' the response of T, in *steady state*, will be analogous. Thus, we try to find a particular solution of the form $T(x,t) = T_0 + T_1(x)\,\mathrm{e}^{\mathrm{i}2\pi f t}$. ($T_1(x)$ might be a complex function, which would mean a phase shift of the temperature with respect to the incident radiation.) The Eq. (4) then reduces to an ordinary differential equation for $T_1(x)$:

$$\frac{\mathrm{d}^2 T_1}{\mathrm{d}x^2}(x) = \frac{\mathrm{i}2\pi f}{\chi}T_1(x)\,, \tag{6}$$

Table 5: Typical assumed values of the material thermal parameters we use for modelling of the Yarkovsky/YORP effect. ϱ_{bulk} denotes the bulk density, ϱ_{surf} the surface density, K the thermal conductivity, C the specific thermal capacity, and A the albedo.

material	ϱ_{bulk}	ϱ_{surf}	K	C	A
	$\mathrm{kg\cdot m^{-3}}$	$\mathrm{kg\cdot m^{-3}}$	$\mathrm{W\cdot m^{-1}\cdot K^{-1}}$	$\mathrm{J\cdot kg^{-1}\cdot K^{-1}}$	
bare basalt	3500		0.5–2.5	680	0.1–0.16
regolith covered	3500	1500	0.001–0.01	680	
metal	8000		~ 40	500	0.09–0.11
C-type	1000		0.1–1	1500	0.03–0.08

which non-divergent solution we find easily:

$$T_1(x) = T_1(0)\,\mathrm{e}^{-\sqrt{\mathrm{i}2\pi f/\chi}\,x} = T_1(0)\,\mathrm{e}^{-(1+\mathrm{i})\sqrt{\pi f/\chi}\,x}\,. \tag{7}$$

We see the *changes* of the temperature decrease with depth as $\mathrm{e}^{-\frac{x}{\delta}}$ and the penetration depth of the thermal wave is of the order $\delta = \sqrt{\chi/(\pi f)}$. (And, moreover, there is some phase shift too.)

We still do not know the surface temperature $T(0,t)$. Here, we exploit the boundary condition (Eq. 5), where we substitute the already known derivative $\frac{\partial T}{\partial x}(x,t) = -(1+\mathrm{i})\sqrt{\pi f/\chi}\,T_1(x)\,\mathrm{e}^{\mathrm{i}2\pi ft}$, so

$$K(1+\mathrm{i})\sqrt{\pi f/\chi}\,T_1(0)\,\mathrm{e}^{\mathrm{i}2\pi ft} + \epsilon\sigma(T_0 + T_1(0)\,\mathrm{e}^{\mathrm{i}2\pi ft})^4 = (1-A)(\mathcal{E}_0 + \mathcal{E}_1\,\mathrm{e}^{\mathrm{i}2\pi ft})\,. \tag{8}$$

The calculation of the fourth power, and especially the solution, would be 'distressful'. Nevertheless, we suppose $T_1(0) \ll T_0$ (i.e., the changes of the temperature are small with repsect to the mean temperature) and *linearize* Eq. (8) as $(T_0+T_1)^4 = T_0 + 4T_0^3T_1 + \mathcal{O}(T_1^2)$. We subtract the terms with T_0 and $\mathcal{E}_0$ (they correspond exactly to the equilibrium temperature in Eq. (1)) and we are left with a linear equation for $T_1(0)$:

$$(1+\mathrm{i})\sqrt{\pi fKC\rho}\,T_1(0) + 4\epsilon\sigma T_{\mathrm{eq}}^3\,T_1(0) = (1-A)\mathcal{E}_1\,.$$

The surface temperature is expressed as:

$$T(0,t) = T_{\mathrm{eq}} + \frac{(1-A)\mathcal{E}_1\,\mathrm{e}^{\mathrm{i}2\pi ft}}{(1+\mathrm{i})\sqrt{\pi fKC\rho} + 4\epsilon\sigma T_{\mathrm{eq}}^3}\,.$$

The denominator is a complex number (it means a phase shift); after an algebra we see that:

$$T(0,t) = T_{\mathrm{eq}} + \frac{(1-A)\mathcal{E}_1}{4\epsilon\sigma T_{\mathrm{eq}}^3}\,\frac{1}{1+2\Theta+2\Theta^2}\,\mathrm{e}^{\mathrm{i}(2\pi ft+\phi_{\mathrm{th}})}\,, \tag{9}$$

where the thermal parameter Θ and phase lag ϕ_{th} are:

$$\Theta = \frac{\sqrt{\pi fKC\rho}}{4\pi\epsilon\sigma T_{\mathrm{eq}}^3}\,, \quad \tan\phi_{\mathrm{th}} = -\frac{\Theta}{1+\Theta}\,. \tag{10}$$

For sake of completeness we can write the temperature at a depth (however, it is not crucial for us, because the dynamical action is driven by $T(0,t)$ only):

$$T(x,t) = T_{\mathrm{eq}} + \frac{(1-A)\mathcal{E}_1}{4\epsilon\sigma T_{\mathrm{eq}}^3}\,\frac{1}{1+2\Theta+2\Theta^2}\,\mathrm{e}^{\mathrm{i}(2\pi ft+\phi_{\mathrm{th}}-\sqrt{\pi f/\chi}\,x)}\,\mathrm{e}^{-\sqrt{\pi f/\chi}\,x}\,. \tag{11}$$

There are two visualisations of this steady-state solution (Eq. 11) of the 1-dimensional heat diffusion equation (Eq. 4) in Figures 25 and 26. Thermal properties of materials, from which asteroids probably consist, are listed in Table 5. The summary of the thermal lag ϕ_{th} values (Eq. 10) and the temperature amplitude values $T_1(0)$ (Eq. 9) for typical diurnal and seasonal frequencies is provided in Table 6. The ratio $T_1(0)/T_{\mathrm{eq}}$, which is of the order $\simeq 0.1$ in some cases, tells us, that we are just approaching the limits of the linear theory and the temperature in a full non-linear theory might differ, probably by $\simeq 10\,\%\cdot T_1$.

Knowing the surface temperature T (on an object of any shape), we calculate the elementary radiation force due to the emission of photons, carrying the momentum away from the single surface element $\mathrm{d}S$, as:

$$\mathrm{d}\mathbf{F}_{\mathrm{Y}} = -\frac{2}{3}\frac{\epsilon\sigma T^4}{c}\mathrm{d}S\mathbf{n}_{\perp}\,. \tag{12}$$

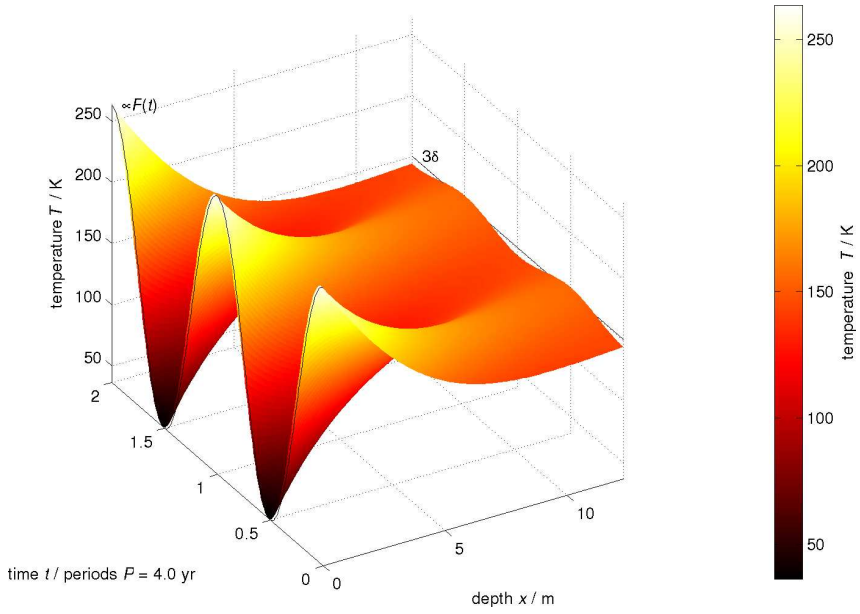

Figure 25: A 3-D plot of the depth x vs. time t vs. temperature T as resulted from the 1-dimensional toy model (Eq. 11). The material properties correspond to a basaltic rock (see Table 5), with the thermal conductivity $K = 1\,\mathrm{W/m/K}$. The flux amplitude $\mathcal{E}_1$ is one half of the equilibrium flux $\mathcal{E}_0$ at 2.5 AU from the Sun; the frequency of the flux $\mathcal{E}(t)$ corresponds to the orbital period of $P = 4\,\mathrm{y}$. The flux is plotted as a thin line in the (t, T) plane and it is scaled the same as the amplitude of the surface temperature $T_1(0)$. The thermal lag between the incident flux $\mathcal{E}(t)$ and the surface temperature $T(0, t)$ is then clearly visible ($\phi_{\mathrm{th}} \doteq -4°$).

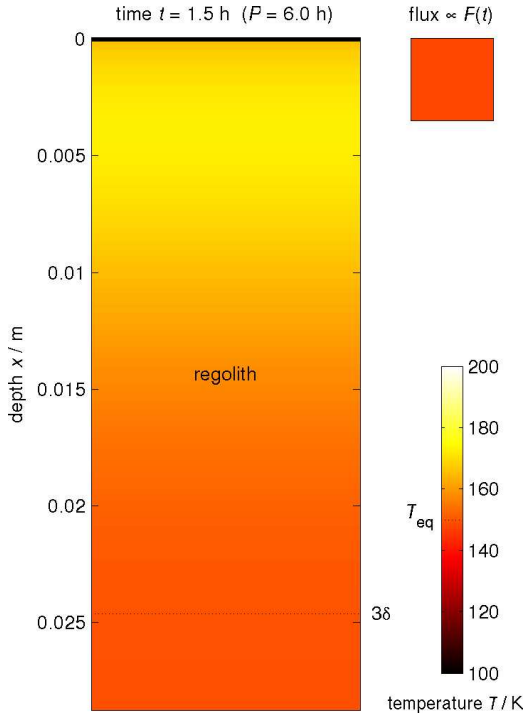

Figure 26: An estimate of the temperature T (colour coded) in the depth x (vertical coordinate) — some sort of "an asteroid cross-section" — for a regolith-like material with the thermal conductivity $K = 0.01\,\mathrm{W/m/K}$ (see Table 5). The situation depicted here corresponds to the 1-D toy model (Eq. 11), with the flux $\mathcal{E}(t)$ period $P = 1/f = 6$ hours, i.e., a typical diurnal motion, and the particular time $t = 1.5\,\mathrm{h}$. The dotted line denotes the depth 3δ, where $\delta = \sqrt{\chi/(\pi f)}$ is the characteristic penetration depth of the thermal wave. There is a colour coded flux $\mathcal{E}(1.5\,\mathrm{h})$, scaled similarly as T, in the upper right square.

Table 6: The penetration depth of the thermal wave δ (Eq. 7), the thermal parameter Θ (Eq. 10), the thermal lag $\phi_{\rm th}$ (Eq. 10) and the amplitude of the surface temperature $T_1(0)$ (Eq. 9) as resulted from the 1-dimensional toy model. The flux amplitude $\mathcal{E}_1$ is one half of the equilibrium flux $\mathcal{E}_0$ at 2.5 AU from the Sun ($T_{\rm eq} \doteq 170\,{\rm K}$). The values were calculated for two types of material (taken from Table 5) and two different periods $P = 1/f$ of the flux $\mathcal{E}(t)$ — a typical diurnal (6 hours) and a seasonal (4 years).

material	P	δ	Θ	$\phi_{\rm th}$	$T_1(0)$
		m		deg	K
basalt	6 h	0.05	6	−40	1
	4 y	4	0.08	−4	82
regolith	6 h	0.008	0.4	−15	47
	4 y	0.6	0.005	−0.3	94

The factor $\frac{2}{3}$ conforms to the Lambert law of scattering; $\mathbf{n}_\perp$ denotes the external normal unit vector. The Yarkovsky acceleration of a homogeneous body with the total mass m is then given by the integration over the whole surface:

$$\mathbf{a}_{\rm Y} = -\frac{2}{3}\frac{\epsilon\sigma}{mc}\int_S {\rm d}S\,\mathbf{n}_\perp T^4 \simeq -\frac{8}{3}\frac{\epsilon\sigma}{mc}T_{\rm eq}^3\int_S {\rm d}S\,\mathbf{n}_\perp T_1\,, \tag{13}$$

where we can use the linearization of T^4 again.

Similarly, we express the total YORP torque (affecting the spin of the body):

$$\mathbf{T}_{\rm Y} = \int_S \mathbf{r}\times{\rm d}\mathbf{F}_{\rm Y} = -\frac{2}{3}\frac{\epsilon\sigma}{c}\int_S \mathbf{r}\times\mathbf{n}_\perp {\rm d}S\,T^4\,. \tag{14}$$

The major orbital perturbation caused by $\mathbf{a}_{\rm Y}$ is the semimajor axis drift. The first Gauss equation reads:

$$\frac{{\rm d}a}{{\rm d}t} = \frac{2\mathcal{T}}{n} + \mathcal{O}(e)\,, \tag{15}$$

where $\mathcal{T}$ denotes the transversal component of $a_{\rm Y}$. As we can see from Eq. (13), the resulting total transverse acceleration $\mathcal{T}$ (hence, the semimajor axis drift rate ${\rm d}a/{\rm d}t$) is: i) proportional to the *deviations* of temperature from the equilibrium, ii) the sine of the thermal lag angle $\sin\phi_{\rm th}$ (see Figure 27), and iii) inversely proportional to the size (because $F_{\rm Y} \propto$ surface area S and $a_{\rm Y} = \frac{F}{m}$).[1]

The YORP torque $\mathbf{T}_{\rm Y}$ changes the angular momentum L of the body: $\frac{{\rm d}\mathbf{L}}{{\rm d}t} = \mathbf{T}_{\rm Y}$. In case the body rotates around the shortest axis of the inertia tensor, then $\mathbf{L} = C\omega\mathbf{e}$, where C denotes the moment of inertia (assumed constant), ω the angular velocity and $\mathbf{e}$ the unit vector along the spin axis. The rate of change of $\mathbf{L}$ is usually expressed in three angular variables:

$$\frac{{\rm d}\omega}{{\rm d}t} = \frac{\mathbf{T}\cdot\mathbf{e}}{C}\,, \tag{16}$$

$$\frac{{\rm d}\gamma}{{\rm d}t} = \frac{\mathbf{T}\cdot\mathbf{e}_{\perp 1}}{C\omega}\,, \qquad \mathbf{e}_{\perp 1} = \frac{(\mathbf{N}\cdot\mathbf{e})\,\mathbf{e} - \mathbf{N}}{\sin\gamma}\,, \tag{17}$$

$$\frac{{\rm d}\psi}{{\rm d}t} = \frac{\mathbf{T}\cdot\mathbf{e}_{\perp 2}}{C\omega}\,, \qquad \mathbf{e}_{\perp 2} = \frac{\mathbf{e}\times\mathbf{N}}{\sin\gamma}\,, \tag{18}$$

where γ is the obliquity, ψ the longitude, $\mathbf{T}$ the total torque (aside the YORP one, there are usually gravitational torques and inertial terms due to the motion of the reference frame), the unitvector $\mathbf{N}$ is perpendicular to the orbital plane. $\frac{{\rm d}\omega}{{\rm d}t}$ scales as $\frac{1}{R^2}$ (because $T_{\rm Y} \propto R^3$ and $C \propto R^5$).[2]

[1] A typical magnitude of the radiation force per $1\,{\rm m}^2$ could be ${\rm d}F_{\rm Y} \doteq \frac{2}{3}\frac{0.9\cdot5.67\cdot10^{-8}\cdot160^4\cdot1}{3\cdot10^8}\,{\rm N} \doteq 10^{-7}\,{\rm N}$. For a typical 1-km asteroid, we have roughly (see the parameters for the regolith material and the diurnal frequency in Table 6): $a_{\rm Y} \doteq \frac{8}{3}\frac{0.9\cdot5.67\cdot10^{-8}\cdot160^3}{(4/3)\cdot3.14\cdot1000^3\cdot3500\cdot3\cdot10^8}\,4\cdot3.14\cdot1000^2\cdot47\,{\rm m\cdot s^{-2}} \doteq 10^{-13}\,{\rm m\cdot s^{-2}}$ (compare it to the gravitational acceleration $a_{\rm G} = \frac{GM_\odot}{r^2} \doteq 10^{-3}\,{\rm m\cdot s^{-2}}$); the transverse component $\mathcal{T} \doteq 10^{-13}\cdot\sin 15^\circ\,{\rm m\cdot s^{-2}} \doteq 10^{-14}\,{\rm m\cdot s^{-2}}$, the mean motion $n = \sqrt{\frac{GM_\odot}{a^3}} \doteq 0.004\,\frac{\rm rad}{\rm day}$ and the resulting semimajor axis drift rate $\frac{{\rm d}a}{{\rm d}t} \doteq \frac{2\cdot10^{-14}\cdot(86400^2/150\cdot10^9)}{0.004}\cdot 365.25\cdot 10^6\,\frac{\rm AU}{\rm My} \doteq 10^{-4}\,\frac{\rm AU}{\rm My}$. These order-of-magnitude estimates are consistent with a more complex 3-D modelling (see Section 2.3.2, Figure 29).

[2] A crude estimate of the YORP torque acting on a 1-km asteroid with an irregular shape might be $T_{\rm Y} = |\int_S \mathbf{r}\times{\rm d}\mathbf{F}_{\rm Y}| \doteq 1000\cdot10^{-7}\cdot10^{-2}\cdot4\cdot3.14\cdot1000^2\,{\rm N\cdot m} \doteq 10^1\,{\rm N\cdot m}$. (Here, we naively assumed that 1 % of the whole surface area radiates in

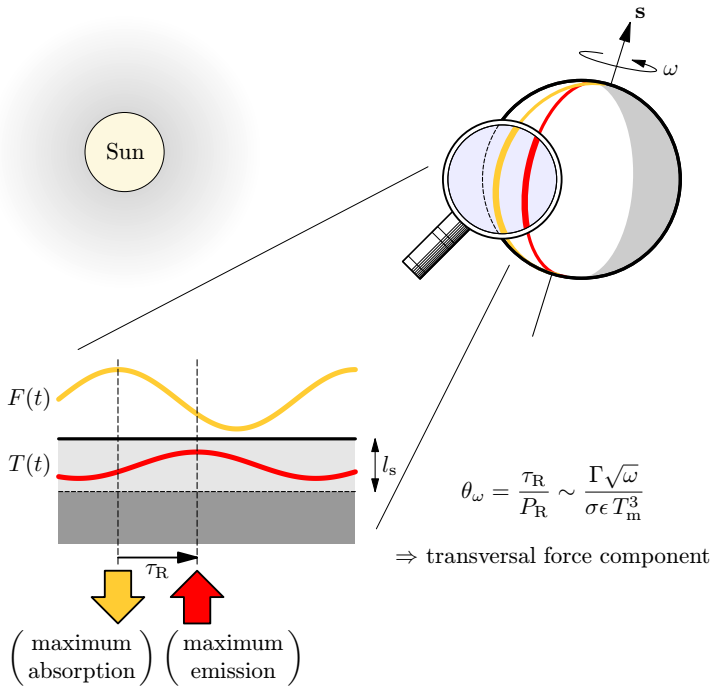

Figure 27: The time lag between the absorption of the solar radiation and the thermal emission arising on a rotating spherical body. The incident solar flux $F(t)$ is maximum at the subsolar point, but the maximum emission takes place somewhat later due to the rotation. Therefore, the radiation force has a non-zero tranversal component, which is proportional to the sine of the thermal lag angle $\sin\phi_{\rm th}$ (measured between the yellow and red semicircles on the sphere).

There are two important aspects we could not account for in the 1-D model above: i) the finite size of the body, and ii) the dependence on the obliquity. If the size is of the order δ or smaller, the conduction of heat across the body effectively equilibrates the surface temperature and thus spherically symmetric bodies are not accelerated any more.

The obliquity γ (i.e., the angle between the rotational axis and the normal to the orbital plane) is also an important parameter. Let us imagine a sphere orbiting the Sun (Figure 28) and distinguish three special cases:

1. The prograde diurnal rotation ($\gamma = 0°$) and the inevitable thermal lag give rise to a non-zero transverse component $\mathcal{T}_{\rm Y}$ of the Yarkovsky acceleration, which causes the body to spiral away from the Sun (semimajor axis steadily increases, in agreenment with the Gauss equation $\frac{{\rm d}a}{{\rm d}t} \doteq \frac{2\mathcal{T}}{n}$).
2. On the contrary, the retrograde rotation ($\gamma = 180°$) forces the semimajor axis to decrease.
3. The spin axis tilted in the orbital plane ($\gamma = 90°$) means, there are large seasonal temperature variations and the corresponding thermal lag (calculated for the orbital frequency) leads to a steady decrease of semimajor axis (regardless on the sense of the diurnal rotation).

Both the dependence on size and obliquity arise naturally in 3-dimensional models (see Section 2.3.2).

2.3.2 A spherically symmetric linear model.

An analytical solution of the heat diffusion equation with a linearized boundary condition is also possible for a sphere and an appropriate solar flux $\mathcal{E}(t)$ (Vokrouhlický (1998), Vokrouhlický & Farinella (1999), Vokrouhlický (1999)). Hereinafter, we use scaled quantities (denoted by dashes): $r' = r/l_{\rm s}$,

one direction tangent to the surface.) The moment of inertia is approximately $C = \frac{8}{15}\pi R^5\rho \doteq 5\cdot 10^{18}\,{\rm kg}\cdot{\rm m}^2$. Therefore, $\frac{{\rm d}\omega}{{\rm d}t} \doteq \frac{10^1}{5\cdot 10^{18}}\,\frac{\rm rad}{\rm s^2} = 2\cdot 10^{-18}\,\frac{\rm rad}{\rm s^2}$. What is the timescale for a complete spin-down? If we start with $\omega_0 = 3\cdot 10^{-4}\,\frac{\rm rad}{\rm s} \doteq 5\,\frac{\rm rev}{\rm day}$, then $\tau_\omega \doteq \frac{3\cdot 10^{-4}}{2\cdot 10^{-18}}\,{\rm s} = 1.5\cdot 10^{14}\,{\rm s} \doteq 10^7\,{\rm y}$. (The timescale for a spin-up is of the same order, because the upper limit is $\omega_{\rm crit} \doteq 11\,\frac{\rm rev}{\rm day}$; if the rotation is faster, gravitationally bound bodies likely disintegrate.) Similarly, $\frac{{\rm d}\gamma}{{\rm d}t} \doteq \frac{10^1}{5\cdot 10^{18}\cdot 3\cdot 10^{-4}}\,\frac{\rm rad}{\rm s} \doteq 10^{-14}\,\frac{\rm rad}{\rm s}$ and a $\frac{\pi}{2}$ change of the tilt can be expected after $\tau_\gamma \doteq \frac{1.57}{10^{-14}}\,{\rm s} \doteq 10^7\,{\rm y}$.

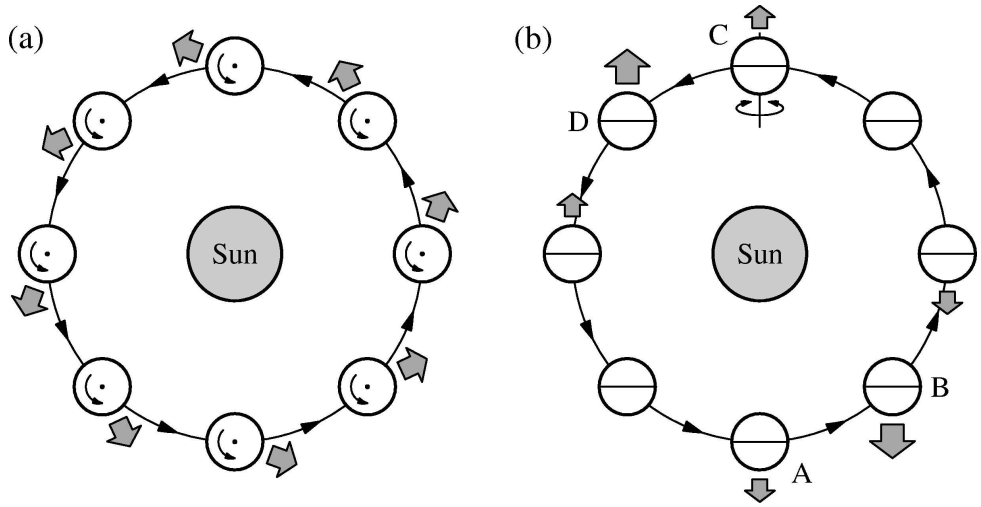

Figure 28: Diurnal and seasonal variants of the Yarkovsky effect and the dependence on the obliquity γ. The gray arrows denote the recoil force acting on the body. (a) The diurnal Yarkovsky effect, when the body rotates around the spin axis perpendicular to the orbital plane. In this case of prograde rotation, the force causes an increase of the semimajor axis a. Generally, the change $\Delta a \propto \cos\gamma$. (b) The seasonal Yarkovsky effect, with the spin axis in the orbital plane. The heating of the hemispheres, mainly at points A and C, and the delayed emission of thermal radiation, mainly at points B and D, produce a recoil force, which magnitude changes along the orbit, but which transverse component is always opposite to the velocity, thus causing a steady decrease of the semimajor axis ($\Delta a \propto -\sin^2\gamma$).

$l_\mathrm{s} = \sqrt{K/\rho C\omega_\mathrm{rev}}$, $\Delta T' = \Delta T/T_\star$, $\epsilon\sigma T_\star^4 = \alpha\mathcal{E}_\star$, $\alpha = (1-A)$, $\Delta\mathcal{E}' = \Delta\mathcal{E}/\mathcal{E}_\star$, $\Delta\mathcal{E} = \mathcal{E} - \mathcal{E}_\star/4$, $\zeta = \mathrm{e}^{\mathrm{i}\lambda}$, $\lambda = \omega_\mathrm{rev}(t-t_0)$. The flux can be written easily in terms of spherical harmonics:

$$\Delta\mathcal{E}' = \sum_{n\geq 1}\sum_{k=-n}^{n} a_{nk}(\zeta)\, Y_{nk}(\theta,\phi)\,. \tag{19}$$

We need three dipole terms only (to express the flux differs from zero on the illuminated hemisphere only):

$$a_{10}(\zeta) = \sqrt{\frac{\pi}{3}}\,\cos\theta_0\,, \qquad a_{1\pm1}(\zeta) = \mp\sqrt{\frac{\pi}{6}}\,\sin\theta_0\, e^{\mp i\phi_0}\,, \tag{20}$$

where (θ_0,ϕ_0) are the coordinates of the Sun, which in turn change periodically with time, according to $\cos\theta_0 = -\sin\gamma\sin\lambda = \frac{i}{2}\sin\gamma(\zeta-\zeta^{-1})$, $\sin\theta_0\, e^{\pm i\phi_0} = -(\sin^2\frac{\gamma}{2}\,\zeta^{\mp(m+1)} + \cos^2\frac{\gamma}{2}\,\zeta^{\mp(m-1)})$, where γ is the obliquity.

The heat diffusion equation and the boundary condition (Eqs. 2 and 3) in spherical coordinates (and after the linearization) now read:

$$i\zeta\frac{\partial}{\partial\zeta}\Delta T'(r';\theta,\phi;\zeta) = \frac{1}{r'^2}\left\{\frac{\partial}{\partial r'}\left(r'^2\frac{\partial}{\partial r'}\right) + \frac{1}{\sin\theta}\left[\frac{\partial}{\partial\theta}\left(\sin\theta\frac{\partial}{\partial\theta}\right) + \frac{1}{\sin\theta}\frac{\partial^2}{\partial\phi^2}\right]\right\}\Delta T'(r';\theta,\phi;\zeta)\,, \tag{21}$$

$$\sqrt{2}\Delta T' + \Theta\left(\frac{\partial\Delta T'}{\partial r'}\right)_{R'} = \Delta\mathcal{E}'\,. \tag{22}$$

It is convenient to look for a solution T', which has a the same structure as the source flux (Eq. 19):

$$\Delta T'(r';\theta,\phi;\zeta) = \sum_{n\geq 1}\sum_{k=-n}^{n} t'_{nk}(r';\zeta)\, Y_{nk}(\theta,\phi)\,. \tag{23}$$

The properties of the Eqs. (21) and (22) (namely the orthogonality of the Y_{nk} functions) lead to a complete separation of radial, angular and time variables and even individual Fourier modes. Vokrouhlický (1999) found the solution for the three necessary dipole coefficients $t'_{10}(R';\zeta)$ and $t'_{1\pm1}(R';\zeta)$. (We do not write them explicitly here, but see Sec. 2.3.3.)

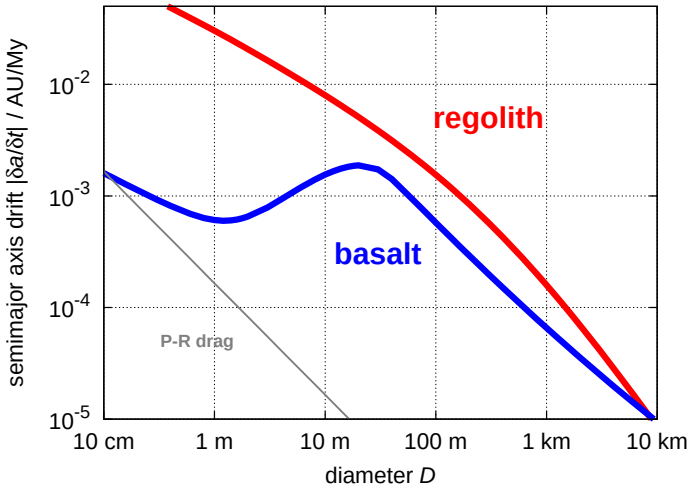

Figure 29: The sum of absolute values $|\mathrm{d}a/\mathrm{d}t|$ of the diurnal and the seasonal semimajor axis drift rates vs. size, calculated for spherical bodies with a moderate value of obliquity $\gamma = 135^\circ$ and consisting of two materials from Table 5: bare basalt and regolith covered, i.e., with high and low thermal conductivity. (Of course, for particular values of γ the diurnal or the seasonal Yarkovsky effect may vanish; they can even cancel each other, when the diurnal rate is positive and the seasonal negative.) Nevertheless, the sum plotted here shows clearly an approximate maximum total drift (per 1 My) one can expect. The mean collisional lifetime is roughly 50 My for a 10-m stony meteoroid and 500 My for a 1-km asteroid (Farinella *et al.* (1998), Bottke *et al.* (2005b)). Note, that we do not expect very small regolith-covered bodies to exist, thus the drift rates larger than 10^{-2} AU/My are not realistic. The drift rate caused by the Poynting-Robertson drag is also plotted; it prevails for sizes smaller than $\lesssim 10$ cm.

The Yarkovsky acceleration is given by the integration over the surface of the sphere:

$$\mathbf{f}(\zeta) = -\frac{2\sqrt{2}}{3\pi}\alpha\,\Phi \int \mathrm{d}\Omega\,\Delta T'(R';\theta,\phi;\zeta)\,\mathbf{n}\,, \tag{24}$$

where $\Phi = (\mathcal{E}_\star \pi R^2/mc)$. We obtain the following expressions for the components (f_X, f_Y, f_Z):

$$f_X(\zeta) + \mathrm{i} f_Y(\zeta) \;=\; -\frac{8}{3\sqrt{3\pi}}\,\alpha\,\Phi\,t'_{1-1}(R';\zeta)\,, \tag{25}$$

$$f_Z(\zeta) \;=\; -\frac{4}{3}\sqrt{\frac{2}{3\pi}}\,\alpha\,\Phi\,t'_{10}(R';\zeta)\,. \tag{26}$$

The equatoreal components (in the XY plane) are called diurnal (because it depends mainly on the rotational frequency), while the along-axis component is called seasonal (because of the orbital frequency). Note, there is zero YORP torque (Eq. 14) within spherical models.

In order to find secular effects of the Yarkovsky acceleration on the semimajor axis, we have to transform it to the heliocentric reference frame, substitute to the Gauss equation $\mathrm{d}a/\mathrm{d}t = 2\mathcal{T}/\omega_{\mathrm{rev}}$ and average over one orbit. The results for the diurnal and seasonal components are of the form:

$$\left(\frac{\mathrm{d}a}{\mathrm{d}t}\right)_{\mathrm{d}} \;\simeq\; -\frac{8\alpha}{9}\,\frac{\Phi}{\omega_{\mathrm{rev}}}\,\frac{E_{R'_m}\sin\delta_{R'_m}}{1+\chi}\,\cos\gamma\,, \tag{27}$$

$$\left(\frac{\mathrm{d}a}{\mathrm{d}t}\right)_{\mathrm{s}} \;=\; \frac{4\alpha}{9}\,\frac{\Phi}{\omega_{\mathrm{rev}}}\,\frac{E_{R'}\sin\delta_{R'}}{1+\chi}\,\sin^2\gamma\,. \tag{28}$$

The dependence of $\mathrm{d}a/\mathrm{d}t$ on the obliquity (discussed already within the 1-D toy model in Section 2.3.1) is recalled here. An example, how the semimajor axis drift rates depend on size is depicted in Figure 29.

2.3.3 The implementation in the `swift_rmvsy` package

Most of the simulations of the long-term orbital evolution presented in Sections 2.3.4 to 7 exploit the spherical linear model of the Yarkovsky acceleration (Sec. 2.3.2). In our previous work (Brož, 1999) we modified

the SWIFT integrator package (see *SWIFT*; Levison & Duncan (1994)) to account for the Yarkovsky diurnal and seasonal accelerations. We distribute this add-on in the package called `swift_rmvsy`, which can be downloaded from *Yarko-site*. The latest version contains also filtering routines suitable for calculation of proper and 'resonant' elements; see Section 9.1 for details.

How do we calculate the Yarkovsky acceleration in the SWIFT integrator? We follow Vokrouhlický (1998) and Vokrouhlický & Farinella (1999), and we include several optimizations, which improve the speed of the calculation and reduce round-off errors. We present the algorithm here as a 'recipe'.[3]

The quantities have similar names as the variables in the relevant Fortran subroutines (`io_init_th.f`, `yarko_seasonal.f`, `getacc_yarko.f`). The global arrays, in which we store quantities for all test particles, keep them in the memory and pass to next subroutines, are indexed by the subscript i. We do not write the respective for-cycles explicitly.

The steps 1–4 have to be performed only once (in the `io_init_th.f` and `io_init_spin.f` subroutines), at the startup.

1. Read the input quantities from the `th.in` file: $R, \rho, \rho_{\rm surf}, K, C, A, \epsilon, [T]_{\rm h}$; and the spin unitvector $(s_1, s_2, s_3)_i$ from the `spin.in` file. If the period $T < 0$, calculate $\omega = \frac{2\pi}{5{\cdot}3600\,{\rm s}} \frac{1}{2R/1000\,{\rm m}}$, otherwise $\omega = \frac{2\pi}{[T]_{\rm h}{\cdot}3600\,{\rm s}}$.

2. Calculate auxilliary quantities : $M = \frac{4}{3}\pi R^3\rho$, $\Gamma = \sqrt{\rho_{\rm surf} C K}$, $l_s = \sqrt{\frac{K}{\rho_{\rm surf} C \omega}}$, $R' = \frac{R}{l_s}$, $R'_{0i} = \frac{R}{\sqrt{K/\rho_{\rm surf} C}}$.

3. Evaluate complex numbers: $z = \frac{1}{\sqrt{2}}(1 - {\rm i})R'$,

   $\sin z = \frac{1}{2{\rm i}} \left(\cos {\rm Re}\{z\} + {\rm i} \sin {\rm Re}\{z\} - [\cos(-{\rm Re}\{z\}) + {\rm i}\sin(-{\rm Re}\{z\})]\, {\rm e}^{2\,{\rm Im}\{z\}} \right)$,

   $\cos z = \frac{1}{2} \left(\cos {\rm Re}\{z\} + {\rm i} \sin {\rm Re}\{z\} + [\cos(-{\rm Re}\{z\}) + {\rm i}\sin(-{\rm Re}\{z\})]\, {\rm e}^{2\,{\rm Im}\{z\}} \right)$

   (both the expressions were divided by the factor ${\rm e}^{{\rm Im}\{z\}}$ to avoid numerical problems; it would cancel anyway in the following fraction),

   $\psi_i = \frac{(z^2-3)\sin z + 3z\cos z}{\sin z - z\cos z}$.

4. Pre-calculate additional thermal parameters of TPs (in order to minimize the number of operations performed every timestep; $S_0 = 1361\,{\rm W}\cdot{\rm m}^{-2}$ is the solar constant): $\lambda_{0i} = \frac{\Gamma\sqrt{\omega}}{\epsilon\sigma\sqrt{2}R'}$, $\theta = \sqrt{2}R'\lambda_{0i}$, $\lambda_{{\rm s}0i} = \frac{\Gamma}{\epsilon\sigma\sqrt{2}}$, $T_{\star 40i} = \frac{(1-A)S_0}{\epsilon\sigma}$, $\rho_{0i} = -\frac{4}{9}\frac{\epsilon\sigma\pi R^2}{Mc}\frac{(86400\,{\rm s})^2}{149597870{\cdot}10^3\,{\rm m}}$, $\theta_{{\rm s}i} = \frac{\Gamma}{\epsilon\sigma T_{\star 40i}^{3/4}}\frac{1}{\sqrt{86400\,{\rm s}/k_{\rm gauss}}}$, $\rho_{{\rm s}0i} = \frac{\pi R^2 S_0}{Mc}(1-A)$.

In the steps 5–7, we evaluate the seasonal Yarkovsky coefficients, which do not depend on the fast mean anomaly, but only on the slow elements. They are computed every ${\rm d}t_{\rm filter}$ (usually 1 y) in the subroutine `yarko_seasonal.f`. The mass m_1 is the subroutine input parameter, the keplerian osculating orbital elements $(a_i, e_i, I_i, \omega_i, \Omega_i)$ are passed in a common block from the `io_write_filter.f` subroutine, where they are calculated anyway.

5. Calculate powers of the eccentricity upto 7 in advance ($e^1 = e_i$, $e^j = e^{j-1}e^1$) and then the development:

   $\alpha_1 = 1 - 3\frac{1}{2^3}e^2 + \frac{5}{6}\frac{1}{2^2}e^4 - \frac{7}{72}\frac{1}{2^7}e^6$,

   $\alpha_2 = 4\left(2\frac{1}{2^2}e^1 - \frac{16}{3}\frac{1}{2^4}e^3 + 4\frac{1}{2^6}e^5\right)$,

   $\alpha_3 = 9\left(3\frac{1}{2^3}e^2 - \frac{45}{4}\frac{1}{2^5}e^4 + \frac{567}{40}\frac{1}{2^7}e^6\right)$,

   $\alpha_4 = 16\left(\frac{16}{3}\frac{1}{2^4}e^3 - \frac{128}{5}\frac{1}{2^6}e^5\right)$,

   $\alpha_5 = 25\left(\frac{125}{12}\frac{1}{2^5}e^4 - \frac{4375}{72}\frac{1}{2^7}e^6\right)$,

   $\alpha_6 = 36\left(\frac{108}{5}\frac{1}{2^6}e^5\right)$,

   $\alpha_7 = 49\left(\frac{16807}{360}\frac{1}{2^7}e^6\right)$,

[3] We focus on the implementation in the SWIFT (which itself includes four different integration schemes), but, of course, this algorith can be theoretically used in any other scheme, assuming it allows to incorporate accelerations, which depend on positions, velocities and also explicitly on time (because we use some developments in eccentricity to calculate the seasonal Yarkovsky effect).

$\beta_1 = 1 - \frac{e^2}{8} + \frac{e^4}{192} - \frac{e^6}{9216}$,
$\beta_2 = \frac{4}{2}e^1\big(1 - \frac{e^2}{3} + \frac{e^4}{24}\big)$,
$\beta_3 = \frac{27}{8}e^2\left(1 - \frac{9}{16}e^2 + \frac{81}{640}e^4\right)$,
$\beta_4 = \frac{16}{3}e^3\left(1 - \frac{4}{5}e^2\right)$,
$\beta_5 = 25\frac{125}{384}e^4\left(1 - \frac{25}{24}e^2\right)$,
$\beta_6 = \frac{972}{80}e^5$,
$\beta_7 = \frac{823543}{46080}e^6$.

6. Calculate the scalar products $\mathbf{P}\cdot\mathbf{s}$ and $\mathbf{Q}\cdot\mathbf{s}$ (one may wish to pre-calculate the sines and cosines) and other thermal quantities:
$sP = (\cos\omega_i\cos\Omega_i - \sin\omega_i\sin\Omega_i\cos I_i)\cdot s_{1i} + (\cos\omega_i\sin\Omega_i + \sin\omega_i\cos\Omega_i\cos I_i)\cdot s_{2i} + (\sin\omega_i\sin I_i)\cdot s_{3i}$,
$sQ = (-\sin\omega_i\cos\Omega_i - \cos\omega_i\sin\Omega_i\cos I_i)\cdot s_{1i} + (-\sin\omega_i\sin\Omega_i + \cos\omega_i\cos\Omega_i\cos I_i)\cdot s_{2i} + (\cos\omega_i\sin I_i)\cdot s_{3i}$,
$\eta = \sqrt{1-e^2}$, $n = \sqrt{m_1}a_i^{-3/2}$, $R' = R'_{0i}\sqrt{n/86400\,\mathrm{s}}$, $X_1 = \sqrt{2}R'$, $\lambda_\mathrm{s} = \theta_{\mathrm{s}i}(a_i\eta)^{3/4}\frac{1}{X_1}$,
$a_{\mathrm{th}0} = \frac{4}{9}\frac{\rho_{\mathrm{s}0i}}{a_i^2(1+\lambda_\mathrm{s})}\frac{(86400\,\mathrm{s})^2}{149597870\cdot10^3\,\mathrm{m}}$,

7. Calculate the seasonal coefficients for each $k = 1$ upto k_seasonal (usually 7); one may whish to pre-calculate $\sin X_k$, $\cos X_k$ and e^{-X_k}:
$X_k = \sqrt{2k}R'$,
$A_k = -\mathrm{e}^{-X_k}(X_k+2) - [(X_k-2)\cos X_k - X_k\sin X_k]$,
$B_k = -\mathrm{e}^{-X_k}X_k - [X_k\cos X_k + (X_k-2)\sin X_k]$,
$C_k = A_k + \frac{\lambda_\mathrm{s}}{1+\lambda_\mathrm{s}}\left\{\mathrm{e}^{-X_k}3(X_k+2) + [3(X_k-2)\cos X_k + X_k(X_k-3)\sin X_k]\right\}$,
$D_k = B_k + \frac{\lambda_\mathrm{s}}{1+\lambda_\mathrm{s}}\left\{\mathrm{e}^{-X_k}X_k(X_k+3) - [X_k(X_k-3)\cos X_k - 3(X_k-2)\sin X_k]\right\}$
(the factor e^{X_k} was cancelled here to prevent numerical problems),
$\cos\delta_k = \frac{A_kC_k+B_kD_k}{C_k^2+D_k^2}$, $\sin\delta_k = \frac{B_kC_k-A_kD_k}{C_k^2+D_k^2}$ (the factor A_kB_k was cancelled),
$K_{cki} = a_{\mathrm{th}0}(sP\,\alpha_k\cos\delta_k + sQ\,\eta\beta_k\sin\delta_k)$,
$K_{ski} = a_{\mathrm{th}0}(-sP\,\alpha_k\sin\delta_k + sQ\,\eta\beta_k\cos\delta_k)$
(optionally, one may wish to calculate seasonal semimajor axis drift rate here[4]).

Finally, the time-critical part (steps 8–10), which has to be computed every timestep $\mathrm{d}t$ (usually $\simeq 10\,\mathrm{d}$) in the subroutine `getacc_yarko.f`. We need to know mean anomaly M_i and epoch t_0 from `io_write_filter.f`.

8. The Yarkovsky diurnal acceleration first (the heliocentric coordinates $x_{\mathrm{h}i}, y_{\mathrm{h}i}, z_{\mathrm{h}i}$ are the input parameters of the subroutine, the values $\mathcal{R}_i = \frac{1}{r_{\mathrm{h}i}}$ were already calculated earlier during the gravitational interaction): $GM = \sqrt{m_1}$, $n_{01} = -x_{\mathrm{h}i}\mathcal{R}_i$, $n_{02} = -y_{\mathrm{h}i}\mathcal{R}_i$, $n_{03} = -z_{\mathrm{h}i}\mathcal{R}_i$,
$\cos\theta_0 = n_{01}s_{1i} + n_{02}s_{2i} + n_{03}s_{3i}$, $\sin\theta_0 = \sqrt{|1-(\cos\theta_0)^2|}$ (note the absolute value due to round-off errors),
$T_{\star4} = T_{\star40i}\mathcal{R}_i^2$, $T_{\star3} = \sqrt{\sqrt{T_{\star4}\cdot T_{\star4}\cdot T_{\star4}}}$ (this is faster than $T_{\star4}^{3/4}$),
$\lambda = \frac{\lambda_{0i}}{T_{\star3}}$, $\Psi_2 = \frac{1}{1+\frac{\lambda}{1+\lambda}\psi_i}$ (a complex number), $\rho = \frac{\rho_{0i}T_{\star4}}{1+\lambda}$
(optionally, we can estimate diurnal semimajor axis drift rate here[5]),
$f_{11} = \rho\sin\theta_0\,\mathrm{Re}\{\Psi_2\}$, $f_{12} = -\rho\sin\theta_0\,\mathrm{Im}\{\Psi_2\}$, $f_{13} = \rho\cos\theta_0$.

[4] In this case, we have to add a summation in the previous for-cycle: $\Delta a := \Delta a + \frac{\sin\delta_k}{k}(sP^2\alpha_k^2 + sQ^2(\eta\beta_k)^2)$ and the final value in $\frac{\mathrm{AU}}{\mathrm{My}}$ units is: $\Delta a_\mathrm{s} = \frac{4}{9n}\frac{\rho_{\mathrm{s}0i}}{a_i^2(1+\lambda_\mathrm{s})}\Delta a\frac{(86400\,\mathrm{s})^2}{149597870\cdot10^3\,m}365.25\cdot10^6$.

[5] We compute $n = GM/a_i^{3/2}$, $\cos\gamma_i = \frac{(\mathbf{r}_{\mathrm{h}i}\times\mathbf{v}_{\mathrm{h}i})\cdot\mathbf{s}_i}{|\mathbf{r}_{\mathrm{h}i}\times\mathbf{v}_{\mathrm{h}i}|}$, where γ_i is the obliquity, $\mathbf{r}_i = (x_{\mathrm{h}i}, y_{\mathrm{h}i}, z_{\mathrm{h}i})$, $\mathbf{v}_i = (v_{\mathrm{xh}i}, v_{\mathrm{xh}i}, v_{\mathrm{zh}i})$, $\mathbf{s}_i = (s_{1i}, s_{2i}, s_{3i})$; and finally $\Delta a_\mathrm{d} = \rho\,\mathrm{Im}\{\Psi_2\}\frac{2}{n}\cos\gamma_i\cdot365.25\cdot10^6$ in $\frac{\mathrm{AU}}{\mathrm{My}}$ units.

9. Transform it to the ecliptic coordinate frame:
   $x_1 = \frac{1}{\sin\theta_0}$, $e_{\mathrm{x}k} = (n_{0k} - \cos\theta_0 s_{ki})\, x_1$ for $k = 1, 2, 3$,
   $e_{\mathrm{y}1} = (s_{2i} n_{03} - s_{3i} n_{02})\, x_1$, $e_{\mathrm{y}2} = (s_{3i} n_{01} - s_{1i} n_{03})\, x_1$, $e_{\mathrm{y}3} = (s_{1i} n_{02} - s_{2i} n_{01})\, x_1$,
   $\mathbf{a}_{\mathrm{Yd}} = (e_{\mathrm{x}1} f_{11} + e_{\mathrm{y}1} f_{12} + s_{1i} f_{13}, e_{\mathrm{x}2} f_{11} + e_{\mathrm{y}2} f_{12} + s_{2i} f_{13}, e_{\mathrm{x}3} f_{11} + e_{\mathrm{y}3} f_{12} + s_{3i} f_{13})$.
10. The seasonal Yarkovsky acceleration second:
    $n = GM \frac{1}{\sqrt{a_i^3}}$, $l = M_i + n(t - t_0)$,
    $a_{\mathrm{th}} = \sum_{k=1}^{k_{\mathrm{seasonal}}} K_{\mathrm{c}ki} \cos kl + K_{\mathrm{s}ki} \sin kl$,
    $\mathbf{a}_{\mathrm{Ys}} = (a_{\mathrm{th}} s_{1i}, a_{\mathrm{th}} s_{2i}, a_{\mathrm{th}} s_{3i})$
    (and finally add the components of $\mathbf{a}_{\mathrm{Yd}}$ and $\mathbf{a}_{\mathrm{Ys}}$ to $a_{\mathrm{x}hi}, a_{\mathrm{y}hi}, a_{\mathrm{z}hi}$)

The small thermal acceleration (thought being dissipative) is treated similarly as the conservative planetary perturbations: it is applied at one instant ('kick') in symplectic integrators (Cordeiro *et al.* (1997); see also Section 9.2 for accuracy tests).

2.3.4 1-D non-linear numerical methods

Čapek & Vokrouhlický (2004) use a numerical approach to calculate the surface temperature for a given shape model of an asteroid. They divide the surface into a triangular mesh (typically consisting of 10^3 facets) and solve the 1-dimensional heat diffusion equation (Eq. 4) individually for all elementary 'columns' of the asteroid, stretching from the surface element to the centre. There are three boundary conditions, which have to be satisfied for every element separately:

1. $-K \frac{\partial T}{\partial x}(0,t) + \epsilon\sigma T^4(0,t) = (1 - A)\mathcal{E}(t)$ (i.e., a fully non-linear case);
2. $\frac{\partial T}{\partial x}(\infty, t) = 0$ (i.e., the core is isothermal);
3. $T(x,t)$ is periodic over the rotation and revolution cycles.

The radiation flux $\mathcal{E}(t)$ varies not only with the position of the Sun (with respect to the given surface element), but the mutual shadowing is also handled properly.[6] The partial derivatives in all equations are transformed to finite differences and the set is solved numerically by the Crank-Nicholson scheme. At $t = 0$ the whole mesh have the same equilibrium temperature, after several iterations it converges to the desired solution.

This method assumes, the size of the body is much larger than the penetration depth δ of the thermal wave (the isothermal core condition is actually applied at $\simeq 10\delta$) and the neighboring columns do not communicate thermally with each other. This is well satisfied for asteroids larger than $\simeq 10\,\mathrm{m}$. The Yarkovsky accelerations and the YORP torques were calculated by Čapek & Vokrouhlický (2004) for (6489) Golevka, 1998 KY26, (243) Ida and for a large set of artificial shapes (represented by random Gaussian spheres).

This numerical method can be generalized relatively easily, e.g., to include the low-conductivity surface layer, its variable thickness across the surface, variable albedo, etc.

[6] The shadowing by small craters, which are not incorporated in the shape model, is not taken into account, but its influence on the dynamics is presumably minor. (On the other hand, such shadowing is surely important for the calculation of the directional infrared flux as observed from the Earth, especially at large phase angles.)

3 Transport of meteoroids ejected from (6) Hebe, (170) Maria or (8) Flora

The Yarkovsky effect and gravitational resonances are the most important transport mechanisms of meteorite precursors, meteoroids or asteroidal fragments in the size-range 1 m to 1 km. In this section, we simulate the orbital evolution of putative particles ejected from three parent bodies: (6) Hebe, (170) Maria and (8) Flora. We also study the interaction of orbits with weak high-order resonances and compute several statistics (e.g., the rate of delivery to Mars-crossing orbits, the probabilities that particles of a given size are captured by a given resonance), which can be used to improve Monte-Carlo models of meteoroid transport (like that of Vokrouhlický & Farinella (2000)). The major results of this study were summarised in the review Bottke et al. (2002b).

3.1 Introduction

More than 20,000 meteorites found on the Earth (Grady (2000)) provide crucial clues for dynamical studies of small Solar System bodies. The mineralogy and petrology of meteorites suggest, that the total number of their parent bodies is quite low, only ~ 100, out of which ~ 27 is chondritic, ~ 2 primitive achondritic, ~ 6 differentiated achondritic, ~ 4 stony-iron, and there are ~ 10 iron groups, and ~ 50 ungrouped irons (Burbine *et al.* (2002)). We note, the meteorites may survive in the Earth environment (and in favourable places like the Antarctic) only upto 0.1 My before they are eroded (Bland *et al.* (1998)). They are thus samples of the interplanetary matter, which has been delivered to the Earth only very recently.

The measured *cosmic ray exposure ages* (CRE) of meteorites are typically 10 My in case of stones and 100 My in case of irons (Burbine *et al.* (2002)). The CRE ages tell us, i) how long meteoroids have travelled from a parent body towards the Earth and that ii) the transport mechanism somehow depends on the material properties. Both observations can be theoretically explained as the interplay between collisions, the Yarkovsky effect and gravitational resonances (Vokrouhlický & Farinella (2000), Bottke *et al.* (2000b); Figures 13 and 14).

Meteorites have spectra generally similar to Main-Belt asteroids, but one-to-one identification of the individual meteorites and parent bodies is far from being complete (Burbine *et al.* (2002), Cellino *et al.* (2002)). One of the obstacles is still uncertain rate of the *space weathering*, which typically produces a reddening of spectra and a weakening of the absorption features; estimates of the relevant timescale range from 50 ky upto 1 Gy (Nesvorný *et al.* (2005)).

Dynamical studies of the near-Earth objects (NEO) and the debiasing of the observed population also strongly suggest the majority of NEO's come from the main asteroid belt and that smaller meteoroids should follow the same dynamical path (Bottke *et al.* (2000a), Bottke *et al.* (2002a)).

The meteorite flux observed today is of the order 3×10^5 kg/y and the calculated removal rate of the NEO's due to planetary scattering is ~ 200 bodies larger than 1 km per My. We already know the Yarkovsky semimajor axis drift is efficient enough to keep both populations of the Earth-crossing meteoroids and near-Earth asteroids in steady state (Vokrouhlický & Farinella (2000), Morbidelli & Vokrouhlický (2003); Figure 15). Note the Yarkovsky effect allows to supply meteoroids ejected from practically any Main-Belt asteroid.

Recently, Bottke *et al.* (2005c) and Bottke *et al.* (2006) modelled the collisional/dynamical evolution of stony and iron meteorites over the Solar System history. According to their results, stony meteorites are likely remnants of a collisional cascade; they originate in the Main Belt, in ~ 20 old ($\sim$ Gy) large-scale ($D > 100$ km) breakup events and in ~ 25 recent ($\ll 1$ Gy) smaller ($D < 100$ km) breakups. This is a good match with the observed value of ~ 30 parent bodies.

The precursors of iron meteorites, on contrary, seem to form very early (1–2 My before ordinary chondrites) in the terrestrial planet region, from which they were ejected to the Main Belt. The small precursors 'wait' there for billions of years, until they can be driven by the Yarkovsky effect into resonances and then to the near-Earth space. This scenario conforms to the observed lack of large differentiated bodies in the Main Belt.

Below we describe a smaller dynamical study of meteoroids and asteroid fragments, from 1 m to 500 m in radius, originating from only three sources: asteroids (6) Hebe, (170) Maria and (8) Flora (Section 3.3). These asteroids are probable parent bodies of many ordinary chondrites (see Section 3.2). We extend the work of Bottke *et al.* (2000b), who studied orbital evolution of 1-m meteoroids from 11 parent asteroids; we compare our results to their in the discussion (Section 3.4).

3.2 The parent bodies

The Main-Belt asteroids (6) Hebe, (170) Maria and (8) Flora are probable parent bodies of many meteorites (Vokrouhlický & Farinella (2000)). All the three asteroids belong to the S taxonomic class (Bus & Binzel (2002b); an illustration of their spectra is at Figure 30). S-type asteroids are very probable sources of ordinary chondrites (Burbine *et al.* (2002), Table 7). More specifically, (6) Hebe likely conforms to H chondrites and (8) Flora is spectroscopically similar to L or LL chondrites.

Table 7: Meteorite types (ordinary chondrites), percentages of the observed falls and S-type asteroids or taxonomic classes, which they are similar to. The L, H and LL chondrites together produce 80 % of all falls. Adapted from Burbine *et al.* (2002).

meteorite type	fall percentage	asteroid analogue
L	38 %	S(IV) asteroids
H	34 %	6 Hebe [S(IV)]
LL	8 %	S(IV) asteroids

They are located close to the powerful low-order resonances: the ν_6 secular resonance (where the longitudes of perihelia precess with same rate as that of Saturn) and the 3/1 mean motion resonance with Jupiter at approximately 2.5 AU (Figure 31, Table 8). (8) Flora is located in the inner belt close to the ν_6 border, (6) Hebe, with its large inclination, is close to both the ν_6 and J3/1, and especially (170) Maria is placed 'strategically' at the outer edge of the J3/1.

Table 8: Approximate osculating orbital elements of asteroids (6) Hebe, (170) Maria and (8) Flora, i.e., the parent bodies of our simulated meteoroids. From the AstOrb catalogue (*AstOrb*).

name	semimajor axis AU	eccentricity	inclination °
(6) Hebe	2.4248	0.2018	14.771
(170) Maria	2.5525	0.0634	14.411
(8) Flora	2.2019	0.1561	5.885

Hebe and Flora have large diameters, 192 km and 136 km respectively, hence being good targets for small impactors, which can eject fragments. Maria is relatively smaller with $D = 46$ km.

There are dynamical families associated with the asteroids Maria and Flora; no family was identified around Hebe (Nesvorný *et al.* (2005), see also Figure 31). The Maria family is probably (3.0 ± 1.0) Gy old, while the Flora family is younger, (1.0 ± 0.5) Gy (Nesvorný *et al.* (2002), Nesvorný *et al.* (2005)).

The Flora family members mostly belong to S-types. The relative reflectance peaks at 750 nm and there is a wider range of spectral slopes; one can also identify several probable interlopers with a more flatter X- or C-type spectra (Figure 30). The parent body of the whole Flora family seems to be rather homogeneous. The spectra variability among family members might be attributed to the space weathering. Probable meteorite analogues are L3, L4, L5, LL chondrites (Cellino *et al.* (2002)).

The Maria family is also an S-type. The spectra, however, are slightly more homogeneous than Flora's, with similar spectral slopes and depths of the 1 μm band. The maximum reflectance is at 770 nm. Generally, the spectra of family members are similar to ordinary chondrites (and also to large near-Earth asteroids (433) Eros and (1036) Ganymedes).

3.3 N-body simulations

We performed N-body numerical simulations of meteoroid transport from the three parent bodies: (6) Hebe, (170) Maria and (8) Flora. The typical integration time span was 150 My. We used the symplectic integrator `swift_rmvsy` with a time step 36 days. We included gravitational forces, the Yarkovsky effect (see Section 2.3) and a simple treatment of collisional dynamics. The osculating orbital elements of meteoroids were sampled every 2 y and then digitally filtered to remove short-period oscillations (see Section 9.1); the output time step of the resulting mean elements is 600 y. For the sake of particular analyses, we also computed averaged orbital elements as an 0.5 My running window average with a time step 0.01 My. Our integrations included 7 planets (excluding Mercury and Pluto), which initial positions

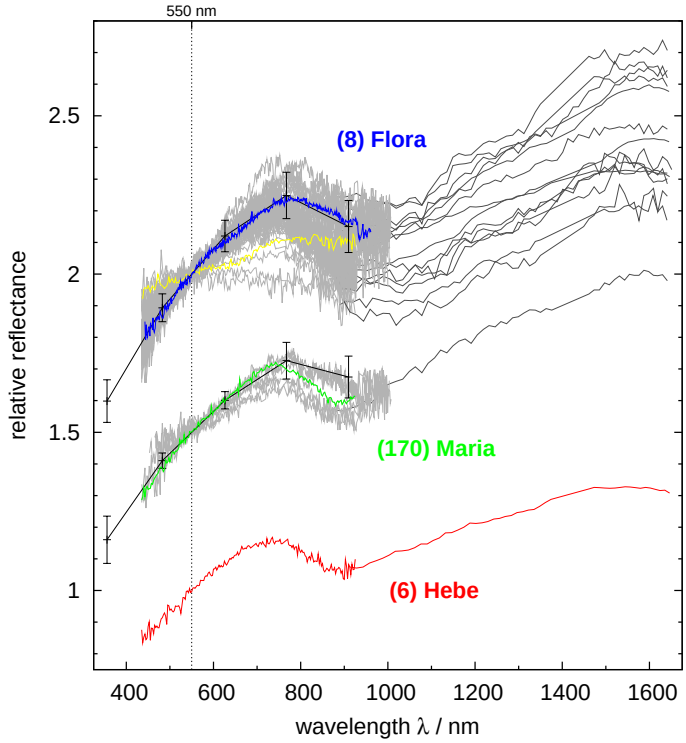

Figure 30: An illustration of the SMASS spectra of the asteroids (6) Hebe (red), (170) Maria (green), (8) Flora (blue), spectra of the Maria and Flora family members (thin gray lines) and also their mean colours from the Sloan Digital Sky Survey (5 black error bars). Note the variability of slopes and depths of the absorption features. Several interlopers among Flora family members are clearly visible (e.g., Xk-type (3533) Toyota denoted by yellow colour). We plotted a mixture of spectra from SMASSI and SMASSII datasets, which are not entirely homogeneous and we have to compare the spectra with caution (e.g., the depth of the 1 μm band seems lower in the SMASSI). Data from *SMASS*, Bus & Binzel (2002a), *SDSS MOC*.

and velocities were taken from the *DE405 ephemeris*. The Hill sphere of Mars was scaled 4 times larger due to fairly large integration time step.

The simulated meteoroids form 30 groups, because we have:

- three parent bodies: Hebe, Maria and Flora;
- five particular sizes of meteoroids: $R = 1\,\mathrm{m}$, $10\,\mathrm{m}$, $50\,\mathrm{m}$, $100\,\mathrm{m}$ and $500\,\mathrm{m}$;
- two types of surface properties: 'regolith' (with a low thermal conductivity $K = 0.0015\,\mathrm{W/m/K}$ and the surface density $\rho_{\mathrm{surf}} = 1500\,\mathrm{kg/m^3}$), and 'basalt' (with high $K = 2.65\,\mathrm{W/m/K}$ and $\rho_{\mathrm{surf}} = 3500\,\mathrm{kg/m^3}$).

Each group contained 50 test particles, i.e., 1,500 test particles were integrated in total. Other thermal parameters of meteoroids were set as follows: the bulk density $\rho = 3500\,\mathrm{kg/m^3}$, the thermal capacity $C = 680\,\mathrm{J/kg/K}$, thermal emissivity $\epsilon = 1$, the Bond albedo $A = 0$. The maximum Yarkovsky semimajor axis drift rates (estimated from the Gauss equations) are summarised in Table 9.

The initial conditions of the putative Hebe, Maria and Flora meteoroids are depicted in Figure 31. The meteoroids were ejected from the parent bodies with an isotropic power-law velocity distribution. We use a procedure by Farinella *et al.* (1994), with the power-law index $\alpha = 3.25$ and the minimum velocity $v_{\mathrm{min}} = 100\,\mathrm{m/s}$.

The initial orientations of spins were isotropic and random. The rotational periods P are proportional to radii R, with $2R = 1000\,\mathrm{m}$ bodies having $P = 5\,\mathrm{h}$. Non-disruptive collisions, which change spin axes orientations of meteoroids, were modelled as random reorientations with a characteristic timescale

$$\tau_{\mathrm{reor}} = 15.01\,\mathrm{My}\sqrt{[R]_{\mathrm{m}}}\,, \tag{29}$$

Table 9: Yarkovsky semimajor axis drift rates $\frac{\mathrm{d}a}{\mathrm{d}t}$ in $\frac{\mathrm{AU}}{\mathrm{My}}$ estimated from the Gauss equations for Hebe meteoroids with radii from 1 m upto 500 m, regolith and basalt thermal properties and the diurnal and seasonal variants of the Yarkovsky effect. The diurnal variant dominates for the regolith-covered bodies, while the seasonal for the basaltic ones. The variants can be combined as $\left(\frac{\mathrm{d}a}{\mathrm{d}t}\right)_{\mathrm{diurnal}} \cos\gamma + \left(\frac{\mathrm{d}a}{\mathrm{d}t}\right)_{\mathrm{seasonal}} \sin^2\gamma$, where γ denotes the obliquity. For Flora, the drift would be slight faster, being closer to the Sun, and for Maria slightly slower.

material	variant	1 m	10 m	50 m	100 m	500 m
regolith	diurnal	0.02985	0.00744	0.00223	0.00121	0.00022
	seasonal	−0.00138	−0.00014	−0.00003	−0.00001	−0.00000
basalt	diurnal	0.00053	0.00017	0.00007	0.00005	0.00002
	seasonal	−0.00065	−0.00363	−0.00106	−0.00052	−0.00010

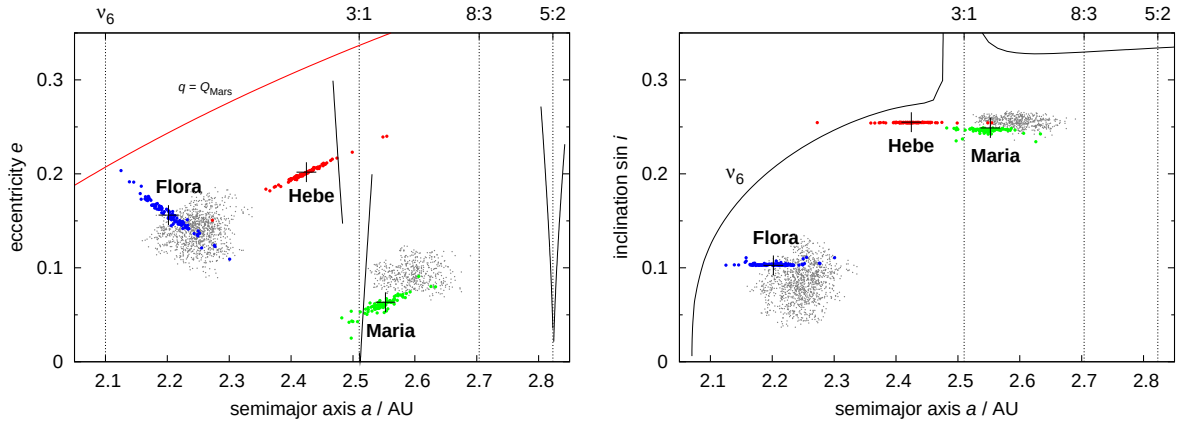

Figure 31: Parent bodies (crosses) and simulated ejecta (colour dots) at the osculating semimajor axis vs. osculating eccentricity plot. We plot also approximate positions of major gravitational resonances (black lines) and the Flora and Maria families (gray dots) in proper elements. We identified the Maria family by the hierarchical clustering method with a cutoff velocity $v_{\mathrm{cutoff}} = 70\,\mathrm{m/s}$, using the *AstDyS* catalogue, version Nov 10^{th} 2004. The Flora family was identified at $v_{\mathrm{cutoff}} = 160\,\mathrm{m/s}$ among asteroids with $H < 15\,\mathrm{mag}$; for a larger dataset, it blends with the background population (for all velocities) and cannot be easily separated by the HCM algorithm.

where $[R]_{\mathrm{m}}$ is the radius of the body in metres (Farinella *et al.* (1998), Bottke *et al.* (2005b), Table 10).[7] The catastrophic disruptions occur in the Main Belt with a similar timescale

$$\tau_{\mathrm{disr}} = 16.78\,\mathrm{My}\sqrt{[R]_{\mathrm{m}}}\,, \tag{30}$$

but they were not taken into account during the integration. The particles were followed either until the end of the integration (150 My) or earlier, when their perihelion dropped to 10^{-3} AU or semimajor axis exceeded 10^3 AU. Nevertheless, we discuss the collisional lifetime issues below.

Table 10: A characteristic timescales of the reorientation τ_{reor} and the disruption τ_{disr} for the Main-Belt meteoroids and asteroid fragments (R denotes their radius). They were calculated from Eqs. (29) and (30).

R	1 m	10 m	50 m	100 m	500 m
τ_{reor} / My	15	47	106	150	336
τ_{disr} / My	17	53	119	168	375

The data analysis was focused on the estimate of i) the temporal decay of the meteoroid population, ii) the probability of crossing gravitational resonances, iii) interaction with higher–order, 3-body and secular resonances.

[7] We computed a random number $x \in [0,1]$ every $\mathrm{d}t_{\mathrm{reor}} = 10^4$ y and compared it to the probability $p = 1 - \exp\left(-\frac{\mathrm{d}t_{\mathrm{reor}}}{\tau_{\mathrm{reor}}}\right)$; if $x < p$ the spin axis orientation was reset randomly.

Let us present several comparisons among our simulations, which demonstrate important aspects of the meteoroid orbital evolution. Figure 32 shows an overview of Hebe meteoroids evolution at the mean semimajor axis vs. time plots. We see clearly, that for regolith meteoroids, the diurnal Yarkovsky effect dominates and meteoroids semimajor axes either increase or decrease. For basaltic, the seasonal variant is more important and consequently all meteoroids drift towards the Sun with the maximum drift rate for the radius 10 m. (This is in concert with analytical estimates in Figure 29 and Table 9.)

When an orbit encounters a strong resonance (J3/1 at 2.5 AU or ν_6 around 2.35 AU), it starts to oscillate and usually it is quickly removed from the Main Belt by close encounters with planets. Nevertheless, we can notice many orbits, especially of the small regolith meteoroids, which drift through the J3/1 resonance and continue further to the next resonances (J8/3, J5/2).

Figure 33 shows a sequence of the mean semimajor axis vs. mean eccentricity for basaltic 10 m meteoroids ejected from Maria. They all drift towards smaller semimajor axes and encounter the J3/1 resonance. We see, what the resonance is capable to do: it drives eccentricities of most (but not all) meteoroids beyond Mars- and then Earth-crossing limits. It happens very quickly, in 1 or 2 My. Close encounters with planets then produce sudden 'jumps' in the semimajor axis. The remaining 10 %–20 % of meteoroids (e.g, particle no. 34) cross the resonance; only their eccentricities are raised from 0.1 to 0.2. Note the group of a few meteoroids (nearby particle no. 17), which is captured in the z_2 secular resonance and is 'lifted' upto the eccentricity 0.2, well before it reaches the J3/1.

Orbital evolution of individual meteoroids can be quite complex: e.g., one 10 m regolith meteoroid from Hebe (depicted at Figure 34): i) initially drifts slowly inwards ($\frac{\mathrm{d}a}{\mathrm{d}t} \doteq -0.004\,\frac{\mathrm{AU}}{\mathrm{My}}$), having the obliquity 106°. ii) En route, the orbit was captured in the outer 1/2 mean motion resonance with Mars; the capture spans the same time as a pure Yarkovsky drift across this region, i.e., the capture does not affect the drift rate in this case. iii) Next, the orbits interacts with the 4J−2S−1 resonance (3-body resonance with Jupiter and Saturn; Nesvorný & Morbidelli (1998)). A jump occurs this time and slightly increases the drift rate. iv) The proximity of the ν_6 secular resonance steadily increases oscillation of the eccentricity and the meteoroid starts to encounter Mars, what produces notable jumps in the semimajor axis (upto 0.02 AU). v) A random reorientation of the spin axis occurs at 95 My and the new value of the obliquity is 53°. A fast outward drift follows ($\frac{\mathrm{d}a}{\mathrm{d}t} \doteq 0.008\,\frac{\mathrm{AU}}{\mathrm{My}}$) and persists until the semimajor axis reaches 2.49 AU, an inner border of the 3/1 mean motion resonance with Jupiter. vi) After 1 My of the in-resonance evolution, the eccentricity was increased beyond 0.9 and a close encounter with Jupiter removes the particle from the Main Belt.

Large asteroid fragments, with $R = 500$ m, drift much slower (see Figure 35), Hebe ejecta of this size do not reach any of the powerful resonances within 150 My. We can however observe numerous captures in weaker resonances. The 7J−2S−2 resonance, for example, does not affect the drift rate. An unidentified narrow resonance, on the other hand, decreases the drift rate by $\sim 10\,\%$.

Another comparison of slow and fast drifting bodies is shown at Figure 36: the mean semimajor axis vs. mean eccentricity plots for Flora 500 m basalt asteroid fragments and Maria 10 m regolith meteoroids. There is a dense 'net' of resonances in the inner belt, which produces a chaotic diffusion in the eccentricity and the slow drifting bodies can reach Mars-crossing orbits this way. The fast drifting bodies in the middle belt (which is dynamically colder) jump over all weak resonances and they are depleted mainly by the J3/1 and J5/2 resonances.

Temporal decay of the meteoroid population. When meteoroids reach Mars-crossing orbits, they mostly continue to Earth-, Venus- or Jupiter-crossing, and they are removed from the Main Belt after some time. We can therefore use a Mars-crossing criterion as a measure of the meteorite flux, keeping in mind, that only a minor part ($\sim 1\,\%$) of the meteoroid population actually collides with the Earth (and most of them fall on the Sun; Gladman *et al.* (1997)).

We use two criteria to decide whether the orbit of a meteoroid crosses the orbit of Mars:

1. the averaged pericentre of the meteoroid $q_{\mathrm{avg}} < 1.665$ AU, with the orbital elements averaged by a running window 0.5 My (the so called q-criterion);

2. the mean heliocentric distance of the meteoroids node (measure along the common nodal line with Martian orbital plane) is smaller than that of Mars[8]; the distances are calculated from mean orbital

[8] The keplerian mean orbital elements of the meteoroid are $(a, e, I, \Omega, \omega)$ and the elements of Mars are denoted by dashes $(a', e', I', \Omega', \omega')$. We define vectors:

$$\mathbf{n} = \begin{pmatrix} \sin I \sin \Omega \\ -\sin I \cos \Omega \\ \cos I \end{pmatrix}, \quad \mathbf{Q} = \begin{pmatrix} -\cos \Omega \sin \omega - \cos I \sin \Omega \cos \omega \\ -\sin \Omega \sin \omega + \cos I \cos \Omega \cos \omega \\ \sin I \cos \omega \end{pmatrix}$$

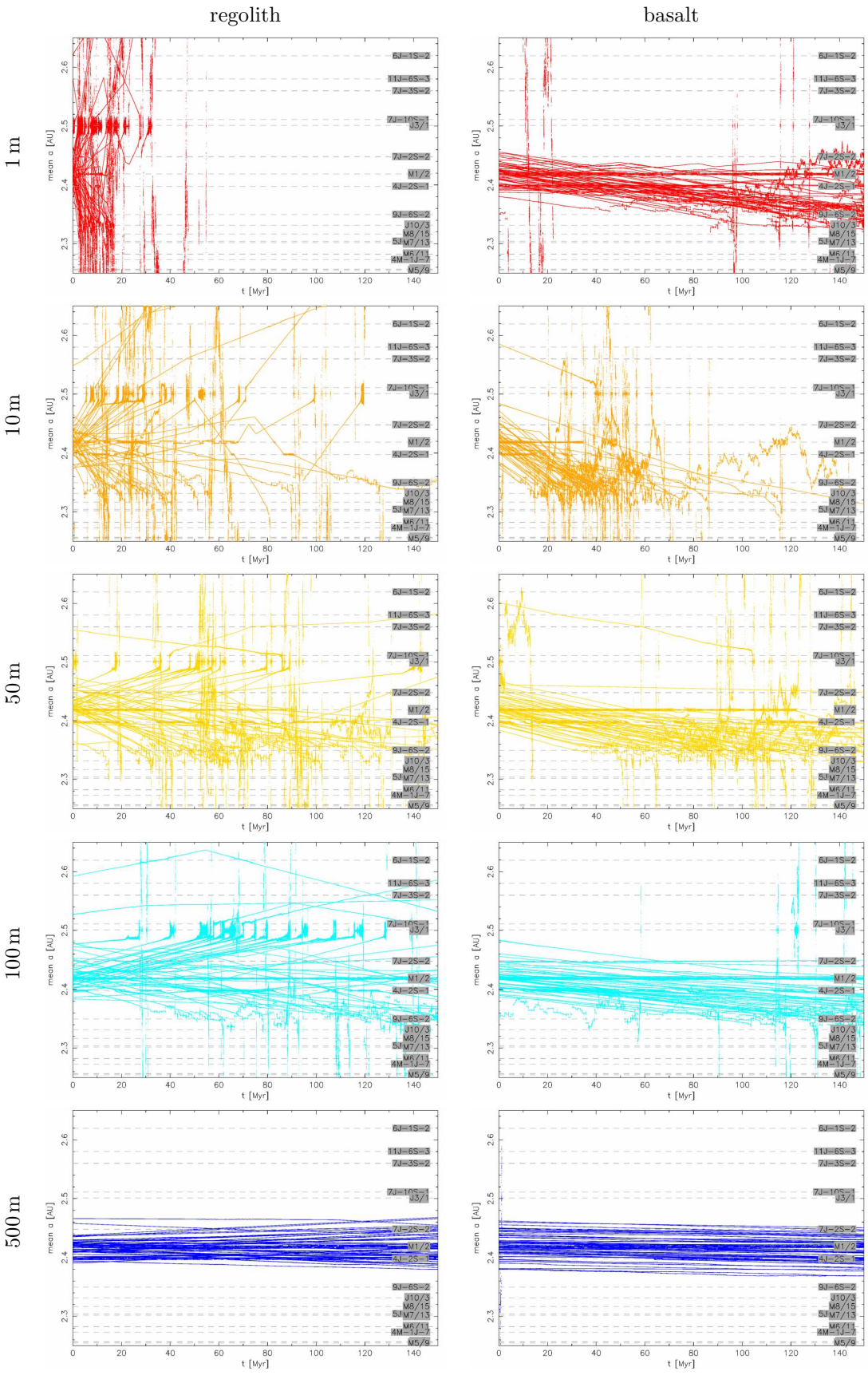

Figure 32: The evolution of Hebe meteoroids at the mean semimajor axis vs. time plots; the meteoroids are grouped according to the five different radii and two materials. The ranges of the t- and a- axes are always (0, 150) My and (2.25, 2.65) AU. Horizontal dashed lines denote positions of various mean motion resonances.

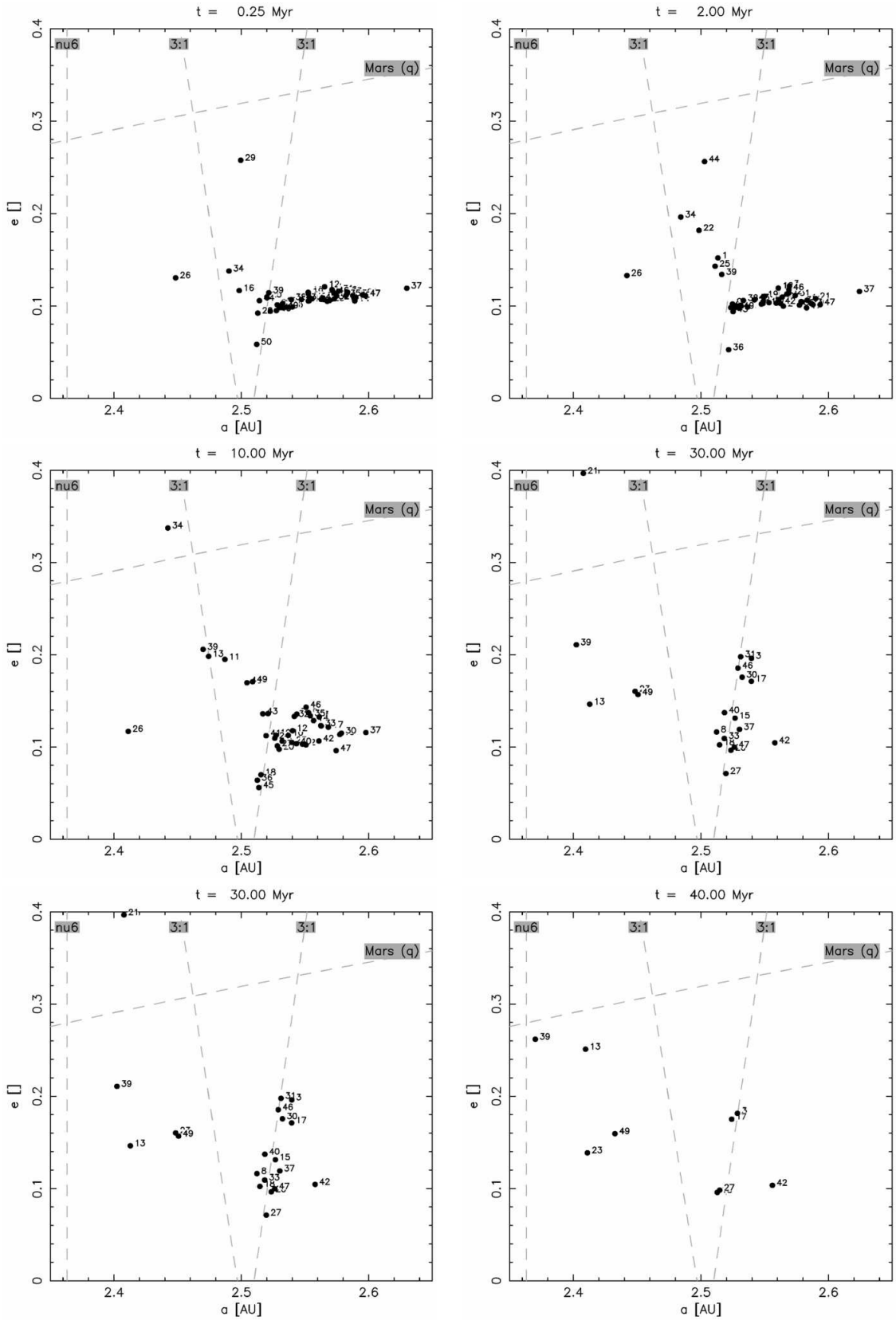

Figure 33: The evolution of 10 m basaltic meteoroids ejected from (170) Maria at the sequence of mean semimajor axis vs. mean eccentricity plots, spanning 40 My. Dashed lines denote approximate borders of the J3/1 resonance, ν_6 resonance and the Mars-crossing region. The group of meteoroids around no. 17 was captured in the z_2 secular resonance before it entered J3/1 resonance.

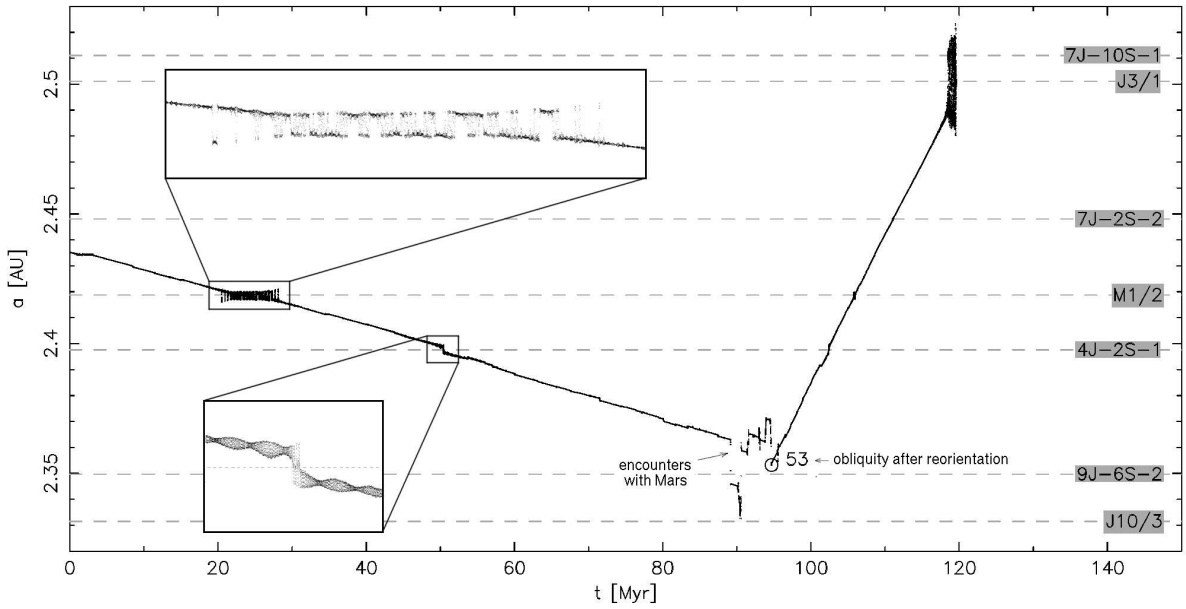

Figure 34: The orbital evolution of a Hebe 10 m regolith meteoroid at the mean semimajor axis vs. time plot. The capture in the M1/2 resonance and the jump over 4J−2S−1 resonance are zoomed-in. The period of close encounters with Mars (around 90 My) was interrupted by a sudden reorientation of the spin axis, which caused a fast outward drift. Finally, the meteoroid reached the J3/1 resonance and was ejected from the Main Belt due to a close encounter with Jupiter.

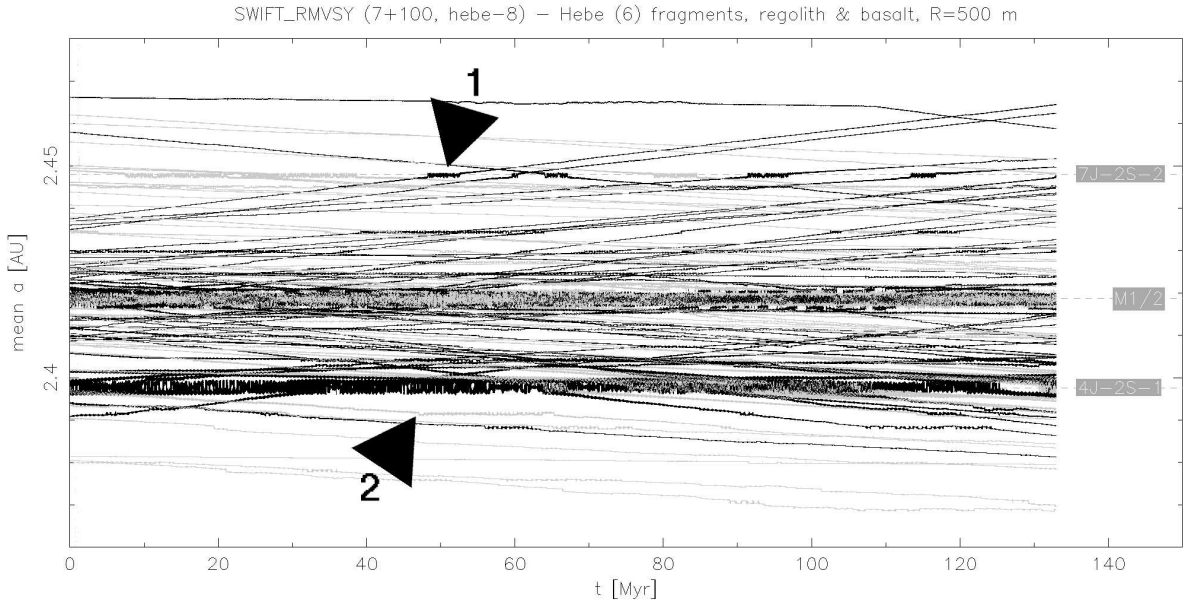

Figure 35: The orbital evolution of Hebe asteroid fragments with $R = 500$ m. Two types of bodies are plotted at once: regolith (dark) and basalt (light). We observe captures in resonances M1/2, 4J−2S−1 and other resonances. The arrow no. 1 points to the capture in the 7J−2S−2 and the arrow no. 2 to an unidentified resonance (which decreases the drift rate slightly).

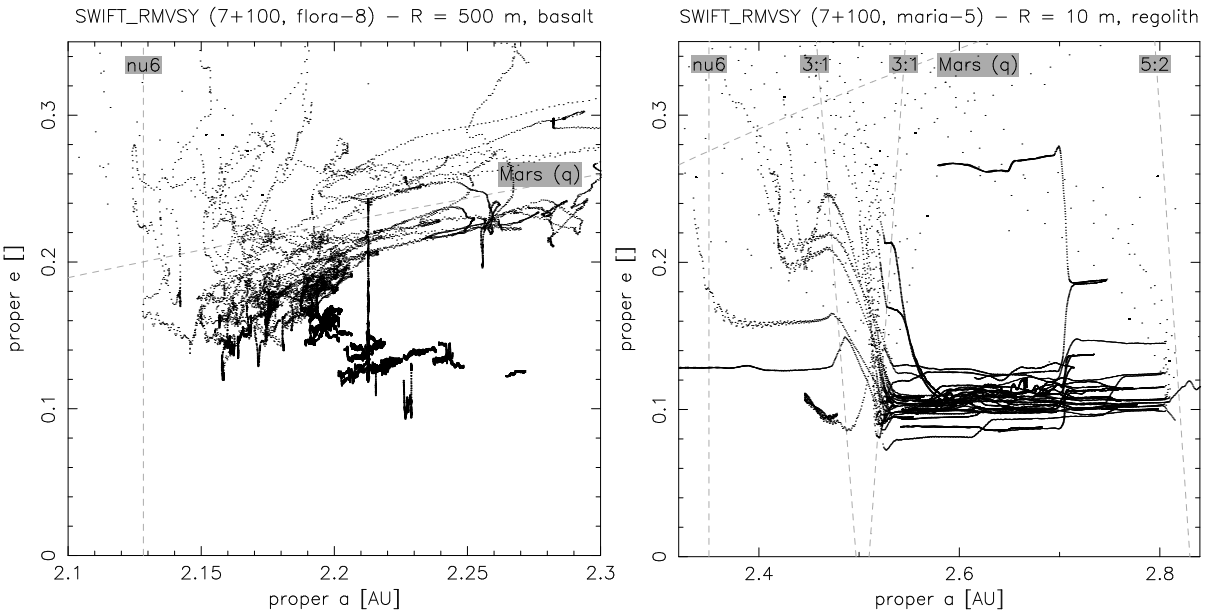

Figure 36: The mean semimajor axis vs. eccentricity plots of the Flora 500 m basalt asteroid fragments (left) and Maria 10 m regolith meteoroids (right). There are many weak resonances in the inner belt, so slowly drifting bodies from Flora diffuse in eccentricity. The fast drifting bodies from Maria, do not evolve in eccentricity unless they reach low-order resonances (J3/1, J5/2, J8/3 or ν_6).

elements with a 600 y time step (MC-criterion).

Usually, the first simple q-criterion is fulfilled a bit later, because the 0.5 My averaging removes large oscillations of the pericentre (which, in turn, cause the second MC-criterion is fulfilled earlier).

Figure 37 shows the temporal decays of all 30 groups according to our N-body simulations and the 1st q-criterion. There is also a comparison with the Monte-Carlo model by Vokrouhlický & Farinella (2000), which accounts for the Yarkovsky semimajor axis drift only (and complex collisional dynamics); their meteoroids are removed, and 'preliminary' considered as Mars-crossers, as soon as they reach nominal borders of major resonances. The differences between the two models, which are clearly visible, can be only partly explained by the different 'Mars-crossing' criteria or by the disruptive collisions, which the Monte-Carlo model accounts for. Mostly, they are caused by resonant phenomena: i) chaotic diffusion in weak high-order resonances, especially in the inner belt, where many outer resonances with Mars and 3-body resonances are present, drives slowly drifting bodies to MC orbits; ii) smaller fast-drifting meteoroids are able to cross the J3/1 resonance; iii) captures in high-order resonances effectively decrease or increase the semimajor axis drift rate en route to low-order resonances; iv) captures in high-order secular resonances do not affect the semimajor axis drift, but they decrease or increase eccentricity or inclination, what is important, if the borders of low-order resonances depend on e or I.

For example, Flora 100 m and 500 m asteroid fragments and even smaller meteoroids often reach the MC-orbits due to the chaotic diffusion in gravitational resonances. The corresponding decays in our N-body simulations are thus almost size independent and faster than in the Monte-Carlo model.

Tables 11 and 12 provide a summary of the median Mars- and Earth-crossing times according to the 2nd MC-criterion. The dependences of these quantities on the radius are plotted at Figure 38. Typical values are of the order 10 My for the fast-drifting bodies and more than 100 My for the slow-drifting. It takes relatively longer time for Flora meteoroids to move from MC to EC orbits, even thought they reach MC orbits quite early.

Recall, we ignored collisional disruptions during the integrations, hence we shall briefly discuss them here. We plotted the characteristic disruption timescale $\tau_{\rm disr}$ (Eq. 30) at Figure 38. We see, that most of Hebe and Maria basalt 1 m meteoroids disrupt before they reach MC orbits, because their transport

and similarly $\mathbf{n}'$ and $\mathbf{Q}'$ for Mars. We compute

$$\phi = \sqrt{1-(\mathbf{n}\cdot n')^2}\,, \quad r_\pm = \frac{a(1-e^2)}{1\pm\frac{e}{\phi}\mathbf{n}'\cdot\mathbf{Q}}\,, \quad r'_\pm = \frac{a'(1-e'^2)}{1\pm\frac{e'}{\phi}\mathbf{n}\cdot\mathbf{Q}'}\,,$$

and finally $r=\min(r_+,r_-)$, $r'=\max(r'_+,r'_-)$. The Mars-crossing criterion is then $r\le r'$.

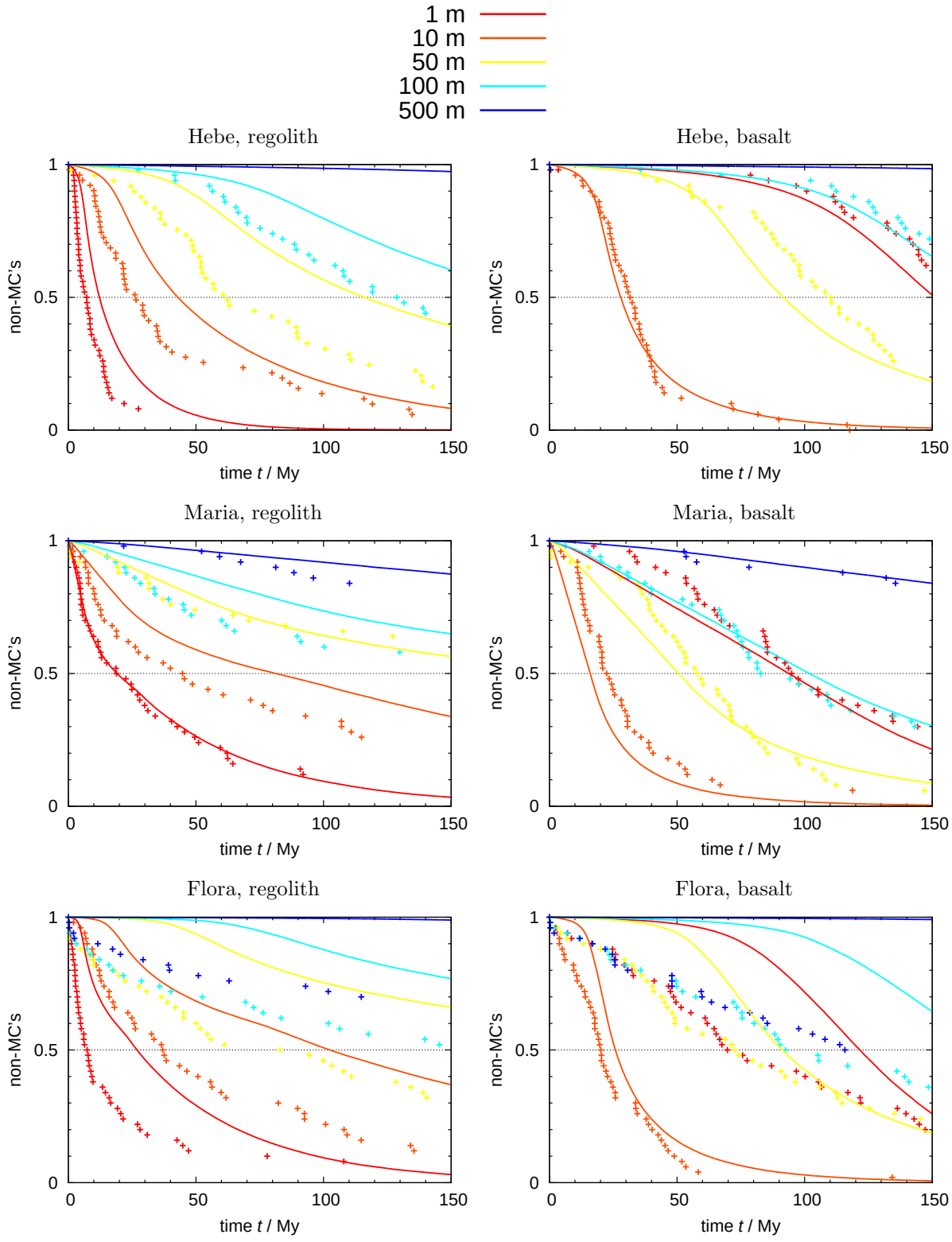

Figure 37: The numbers of meteoroids, which are not Mars crossers, vs. time for the three parent bodies and two materials. Colours denote radii: 1 m (red), 10 m (orange), 50 m (yellow), 100 m (cyan), 500 m (blue). The crosses denote our N-body simulations (we use $q < 1.665$ AU Mars-crossing criterion with 0.5 My averaging) and the lines correspond to simpler analytical Yarkovsky semimajor axis drifts and fixed resonant borders, which are used in the Monte-Carlo model by Vokrouhlický & Farinella (2000).

Table 11: Median Mars-crossing times $t_{\rm MC}$ in My and the corresponding number of meteoroids (out of 50), which reached Mars-crossing orbits within 150 My, for the six meteoroid populations.

R	1 m	10 m	50 m	100 m	500 m
Hebe, regolith	6.0	24.6	53.0	112.7	>150
Hebe, basalt	126.1	28.2	>150	>150	>150
Maria, regolith	14.0	42.3	>150	>150	>150
Maria, basalt	94.6	23.3	52.6	81.5	>150
Flora, regolith	2.3	13.7	37.3	34.1	110.3
Flora, basalt	18.4	4.9	34.4	35.8	37.2
R	1 m	10 m	50 m	100 m	500 m
Hebe, regolith	50	47	43	33	0
Hebe, basalt	33	50	7	22	3
Maria, regolith	49	41	19	21	8
Maria, basalt	37	50	46	38	10
Flora, regolith	50	46	37	30	27
Flora, basalt	44	49	44	40	33

Table 12: Median Earth-crossing times $t_{\rm EC}$ in My and the corresponding number of meteoroids (out of 50), which reached Earth-crossing orbits within 150 My, for the six meteoroid populations.

R	1 m	10 m	50 m	100 m	500 m
Hebe, regolith	8.3	29.4	80.5	137.7	>150
Hebe, basalt	>150	41.9	>150	>150	>150
Maria, regolith	20.9	42.5	>150	>150	>150
Maria, basalt	96.4	23.9	57.1	82.3	>150
Flora, regolith	10.1	45.2	109.0	>150	>150
Flora, basalt	105.0	25.7	91.5	146.9	>150
R	1 m	10 m	50 m	100 m	500 m
Hebe, regolith	50	46	41	26	0
Hebe, basalt	9	49	7	12	1
Maria, regolith	48	40	19	21	8
Maria, basalt	34	50	46	38	10
Flora, regolith	49	43	31	21	13
Flora, basalt	37	49	34	26	23

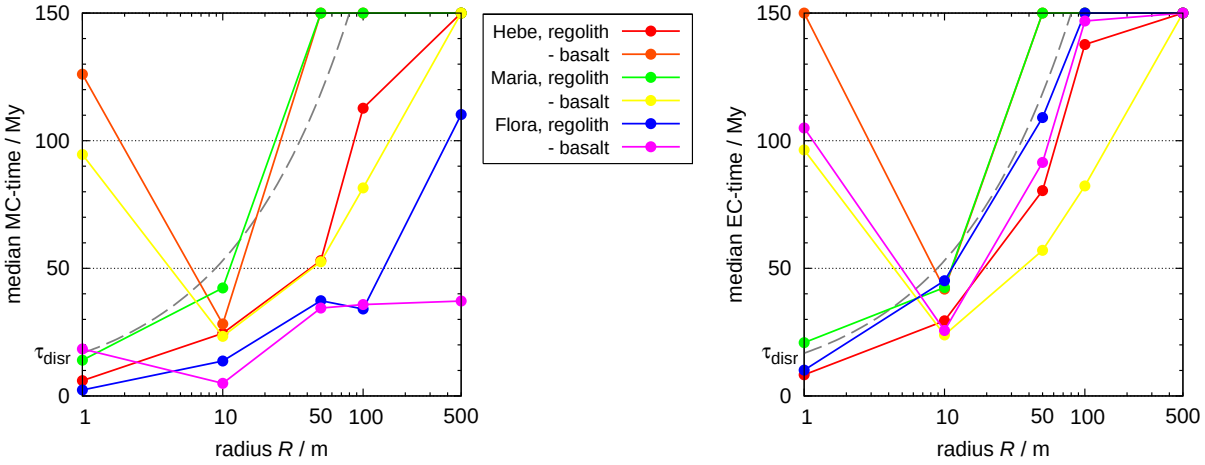

Figure 38: The dependence of median Mars- and Earth-crossing time on radius for regolith or basalt meteoroids originating from five parent bodies. Typical values are of the order 10 My, but the meteoroids drifting slowly or located far from major escape routes have the median equal to 150 My (i.e., the time span of the integration), because less than half of the bodies ever reached MC (EC) orbits. The dashed curves indicate the characteristic disruption timescale $\tau_{\rm disr}(R)$ given by Eq. (30).

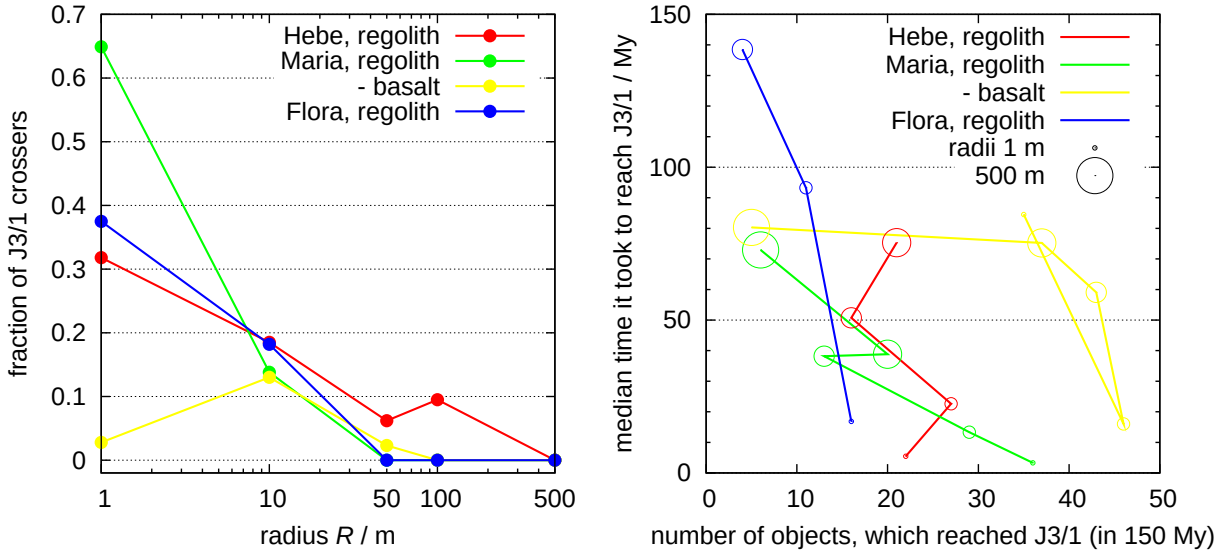

Figure 39: (Left) The fraction of the J3/1 crossers vs. their radius. (Right) The median time, it took to reach J3/1 resonance vs. the number of objects (out of 50), which actually did that within the time span of the integration (i.e., 150 My). The errors of the fraction are of the order 0.1 due to the limited number of meteoroids. The Hebe and Flora basalt meteoroids mostly drift away from the J3/1 resonance and hence we do not plot statistics for them.

takes much longer time than $\tau_{\rm disr}$. Some Maria regolith meteoroids of all sizes may also disrupt en route. On contrary, Hebe basalt fragments probably survive intact (their MC time $\ll \tau_{\rm disr}$). Disruptions and reorientations of $R = 500$ m bodies are not important on the 150 My time span. We will not calculate the effect of collisions on median MC (EC) times in detail, only note, that the disrupted bodies can be resupplied by disruptions of larger ones.

The J3/1 resonance crossing. There is a significant number meteoroids, which crossed the 3/1 mean motion resonance with Jupiter and did not reached Mars-crossing orbits. This is due to the fast Yarkovsky drift, which allows bodies to escape from the resonance, before their eccentricity is pumped-up. We calculated the statistics of the J3/1 crossing (Figure 39) and we conclude, that the fraction of the 'crossers' is: ~ 60 % for Maria 1 m regolith meteoroids, ~ 30 % for Hebe and Flora regolith 1 m meteoroids and ~ 15% for Maria 10 m basalt meteoroids. Note the errors here are roughly 10 % due to the limited number of meteoroids, which ever reached the J3/1 border. On average, the eccentricity of the crossers from Maria was increased by 0.1. We were not able to calculate a precise statistics for larger 100 m or 500 m asteroid fragments, because they did not reached the J3/1 resonance mostly. Nevertheless, the probability of their crossing is presumably very low (<5 %).

This phenomenon may modify some of the conclusions of the Monte-Carlo models of the meteoroid transport (Vokrouhlický & Farinella (2000)). E.g., the delivery times of small meteoroids might be a bit longer and more meteoroids can escape from the Main Belt through the ν_6 or J5/2 resonance.

The ν_6 resonance and Mars-crossing orbits. The Mars-crossing orbits occur earlier that the body reaches the nominal position of the $\nu_6 \equiv g - g_6$ resonance. The boundary of the ν_6 resonance is not sharp and In order to quantify this effect, we calculated proper g-frequencies of meteoroids at the moment, when they reach Mars-crossing orbit for the first time, and compared them with the g_6 value (Figure 40).

We see, the distribution of g's is clustered a bit higher than g_6, so that about one half of meteoroids reaches MC orbits earlier and the other half later. This shift in the frequency space, with respect to the border of the ν_6, corresponds to some shift in the (a, e, I) space, because g's depend on the actual values of the orbital elements (the g-frequencies decrease as the semimajor axis decrease and the inclination increase). The result might be useful for Monte-Carlo models of meteoroid transport, which include a fixed analytical ν_6 border only.

High-order secular resonances. Meteoroids, driven by the Yarkovsky effect, can reach the position of a secular resonance and become trapped. The Yarkovsky semimajor axis drift continues, but the

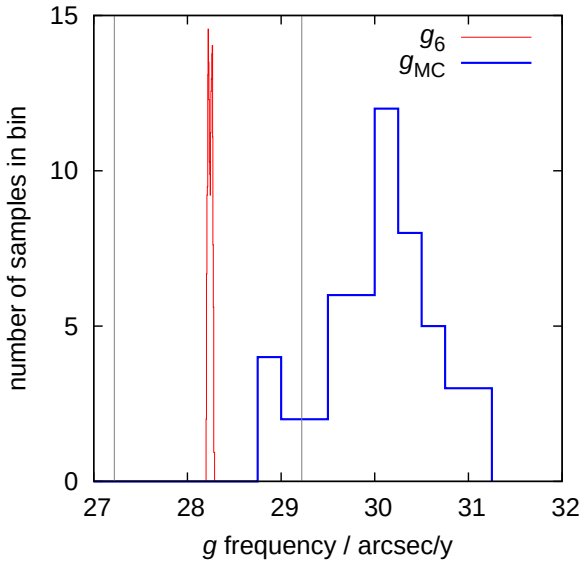

Figure 40: The histogram of the $g_{\rm MC}$ frequencies, i.e., the proper frequencies of longitudes of perihelia calculated by the FMFT method (see Section 9.1), and the comparison to the g_6 frequency of Saturn. The interval $\pm 1''/$y around the g_6, i.e., the 'area of influence' of the ν_6, is denoted. This calculation was performed for 50 Flora basalt meteoroids with $R = 10$ m.

resonance, being a 3-dimensional structure in the (a, e, I) space, drives the eccentricity or inclination (it depends, if the critical argument of the resonance involves pericentric g- or nodal s-frequencies or both). e or I can increase or decrease (it depends on the orientation of the secular resonance in the (a, e, I) space and the direction of the Yarkovsky drift.

We already mentioned Maria meteoroids influenced by the z_2 secular resonance (Figure 33), which increased their eccentricities by 0.1 before they entered J3/1 mean motion resonance. Here, we present another example (Figure 41). Larger Flora meteoroids were often captured in the z_2 resonance too. The eccentricities and inclinations of the inward-drifting bodies were decreased a bit, what substantially prolonged the time until they reached Mars-crossing orbits, because the chaotic diffusion in e was inhibited this way and also the border of the ν_6 resonance, depending strongly on the inclination, is shifted more inwards.

3.4 Discussion

We have verified that meteoroids can be delivered to Mars- and Earth-crossing orbits by the Yarkovsky effect and gravitational resonances on the timescale of the order 10 My. Larger asteroids can escape from the Main Belt due to chaotic diffusion in weaker resonances, which are very common in the inner Main Belt. Transport times to the EC- orbits might be generally consistent with the observed long CRE ages of meteorites.

We presented examples of various processes involved in the meteoroid transport: i) Yarkovsky drift and captures in low-order mean motion resonances (e.g., J3/1, J8/3) or the powerful ν_6 secular resonance; ii) crossing of resonances (which occurs commonly in the J3/1 case and rarely in the ν_6 case for the fastest drifting meteoroids); iii) interaction with weaker high-order resonances (e.g., J10/3); iv) outer resonances with Mars (M1/2); v) 3-body resonances (4J−2S−1); vi) capture in high-order secular resonances (z_1, z_2, $g + g_5 - 2g_6$, etc.); vii) frequent collisional reorientations, which cause a random walk behaviour for low-conductivity bodies and effectively decrease the diurnal Yarkovsky drift. All these processes affect delivery rates to Mars- and Earth-crossing orbits, they can both increase or decrease the rate as compared to a simple Yarkovsky semimajor axis drift towards the nominal position of gravitational resonances; it depends on individual source regions and meteoroid properties.

Our results are consistent with Bottke *et al.* (2000b). Compared to their work, we integrated meteoroids not only 1 m in radius, but also larger bodies. The time span of our integration was substantially longer (150 My vs. 50 My), which allowed us to calculate population decay rates for the sizes $R = 1$ m, 10 m, 50 m and 100 m. (The time span was still too short to properly model the decay of 500 m bodies.) We use a more precise Mars-crossing criterion and we provide a direct comparison to the analytical decay

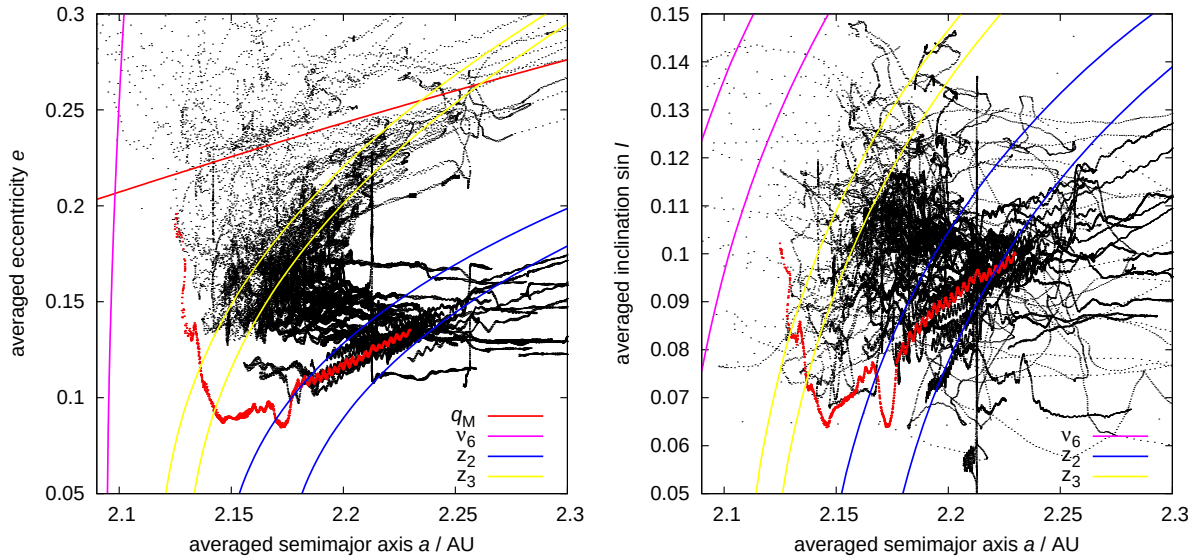

Figure 41: The role of hight-order secular resonances on the orbital evolution of meteoroids: (left) the averaged semimajor axis vs. eccentricity for Flora 100 m regolith meteoroids, with captures in the z_2 resonance; (right) the semimajor vs. sine of inclination. The $\pm 1\,''$/y borders of the secular resonances were calculated using the `secre8` program by A. Milani and Z. Knežević.

rates used in the Monte-Carlo model by Vokrouhlický & Farinella (2000), which were calculated from pure Yarkovsky semimajor axis drift rates and fixed positions of major resonances. In the previous work, the initial velocities with respect to the parent bodies were zero, but in our case we included the initial spread. Additionally, we reported interactions with high-order secular resonances and we estimated the crossing probability of the J3/1 resonance.

We can use the results of our N-body integrations to improve Monte-Carlo models of meteoroid delivery (like Vokrouhlický & Farinella (2000)), which include a complex collisional dynamics compared to our model, but a simplified orbital dynamics only (i.e., there is only the Yarkovsky semimajor axis drift, with no chaotic diffusion in eccentricity and inclination and no possibility of resonance crossing).

There are more proposals for future work: i) we can substantially increase the number of integrated particles in order to improve the statistics, and ii) incorporate the YORP effect, which can possibly change rotational axes of meteoroids.

4 Yarkovsky driven orbit and spin axis of (2953) Vysheslavia

The asteroid (2953) Vysheslavia and several others, located just above the 5/2 mean motion resonance with Jupiter, are known to have unstable orbits. Vokrouhlický et al. (2001) and Brož & Vokrouhlický (2002) brought evidence, that all these asteroids were transported to this unstable region from stable regions (with larger semimajor axes) by the Yarkovsky semimajor axis drift. This scenario requires the asteroids have retrograde orientations of the spin axes (in order to drift towards the J5/2 resonance) and this was later confirmed for Vysheslavia by photometric observations, as reported by Vokrouhlický et al. (2005e). This chapter is based on the two latter articles. The co-authors are D. Vokrouhlický, T. Michałowski, S.M. Slivan, F. Colas, L. Šarounová and F.P. Velichko. MB is responsible for the numerical simulations of the Yarkovsky transport and the construction of the stability map (Section 4.2).

Abstract

The orbit of asteroid (2953) Vysheslavia is presently locked in a tiny chaotic zone very close to the 5/2 mean motion jovian resonance. Its dynamical lifetime is estimated to be of the order of only 10 My. Such a situation poses a problem, since Vysheslavia is a member of the Koronis family, which is likely more than 2 Gy old. Three main hypotheses were developed to solve this apparent contradiction: (i) Vysheslavia might be an outcome of a recent secondary fragmentation event in the family, (ii) Vysheslavia might have been placed on its peculiar orbit by close encounters with nearby massive asteroids, or (iii) the asteroid might have been transported by a slow inward–drift of the semimajor axis due to the Yarkovsky effect. Though we cannot disprove the first two possibilities completely, here we bring evidence for the third scenario.

At first, we present numerical simulations of the orbital evolution (with the Yarkovsky effect included) for Vysheslavia and several neighbouring asteroids. We also argue against the possibility that Vysheslavia reached its current orbit by a recent collisional breakup.

Second, photometric observations were made during the years 2000–2005 and used to determine the pole orientation of (2953) Vysheslavia. We find admissible solutions for ecliptic latitude and longitude of the rotation pole P_3: $\beta_{\rm p} = -64^\circ \pm 10^\circ$ and $\lambda_{\rm p} = 11^\circ \pm 8^\circ$ or P_4: $\beta_{\rm p} = -68^\circ \pm 8^\circ$ and $\lambda_{\rm p} = 192^\circ \pm 8^\circ$. These imply obliquity values $\gamma = 154^\circ \pm 14^\circ$ and $\gamma = 157^\circ \pm 11^\circ$, respectively. The sidereal rotation period is $P_{\rm sid} = (0.2622722 \pm 0.0000018)$ day. This result is consistent with the prediction done by Vokrouhlický *et al.* (2001) that Vysheslavia has the obliquity between 90° and 180°, because it has been transported to its unstable orbit by the Yarkovsky effect. Moreover, with the obliquity close to 180°, Vysheslavia seems to belong to one of the two distinct groups in the Koronis family found recently by Slivan (2002).

4.1 Introduction and motivations

The fundamental argument of our work derives from the important finding of Milani & Farinella (1995) who noticed that asteroid (2953) Vysheslavia is located in a tiny chaotic zone (about 10^{-3} AU wide) very close to the outer border of the strong 5/2 mean motion resonance with Jupiter. The expected dynamical lifetime of such an orbit before falling into the resonance is of order of only 10 My, what is in an apparent contradiction with the estimated age of the whole Koronis family 2–3 Gy (Chapman 2002; Bottke *et al.* 2001; Vokrouhlický *et al.* 2003). Vysheslavia is presumably its member: the spectroscopic analysis indicates that Vysheslavia is an ordinary S–type asteroid (Bus & Binzel (2002a)) and the statistical analysis of the Koronis family predicts very few interlopers of the Vysheslavia size (Migliorini *et al.* (1995)). Knežević *et al.* (1997) tentatively identified two other Koronis members very close to the mentioned chaotic zone.

Milani & Farinella (1995) proposed two hypotheses: (i) Vysheslavia might be an outcome of a recent secondary fragmentation event in the family, or (ii) Vysheslavia might have been placed on its present orbit by close encounters with massive asteroids. However, none of these two possibilities were found very likely: the probability of the disruption of large (25–50 km) parent asteroid during the last 100 My is less than 5 % and the gravitational fluctuations in the semimajor axis due to Ceres and Pallas may statistically accumulate to $\approx 10^{-3}$ AU over the age of the Solar System.

In Vokrouhlický *et al.* (2001) we proposed the Yarkovsky-driven origin of the Vysheslavia's metastable orbit. We have checked that the Yarkovsky force is able to change the semimajor axis of multikilometer size asteroids by 0.01–0.02 AU within their expected collisional lifetime. Objects, originally located on stable orbits further from the 5/2 resonance, may be thus brought to its vicinity. In course of this evolution they may be temporarily captured in chaotic regions related to weaker resonances and thus explain origin of the orbit of Vysheslavia. The probability of this process appears much higher than in the previously mentioned possibilities. Here we report 9–14 more asteroids (likely members of the

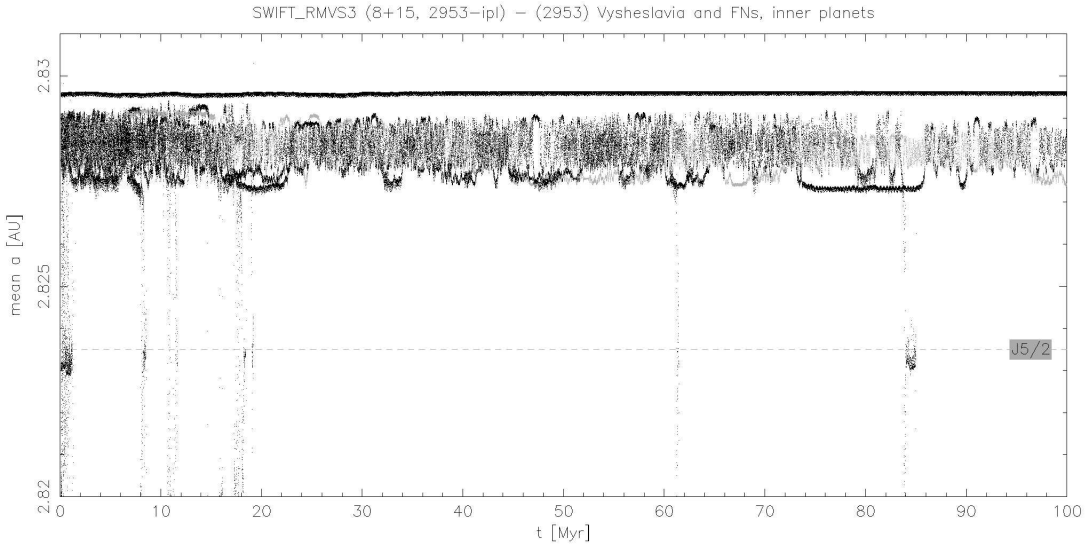

Figure 42: Mean semimajor axis (in AU) vs. time (in My) for Vysheslavia and its 14 "fictitious neighbours". The Yarkovsky effect is not included in this simulation, but the perturbations by all the planets (except Pluto) are considered. The median lifetime against the fall to the 5/2 resonance is 11 My for this integration, while the lifetime of the objects temporarily residing inside the 5/2 resonance is less than 1 My.

Koronis family) that have similarly metastable orbits as Vysheslavia, and we argue that this brings more evidence for the Yarkovsky-driven origin of these orbits, including Vysheslavia's.

In this section, we also report photometric observations of Vysheslavia that allowed us to determine its pole orientation, and thus its obliquity. Our results confirm the Yarkovsky-driven scenario outlined above and, additionally, they maintain the surprising dichotomy in the obliquity distribution of large Koronis members (Slivan 2002; Slivan *et al.* 2003).

4.2 Numerical simulations

We have implemented linearised versions of both diurnal and seasonal variants of the Yarkovsky effect in different numerical integrators; most importantly, we created a quasi-symplectic integrator `swift_rmvsy` (based originally on `swift_rmvs3` code by Levison & Duncan (1994)) that allows fast simulations. Though the properties of symplecticity are violated due to the weak dissipation caused by the Yarkovsky effect, we have extensively tested our code (by comparing its results with more precise integrators and by reproducing the analytic results when available). These tests, as well as the Yarkovsky effect implementation, are listed in Brož (1999) and Sections 2.3.2, 9.2.

Due to its peculiar location the Lyapunov time of the Vysheslavia's orbit is ≈ 27 ky only. This is much shorter than the time span of most of our simulations, and thus the simulations have a statistical meaning only. This is, however, not an obstacle for our work, since our fundamental conclusions are of statistical nature. To make a statistical sense of our work we have used a technique of integrating neighbour orbits. We used two levels of "zooming" in this respect: (i) "fictitious neighbours" (FNs) cover a larger area around a given orbit (typically up to displacements $\Delta a = 10^{-3}$ AU in the semimajor axis and $\Delta e = 10^{-3}$ in eccentricity), and (ii) "close clones" (CCs) that span basically the 3σ uncertainty ellipsoid of the given orbit initial data (notably up to displacements $\Delta a = 10^{-7}$ AU and $\Delta e = 10^{-6}$).

The orbits of FNs and CCs were integrated both with and without the influence of the Yarkovsky effect (we typically used 4 outer planets in our simulations, but checks with 8 planets except Pluto and even with two massive asteroids Ceres and Pallas were systematically performed). Since we are dealing with multikilometer asteroids, we assumed low surface thermal conductivity ($K = 0.0015$ W/m/K), as indicated by many observations, but again checks with a higher value of K were performed. The major unknown factor, that influences the strength of the Yarkovsky effect, is then the orientation of the asteroid spin axis (and its possible temporal evolution). For that reason, we have performed tests with different orientations of the spin axis.

Vysheslavia's chaotic zone is visible in Figure 42, where the evolution (without the Yarkovsky effect) of the mean semimajor axis of Vysheslavia and its 14 FNs is plotted. One recognises the zone 0.0015 AU

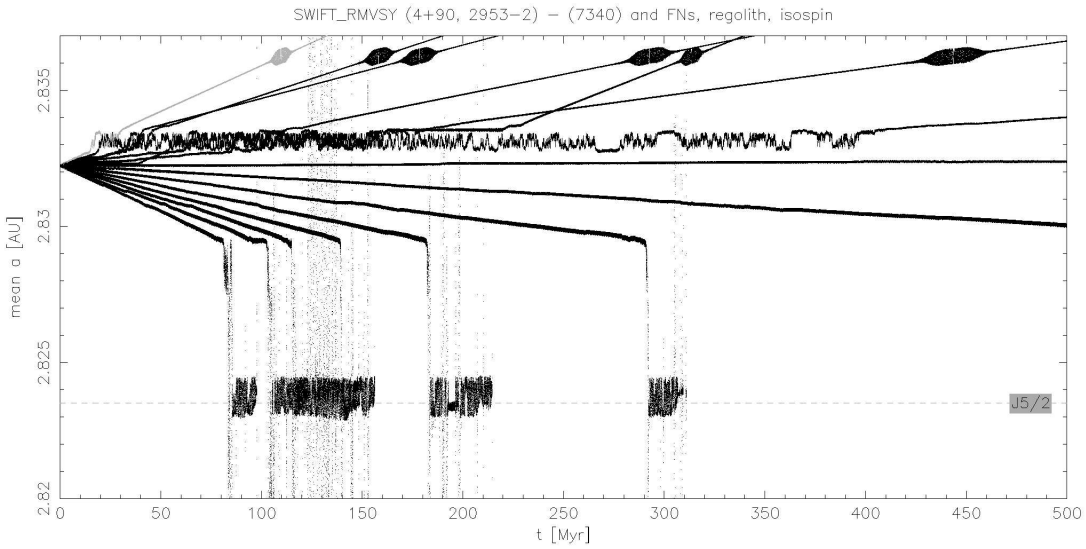

Figure 43: Mean semimajor axis (in AU) vs. time (in My) for asteroid (7340) = 1991 UA_2 and its 14 fictitious neighbours. The low value $K = 0.0015$ W/m/K of the surface conductivity is assumed, the orientations of the spin axes are distributed isotropically in space (FNs here mean that the initial conditions were the same for all objects, but the orientation of their spin axes was different). Apart from the Vysheslavia's chaotic zone at 2.829 AU, one may notice another tiny zone at about 2.833 AU. Given the orientation of the spin axis, the asteroids may drift outwards or inwards. While being originally on a stable orbits, about a half of the FNs reaches the Vysheslavia's chaotic zone (and then the 5/2 resonance) in 70–500 My.

wide easily, because the semimajor axis randomly fluctuates. Notice also sporadic instants, when some of the integrated objects fall into the 5/2 resonance. The uppermost FN has been placed on a stable orbit, to contrast its behaviour with the others.

The transport towards the 5/2 resonance is depicted in Figure 43. It indicates the importance of the Yarkovsky effect for overall mixing of small multikilometer asteroids in families (here the Koronis family asteroid (7340) is integrated with its 14 FNs of different spin orientations; low surface conductivity is assumed). Several facts may be concluded from this integration: (i) the Yarkovsky effect may spread semimajor axes of small asteroids, initially of the same orbit, by as much as ≈ 0.05 AU within their estimated collisional lifetime, (ii) the asteroid (7340) may slowly evolve toward the Vysheslavia's dynamical state (and thus Vysheslavia might have been originally on a similar orbit as (7340)), and (iii) even if the asteroids drift outward from the 5/2 resonance, their origin in past is constrained by the presence of the resonance.

Other asteroids on metastable orbits. We have selected ≈ 400 objects in the outer vicinity of the 5/2 resonance from the `astorb.dat` catalogue (vers. Jul 6, 2000; Bowell *et al.* (1994)) and integrated them for 10 My (Yarkovsky effect was not included in these integrations). After eliminating objects initially inside the 5/2 resonance and those on stable orbits, we have identified 9 objects with metastable orbits, similar to that of Vysheslavia (5 more candidates with poorly known orbits were discarded from the following considerations). Moreover, we found 3 objects on unstable orbits in between the Vysheslavia's chaotic zone and the 5/2 resonance and 1 asteroid just at the upper edge of the Vysheslavia's zone (having an unstable orbit on a very long time span; 5 more candidates of this type have been also found but not integrated for sufficiently long time interval). We selected some of these objects and integrated them (with a limited number of CCs) up to 500 My. Figure 44 shows the characteristic behaviour of the three classes of orbits and we give information about the 7 objects, whose orbits have been integrated, in Table 13. None of these new objects on metastable orbits is of Vysheslavia size, but there are about 7 of them with half of its size (i.e., radii between 3.3–4 km). Others are smaller, with typical radii between 1–2.7 km. Their entire estimated mass is by about 20 % larger than that of Vysheslavia.

We note that the collisional lifetime of a hypothetical $20 - 30$ km size parent body for Vysheslavia is likely $\gtrsim 5 - 10$ Gy (Bottke *et al.* 2005a,b), making the probability of the recent secondary break-up in the Koronis family, with Vysheslavia being the largest fragment, less then 1 %.

We shall also consider the recent break-up of the Karin cluster (Nesvorný *et al.* 2002) as a "benchmark"

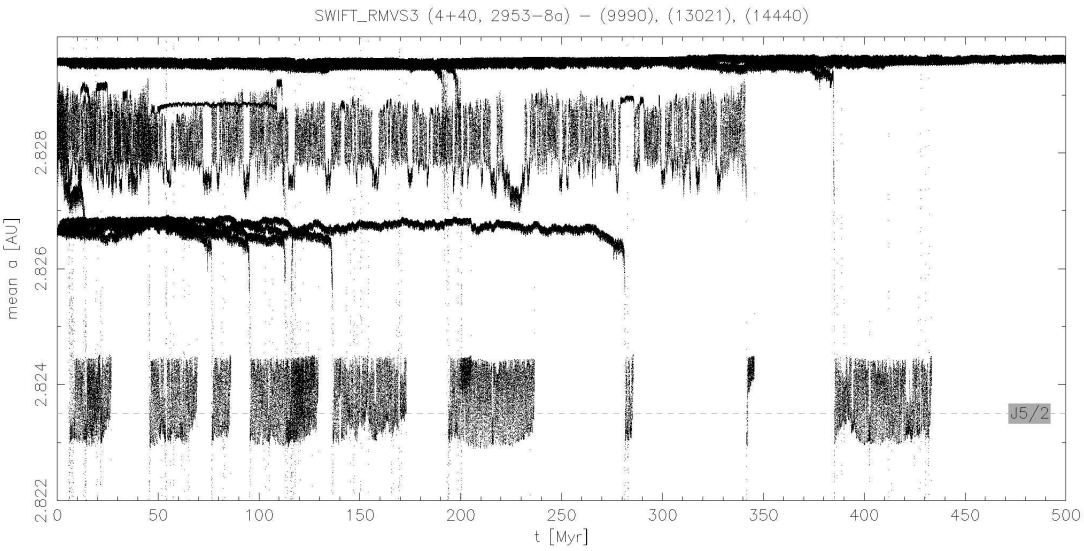

Figure 44: Mean semimajor axis (in AU) vs. time (in My) for asteroids (9990), (13021), (14440), each with 4 "close clones". The Yarkovsky effect is not included here; (9990) (upper body) is on an almost stable orbit but some of the clones may drop to the 5/2 resonance, (13021) (middle body) exhibits behaviour very similar to that of Vysheslavia (see Figure 42), and (14440) (lower body) is on a peculiar orbit very close to the 5/2 resonance. None of these objects could be located on its orbit for the entire lifetime of the Koronis family ($\approx 2\,\mathrm{Gy}$).

Table 13: The sample of asteroids located on metastable orbits close to the 5/2 resonance (most likely Koronis family members); radii estimated from absolute magnitudes and geometric albedo 0.2, dynamical lifetimes against the fall into the 5/2 resonance are given as a median over 5 integrated close clones, proper elements for numbered asteroids are taken from `AstDyS` (`http://newton.dm.unipi.it/`).

asteroid	radius [km]	lifetime [My]	proper a [AU]	proper e
(2953)	7.2	11	2.82767	0.0531
(6814)	3.6	>100	2.82856	0.0417
(9631)	2.7	268	2.82736	0.0393
(9990)	3.3	395	2.82967	0.0606
(13021)	3.6	147	2.82786	0.0550
(14440)	2.7	116	2.82692	0.0286
1996 TE	2.1	14		
2000 GQ_6	3.4	>100		

and deduce what fraction of observable ejecta from a hypothetical secondary disruption event would survive dynamical evolution until the present. Assuming the same velocity distribution as observed in the Karin cluster but centered on the position of Vysheslavia, we predict that from initially $20-40$ fragments larger than $\simeq 3$ km (depending on steepness of the size distribution), some $8-16$ should survive 15 My. This is based on the analysis of the dynamical stability of the fragments' orbits (Figure 45). We find only one object in this close vicinity to Vysheslavia today. Taken together with the low probability of a secondary break-up described above, the absence of accompanying ejecta in the Vysheslavia neighbourhood make the recent collisional disruption scenario exceedingly unlikely.

4.3 Photometric observations

We observed Vysheslavia on 35 nights during five apparitions: January 2000, March–April 2001, September 2002, September–December 2003 and January–February 2005. The longest time span between the first and the last observation within one apparition – 81 days in 2003 – allows us to unambiguously link the sidereal rotation phase of all the other observations, prerequisite for a successful solution. The aspect data of the observations and other information are summarized in Table I.

The January 2000 Vysheslavia observation was performed at Saint Veran Observatory (France) using

Table 14: Aspect data of the (2953) Vysheslavia observations.

Date (UT)	r (AU)	Δ (AU)	ϕ (°)	λ (°)	β (°)	α (°)	δ (°)	Filter	Observation site
				2000					
Jan 16.1	2.882	1.903	2.2	119.37	−0.79	123.42	18.66	R	Saint Veran
Jan 17.1	2.882	1.901	1.8	119.58	−0.80	123.20	18.70	R	Saint Veran
				2001					
Mar 16.4	2.786	2.002	14.9	207.00	−0.75	219.14	−16.40	V	River Oaks
Mar 20.3	2.786	1.963	13.8	207.82	−0.74	218.90	−16.33	V	River Oaks
Mar 21.3	2.785	1.954	13.5	208.06	−0.74	218.82	−16.31	V	River Oaks
Apr 26.1	2.778	1.772	0.4	215.74	−0.62	212.97	−14.32	R	Pic du Midi
Apr 27.0	2.778	1.772	0.6	215.92	−0.62	212.79	−14.25	R	Pic du Midi
Apr 28.0	2.778	1.772	1.0	216.13	−0.62	212.58	−14.17	R	Pic du Midi
				2002					
Sep 02.0	2.795	1.853	9.1	322.50	1.01	315.44	−15.33	R	Pic du Midi
Sep 03.0	2.795	1.859	9.4	322.71	1.01	315.29	−15.37	R	Pic du Midi
				2003[a]					
Sep 24.3	2.884	2.233	17.3	41.93	0.53	56.86	20.65	V	Whitin
Sep 25.3	2.884	2.222	17.1	42.12	0.52	56.86	20.65	V	Whitin
Sep 30.2	2.885	2.167	16.0	43.12	0.51	56.80	20.63	V	Whitin
Oct 01.2	2.885	2.156	15.8	43.32	0.50	56.76	20.62	V	Whitin
Oct 04.3	2.886	2.126	15.1	43.92	0.49	56.62	20.59	V	Whitin
Oct 20.3	2.888	1.990	10.3	47.10	0.44	54.93	20.20	V	Whitin
Oct 29.0	2.889	1.939	7.0	48.88	0.41	53.42	19.82	V	Kharkiv
Nov 01.2	2.890	1.926	5.8	49.48	0.40	52.78	19.65	V	Whitin
Nov 05.1	2.890	1.913	4.2	50.29	0.38	51.96	19.45	R	Ondřejov
Nov 06.1	2.890	1.911	2.8	50.49	0.38	51.75	19.40	R	Ondřejov
Nov 15.2	2.891	1.902	0.2	52.26	0.35	49.71	18.83	V	Whitin
Nov 15.3	2.891	1.902	0.2	52.26	0.35	49.69	18.82	V	Oakley
Nov 16.3	2.891	1.902	0.4	52.45	0.35	49.47	18.78	V	Oakley
Nov 18.3	2.892	1.904	1.2	52.85	0.34	49.02	18.65	V	Oakley
Dec 01.7	2.893	1.949	6.8	55.56	0.29	46.21	17.83	R	Kharkiv
Dec 02.7	2.893	1.953	7.2	55.76	0.29	46.03	17.77	R	Kharkiv
Dec 13.1	2.894	2.022	10.8	57.80	0.25	44.39	17.24	R	Whitin
Dec 14.0	2.894	2.030	11.1	58.00	0.25	44.27	17.20	R	Whitin
				2005					
Jan 05.1	2.866	2.077	13.8	134.93	-0.96	150.41	10.67	R	Pic du Midi
Jan 06.2	2.866	2.067	13.5	135.13	-0.96	150.32	10.69	R	Pic du Midi
Feb 06.2	2.859	1.877	2.2	141.40	-1.01	145.36	12.22	R	Whitin
Feb 07.0	2.859	1.875	1.8	141.61	-1.01	145.19	12.28	R	Pic du Midi
Feb 07.1	2.859	1.875	1.7	141.61	-1.01	145.17	12.28	R	Whitin
Feb 07.9	2.859	1.874	1.3	141.81	-1.01	144.99	12.33	R	Kharkiv
Feb 10.1	2.858	1.872	0.6	142.21	-1.01	144.52	12.50	R	Pic du Midi

[†]Date is the mean epoch of the observation, r and Δ are the heliocentric and geocentric distances, ϕ is the phase angle, (λ, β) are the ecliptic longitude and latitude in the J2000.0 reference frame, and (α, δ) are the J2000.0 right ascension and declination.

[‡]The light-curve data can be found at `http://sirrah.troja.mff.cuni.cz/yarko-site/2953_photometry/`.

[a]The 2003 observations provide the longest run within one apparition and enable unambiguous linking of sidereal rotation phase throughout the whole period 2000–2005.

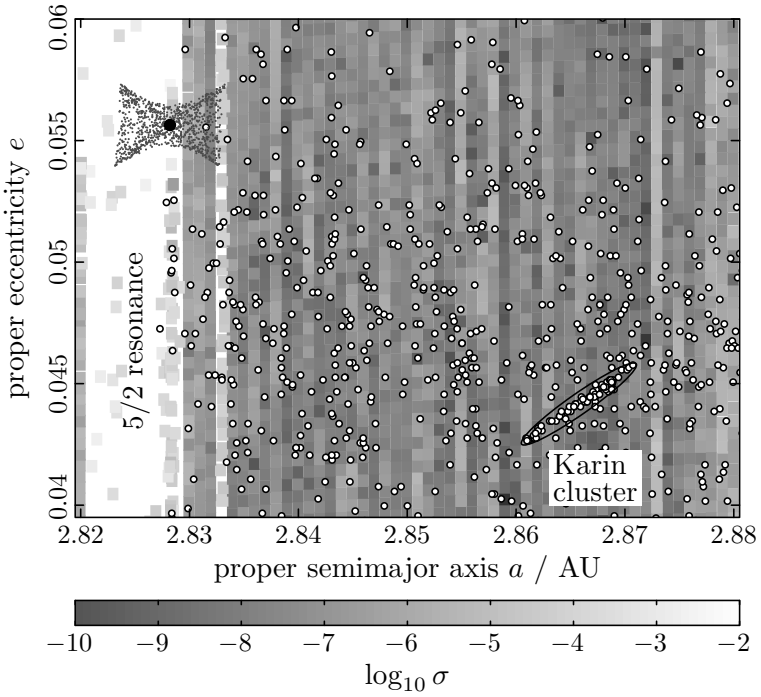

Figure 45: Koronis family members (open circles) projected on the plane of synthetic proper semimajor axis and proper eccentricity (Knežević *et al.* 2002); the Karin cluster is indicated in the lower right corner. Assuming an isotropic velocity field, ejecta from a hypothetical secondary collisional disruption near Vysheslavia (full circle) would fall in the region indicated by grey dots. Only one of the observed Koronis asteroids falls in this zone, notably in its stable part exterior to the 5/2 mean-motion resonance with Jupiter. Orbital stability is indicated by grey shading indicating a parameter $\sigma = 1 - n^{(2)}/n^{(1)}$, where $n^{(1)}$ and $n^{(2)}$ are proper mean motions of test particles calculated in the two consecutive time intervals, each spanning 1.2 My (see Robutel and Laskar, 2001; dark zones of small σ value imply stability, white areas of high σ value, such as the 5/2 mean motion resonance with Jupiter, are unstable). The family members were identified using the hierarchical clustering method with the standard metric and the velocity cutoff 60 m/s (e.g., Zappalà *et al.* 1995; Bottke *et al.* 2001).

a 0.62-m telescope equipped with a HiSys22 CCD camera (KAF400 chip) and a non-standard R filter. As a result, no transformation to the standard photometric system was possible. The data were processed with the software APHOT developed at Ondřejov Observatory. The aperture photometry was used as described by Pravec *et al.* (1996).

During the next four apparitions the asteroid was observed at Pic du Midi Observatory (France) using a 1.05-m reflector equipped with the Thomson 7863 CCD camera and R filter. A standard reduction was performed with the ASTROL software developed at the Institut de Mécanique Céleste in Paris. The aperture photometry was obtained with the CCLRS STARLINK package (see also Michałowski *et al.*2000). Due to occasional non-photometric weather conditions, the data obtained were not transformed to the standard system and only relative instrumental magnitudes were used.

In March 2001, Vysheslavia was also observed by Bill Holliday at the River Oaks Observatory, New Braunfels (Texas) using a 0.4-m Newtonian telescope equipped with an SBIG ST8E CCD camera. The standard dark subtraction, flat fielding and differential photometry were performed using the Mira software (`http://www.axres.com`).

In 2003 and 2005 lightcurve observations were made at the Whitin Observatory at Wellesley College (Massachusetts), using the 0.61-m Sawyer telescope with a Photometrics camera housing a Tektronics (SITe) back-illuminated CCD detector. The data were calibrated to the standard system, yielding V and R magnitudes in 2003 and R magnitudes in 2005. Image processing and synthetic aperture photometry were performed using the IRAF software applications from NOAO. The calibrated data from 2003 are sufficient to derive the color index $V - R = 0.49 \pm 0.01$, and also Lumme-Bowell solar phase coefficients at that aspect: $H = 11.92 \pm 0.04$ and $G = 0.19 \pm 0.02$.

At the Kharkiv Observatory, where observations were also performed in 2003 and 2005, we used the 0.7-m reflector equipped with a CCD camera (ST-6UV in 2003 and IMG1024S in 2005) and standard V and R filters. Frames were reduced with the synthetic aperture package ASTPHOT developed at DLR

(e.g., Mottola *et al.* 1995).

Three additional lightcurves were kindly provided by Richard Ditteon, who observed Vysheslavia in mid November 2003 from Oakley Observatory, Terre Haute (Indiana). A 0.36-m telescope was equipped with an AP7 CCD camera and a standard V filter. Relative photometry was obtained and analysed using the Canopus program.

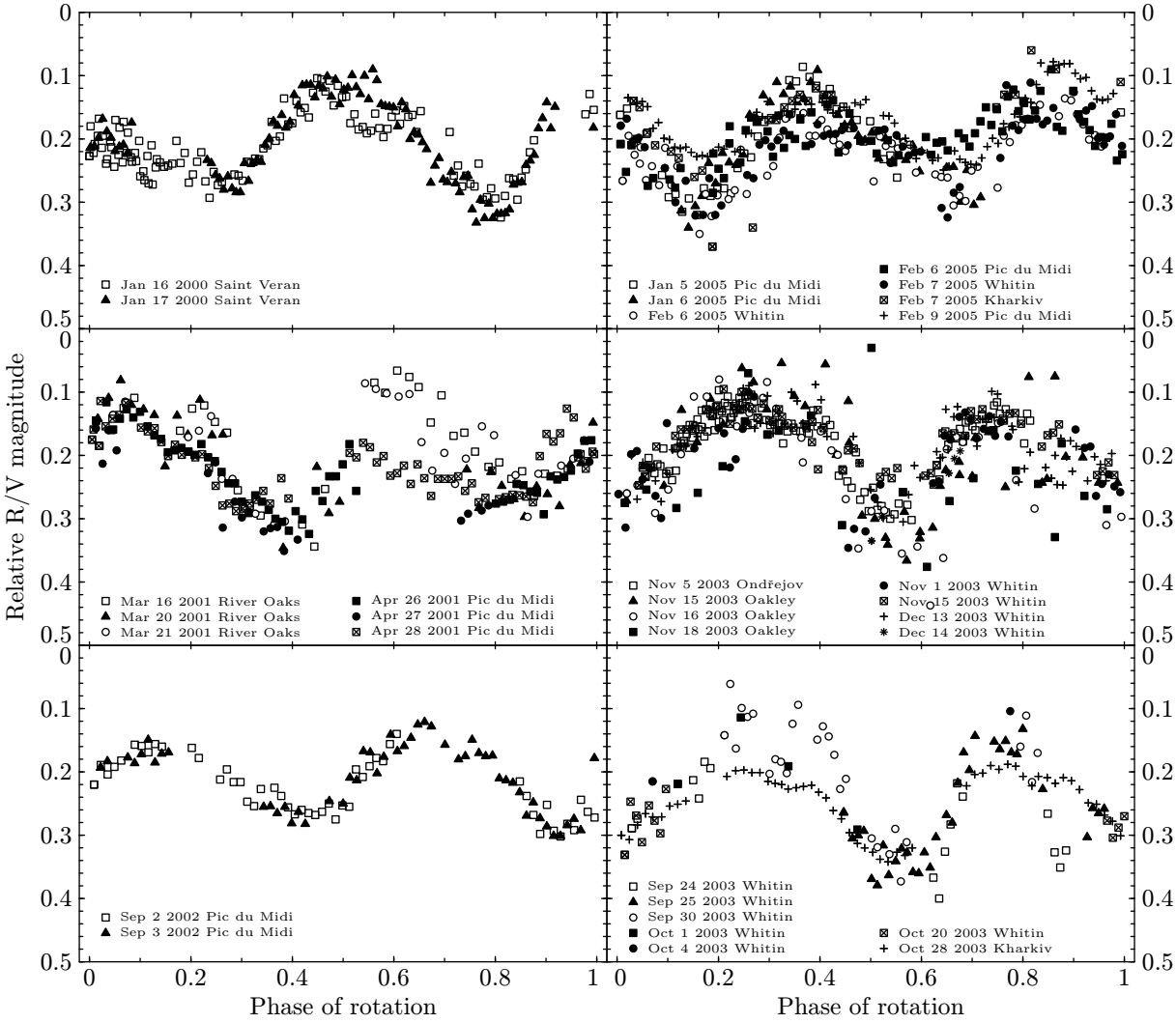

Figure 46: Composite rotation lightcurves of (2953) Vysheslavia in five consecutive apparitions: January 2000, March–April 2001, September 2002, September–December 2003 and January–February 2005. The abscissa is the rotational phase with a common zero point corrected for light-time and related to the first observation in the panel and a synodic period 6.295 h. On the ordinate, relative instrumental magnitudes, either in the R or V bands, adjusted so that dispersion with respect to the neighbours is minimized. Variations in the lightcurves are mainly due to changing Sun-asteroid-observer geometry (see the phase angle in Table 1). Data are on our web site `http://sirrah.troja.mff.cuni.cz/yarko-site/2953_photometry/`.

The observations are presented as composite lightcurves (Fig. 1) consistent with a synodic period of (6.295 ± 0.001) hours. For presentation purposes the magnitude offset of each lightcurve was obtained by minimizing the dispersion of data points relative to their neighbours. The variations in the lightcurve amplitudes are due mainly to changes in the Sun-asteroid-observer phase angle; the mean amplitudes range from about 0.09 magnitude at the smallest phase angles to $0.15 - 0.17$ magnitude at the largest phase angles. We estimate the error of the lightcurve amplitudes to be $\simeq 0.02$ magnitude, while the error of the lightcurve maximum/minimum epochs is $\simeq 10$ minutes. A preliminary look at the data, notably the small amplitude variations remaining after accounting for phase angle changes across the $(0°, 17°)$ interval, suggest a non-ecliptic pole for Vysheslavia.

4.4 Shape and spin model of (2953) Vysheslavia

To strengthen the robustness of our conclusions we used two independent and different solution methods described below. Because we confirm the pole aspect close to 90°, further observations will help reduce the uncertainty in the pole solution but probably will not improve much the shape solution. Already, the 2005 apparition appears to closely repeat the 2000 configuration with only a moderate shift in the ecliptic longitude. Further data will improve the longitude coverage, but will likely not change the solution in a significant way.

4.4.1 Method # 1

First, the orientation of the spin vector, sidereal period, and triaxial ellipsoid model of Vysheslavia have been determined using the method described by Michałowski (1993). This approach combines epoch, amplitude-aspect, and magnitude-aspect methods by building a set of nonlinear equations whose solutions are found by least squares fitting the model to the times of lightcurve maxima, the lightcurve amplitudes, and (if available) the calibrated magnitudes. The amplitude-aspect equations represent basically the weighted amplitude-aspect (WAA) method (see also Drummond *et al.* 1988) that models the asteroid as a triaxial ellipsoid of uniform surface reflectivity. To a good approximation the brightness variations are given directly by the changing cross-section of the asteroid as it rotates about the shortest body axis; lightcurve amplitudes observed at different viewing aspects are used to deduce the spin axis orientation. The magnitude-aspect equations are based on a similar approach, except that they model lightcurves' overall brightnesses instead of their amplitudes. To resolve the sense of rotation about the axis we complemented the amplitude and magnitude information with equations representing the epoch method, namely tracking in time a chosen "prominent feature" on the rotation curve, assuming that it corresponds to a pattern at a fixed longitude on the asteroid.

This combined amplitude-magnitude-epoch analysis leads to a set of nonlinear equations for the pole longitude $\lambda_{\rm p}$ and latitude $\beta_{\rm p}$, the sidereal rotation period $P_{\rm sid}$, and ratios a/b and b/c of the best-fit ellipsoid axes; Michałowski (1993) discusses the appropriate iterative method of their solution. At convergence, we obtained the following best-fit solutions (there is an obvious near-180° ambiguity in determination of the ecliptic longitude of the pole):

$$\begin{aligned} P_{\rm sid} &= (0.2622732 \pm 0.0000008) \text{ days} , \\ P_3: \quad \lambda_{\rm p} &= 15^\circ \pm 3^\circ , \quad \beta_{\rm p} = -60^\circ \pm 8^\circ , \\ P_4: \quad \lambda_{\rm p} &= 190^\circ \pm 3^\circ , \quad \beta_{\rm p} = -65^\circ \pm 8^\circ , \\ a/b &= 1.15 \pm 0.01 , \quad b/c = 1.0 \pm 0.1 , \end{aligned}$$

implying indeed a retrograde sense of rotation and a pole far from the ecliptic. The mirror solutions, P_1 and P_2, with prograde rotation are rejected having χ^2 value 3 times larger than P_3 and P_4 and statistically poor. This configuration is unfavorable to solve for the ratio b/c, and its value above is only formal (see eqs. (3) and (5) in Michałowski, 1993).

4.4.2 Method # 2

An independent analysis of the same data was done using the method described by Slivan *et al.* (2003). Brightness and epoch information related to low-order shape were extracted from the lightcurves by least-squares fitting Fourier series, and then analyzed with the sidereal photometric astrometry (SPA), weighted amplitude-aspect (WAA), and simultaneous amplitude-magnitude (SAM) methods based on those of Drummond *et al.* (1988).

Using only the timing information, SPA constrains the pair of pole solutions to be quite far from the ecliptic plane, with retrograde rotation and ecliptic longitude near 0° or 180°. A second pair of solutions with prograde rotation and ecliptic longitude near 90° or 270° is rejected, because the fit to the epochs is poor and unlikely multiple exchanges of the primary and secondary extrema are required over the range of aspects observed. The χ^2 acquires a value 2.3 times larger than that of the favored retrograde poles.

It is more difficult to use the lightcurve amplitude and brightness methods to reliably determine the spin axis of Vysheslavia, because the observed aspect-dependent changes in the available data are so small that they are comparable to the measurement uncertainties. In fact, for the adopted poles, neither the largest- nor the smallest-amplitude aspects have yet been observed. The WAA analysis of the amplitudes alone does not give satisfactory results; it finds spin axes consistent with only the rejected SPA solutions. The SAM analysis uses both amplitudes and overall brightness, and it does find axis solutions consistent

with the favored SPA solutions, but the standard-calibrated data it needs have been recorded during only two of the five apparitions observed so far.

The adopted poles for method #2 were found at the intersections of the SPA "E-Method arcs" and the SAM "AM Solution Curves" as described by Magnusson (1986). These poles were used with SPA to calculate the sidereal period. The same poles were also used with SAM to calculate axial ratios, but the limited aspect coverage of calibrated lightcurves leads to very large formal uncertainties and no useful constraints on the shape. We thus obtained (the shape parameters are not reported):

$$\begin{aligned} P_{\rm sid} &= (0.2622713 \pm 0.0000002) \text{ days} , \\ P_3: \quad \lambda_{\rm p} &= 8^\circ \pm 6^\circ , \quad \beta_{\rm p} = -68^\circ \pm 4^\circ , \\ P_4: \quad \lambda_{\rm p} &= 194^\circ \pm 7^\circ , \quad \beta_{\rm p} = -71^\circ \pm 4^\circ . \end{aligned}$$

4.4.3 Adopted solution

The previous results indicate formal statistical errors of the solved parameters. They are close to each other[9], but the fact they are not identical signals a presence of non-random errors in the data and/or not complete adequacy of the used solution methods and their assumptions (such as the triaxial shape of the asteroid). We also note that the numerical algorithms to solve for the best-fit parameters are different in methods #1 and #2, and this may also contribute to the observed difference in the two solutions.

A conservative, though perhaps too pessimistic, approach to merge the previous results into a single, adopted solution is to use an average of the best-fit values for the corresponding parameters and "realistic" errors that embrace formal uncertainty intervals of both solutions. With that approach we obtain:

$$\begin{aligned} P_{\rm sid} &= 0.2622722 \pm 0.0000018 \text{ (days)} \\ P_3: \quad \lambda_{\rm p} &= 11^\circ \pm 10^\circ , \quad \beta_{\rm p} = -64^\circ \pm 10^\circ \\ P_4: \quad \lambda_{\rm p} &= 192^\circ \pm 8^\circ , \quad \beta_{\rm p} = -68^\circ \pm 8^\circ . \end{aligned}$$

Using the orbital inclination of 1.1° and longitude of the ascending node 251.3° for Vysheslavia, we thus obtain obliquity values $\gamma = 154^\circ \pm 14^\circ$ (P_3) and $\gamma = 157^\circ \pm 11^\circ$ (P_4), respectively.

The spin vector determination methods we used also suggest a low-order shape for Vysheslavia, but this shape information is very approximate owing to the simplifying assumptions of the models and the limited data available. Given sufficient data a more sophisticated analysis such as the convex inversion approach of Kaasalainen *et al.* (2001) should give better shape information, however, the science implications discussed in the following section do not depend on details of the shape model used, so such analysis is outside the scope of our present work. Slivan *et al.* (2003), and more recently Michałowski *et al.* (2004), demonstrated that the amplitude-magnitude-epoch and convex inversion methods give generally good agreement between derived pole locations, even if there are not enough data to derive a detailed model shape.

4.5 Discussion

Our solution for the Vysheslavia pole has two interesting implications. Together with the dynamics of Vysheslavia's neighbours (Section 4.2), it agrees with a general model of dynamical evolution of asteroid families in which they continually spread due to the Yarkovsky effect (e.g., Bottke *et al.* 2001, Tsiganis *et al.* 2003; Vokrouhlický *et al.* 2005a,b). Vysheslavia makes sense as the largest member of an asteroid population "on the brink", continually resupplied by new objects. In the Koronis family, another argument for the ongoing spread in the semimajor axes is the existence of the Prometheus clan, whose asteroids have a significantly higher eccentricity value beyond the $g + 2g_5 - 3g_6$ secular resonance (Bottke *et al.* 2001).

The alternative possibility, discussed by Milani and Farinella (1995), is that Vysheslavia has a collisional origin, either as a result of a recent disruptive secondary break-up in the Koronis family or that a non-disruptive impact on Vysheslavia shifted its semimajor axis into the dynamically unstable region. A possible result of this collision could be a non-principal-axis rotation of Vysheslavia, provided it occurred so recently that internal dissipation would not damp the wobble energy. For a $\simeq 15$ km size asteroid and 6.29 h rotation period the characteristic damping time scale is $0.5 - 5$ My, depending on the physical parameters of the body (e.g., Vokrouhlický and Čapek, 2002; Paolicchi *et al.*2002). The higher value, if

[9]The sky plane uncertainty ellipses of the pole solution overlap but the sidereal rotation period uncertainty intervals are disjunct.

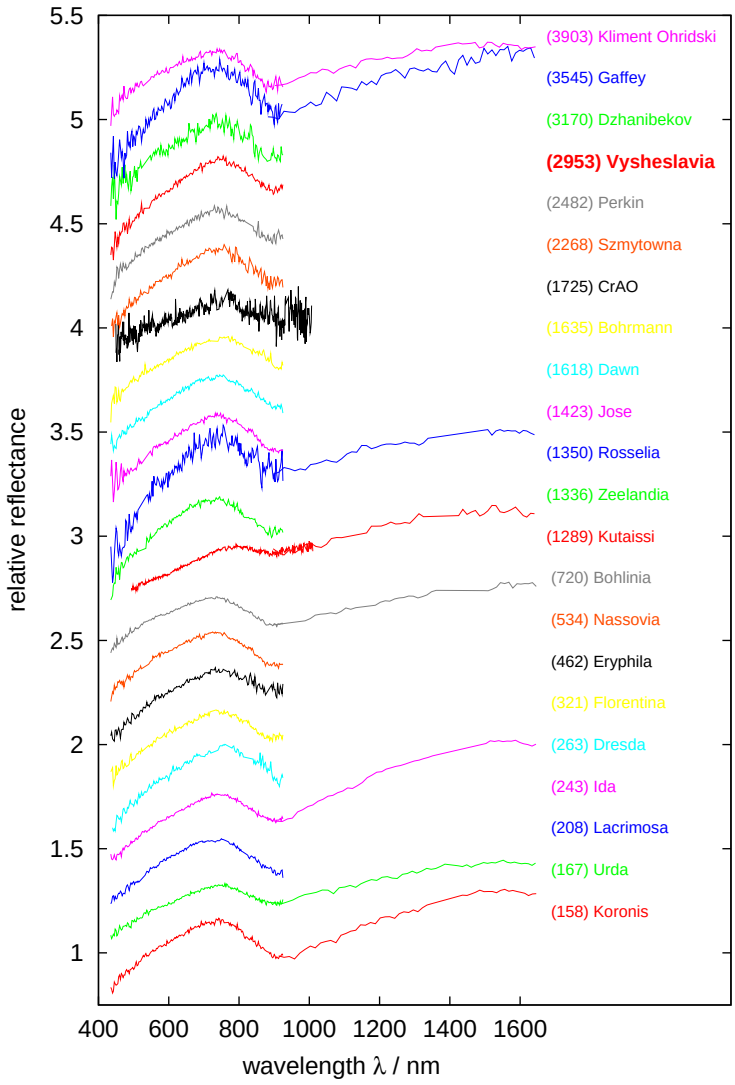

Figure 47: Spectra (relative reflectaces) of 22 Koronis family members; the first one, for (158) Koronis, is in order, the rest are subsequently shifted by 0.2 due to visibility. Data from the SMASSII web site `http://smass.mit.edu`.

correct, is a non-negligible fraction of the dynamical lifetime of Vysheslavia's orbit. Our observations, however, do not support the non-principal-axis rotation. Rather, they are consistent with a stable rotation mode about the short axis with a single rotation period over all five apparitions. This obviously does not rule out the recent collisional origin of Vysheslavia, but it makes it less likely.

Additionally, we examined spectra of 22 Koronis members, including Vysheslavia, available at the SMASSII web site `http://smass.mit.edu`. The reflectance spectrum of Vysheslavia is quite typical for the Koronis family (S-type; e.g., Chapman *et al.* 1989; Bus and Binzel 2002) and does not exhibit any anomalous feature that would be possibly related to its hypothetical younger age (Figures 47 and 48).

Secondly, Slivan (2002) and Slivan *et al.* (2003) analyzed spin vectors of the largest members in the Koronis family. They found a markedly non-random distribution with two statistically significant clusters having obliquity near 50° (prograde rotators) and between $150 - 180°$ (retrograde rotators). Though Vysheslavia is little smaller than the asteroids observed by Slivan *et al.* (with sizes of $20 - 40$ km), it still seems to marginally fit the bimodal distribution of the pole directions in the family, namely it matches the observed characteristics of the retrograde rotators. Vokrouhlický *et al.* (2003) argue that the known spin vectors of Koronis members underwent a remarkable dynamical evolution driven by YORP effect, a rotational variant of the Yarkovsky effect. They also predict, that at small sizes the bimodal pattern should disappear, because of increasing strength of the YORP effect. It appears that Vysheslavia may be just in a transition interval of sizes. Photometric observations of further $10 - 20$ km sized Koronis family members, with the goal to determine their spin vectors, is thus an important project for the future.

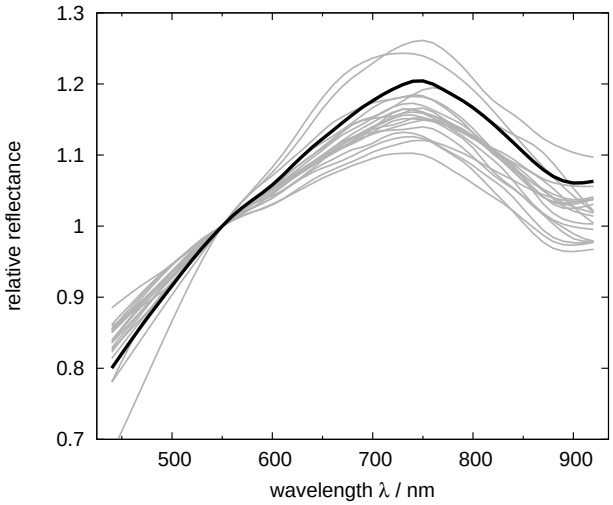

Figure 48: Smoothed visible spectra of 22 Koronis family members, all normalized to unity at 550 nm. The asteroid (2953) Vysheslavia is plotted in bold; it does not exhibit anomalous features with respect to the other asteroids. Data from the SMASSII web site `http://smass.mit.edu`.

Acknowledgments. We are grateful to Anton Paschke and Luděk Vašta for their help during the observations taken at Saint Veran Observatory, Bill Holliday for providing us with his observations at the River Oaks Observatory, Richard Ditteon for providing us with his observations at the Oakley Observatory, and Rebecca Soule for help with observations at the Whitin Observatory. Bill Bottke suggested several improvements to the original manuscript, and Josef Ďurech had many comments and suggestions. This work has been supported by the Grant Agency of the Czech Republic, under the grant No. 205/05/2737, and by the Polish KBN Grant 1 P03D 020 27.

5 Yarkovsky origin of the unstable asteroids in the 2/1 resonance with Jupiter

The asteroidal population inside the J2/1 mean motion resonance was recently identified by Brož et al. (2005a) and the Yarkovsky model, which succesfully explains the existence unstable asteroids, was constructed by Brož et al. (2005b); this chapter is a sligtly extended version of these articles. The co-authors are: D. Vokrouhlický, F. Roig, D. Nesvorný, W.F. Bottke and A. Morbidelli; MB is responsible for the update of the resonant population and all N-body simulations in Sections 5.2, 5.3.1 and 5.3.3.

Abstract

The 2/1 mean motion resonance with Jupiter, intersecting the main asteroid belt at ≈ 3.27 AU, contains a small population of objects. Numerical investigations have classified three groups within this population: asteroids residing on stable orbits (i.e., Zhongguos), marginally stable orbits with dynamical lifetimes on the order 100 My (i.e., Griquas) and unstable orbits. In this paper, we reexamine the origin, evolution and survivability of objects in the 2/1 population. Using recent asteroid survey data, we have identified one hundred new members since the last search, which increases the resonant population to 153. The most interesting new asteroids are those located in the theoretically-predicted stable island A, which until now had though to be empty. Next, we investigated whether the population of objects residing on the unstable orbits could be resupplied by material from the edges of the 2/1 resonance by the thermal drag force called the Yarkovsky effect (and the YORP effect, which is related to the rotational dynamics). Using N-body simulations, we showed that test particles pushed into the 2/1 resonance by the Yarkovsky effect visit the same regions occupied by the unstable asteroids. We also found that our test bodies had dynamical lifetimes consistent with the integrated orbits of the unstable population. Using a semi-analytical Monte-Carlo model, we computed the steady-state size distribution of magnitude $H < 14$ asteroids on unstable orbits within the resonance. Our results provide a good match with the available observational data. Finally, we discuss whether some 2/1 objects may be temporarily-captured Jupiter family comets or near-Earth asteroids.

5.1 Introduction

In 1869 the first asteroid, 108 Hecuba, was found to reside near the 2/1 mean motion resonance with Jupiter (Luther 1869; Tietjen 1869). (Hereafter, we denote this resonance as J2/1, with other resonances denoted accordingly.) Since that time, asteroidal dynamics near or inside mean motion resonances with Jupiter have attracted attention. For example, Hansen, Bohlin and von Zeipel were among the first in a long list of researchers who tried to deal with the difficulties of insufficient convergence of the resonant trigonometric perturbation series for Hecuba-like orbits (historical notes in Hagihara 1975). These cases demonstrated the limits of analytical methods (e.g., perturbation theory). More recently, semi-analytical and numerical methods have allowed to make great progress in our understanding of resonant dynamics. In particular, we can now decipher some of the minute details of asteroid motion inside the J2/1 (e.g. Murray 1986; Henrard & Lemaître 1987; Lemaître & Henrard 1990; Morbidelli & Moons 1993; Ferraz-Mello 1994; Henrard et al. 1995; Morbidelli 1996; Nesvorný & Ferraz-Mello 1997; Moons et al. 1998; Morbidelli 2002).

Although today we recognize that Hecuba itself is just outside the J2/1, we know that more than hundred asteroids reside *inside* the J2/1. This sample is large enough to allow us to quantitatively analyse their origin. Recently, Roig et al. (2002) published a catalogue of 53 asteroids residing in the J2/1 and placed them into 3 groups according to their dynamical lifetime in the resonance ($t_{\mathrm{J2/1}}$). Half of the orbits were found to be stable ($t_{\mathrm{J2/1}} \approx 1$ Gy), much like that of (3789) Zhongguo, the first stable asteroid discovered in the J2/1 resonance. The remaining bodies are either marginally stable ($t_{\mathrm{J2/1}} \approx 100$ My) or unstable ($t_{\mathrm{J2/1}} \approx 10$ My), with the leading asteroids in each group being (1362) Griqua and (1922) Zulu. Importantly, the largest asteroids of all three groups are between $D = 20 - 30$ km in diameter.

Asteroidal sizes and dynamical lifetimes are very basic indicators of their origin. We know that unstable resonant asteroids are not primordial because they cannot reside on their current orbits for 4.6 Gy.[10] Moreover, small asteroids are unlikely to survive 4.6 Gy of collisional evolution. Bottke et al. (2004) estimate the collisional lifetimes of $D < 10$ km asteroids are less than the age of the Solar system.

[10] Besides that, Michtchenko & Ferraz-Mello (1997) and Ferraz-Mello et al. (1998) have pointed out that stability inside the J2/1 might have been significantly reduced early after formation of the Solar system during the migration of giant planets. The period of the Great Inequality in Jupiter's motion could have been closer to the libration period of asteroids inside the J2/1, which would have caused significant depletion of any primordial resonant population.

The situation is different for asteroidal populations inside the J3/2 (the so called Hilda group) and in the J4/3 (the Thule group). The dynamical lifetimes of their members tend to be long (e.g. Nesvorný & Ferraz-Mello 1997), while the largest observed asteroids are substantially larger (D = 170 km and 125 km respectively) that those in the J2/1 ($D = 20 - 30$ km). Given that these objects are big and their eccentric orbits cross only a portion of the main belt (e.g. Dahlgren 1998), their collisional lifetimes are definitely larger than the age of the Solar system. As a consequence, the Hilda and Thule groups are likely to be primordial.

There are two end-member cases to explain the origin of the J2/1 population:

1. The population is far from steady state, such that the observed objects were produced by a recent disruption event (*instantaneous-injection model*), or

2. The population is in steady state and we need to find the process that sustains it (*continuous-flow model*).

It is also possible that both cases are partially correct, and that different resonant groups have different origins.

In the 1990's, the preferred hypothesis was type (i). Here the resonant asteroids were fragments injected into the J2/1 during the Themis family formation event (e.g. Morbidelli et al. 1995; Moons et al. 1998). Recent asteroid family results, however, suggest this possibility is unlikely. Numerical simulations of large break-up events in the asteroid belt predict escape velocities significantly smaller than would be needed to directly inject asteroids into the J2/1 (Michel et al. 2001; in fact, characteristic velocities are too small to populate the currently observed family outside the resonance). In addition, there are several lines of evidence to suggest that prominent asteroid families like Koronis (Vokrouhlický et al. 2003) or Themis are several Gy old (Morbidelli et al. 2003; Bottke et al. 2004). Such ages are incompatible with the relatively short dynamical lifetimes of the Griquas and unstable resonant asteroids. On the other hand, Roig et al. (2002) argue that the steep size distribution seen among the Zhongguos (i.e., the stable J2/1 objects) may be more consistent with a recent collisional origin.

At first glance it might seem possible, that the majority of the unstable asteroids were produced by a *recent* catastrophic disruption event, with some of the fragments directly injected into the J2/1. Although the stochastic nature of such events make it difficult to rule this scenario out *apriori*, we believe the available evidence suggests that most J2/1 asteroids are unlikely to have formed by this process, mainly because the dynamical lifetime of most unstable asteroids is of the order 10 My and this time-scale implies that a collisional event capable of injecting fragments into the J2/1 should have leave behind an observable asteroid family along the J2/1 border. As described in Nesvorný et al. (2003), it is now possible to systematically search for clusters of bodies in proper element space using a database of more than 100,000 asteroids computed by A. Milani and Z. Knežević (e.g. Knežević et al. 2003). Though the outer main belt is more observationally incomplete than the inner main belt, Nesvorný et al. (2003) found no evidence for new families along the J2/1 border. This limits the size of any potentially-disrupted parent bodies to objects smaller than Karin, a $D \simeq 30$ km asteroid that disrupted and produced a small cluster of fragments in the Koronis asteroid family 5.8 My ago (Nesvorný et al. 2002b; Nesvorný & Bottke 2004). Because some unstable asteroids are comparable in size to the Karin parent body, it appears that Karin-sized disruption events cannot produce the largest unstable asteroids. For smaller unstable asteroids, we can use the limits provided by the Karin cluster to estimate, in a back-of-the-envelope fashion, whether they could have been produced by a recent breakup event. Here we assume the unstable asteroids were the by-product of a recent disruption among one of the $D = 20 - 30$ km asteroids bordering the J2/1. As shown by Nesvorný et al. (2002b), the Karin disruption event ejected km-sized fragments at velocities of $\leq$ 15 m/s, with the maximum distance reached by the observed fragments from the centre of the family being $\Delta a \simeq 0.005$ AU. This constrains our putative forming event for the unstable asteroids to a distance of 0.005 AU or smaller from the J2/1 border. Searching main belt orbital elements, we find that only $\simeq 1\%$ of $D = 20 - 30$ km asteroids fulfil this criterion. If the time interval between $D = 20 - 30$ km disruption events across the whole main belt is $\simeq 10$ My (Bottke et al. 2004), there is only a $0.5 - 3\%$ chance that such an event occurred near the J2/1 border within the dynamical lifetime of the unstable asteroids ($5 - 30$ My). Given these odds and the lack of evidence for any recent family-forming events near the J2/1, we conclude that most unstable asteroids were not produced by a collisional injection.

Alternatively, the current view of asteroid family evolution, namely that the initial break-up event was followed by a subsequent dynamical spreading due to the effect of the Yarkovsky forces and chaos in weak resonances (e.g. Bottke et al. 2001; Nesvorný et al. 2002a; Bottke et al. 2003), offers a natural continuous-flow model of type (ii) mentioned above. As asteroids slowly diffuse in semimajor axis over

time, they can reach the border of a resonance and fall into it. This scenario provides a continuous resupply of resonant asteroids (dominated by the Yarkovsky effect), and is supported by observations of asteroids on highly unstable orbits adjacent to the resonances (e.g. Milani & Farinella 1995; Vokrouhlický et al. 2001; Guillens et al. 2003) and by a quantitative model of the transport of near-Earth asteroids (NEAs) from the main belt (Morbidelli & Vokrouhlický 2003).

In this paper, we show the continuous-flow of asteroids driven by the Yarkovsky effect may explain the presence of unstable asteroids in the J2/1 (as already suggested by Roig et al. 2002). We note that Tsiganis et al. (2003) developed a similar model for the small unstable population in the J7/3, where the asteroids are resupplied from the Koronis and Eos families, and Vokrouhlický et al. (2006) did comparable work for the J9/4 being visited by members of the Eos family. Because the population of bodies in the J2/1 is substantially larger than in the weaker J7/3 and J9/4, the model for the J2/1 can be tested in a more quantitative way. In fact, our work combines techniques that have been used to explain properties of the NEA population, namely (i) Tracking test bodies from their source region into a target region using numerical integration techniques (e.g. Bottke et al. 2000; Bottke et al. 2002), and (ii) A semi-analytical technique for investigating the steady-state size distribution of bodies in the target region, including the absolute number of objects (e.g. Morbidelli & Vokrouhlický 2003).

In Section 5.2, we update the observed population in the J2/1. In Secs. 5.3.1 and 5.3.2, we describe our numerical and semi-analytical models of Yarkovsky-driven transport from the main belt on to resonant orbits, as well as results from those models. In the Sec. 5.3.3, we discuss other possible sources of very unstable resonant asteroids in the J2/1.

5.2 Update of the resonant population

Our first task is to update the known population of asteroids inside the J2/1. Note that a preliminary analysis which included a more detailed description of some of our techniques was reported in Brož et al. (2005a). We find many new asteroids have been discovered in the J2/1 since the work of Roig et al. (2002), with most of the new data provided by NEA survey systems like LINEAR, Spacewatch, NEAT, LONEOS, etc. (e.g. Stokes et al. 2003). Moreover, refined orbital identification techniques make the orbits more accurate than in the past (e.g. Milani et al. 2001). We discuss the new objects below.

5.2.1 Pseudo-proper resonant elements

In order to identify and classify resonant asteroids, we need to properly characterize their orbits. However, the osculating orbital elements (including semimajor axis) undergo large changes inside the resonance due to planetary perturbations, and their elimination requires a different technique than that used in the case of non-resonant asteroids (e.g. Knežević et al. 2003) — the averaging over a fundamental variable is not possible here. In the case of J2/1, we have the resonance critical angle defined as

$$\sigma = 2\lambda_J - \lambda - \varpi, \tag{31}$$

where λ_J is the mean longitude of Jupiter's orbit, λ is the asteroid's mean longitude and ϖ is the asteroid's longitude of pericentre.

The easiest surrogate to this problem is to define intersections of trajectories with some suitably defined plane (Roig et al. 2002) and record the values of orbital semimajor axis, eccentricity and inclination only here. These values are nearly fixed, apart from short-periodic variations, and may be called *pseudo-proper (resonant) elements*. Previous experience shows that a combined constraint

$$\sigma = 0 \wedge \frac{d\sigma}{dt} > 0 \wedge \varpi - \varpi_\mathrm{J} = 0 \wedge \Omega - \Omega_\mathrm{J} = 0 \tag{32}$$

is a good choice (here ϖ_J and Ω_J are Jupiter's longitude of pericentre and longitude of node). When these conditions are satisfied, the semimajor axis a is minimum, the eccentricity e is maximum and the inclination I is maximum over a fairly long ($\approx 10\,\mathrm{ky}$) interval of time.

In practice, however, short-period perturbations or secular-resonance effects make difficult to satisfy the above conditions exactly. A good operational compromise (e.g. Roig et al. 2002) is

$$|\sigma| < 5^\circ \wedge \frac{\Delta\sigma}{\Delta t} > 0 \wedge |\varpi - \varpi_\mathrm{J}| < 5^\circ, \tag{33}$$

i.e., the condition for σ and $\varpi - \varpi_\mathrm{J}$ is satisfied only with a 5° precision and the time derivative of σ is substituted by the difference of σ in the two successive time steps.

Time series of the resulting pseudo-proper elements, hereafter denoted a_p, e_p and I_p, are thus not technically constant but their variations are very small for stable orbits. Conversely, large variations of the pseudo-proper elements indicate orbit instability. We thus record pseudo-proper elements once per ≈ 10 ky, which is the characteristic circulation period of $\varpi - \varpi_J$). From these data, we compute the standard deviations, σ_a, σ_e and σ_I over 1 My (see Table 15).

To make our work efficient, we implemented an on-line procedure for the pseudo-proper element computation and the second-order symplectic integrator[11] by Laskar & Robutel (2001) in the framework of the SWIFT package (Levison & Duncan 1994). The numerical simulations include gravitational perturbations by 4 giant planets and, when necessary (Sec. 5.3.1), Yarkovsky thermal forces. Perturbations by the terrestrial planets are neglected, except for a barycentric correction which we applied to the initial conditions of both massive planets and massless bodies. This approximation is reasonable for small eccentricity orbits in the outer part of the asteroid belt. The terrestrial planets are of minor importance even for high-eccentricity resonant orbits that cross their paths because the removal from the J2/1 resonance mostly happens when bodies have close encounters with Jupiter (e.g. Gladman et al. 1997). The terrestrial planets become more important when discussing whether Jupiter family comets or NEAs provide some objects to the J2/1 (Sec. 5.3.3), however, a full description of this issue is beyond the scope of this paper.

5.2.2 Resonant population

To properly characterize the J2/1 asteroid population, we proceed in two steps:

1. We integrate a large number of multi-opposition asteroids located near the J2/1 for 10 ky to identify those residing in the resonance;

2. We track the orbital evolution of the identified resonant asteroids for 1 Gy, with the goal being to place them in one of the three resonant groups mentioned above.

Numerical simulations discussed in this section do not include Yarkovsky thermal forces. Initial orbital data for the asteroids were taken from the `AstOrb` (`ftp.lowell.edu`) database as of May 2004, while the initial orbital data and masses for the planets were from the JPL DE405 ephemeris. We only used numbered and multi-opposition asteroids in order to eliminate poorly constrained orbits. To select the initial sample of asteroids, we used the same criterion as Roig et al. (2002; Fig. 1), namely we considered asteroids whose osculating orbital elements are located in some broad region near the J2/1. With that procedure, we obtained ≈ 4200 asteroids whose orbits were propagated forward for 10 ky. We note the second-order symplectic integrator allows a longer time-step, 91.3125 days in our case, which speeds up the computation.

We output time series of the resonance critical angle σ for each asteroid. The orbits, characterized by the libration of σ and the osculating semimajor axes oscillating about an approximate centre at $\simeq 3.276$ AU, reside inside the J2/1. We find 153 such cases,[12] including all asteroids found by Roig et al. (2002). We find additional 100 J2/1 objects, some discovered after 2001 and others that are previously known objects with more accurate orbits.

As a second step, we integrated our J2/1 asteroids for 1 Gy, with the goal being to classify them into one of the three groups described by Roig et al. (2002). Because of the inherent chaoticity of resonant motion, finite orbit accuracy, roundoff errors etc., any single integrated orbit may not represent that body's true future motion (especially on time-scales significantly longer than the Lyapunov time, which is of order 10 ky here). To account for this, we gave each body a multitude of orbits so near the nominal solution that they represent statistically equal realizations of the orbit. We call these fictitious bodies "close clones". Unlike previous studies, we consider 12 close clones for each of the identified resonant asteroids, produced by changing the nominal value of the semimajor axis by multiples of 10^{-9} AU and the eccentricity by multiples of 10^{-9} (well inside 1σ uncertainty interval, as resulted from the orbit determination procedure).

[11] The code, its documentation and a former poster presentation at the Asteroids, Comets and Meteors 2002 conference are publicly available at the web-site `http://sirrah.troja.mff.cuni.cz/yarko-site/`. We present tests of numerical integration accuracy, particularly in regards to how it depends on the selected time-step. This led us to the optimum time-step value used in this work.

[12] We also found additional 9 asteroids for which the critical angle alternates between periods of circulation and libration in our 10 ky integration; these bodies are probably at the edge of the J2/1. There are also large families of non-resonant orbits, which exhibit libration of σ, but they circulate about the pericentric and apocentric branches of periodic orbits (e.g. Lemaître & Henrard 1990; Morbidelli & Moons 1993). We consider neither of them in our analysis.

Table 15: Numbered and multi-opposition asteroids (situation as of May 2004) residing in the in the 2/1 mean motion resonance with Jupiter: the unstable population with median residence lifetime $t_{J2/1} \leq 70\,\mathrm{My}$ in our numerical simulation. a_p, e_p and I_p are pseudo-proper resonant elements, computed with the method recalled in Sec. 5.2.1, and σ_a, σ_e and σ_I are their standard deviations computed over 1 My time interval. H is the absolute magnitude taken from the `AstOrb` database. The term "NEA" indicates bodies that are currently near-Earth asteroids; some additional objects will become NEAs in the next $\sim 10\,\mathrm{ky}$ due to the resonant variations of orbital semimajor axis and eccentricity.

No.	Name	a_p [AU]	e_p	I_p [deg]	σ_a [AU]	σ_e	σ_I [deg]	$t_{J2/1}$ [My]	H [mag]	Remark
1921	Pala	3.193	0.398	17.791	0.004	0.103	3.63	6	14.3	
1922	Zulu	3.231	0.457	33.672	0.001	0.019	3.03	8	12.2	
5201	Ferraz-Mello	3.100	0.531	4.984	—	—	—	0	14.8	
5370	Taranis	3.212	0.457	29.510	0.005	0.154	11.47	7	15.7	NEA
8373	Stephengould	3.248	0.578	30.923	0.007	0.195	11.64	7	13.8	
9767	Midsomer Norton	3.163	0.697	34.687	0.005	0.196	7.13	0	16.4	
23577	1995 DY8	3.203	0.302	1.435	0.001	0.008	0.37	28	14.6	
26166	1995 QN3	3.251	0.524	28.578	0.002	0.106	10.53	8	17.3	NEA
31339	1998 KY30	3.198	0.311	15.793	0.003	0.058	3.22	9	13.5	
37237	2000 WZ161	3.171	0.514	13.131	0.007	0.164	2.60	1	13.6	
55068	2001 QX83	3.211	0.218	18.071	0.004	0.042	2.20	15	13.2	
65541	9593 P-L	3.190	0.423	8.266	0.002	0.018	1.84	10	14.2	
82009	2000 RF68	3.220	0.224	22.374	0.002	0.016	0.53	25	13.22	
83943	2001 WK14	3.192	0.432	22.758	0.001	0.048	3.26	7	13.40	
86358	1999 XB143	3.186	0.419	7.300	0.002	0.036	2.77	8	12.65	
86367	1999 XY223	3.178	0.366	5.411	0.002	0.019	0.59	17	14.65	
	1977 OX	3.177	0.444	21.623	0.005	0.190	12.08	1	15.20	
	1994 JC	3.167	0.930	30.446	—	—	—	0	15.14	
	1997 WW	3.201	0.377	14.567	0.002	0.031	3.93	14	16.47	
	1997 YM3	3.195	0.511	15.583	0.004	0.149	8.11	13	16.95	NEA
	1999 RM19	3.160	0.505	14.064	0.005	0.061	2.55	0	13.68	
	2000 DB62	3.221	0.175	7.752	0.003	0.021	1.58	21	13.95	
	2000 EU170	3.204	0.294	12.022	0.004	0.076	4.76	11	13.64	
	2000 FH13	3.239	0.124	15.768	0.008	0.034	1.89	39	13.38	
	2000 JV60	3.181	0.347	11.824	0.002	0.016	1.56	4	17.21	
	2000 WL10	3.142	0.633	27.852	—	—	—	0	17.99	NEA
	2001 FF185	3.195	0.431	1.094	0.002	0.011	0.47	51	16.32	
	2001 KD50	3.216	0.287	26.087	0.002	0.016	0.69	45	13.35	
	2001 RP53	3.212	0.266	27.293	0.004	0.058	1.78	10	14.21	
	2001 TK15	3.207	0.294	13.039	0.001	0.009	0.53	43	13.50	
	2001 VE	3.196	0.500	24.716	0.002	0.090	5.06	4	15.05	
	2002 CP56	3.205	0.385	5.863	0.002	0.009	2.62	25	15.00	
	2002 GQ1	3.207	0.431	19.687	0.002	0.020	2.80	21	14.39	
	2002 JH36	3.190	0.354	14.123	0.004	0.073	2.07	12	15.91	
	2002 LN53	3.204	0.313	19.867	0.004	0.067	6.28	9	14.53	
	2002 RC20	3.155	0.449	7.480	—	—	—	0	15.95	
	2002 RB107	3.186	0.427	23.613	0.003	0.118	7.67	0	14.09	
	2002 WL	3.210	0.403	31.064	0.005	0.129	7.32	9	14.43	
	2003 GP45	3.169	0.363	7.937	0.005	0.033	0.88	0	16.53	
	2003 HG38	3.162	0.390	8.435	0.004	0.019	0.64	0	15.65	
	2003 NS8	3.191	0.361	23.914	0.003	0.066	2.27	2	13.72	
	2003 QW42	3.165	0.606	1.127	0.007	0.074	0.24	9	14.41	
	2003 UL12	3.214	0.408	41.632	0.003	0.092	4.21	1	17.19	NEA
	2003 WB8	3.206	0.485	26.748	0.003	0.127	5.86	6	13.98	
	2003 WO87	3.203	0.422	8.123	0.002	0.018	4.37	23	14.43	
	2004 GT2	3.228	0.179	37.394	0.006	0.056	0.89	8	14.42	
	3260 T-1	3.166	0.409	12.321	0.004	0.045	1.56	0	15.11	

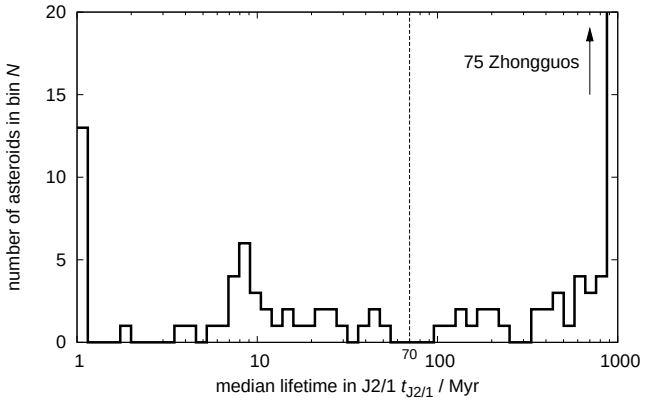

Figure 49: The distribution of the residence lifetime $t_{J2/1}$ for the 153 asteroids inside the 2/1 mean motion resonance with Jupiter; note the log-scale on the abscissa. The unstable asteroids (i.e., those with $t_{J2/1} \leq 70$ My) are separated from the long-lived asteroids by a dotted line. The first set includes two groups, one with extremely unstable asteroids ($t_{J2/1} \leq 2$ My) in the first bin and another with relatively longer lifetimes ($t_{J2/1} > 2$ My). The Griquas (i.e., dynamical lifetime greater than 70 My but shorter than the time-span of our 1 Gy integration) do not seem separated from the Zhongguos (with $t_{J2/1} > 1$ Gy).

Table 16: Numbered and multi-opposition asteroids residing in the stable island A of the J2/1. The quantities are the same as in Table 15. The last column indicates, whether the asteroid is classified as a Zhongguo (Z) or Griqua-like (G). Asteroid (4177) Kohman is a border-line case (see the text for discussion).

No.	Name	a_p [AU]	e_p	I_p [deg]	σ_a [AU]	σ_e	σ_I [deg]	$t_{J2/1}$ [My]	H [mag]	Remark
78801	2003 AK88	3.260	0.318	7.309	0.002	0.006	0.14	1000	15.2	Z
	1999 VU218	3.241	0.295	14.125	0.001	0.002	0.82	771	15.25	G
	2001 FY84	3.253	0.217	26.727	0.007	0.020	0.89	152	14.06	G
	2003 SA197	3.252	0.351	15.807	0.001	0.006	0.09	1000	14.63	Z
	2003 YN94	3.255	0.293	10.451	0.002	0.005	0.24	1000	15.20	Z
	2004 FG32	3.247	0.278	21.816	0.001	0.004	0.37	536	14.53	G
4177	Kohman	3.233	0.320	16.598	0.001	0.001	1.52	1000	12.7	Z

About half of the objects were eliminated before the end of integration (due to perihelion distances smaller than the solar radius or heliocentric distances larger than 100 AU). This indicates they belong to the unstable or marginally stable populations. The remaining half of the objects survived in our simulation for 1 Gy inside the J2/1, suggesting a low diffusion rate among the stable population. We combine results for the close clones with that of the nominal orbit and define the residence lifetime $t_{J2/1}$ for an asteroid inside the 2/1 resonance as their median value. Figure 49 shows the distribution of the lifetime values $t_{J2/1}$ for the entire population of 153 resonant asteroids. Hereafter, we use this distribution to define the various asteroidal groups:

- long-lived: $t_{J2/1} > 70$ My,
  - stable ("Zhongguos"): $t_{J2/1} > 1$ Gy,
  - marginally stable ("Griquas"): $t_{J2/1} \in (70, 1000\rangle$ My,
- short-lived (unstable): $t_{J2/1} \leq 70$ My,
  - extremely unstable: $t_{J2/1} \leq 2$ My.

The results for individual unstable asteroids are summarized in Table 15. The Zhongguos and Griquas are listed in Tables 16 to 19. The classification and properties of all resonant asteroids can be also accessed at our web-site `http://sirrah.troja.mff.cuni.cz/yarko-site/`.

Figure 1 shows it is reasonable to divide the short-lived and long-lived populations with an approximate threshold at 70 My. Our data further indicate that the unstable population – 47 asteroids in total – may

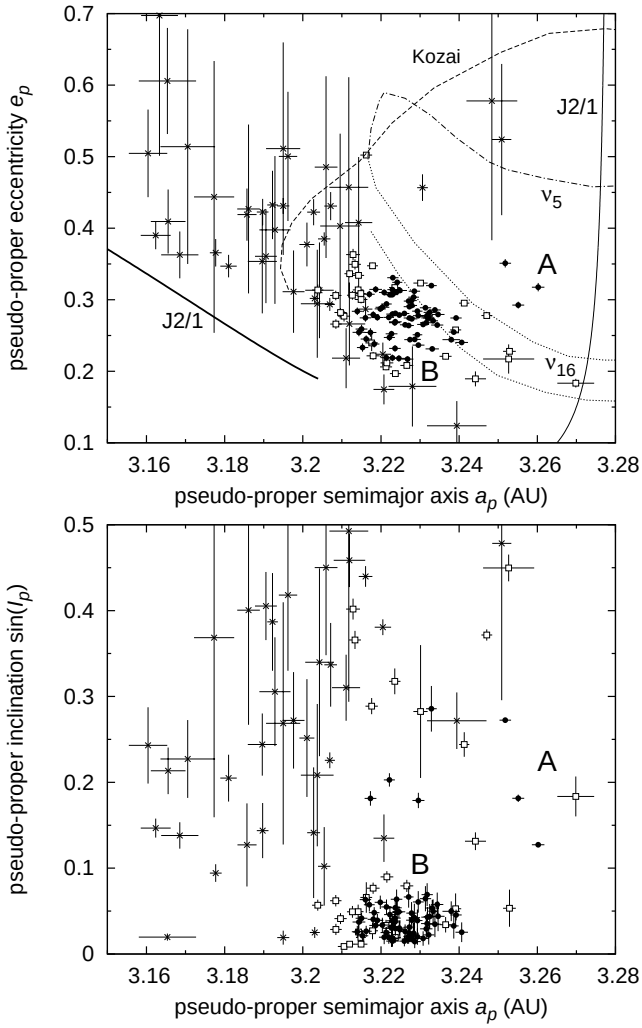

Figure 50: Pseudo-proper orbital elements of the asteroids residing in the J2/1 – semimajor axis a_p vs. eccentricity e_p (top), semimajor axis a_p vs. inclination $\sin I_p$ (bottom). Bodies of different populations are indicated by different symbols: (i) the stable Zhongguos by full circles, (ii) the marginally stable Griquas by open squares, and (iii) the unstable asteroids by crosses. The error bars depict standard deviations of the pseudo-proper elements computed from a 1 My interval of time. The thin solid line labelled J2/1 is the libration centre (the pericentric branch) and the thick solid line J2/1 is the separatrix of the resonance (both shown for $I = 0^\circ$). The dashed and dashed-dotted lines indicate borders of the most important secular resonances embedded inside the J2/1 (all shown for $I = 10^\circ$; adapted from Moons et al. 1998), namely the ν_{16} resonance (short-dashed), the Kozai resonance (dashed) and the ν_5 resonance (dash-dotted). A majority of the stable asteroids is clustered in the island B, while a few of them (see Table 16) are located in the island A, characterized by a higher mean eccentricity and inclination. All unstable asteroids are located in the chaotic zone where various secular resonances overlap. Griquas are a border-line population mostly at the edge of the B-region. In fact, 2-D projections shown here always lack clarity in showing 3-D structures; for that reason we posted a 3-D animation of the resonance structure with positions of the embedded asteroids at our web-site `http://sirrah.troja.mff.cuni.cz/yarko-site/`.

Table 17: Numbered and multi-opposition asteroids residing in the J2/1 resonance: the stable population in the island B (B-Zhongguos) with median residence lifetime $t_{\mathrm{J2/1}}$ longer than 1 Gy in our numerical simulation. The quantities are the same as in Table 15. The ν_{16} symbol means the asteroid is close to the corresponding secular resonance.

No.	Name	a_p [AU]	e_p	I_p [deg]	σ_a [AU]	σ_e	σ_I [deg]	$t_{\mathrm{J2/1}}$ [My]	H [mag]	Dynamical class
11097	1994 UD1	3.232	0.268	1.684	0.002	0.002	0.66	1000	13.4	B
11266	1981 ES41	3.224	0.268	2.138	0.001	0.004	0.47	1000	13.7	B
11573	Helmholtz	3.221	0.294	3.141	0.001	0.003	0.50	1000	12.9	B
13963	Euphrates	3.219	0.314	1.907	0.002	0.004	0.50	1000	13.7	B
14871	Pyramus	3.214	0.284	1.483	0.001	0.005	0.40	1000	13.7	B
16882	1998 BO13	3.227	0.274	1.388	0.001	0.003	0.57	1000	13.7	B
18888	2000 AV246	3.231	0.265	1.036	0.002	0.002	0.48	1000	13.6	B
22740	1998 SX146	3.233	0.231	3.073	0.002	0.003	0.54	1000	13.2	B
24514	2001 BB58	3.226	0.281	0.863	0.001	0.003	0.35	1000	14.2	B
26112	1991 PG18	3.238	0.244	2.853	0.002	0.004	0.66	1000	13.6	B
26553	2000 DO75	3.229	0.245	0.825	0.002	0.003	0.43	1000	14.2	B
29524	1998 AE	3.217	0.254	10.447	0.002	0.006	0.49	1000	13.4	B_i
31249	1998 DF14	3.223	0.307	0.973	0.001	0.003	0.50	1000	14.6	B
31293	1998 FP70	3.234	0.286	1.990	0.002	0.001	0.86	1000	14.1	B
34901	2699 P-L	3.216	0.245	1.515	0.001	0.005	0.37	1000	15.1	B
36140	1999 RC168	3.227	0.217	0.995	0.002	0.004	0.31	1000	14.0	B
37528	1975 SX	3.223	0.219	2.214	0.002	0.005	0.36	1000	14.8	B
37991	1998 KZ5	3.224	0.269	3.084	0.002	0.004	0.47	1000	14.5	B
38984	2000 UZ4	3.228	0.292	1.030	0.001	0.002	0.25	1000	14.9	B
39018	2000 UM53	3.232	0.278	3.966	0.001	0.002	0.76	1000	14.4	B
39309	2001 TE59	3.224	0.232	2.397	0.001	0.004	0.39	1000	14.4	B
41262	1999 XZ55	3.221	0.219	1.432	0.001	0.005	0.38	1000	14.8	B
46168	2001 FK86	3.226	0.265	1.508	0.001	0.002	0.47	1000	14.7	B
46204	2001 FC155	3.232	0.275	2.463	0.002	0.002	0.68	1000	14.2	B
47547	2000 AM121	3.233	0.271	2.858	0.001	0.001	0.79	1000	13.8	B
51070	2000 GO158	3.219	0.275	2.249	0.002	0.004	0.44	1000	14.0	B
51537	2001 FT133	3.223	0.314	1.825	0.001	0.003	0.64	1000	15.5	B
55192	2001 RN2	3.222	0.247	11.704	0.001	0.005	0.45	1000	14.5	B_i
55222	2001 RP63	3.241	0.240	1.454	0.002	0.002	0.66	1000	15.0	B
68738	2002 EJ35	3.223	0.331	1.043	0.001	0.003	0.12	1000	15.9	B
71694	2000 FN44	3.218	0.238	2.762	0.001	0.005	0.37	1000	14.1	B
73396	2002 LV18	3.214	0.254	2.133	0.002	0.006	0.40	1000	15.1	B
73995	1998 FQ25	3.230	0.237	10.301	0.002	0.003	0.51	1000	14.5	B_i
77869	2001 SA	3.225	0.279	1.730	0.001	0.003	0.48	1000	14.5	B
79482	1998 EX12	3.227	0.244	1.266	0.001	0.003	0.43	1000	13.97	B
79500	1998 FK133	3.223	0.307	1.061	0.001	0.003	0.51	1000	14.87	B
86343	1999 XZ56	3.239	0.255	1.880	0.001	0.001	0.85	1000	14.01	B
87362	2000 QS45	3.228	0.273	2.257	0.001	0.003	0.61	1000	13.83	B
89175	2001 UM57	3.215	0.259	2.392	0.002	0.006	0.36	1000	15.21	B
89908	2002 DK17	3.220	0.287	3.452	0.001	0.004	0.45	1000	14.10	B
	1993 FB25	3.227	0.290	1.792	0.001	0.003	0.65	1000	14.90	B
	1994 SK1	3.232	0.282	2.500	0.002	0.001	0.84	1000	15.08	B
	1997 EQ38	3.232	0.277	2.031	0.002	0.001	0.75	1000	14.51	B
	1998 RO49	3.223	0.280	0.864	0.002	0.004	0.39	1000	14.84	B
	1999 FE42	3.224	0.324	2.783	0.001	0.003	0.73	1000	15.12	B
	1999 XT23	3.232	0.275	1.273	0.001	0.002	0.64	1000	14.07	B
	2000 AY135	3.225	0.313	1.625	0.002	0.003	0.64	1000	14.19	B
	2000 EF60	3.239	0.274	2.606	0.001	0.001	0.36	1000	15.51	B/ν_{16}
	2000 HN33	3.217	0.308	3.287	0.001	0.005	0.44	1000	14.87	B
	2000 JS29	3.224	0.311	3.658	0.001	0.003	0.65	1000	14.67	B

Table 18: Continuation of Table 17; B-Zhongguos residing in the J2/1.

No.	Name	a_p [AU]	e_p	I_p [deg]	σ_a [AU]	σ_e	σ_I [deg]	$t_{J2/1}$ [My]	H [mag]	Dynamical class
	2000 SL77	3.228	0.299	2.732	0.001	0.002	0.74	1000	14.79	B
	2000 SF206	3.234	0.265	3.310	0.002	0.002	0.79	1000	15.00	B
	2000 TG65	3.229	0.312	2.427	0.001	0.002	0.92	1000	14.41	B
	2001 AO22	3.235	0.279	2.516	0.002	0.001	0.99	1000	14.89	B
	2001 DY27	3.227	0.264	1.181	0.001	0.003	0.50	1000	14.46	B
	2001 HZ11	3.230	0.278	3.479	0.001	0.002	0.72	1000	14.57	B
	2001 QH88	3.223	0.252	1.738	0.002	0.004	0.44	1000	16.02	B
	2001 SM234	3.231	0.289	3.695	0.001	0.002	0.84	1000	14.88	B
	2001 XZ58	3.229	0.284	2.235	0.001	0.002	0.73	1000	14.29	B
	2001 XZ59	3.229	0.251	1.150	0.001	0.003	0.53	1000	14.59	B
	2001 XQ129	3.218	0.279	2.314	0.001	0.005	0.43	1000	15.69	B
	2002 AL75	3.215	0.233	1.216	0.001	0.006	0.36	1000	15.18	B
	2002 EP69	3.225	0.218	2.820	0.002	0.004	0.39	1000	14.99	B
	2002 GT45	3.227	0.298	3.814	0.001	0.002	0.72	1000	14.56	B
	2002 JO22	3.220	0.289	1.931	0.002	0.005	0.49	1000	13.70	B
	2002 VD35	3.216	0.275	3.634	0.001	0.005	0.39	1000	14.85	B
	2002 VB124	3.222	0.275	1.123	0.001	0.003	0.44	1000	15.69	B
	2003 BS48	3.224	0.281	1.701	0.001	0.003	0.47	1000	14.93	B
	2003 LU5	3.228	0.303	1.389	0.001	0.002	0.71	1000	14.92	B
	2003 SZ204	3.222	0.307	2.629	0.002	0.003	0.55	1000	14.75	B
	1294 T-2	3.221	0.310	1.123	0.001	0.004	0.46	1000	15.55	B

contain $\approx 25\,\%$ of objects on extremely unstable orbits (with $t_{J2/1} \leq 2\,\mathrm{My}$). These objects may be separate from the remaining asteroids in this group. In the past, asteroids with long-lived orbits were previously classified as either Griquas (marginally stable) and Zhongguos (stable). We find, however, that this division is somewhat arbitrary and depends on the integration time-span and the exact definition of the lifetime.[13] Indeed, Fig. 49 suggests there is no significant separation of lifetime values of the stable and marginally stable orbits. The marginally stable population appears to be a short-lived "tail" that adheres to the stable population; out of the 106 long-lived orbits we find 75 have lifetimes longer than 1 Gy, thus considered "stable". In fact, our analysis, based on the 1 Gy integration only, does not permit a fine characterization of the stable population (e.g. the distribution of $t_{J2/1}$ beyond the 1 Gy threshold).

Figure 50 shows a projection of the pseudo-proper orbital elements of the resonant asteroids on to the (a_p, e_p) and $(a_p, \sin I_p)$ planes. The most important result here is a confirmation of the population classification discussed above. Orbits found to be unstable are located in the phase space region right where a number of secular resonances (like ν_{16}, ν_5 or Kozai resonance) embedded in the J2/1 overlap with one another. Because this zone of overlap extends to high orbital eccentricity values, the chaos caused by these overlapping resonances produces strong instability. Five bodies within the unstable population are currently NEAs, and several more will become NEAs within the next period of their libration cycle. This indicates there is an open "communication" between the NEA zone and the J2/1. In Sec. 5.4, we consider the possibility that NEAs feed part of the unstable population inside the J2/1. Conversely, the long-lived orbits are located in a stable zone, predicted previously by numerical and analytical methods (e.g. Nesvorný & Ferraz-Mello 1997; Moons et al. 1998). The marginally stable orbits occupy borders of this zone, while the stable orbits are confined near its centre. This explains the close connection between the two groups.

The long-lived asteroids in our sample tend to populate the stable niche called island B (Nesvorný & Ferraz-Mello 1997; Moons et al. 1998). However, Brož et al. (2005a) reported for the first time the presence of several asteroids inside the twin niche of stability called island A (Fig. 50). We detect 6 asteroids inside the island A (Tab. 16), i.e., having higher eccentricities and inclinations than the

[13] As a result, a number of asteroids classified stable by Roig et al. (2002) using their 520 My integration are marginally stable in our simulation spanning 1 Gy. For example, (3789) Zhongguo itself appears to reside on a marginally stable orbit with a median lifetime of 943 My (see also Moons et al. (1998) who reported a similar result). Note that we define characteristic lifetime as a median of the individual values for 12 close clones and the nominal orbit, while the previous studies usually only considered the nominal orbit.

Table 19: Numbered and multi-opposition asteroids residing in the J2/1: the marginally stable population in the surrounding of the stable island B (B-Griquas) with median residence lifetime $t_{J2/1} \in \langle 70, 1000 \rangle$ My. The quantities are the same as in Table 15. ν_{16} or "Kozai" means the motion probably interacts with the corresponding secular resonance.

No.	Name	a_p [AU]	e_p	I_p [deg]	σ_a [AU]	σ_e	σ_I [deg]	$t_{J2/1}$ [My]	H [mag]	Dynamical class
1362	Griqua	3.213	0.363	23.691	0.002	0.008	0.70	131	11.18	
3688	Navajo	3.216	0.502	3.776	0.002	0.002	1.02	179	14.9	Kozai
3789	Zhongguo	3.237	0.221	1.956	0.002	0.004	0.52	943	12.4	B
11665	Dirichlet	3.218	0.240	16.783	0.002	0.011	0.54	143	14.1	
24491	2000 YT123	3.224	0.197	1.107	0.001	0.005	0.35	439	13.5	B
28459	2000 AW144	3.218	0.348	1.549	0.001	0.004	0.56	883	14.3	B
35989	1999 NF10	3.211	0.277	0.504	0.002	0.007	0.20	619	14.6	B
45511	2000 BC23	3.221	0.206	1.905	0.002	0.005	0.38	865	13.8	B
45796	2000 OG54	3.210	0.282	2.361	0.002	0.006	0.37	620	14.5	B
52700	1998 FG62	3.253	0.228	3.057	0.002	0.003	1.24	470	15.0	ν_{16}
57838	2001 XF49	3.212	0.336	0.657	0.001	0.005	0.13	201	15.3	B
65297	2002 JB31	3.239	0.258	3.025	0.001	0.002	1.02	472	15.2	B
68706	2002 CX234	3.224	0.317	18.520	0.001	0.005	0.86	570	15.0	ν_{16}
77911	2001 TB239	3.270	0.183	10.575	0.005	0.006	1.33	179	13.0	ν_{16}
78814	2003 PX3	3.204	0.314	3.262	0.001	0.008	0.37	108	14.7	B
87375	2000 QN55	3.208	0.266	1.641	0.001	0.007	0.37	204	13.6	B
	1999 XS52	3.214	0.314	2.826	0.001	0.006	0.47	698	15.08	B
	2000 HY9	3.215	0.300	0.656	0.002	0.005	0.19	758	14.75	B
	2000 WK17	3.214	0.334	1.466	0.001	0.005	0.48	412	15.16	B
	2001 QP242	3.230	0.323	16.406	0.002	0.004	4.44	371	14.23	ν_{16}
	2001 XC85	3.244	0.189	7.548	0.003	0.010	0.60	113	14.05	
	2001 YZ113	3.213	0.306	2.815	0.001	0.006	0.39	229	14.77	B
	2002 HB11	3.218	0.222	4.399	0.002	0.005	0.37	639	14.37	B
	2002 QD23	3.222	0.212	5.153	0.002	0.004	0.39	756	14.92	B
	2002 TD170	3.213	0.349	21.460	0.002	0.007	0.61	347	14.94	
	2002 TU252	3.227	0.208	4.552	0.002	0.005	0.40	390	14.45	B
	2004 BY19	3.208	0.306	3.559	0.001	0.007	0.38	181	15.34	B
	2004 DR26	3.215	0.309	1.100	0.001	0.004	0.43	433	16.53	B

separatrix of the ν_{16} secular resonance. Three of them reside on the marginally stable orbits and another three on the stable orbits. One of the Zhongguos – asteroid (4177) Kohman – is a border-line case because the critical angle of the ν_{16} secular resonance ($\Omega - \Omega_S$) alternates between periods of circulation and libration. Except (4177) Kohman, all asteroids inside the stable island A are small, with sizes ranging from 5.5 to 7.5 km (if 0.05 albedo is assumed). Interestingly, all asteroids in the island A have orbits with high inclination. Their proximity to the ν_{16} secular resonance may be the reason, but we did not investigate this possible link in detail.

Despite these new island A asteroids, we confirm previous results suggesting that the stable island A appears under-populated as compared to the stable island B (e.g. Nesvorný & Ferraz-Mello 1997; Moons et al. 1998). In addition, our work allows us to place a quantitative constraint on the ratio of the number of A-Zhongguos (excluding A-Griquas) and the the number of B-Zhongguos: $3/71 \sim 0.04$, but this ratio may change substantially as new asteroids residing on the stable islands will be discovered. Anyway, future work aim at explaining the origin of the long-lived resonant population should meet this constraint.

Figure 51 shows cumulative distributions of the absolute magnitude H for the resonant groups (we use magnitudes from the `AstOrb` database). We approximate these distributions over $H = 12 - 14$, with a power law: $N(<H) \propto 10^{\gamma H}$. The indices γ (slopes), calculated for the resonant groups, have the following mean values: 0.69 (with the interval of variation (0.64, 0.79)) for long-lived asteroids, 0.91 (0.81, 1.01) for Zhongguos, 0.33 (0.28, 0.48) for Griquas, and 0.78 (0.68, 0.88) for unstable asteroids. If we discard extremely unstable asteroids (i.e. those with $t_{J2/1} \leq 2$ My) from the unstable group, we obtain somewhat shallower size distribution with the power-law slope of 0.66 (and the variation (0.56, 0.76)). We give here

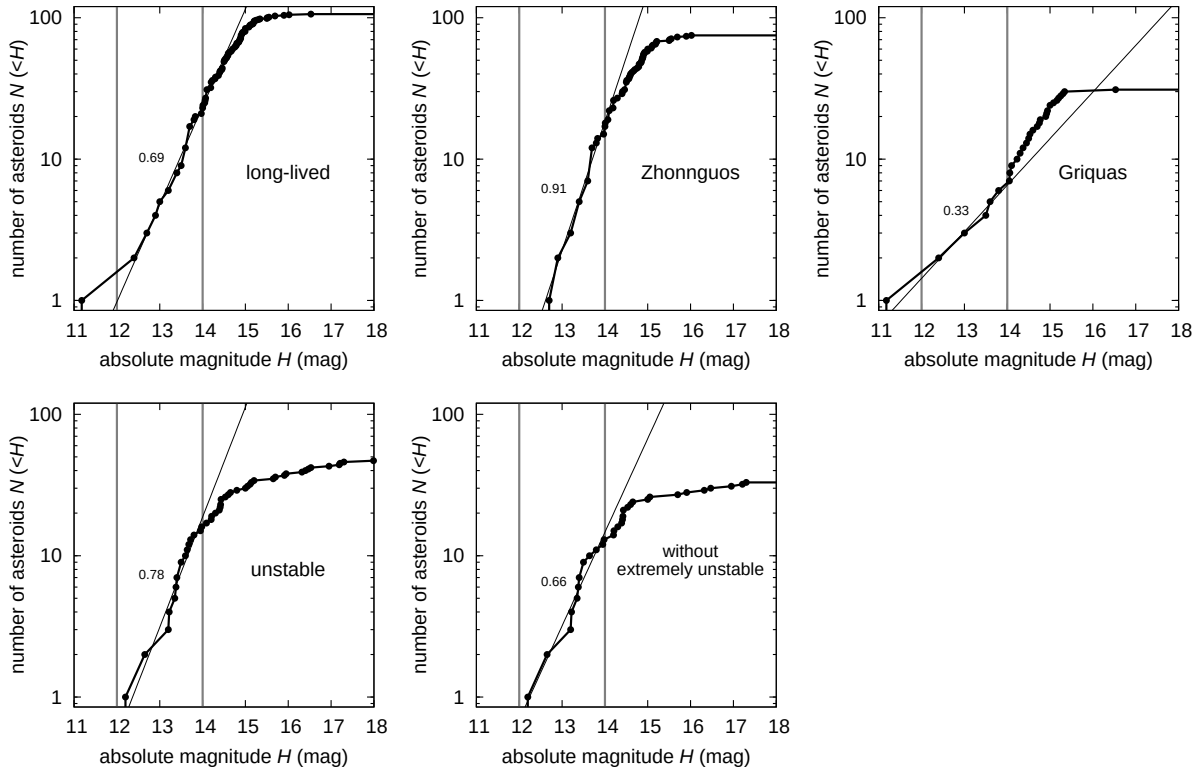

Figure 51: Cumulative distribution of the absolute magnitude for asteroidal populations inside the J2/1: (i) the long-lived asteroids together (top left), (ii) Zhongguos (top middle), (iii) Griquas (top right), (iv) the short-lived (unstable) asteroids (bottom left), and (v) the short-lived (unstable) asteroids with $t_{\mathrm{J2/1}} > 2$ My (i.e. extremely short-lived objects excluded; bottom right); note the semi-log axes. The straight lines indicate the best fit power-law approximations $N(<H) \propto 10^{\gamma H}$ in the H-range of $12-14$, delimited by vertical grey lines. The adjacent numerical labels are the resulting power-law indices γ. To convert γ into the slope of a power-law size distribution, we multiply by -5, making their cumulative slopes -3.5, -4.6, -1.7, -3.9, and -3.3 respectively. For reference, a Dohnanyi-like cumulative slope is -2.5 (Dohnanyi 1969).

realistic maximal errors that were obtained by the variation of the interval over which γ was fitted and by random removal of a single asteroid from the population. To convert γ into the slope of a cumulative power-law size distribution, we multiply it by -5, making their mean cumulative slopes: -3.5 (with the variation $(-4.0, -3.2)$), -4.6 $(-5.1, -4.1)$, -1.7 $(-2.5, -1.4)$, -3.9 $(-4.4, -3.4)$, and -3.3 $(-3.8, -2.8)$ respectively. For reference, a Dohnanyi-like cumulative slope is -2.5 (Dohnanyi 1969). The indices for Zhongguos, Griquas and unstable asteroids are significantly different from each other, but the results for Zhongguos and Griquas depend sensitively on the threshold chosen for the division of the long-lived asteroids (1 Gy in our case).[14] Moreover, the Griquas have an unusual distribution of H that becomes steeper between $H = 14-15$. Because the Zhongguos and Griquas are not easily separable from each other, these source of these differences is difficult to investigate.

There are 16 asteroids with $H \leq 14$ residing on unstable orbits. (This number is relevant for our analysis in Sec. 5.3.2.) Out of these 16 asteroids, 2 have extremely unstable orbits.

Except the problems with partitioning the long-lived population (which is not critical for this work), our results confirm those of Roig et al. (2002): at large sizes the resonant populations have a rather steep size distribution. Their slopes are steeper than a simple Dohnanyi-like collisionally evolved system would predict (Dohnanyi 1969), though this kind of system is unlikely to represent the main belt population except for bodies with $D < 0.1$ km (e.g., Durda et al. 1998; O'Brien and Greenberg 2003; Bottke et al. 2004).

[14] If we select a smaller dynamical lifetime threshold, the size distribution of the Zhongguos generally becomes shallower and that of the Griquas becomes steeper. For example, for 0.5 Gy $\gamma_{\mathrm{Zhongguos}} = 0.77$ and $\gamma_{\mathrm{Griquas}} = 0.45$.

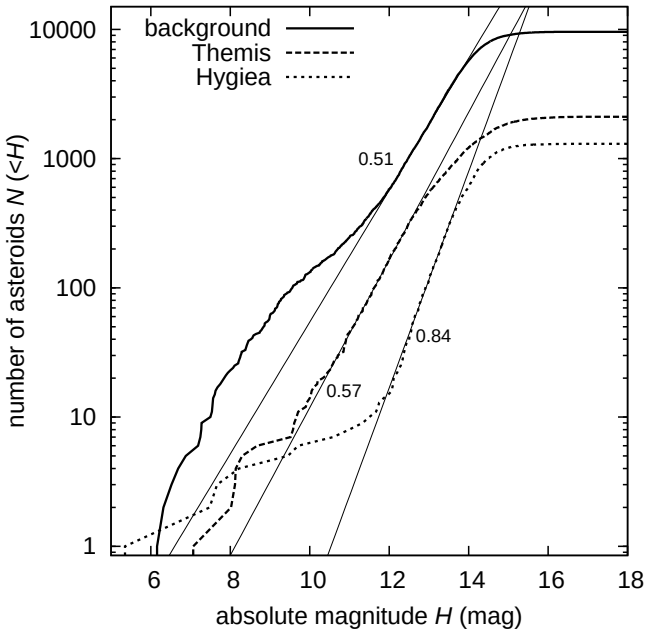

Figure 52: Cumulative distribution of the absolute magnitude for the three plausible source populations adhering to the J2/1 resonance: (i) the background asteroids (solid line), (ii) the Themis family (dashed line), (iii) the Hygiea family (dotted line). Lines are power-law approximations as in Fig. 51.

5.2.3 Source populations

An important conclusion follows from the comparison of the size distributions of the resonant groups and that of the plausible source populations: background asteroids, Themis family and Hygiea family. (These are the same populations as discussed later in Sec. 5.3.) Figure 52 shows the distribution of the absolute magnitudes for them, with the following fitted values of the power-indices: background 0.51 ± 0.01, Themis 0.57 ± 0.02 and Hygiea 0.84 ± 0.02. We note the first two populations have distributions compatible with a Dohnanyi-like collisionally relaxed system for $H \leq 12$ and $H \leq 11$, respectively (thus sizes approximately larger than $25 - 35$ km). Hygiea's distribution is considerably steeper at large sizes, but as shown by Morbidelli et al. (2003) it becomes significantly shallower at small sizes.

A significant difference in the exponent γ can be found between the source and resonant populations. The background asteroids differ from the unstable resonant asteroids by $\simeq 0.2 \pm 0.1$ (depending whether the extremely unstable asteroids are included in this comparison or not). A slope difference near 0.2 is compatible with the Yarkovsky-driven transport from the source region, because the Yarkovsky effect is size dependent (it scales as D^{-1} for "our" asteroids) and thus naturally causes this change of the source size distribution. On the other hand, the YORP effect, acting together with Yarkovsky, may cause the slope difference to decrease by $\simeq 20\,\%$ (i.e. down to $\simeq 0.15$; Morbidelli & Vokrouhlický 2003).

5.3 Origin of the unstable resonant population

We now turn our attention to the origin of the unstable population. Our working hypothesis, motivated by similar studies of the NEAs and some of the weaker main-belt resonances, is that asteroids drifting in semimajor axis via Yarkovsky thermal forces should continuously resupply bodies to the J2/1 and keep the unstable population in an approximate steady state. For now, we assume that other sources, such as planet-crossing asteroids, Jupiter-family comets, collisional injection of material, and dynamical injections of bodies from weak resonances, provide only few bodies to the J2/1. We discuss this issue further in Sec. 5.3.3.

To test our hypothesis, we use both numerical and semi-analytical methods. Each has its strengths and weaknesses. For example, direct N-body simulations allow us to characterize the resonant dynamics, but computer time requirements do not allow us to track a statistically large sample of orbits. On the other hand, the semi-analytical approach foregoes any detailed description of a test body's orbital evolution, but it does allow us to track a large enough sample of bodies that we can quantify results statistically while testing a wide range of model parameters. Our results for both approaches are described below.

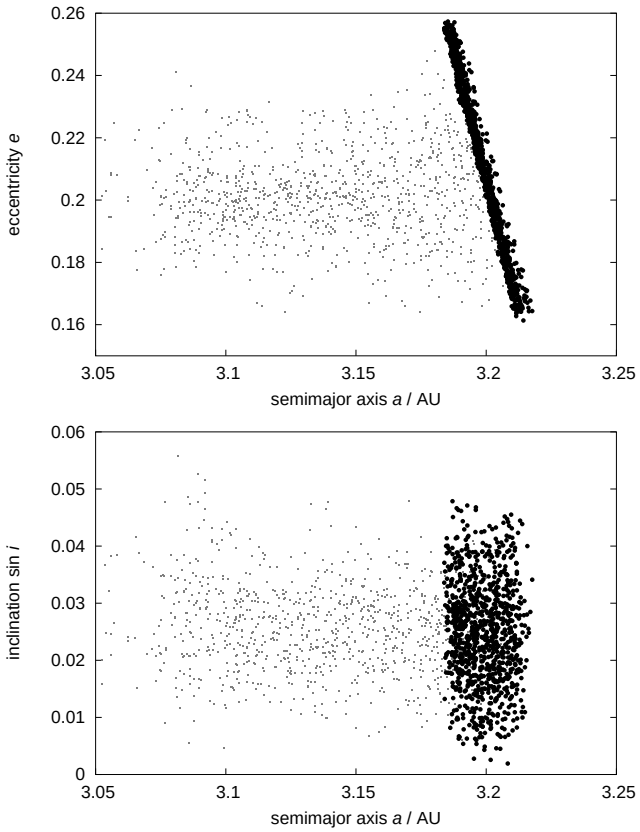

Figure 53: Initial orbital data for our numerical propagation of Themis family asteroids into the J2/1 resonance: pseudo-proper semimajor axis vs. eccentricity (top), semimajor axis vs. sine of inclination (bottom). The two groups of bodies are compared: (i) the Themis family members (gray dots), which were firstly identified in the proper element space at 70 m/s cutoff velocity (using data from `AstDyS` database) and then we calculated their pseudo-proper elements using the method described in Sec. 5.2.1; (ii) the test particles in our simulation (black circles). The initial osculating elements (not shown here) of the test particles are very close to the pseudo-proper ones, because of our choice of the initial longitude of pericentre. There is a large difference between the proper (non-resonant) and pseudo-proper (resonant) semimajor axis and eccentricity of the Themis family members; inclination is much less affected (this is because the fundamental resonant angle σ does not depend on the nodal longitude).

5.3.1 Numerical N-body model

Using a N-body model, our primary goals are to determine:

1. Residence time probability distributions (maps) indicating which portions of the orbital phase space are statistically most likely to be visited by test particles injected into J2/1 by Yarkovsky forces; and

2. The characteristic lifetime test bodies spend inside the J2/1 before leaving it.

In a steady-state scenario, (i) can be directly compared with the orbital parameters of the observed asteroids, with a positive match supporting our model results. For (ii), the results, after some analysis and normalization, should be comparable to the dynamical lifetime distribution obtained for the observed population in Fig. 49. This information is also used in the semi-analytical analysis described in Sec. 5.3.2.

Here we use the second-order symplectic integrator from Sec. 5.2 with Yarkovsky forces included. This is done by including Yarkovsky forces at the perturbation phase of the integrator. Test simulations verified analytical semimajor axis drift results for the thermal effects on asteroids on circular orbits. Both diurnal and seasonal variants of the thermal effects were included using a linearized approximation; the diurnal part is described in Vokrouhlický (1998, 1999) and the seasonal part is described in Appendix of Vokrouhlický & Farinella (1999). We use thermal parameters that are consistent with those expected for C-type asteroids: thermal conductivity $K = 0.01$ W/m/K, specific thermal capacity $C = 800$ J/kg/K, and surface and bulk densities $\rho_s = \rho_b = 1.5$ g/cm^3. To let the bodies drift outward toward the J2/1,

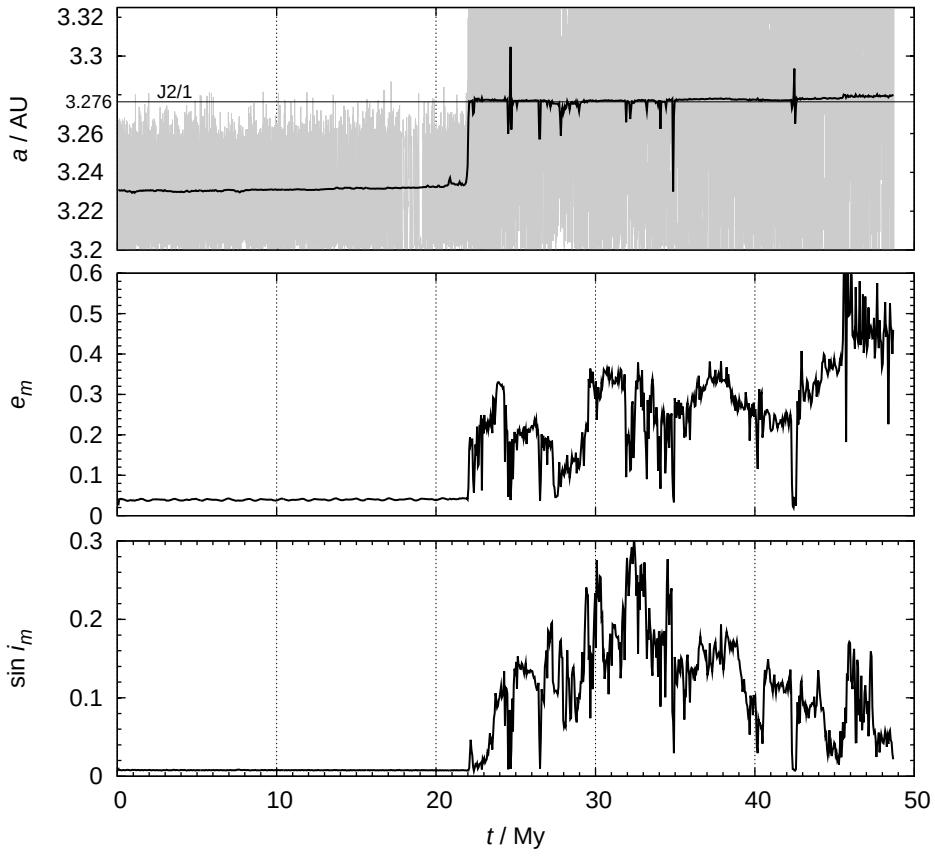

Figure 54: An example of a test body evolving into the J2/1 via Yarkovsky thermal forces; running-box mean orbital elements are shown as functions of time by bold black lines: semimajor axis a_m (top), eccentricity e_m (middle), and sine of inclination $\sin I_m$ (bottom). The grey curve in the upper panel shows the osculating semimajor axis. At 22 My, the test body falls into the resonance, with the mean value of the semimajor axis "jumping" to $\simeq 3.276$ AU (that of the stable periodic orbit in the resonance) while the osculating value starts to exhibit large oscillations. The eccentricity and inclination are pushed to high values, with their values affected by the ν_5 and ν_{16} secular resonances embedded in the J2/1.

we set the initial obliquity to be 45°. We assumed rotation periods uniformly distributed in the range $4 - 12$ h. Because Yarkovsky forces are size-dependent, we consider bodies with diameters in the range $D = 4 - 40$ km. A combination of these parameters determines the magnitude and direction of the Yarkovsky perturbation and thus the orbital drift rate. However, our results only weakly depend on the strength of the Yarkovsky forces (see also Roig et al. 2002). The primary role of the Yarkovsky forces is to deliver the asteroids to the J2/1.

To test our hypotheses, we performed 3 simulations using 3 different source regions: (i) Themis family (using 1000 test particles with sizes from 4 to 40 km), (ii) Hygiea family, and (iii) the background main-belt population (both with 500 test particles with sizes from 16 to 40 km). The main difference between (i)-(iii) is the confinement of each source region's initial eccentricity and inclination values. The initial inclination of Themis and Hygiea family members are $\simeq 1°$ and $\simeq 5°$, respectively. The orbital data of the background population, however, have inclinations over the interval $\langle 0°, 18° \rangle$. As an example, Fig. 53 shows the initial conditions of our simulation for asteroids evolving from the Themis family. All our test particles are started outside the J2/1 (the critical angle σ initially circulates), though to save computer time, they are placed close to the resonance. To that end, we chose the initial longitude of perihelion equal to that of Jupiter; this implies their eccentricity is at the top of the perturbation cycle. We note the pseudo-proper elements of the integrated particles match those of the family. Typically it takes several My to tens of My for our particles to evolve into the resonance (e.g. Fig. 54).

Example of an orbit evolving to the 2/1 resonance. Figure 54 shows a representative example of a test body evolving toward the J2/1 by the Yarkovsky effect. For analysis purposes, we compute mean

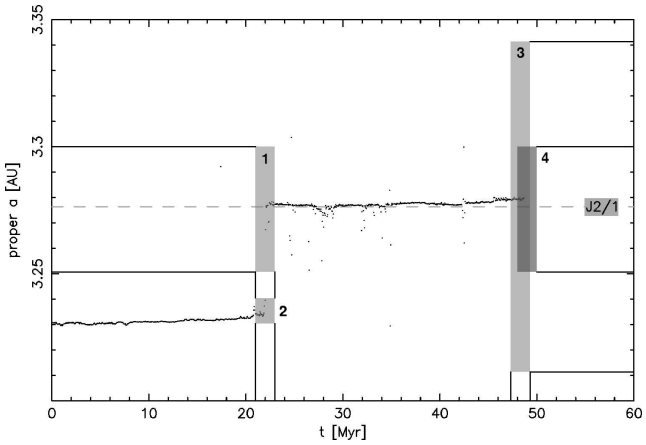

Figure 55: Mean semimajor axis a_m of the orbit from Fig. 54 as a function of time. Rectangles 1 to 4 represent diagnostic zones for the measurement of residence time in the J2/1. They move in time together with the orbital evolution, with rectangles 1, 3 and 4 staying centred at $a_{\mathrm{J2/1}} \simeq 3.2764\,\mathrm{AU}$. Here we designate the rectangles R_i, their widths t_I, and their heights a_i $(i = 1, \ldots, 4)$. The operational condition for the entry time into the J2/1 is at least n_1 data points are in R_1 and the oscillations of a_m are smaller than R_2. A similar condition for their ejection time out of J2/1 is at least n_3 data points are outside R_3 or at most n_4 data points are in R_4. In practice we use the following values: $t_i = 2\,\mathrm{My}$ $(i = 1, \ldots, 4)$, $a_1 = a_4 = 0.05\,\mathrm{AU}$, $a_2 = 0.01\,\mathrm{AU}$, $a_3 = 0.13\,\mathrm{AU}$, $n_1 = n_3 = 50\,\%$, $n_4 = 10\,\%$.

values of the orbital elements – a_m, e_m, I_m – using on-line digital filters based on Kaiser window (Quinn et al. 1991) with an output time step 5 ky and further averaged over a running window 50 ky wide. Such "mean elements" do not have theoretical significance but they are useful auxiliary variables for our work.

We find the mean semimajor axis value a_m instantly jumps to $\simeq 3.276$ AU upon entering the J2/1, with the osculating semimajor axis exhibiting large oscillations. This value corresponds to the J2/1 centre. Since the width of the J2/1 in semimajor axis is large, tracking the a_m time series allows us to easily determine when the orbit becomes trapped in the resonance (Fig. 55). A similar criterion applies to the instant the orbit leaves the resonance. For the latter, this mostly occurs when the J2/1 pushes the test body's orbital eccentricity to a high enough value that it falls into the Sun or it is ejected from the inner Solar system as a consequence of a close encounter with Jupiter. We also computed the pseudo-proper orbital elements for each of the integrated orbits. These values were used to compare the evolutionary tracks of our test particles to observed asteroids located inside the J2/1 (Fig. 50).

In the next sections we separately analyse results for test bodies started in the Themis, Hygiea and the background populations.

Themis family asteroids. To determine whether test bodies entering the J2/1 match with the location of asteroids inside the resonance, we need to define a quantitative measure of their residence. To do that, we assume there is a steady-state flow of asteroids into the J2/1 (see Sec. 1). Thus, any particle removed from the J2/1 is replaced by another from the source region. Assuming our sample of integrated orbits is representative, we track the amount of time spent by these test bodies in different regions of the J2/1. The cumulative time distribution produced by this procedure is believed to represent the true steady-state population inside the resonance (see Bottke et al. 2000, 2002 for similar ideas on populating the near-Earth asteroid orbits).

We construct a local *number density* n_{TP} of the test particles by summing the number of particles residing in the cell of the volume $(\Delta a_p, \Delta e_p, \Delta \sin I_p)$ around the point $(a_p, e_p, \sin I_p)$ for *all* time steps during the *whole* span of our integration. Of course, values of the spatially dependent $n_{\mathrm{TP}}(a_p, e_p, \sin I_p)$ scale in some simple way with the volume of the cells, the time step Δt of the proper elements sampling and the time span ΔT of the integration. In our case, we have $\Delta a_p = 0.0075\,\mathrm{AU}$, $\Delta e_p = 0.0025$, $\Delta \sin I_p = 0.04$, $\Delta t = 0.01\,\mathrm{My}$, and $\Delta T = 1\,\mathrm{Gy}$. If one test particle stays in one cell for the whole 1 Gy, it would cause $n_{\mathrm{TP}} = 10^5$. Regions with high n_{TP} values are likely locations to find observed asteroids (provided our hypothesis is correct). Regions with $n_{\mathrm{TP}} = 0$ are never visited by any of our integrated test particles and observed asteroids found in those locations cannot be explained by the Yarkovsky-driven transport from the given source region. Below, we show that the observed unstable asteroids are located in the regions of high n_{TP}, but the Zhongguos and Griquas are not. For the purpose of two-dimensional

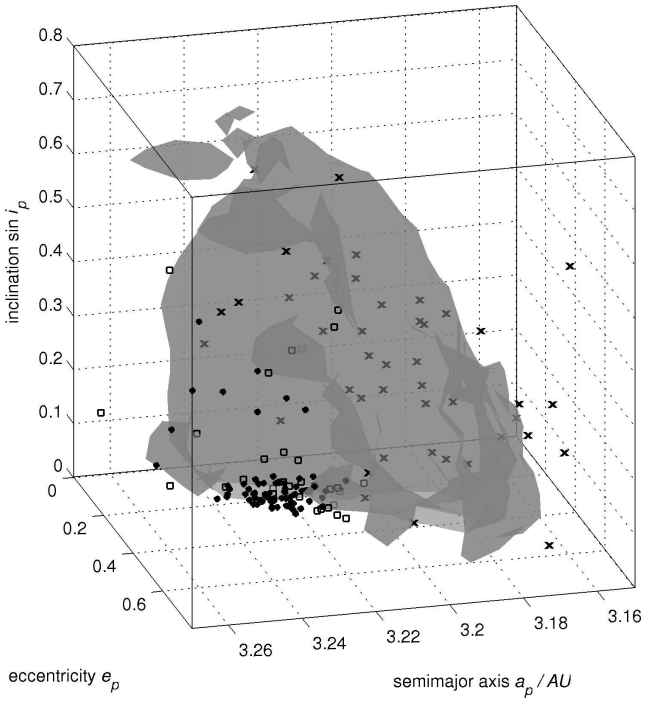

Figure 56: An $n_{\rm TP} = 500$ iso-surface of the number density in the pseudo-proper orbital element space, resulting from our numerical simulation of test particles originating from the Themis family; $n_{\rm TP}$ reaches its maximum value of $\simeq 3\times10^4$ inside this zone. Symbols denote positions of the observed populations inside the 2/1 resonance: (i) Zhongguos (filled circles), (ii) Griquas (squares), and (iii) the unstable asteroids (crosses). The 3-D surface is plotted as semi-transparent and one can distinguish the objects, which are in front of, inside or behind the surface, because they are gradually more and more gray/hidden. An illustrative animation with several coloured and partially transparent iso-surfaces can be found on `http://sirrah.troja.mff.cuni.cz/yarko-site/`.

projections, we also define a column number density $Q_{\rm TP}$ as a sum of $n_{\rm TP}$ over all cells in the given direction, e.g. $Q_{\rm TP}(a_p, e_p) = \sum_{\sin I_p} n_{\rm TP}(a_p, e_p, \sin I_p)$.

One difficulty in plotting our results is that the space of our pseudo-proper elements is in 3-D. This means that 2-D projections such as in Fig. 50 may result in misinterpretations. For that reason, we start with the complete 3-D representation and only with caution we use the 2-D maps. Figure 56 shows an iso-surface of moderately high value of the number density $n_{\rm TP} = 500$ in the space of pseudo-proper orbital elements. (its maximum value occurs inside the region). There is no important dependence of $n_{\rm TP}$ on size: bodies with size ≥ 10 km in our simulation yield the same result as those with size < 10 km. Thus we present results for all particles together. Positions of the observed asteroids inside the J2/1 are shown by different symbols: Zhongguos (filled circles), Griquas (squares) and the unstable asteroids (crosses). Both long-lived populations (Zhongguos and Griquas) are situated outside the region of high $n_{\rm TP}$ values. The unstable asteroids, however, are located inside or close to the depicted iso-surface. This suggests their origin is compatible with our model of the Yarkovsky-driven transport into the J2/1.

Figure 57 shows 2-D projections of our previous results, where we focus on the long-lived asteroids. Note that their orbits tend to have low values of the pseudo-proper eccentricity and inclination. Thus, in plotting the (a_p, e_p) projection, we restrict ourselves to orbits with $I_p \leq 5^\circ$ only (left panel), while in plotting the $(a_p, \sin I_p)$ projection, we restrict ourselves to orbits with $e_p \leq 0.3$ (right panel; see also Fig. 56 to get insight to the procedure). The value of the appropriate column number density $Q_{\rm TP}$ is given as the grey-scale colour. Our results confirm that the long-lived asteroids are mostly located in the blank regions where $Q_{\rm TP} = 0$. Accordingly, their origin is incompatible with the delivery to the J2/1 by Yarkovsky forces. Note that while the 2-D representation suggests our integrated orbits populate the correct inclination values, this is not the case when the pseudo-proper eccentricity is also taken into account (left panel and Fig. 56).

Figure 58 shows additional 2-D projections of our results, but now we focus on the unstable asteroids that typically have large eccentricity and/or inclination values (Table 15). Here we restrict to $I_p \geq 5^\circ$ in the projection on the (a_p, e_p) plane (left panel) and to $e_p \geq 0.3$ in the projection on to the $(a_p, \sin I_p)$ plane (right panel). The orbits of the unstable asteroids, shown by crosses, match the zone of maximum

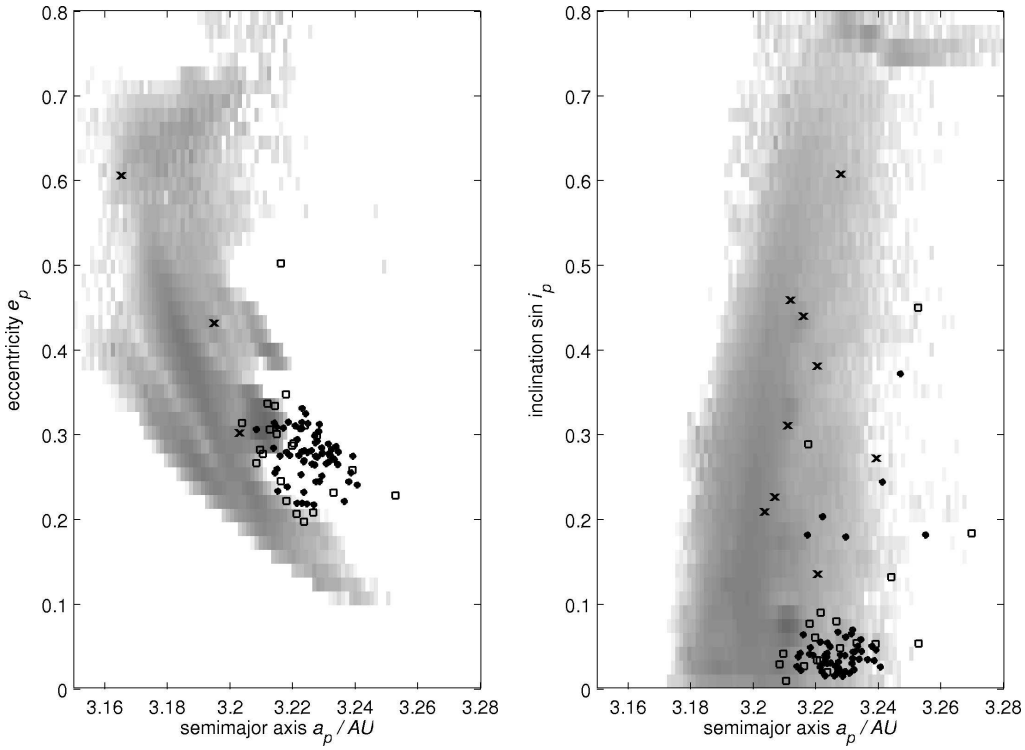

Figure 57: Two-dimensional projections $Q_{\rm TP}$ of the density particle function $n_{\rm TP}$ on to (i) (a_p, e_p) axes (with the restriction of $I_p \leq 5°$; left panel), and $(a_p, \sin I_p)$ axes (with the restriction of $e_p \leq 0.3$; right panel). The scale of grey indicates $Q_{\rm TP}$ in a logarithmic measure (blank for $Q_{\rm TP} = 0$ and the darkest for the maximum $Q_{\rm TP}$). Symbols denote positions of the observed populations inside the J2/1: (i) Zhongguos (filled circles), (ii) Griquas (squares), and (iii) the unstable asteroids (crosses).

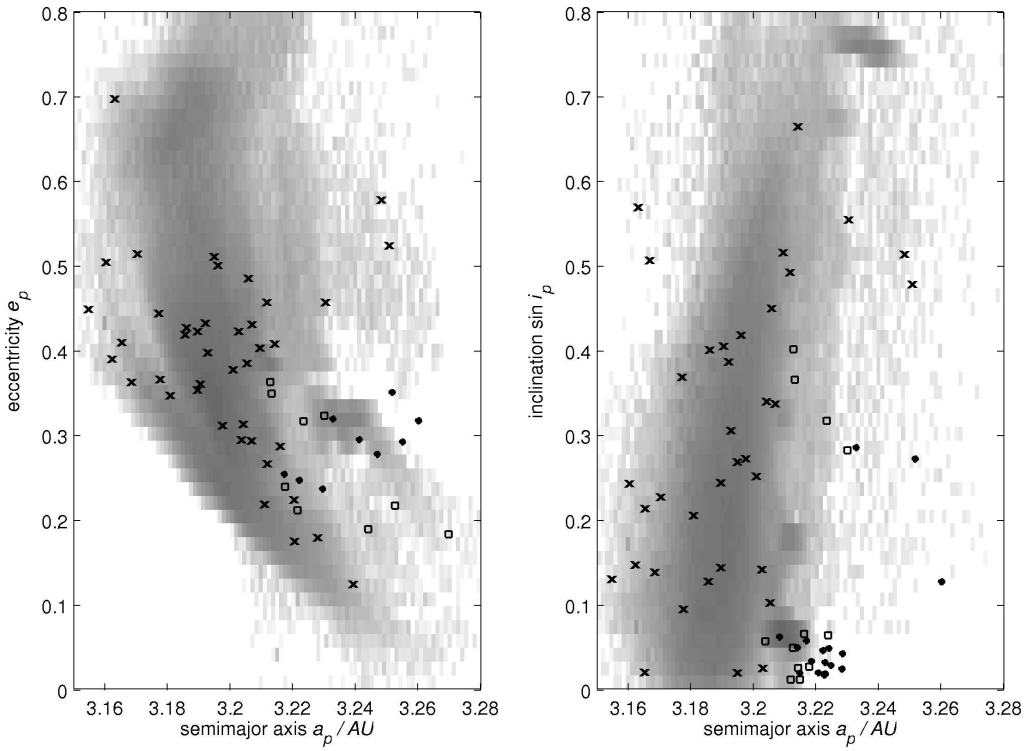

Figure 58: The same as in Fig. 57 but now data in the (a_p, e_p) projection show orbits with $I_p \geq 5°$ (left panel), and the $(a_p, \sin I_p)$ projection show orbits with $e_p \geq 0.3$ (right panel). Symbols as in Fig. 57.

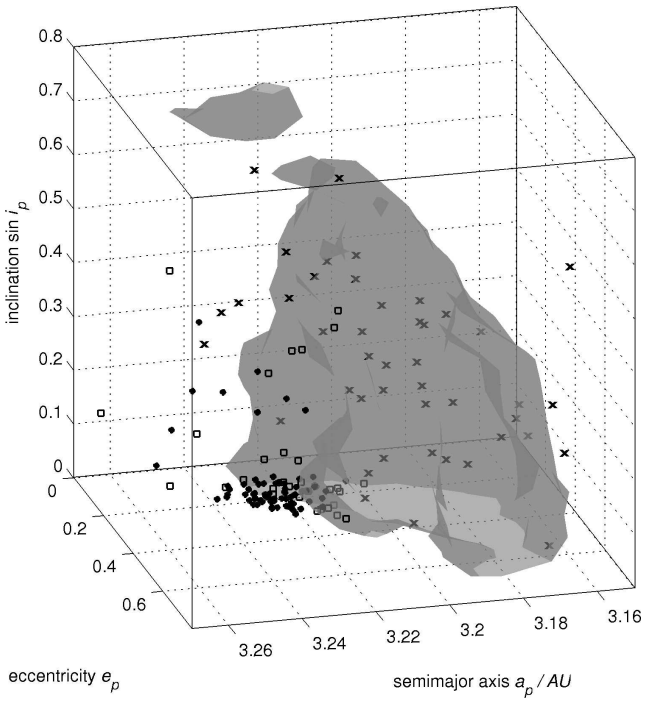

Figure 59: Here we show the same quantity as in Fig. 56 but now for the number density n_{TP} given as a weighted mean of the contributions by the three source populations: the background population (contributing by 84.5 %), the Themis family (contributing by 14.2 %) and the Hygiea family (contributing by 1.3%).

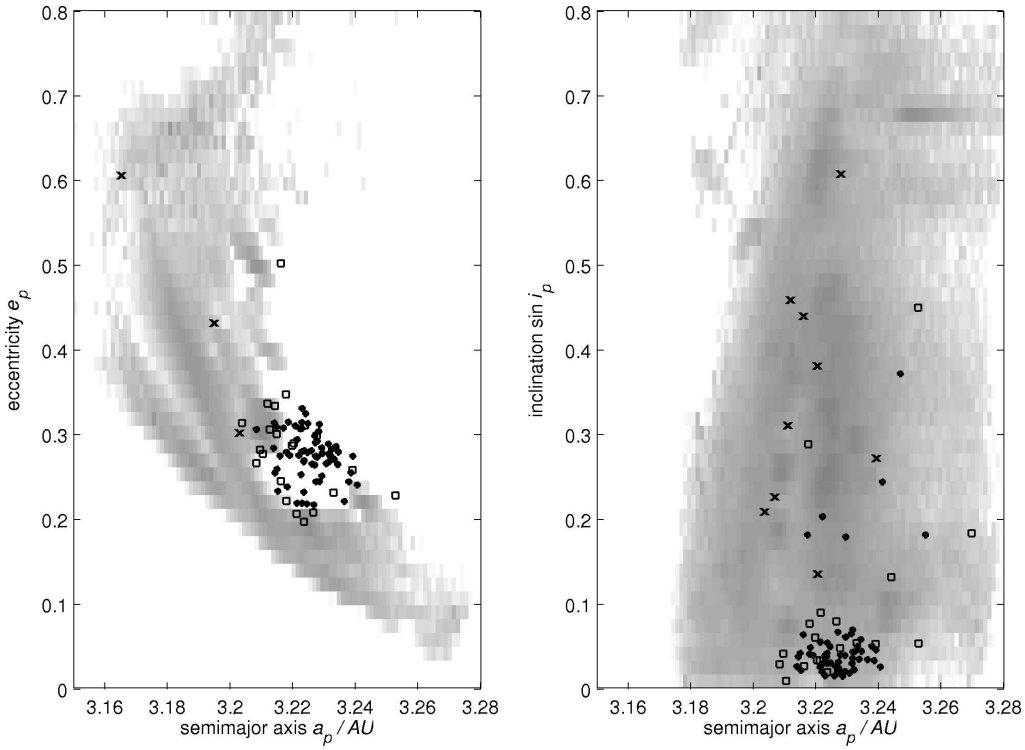

Figure 60: Here we show the same as in Fig. 57 but now for the column number density Q_{TP} given as a weighted mean of the contributions by the three source populations.

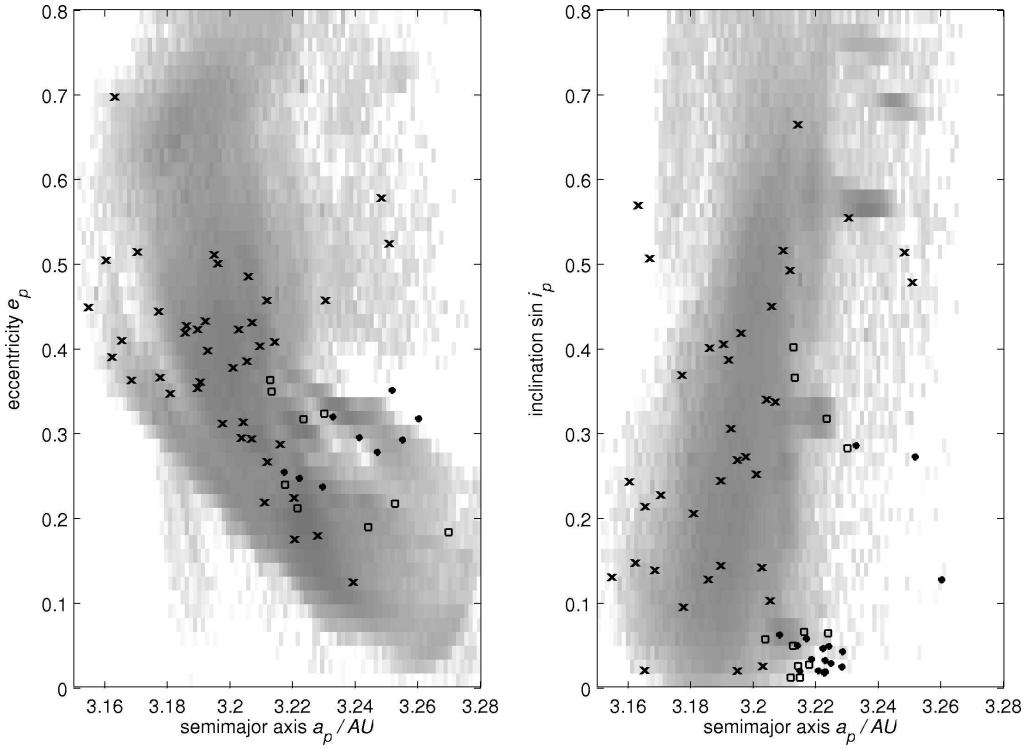

Figure 61: Here we show the same as in Fig. 58 but now for the column number density Q_{TP} given as a weighted mean of the contributions by the three source populations.

$Q_{\rm TP}$ value (dark grey) in both projections. Only a few outliers can be found. This suggests our test bodies preferentially populate the resonant orbits occupied by the asteroids residing on the unstable orbits. In a few rare cases not shown here, we also observe test particles that jump across the J2/1 and populate the Cybele region (i.e., asteroids having $a \in (3.3, 3.6)$ AU).

Hygiea family and background asteroids. We repeat our analysis for the Hygiea family and the entire background asteroid population. We find our results are nearly identical to those given above, such that we only plot the composite $n_{\rm TP}$ values constructed as a weighted sums from the three source regions. The weights used are the source contribution to the resonant population of $H \leq 14$ asteroids estimated by our semi-analytical Monte-Carlo model (Sec. 5.3.2): the background population contributes by 84.5 %, Themis and Hygiea families by 14.2 % and 1.3 %, respectively.

Figures 59 to 61 show the same results as Figs. 56 to 58, but now the composite number density $n_{\rm TP}$ is given. These results confirm that our test particles, evolving by the Yarkovsky forces from the adjacent main belt population to the J2/1, visit cells where the unstable asteroids are located and shy away from regions where long-lived asteroids are found. We note that none of our source regions match the distribution of the unstable population better than any other. This suggests the inclination of asteroids driven into the J2/1 is quickly mixed upon entry into the resonance, such that we cannot use the unstable population's orbital elements to estimate the source of a given resonant asteroid.

Figure 62 shows the residence time distribution $t_{\rm J2/1}$ for our test particles (bold solid line). As above, this is a weighted mean of the results for the 3 different source regions (the background population, Themis and Hygiea families), but there is only minor statistical difference between them. For the same reason, we also combine results here for large (≥ 10 km size) and small (< 10 km size) bodies. No permanent captures in the J2/1 were found, and no object entered stable resonant islands (see, e.g., Figs. 59 and 60).

A comparison between our test body residence times and those of the observed unstable objects shows the same order of magnitude (Fig. 49 and the dashed curve in Fig. 62). If we do not take into account the extremely unstable J2/1 object (with $t_{\rm J2/1} \leq 2$ My), the median of $t_{\rm J2/1}$ is 10.3 My for the observed unstable population (with $t_{\rm J2/1} \in (2, 70\rangle$ My), and 14.7 My for our test particles. To make a more detailed comparison, we would need to perform additional modelling, mainly because we do not know how much time each of the observed asteroids already spent in the resonance. (The difference between the medians

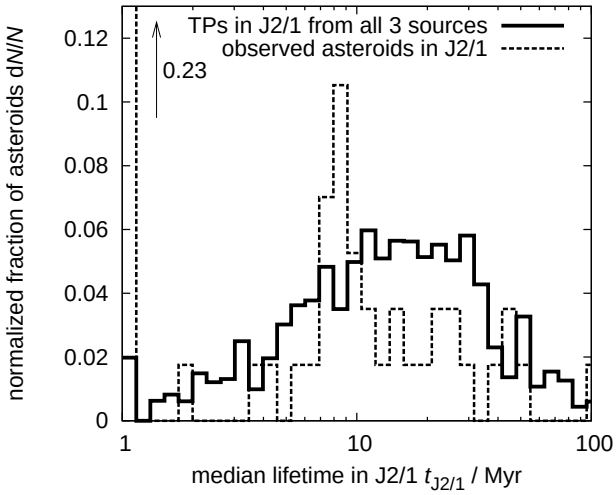

Figure 62: Distribution of the residence time inside the J2/1 for: (i) test bodies which were delivered into the J2/1 by the Yarkovsky effect (bold solid curve) and (ii) observed members of the unstable J2/1 population currently residing in the resonance (dashed curve; see also Fig. 49). In the case (i), the residence time records the time interval from entry into the J2/1 till escape out of the J2/1, while the case (ii) records the time interval from the present day to escape. The number of bodies dN in each logarithmic bin has been normalized by their total number N.

of $t_{J2/1}$ can be attributed to this effect.) However, the most important difference between the two plots is that our model does not predict the anomalously large number of extremely unstable J2/1 objects. We suspect some of these objects may be populated by other sources (Sec. 5.3.3).

5.3.2 Semi-analytical Monte-Carlo model

Next, we apply our semi-analytical model to the problem. Our primary goals are to determine, for a given source population adjacent to the J2/1:

1. The steady-state number of unstable asteroids inside the J2/1 with sizes larger than some threshold; and

2. The slope of their size distribution.

We assume the steady-state situation for unstable J2/1 objects is valid and that the ≈ 16 unstable asteroids with $H \leq 14$ are the steady-state number. We use the residence lifetimes of J2/1 test bodies estimated in the previous section. Given that Yarkovsky forces are size-dependent, we expect small asteroids will be delivered to the 2/1 resonance more efficiently than large ones. As a result, the size distribution of the target population should be different (steeper) than that of the source population. Figures 51 and 52 are consistent with this hypothesis, but we need to verify that the change of the power-law slope is what our model would predict.

Model setup. Our method is essentially the same as of Morbidelli & Vokrouhlický (2003). The first task is to characterize the source population for the J2/1. We then let the population evolve into the J2/1 by Yarkovsky forces, where the semimajor axis drift speed depends on the spin-axis obliquity of each object. We assume that every asteroid removed from the J2/1 is replaced by a new object in the source population, which maintains a steady state. We neglect collisional disruption events since the dynamical lifetime for our bodies of interest in the J2/1 is short ($\sim$10 My) compared to their collisional disruption lifetime ($\sim 1-2$ Gy for 10 km bodies; Bottke et al. 2004). Once the population in the J2/1 has reached the steady state, we compute the power-law slope of the resonant size distribution and compare it to observations (Fig. 51). Fluctuations in this population occur from time to time due to random injections of individual bodies (especially at large sizes). Our simulation is run for 4 Gy.

To construct the source region, we use the `AstDyS` (`http://newton.dm.unipi.it`) database, which includes all numbered and multi-opposition asteroids for which proper orbital elements have been computed. Somewhat arbitrarily, we use all asteroids that have proper semimajor axis $a > 3.1$ AU and are

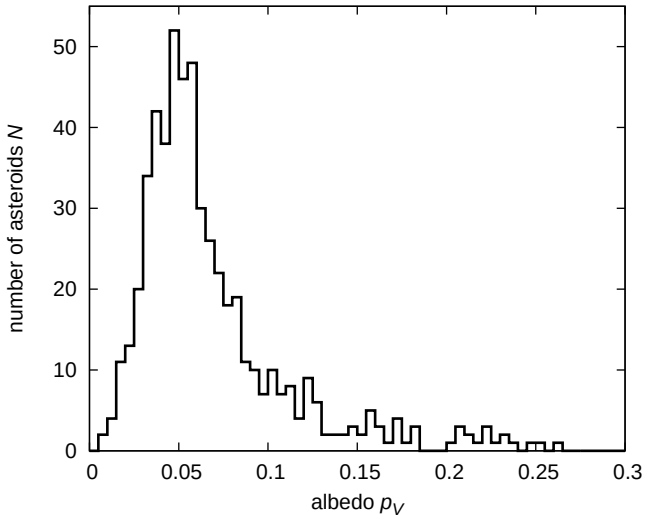

Figure 63: The distribution of albedo values derived by Tedesco et al. (2002) for asteroids located near the J2/1.

located below the border of the J2/1. The J2/1 border is approximated in the proper semimajor axis a – proper eccentricity e plane by

$$e = c_0 + c_1\, a\ , \tag{34}$$

where $c_0 \simeq 10.82$ and $c_1 \simeq -3.32\,\mathrm{AU}^{-1}$. Tests show that our results are not sensitive to these limits.

To compare our results with those in Sec. 5.3.1, we again split the population into 3 groups (i.e., Themis, Hygiea, and the background population). In Sec. 5.2, we characterized each in terms of their absolute magnitude H distribution (Fig. 52), but here we need to convert H into diameter D to obtain the correct strength of the Yarkovsky effect for each body.

The H–D relationship depends on *apriori* unknown value of the geometric albedo p_V for each test asteroid. For this reason, we used two approaches: (i) we assumed a constant value $p_V = 0.05$ appropriate for C-type asteroids, and (ii) we characterized p_V by a distribution function spanning some finite interval of values. For (ii), the albedo becomes a statistical quantity and thus our results become statistical properties requiring numerous simulations. The albedo distribution function maps on to parameters such as the estimated number of $H \leq 14$ unstable asteroids residing inside the J2/1 resonance.

To determine appropriate albedo distribution for our model, we use values derived by Tedesco et al. (2002) from IRAS infrared observations. Unfortunately, the only resonant asteroid listed in this catalogue is (1362) Griqua. For this reason, we assume the albedo distribution of the resonant asteroids is similar to that of main belt asteroids in the neighbourhood of the J2/1. We thus select IRAS asteroids that fulfil the condition $a > 3.1\,\mathrm{AU} \wedge a < (3.260 + 0.301e)\,\mathrm{AU}$, where a is the osculating semimajor axis and e the osculating eccentricity. The procedure yields 542 objects and a reasonably constrained albedo distribution (Fig. 63; we also verified that this distribution depends weakly on the orbit threshold chosen for the J2/1 border). Our albedo distribution peaks at 0.05, that same as assumed in (i), but there is a significant spread.

Figure 52 indicates the background population dominates the family contribution by a factor $\simeq 5$ for $H \leq 14 - 15$, though we need to account for observational biases. To estimate the true background population, we extrapolated the observed H distribution above the $H \simeq 14$ threshold using the exponent $\gamma \simeq 0.51$ (see Sec. 2.3). Using this procedure, we obtain a bias factor that is given by the ratio between the estimated and observed populations for different values of H for $H > 14$. The same factor is applied to the Themis and Hygiea families since they occupy roughly same main belt region. As described in Morbidelli et al. (2003), this procedure produces a bend in the slope of the family size distributions that is more shallow than the background main belt slope (this is especially remarkable for the Hygiea case, since it has a steep size distribution among its $H < 14$ bodies). This simple debiasing procedure is acceptable for our purposes. Note that the $H \leq 14$ source population is only increased $\simeq 5\%$ relative to the observed sample. In our simulation, we consider asteroids down to $H < 17.5$, with the cumulative number being roughly half a million.[15]

[15]Data on the faint asteroids, dominated by the inner main belt population, indicate the absolute magnitude distribution

Because our approach tracks individual test asteroids, every body has to have initial proper elements assigned to them. The observed asteroids are assigned their own orbital elements. The test asteroids obtain orbital elements of a randomly-chosen observed asteroid in the source population. This procedure somewhat neglects high inclination asteroids, which are harder to detect than low inclination asteroids, but this problem does not significantly affect our results.

We use a simplified orbital evolution model for our test asteroids that only accounts for changes in proper semimajor axis due to the Yarkovsky effect. We neglect the effects of weak mean motion resonances that force the population to diffuse in proper eccentricity and inclination (e.g. Nesvorný & Morbidelli 1998; Morbidelli & Nesvorný 1999). The proper semimajor axis of each asteroid changes according to:

$$\frac{da}{dt} = \kappa_1 \cos\epsilon + \kappa_2 \sin^2\epsilon \,, \tag{35}$$

corresponding to the linearized analysis of the thermal effects (e.g. Vokrouhlický 1999). Here the first term is the contribution of the diurnal variant and second term is the contribution of the seasonal variant of the Yarkovsky effect. Both are dependant on the obliquity ϵ. The diurnal case (κ_1) is dependant on the rotation frequency ω, while the seasonal case (κ_2) is dependant on the mean orbital motion n. The dependence on thermal and bulk parameters, given in Sec. 5.3.1, is the same for both κ_1 and κ_2 functions. For our test asteroids, the diurnal Yarkovsky effect dominates, with κ_1 larger by about an order of magnitude than κ_2. Hence, a test asteroid can migrate both inward or outward, depending on its obliquity ϵ. For multi-kilometre bodies, both κ-functions are inversely proportional to the size of the body.

The orbital evolution of each asteroid is coupled to the evolution of its rotation frequency ω and obliquity ϵ. The evolution of these terms is complicated by torques from the variant of the Yarkovsky effect called Yarkovsky-Öpik-Radzievskii-Paddack (YORP) (e.g. Rubincam 2000; Vokrouhlický & Čapek 2002; Bottke et al. 2003; Vokrouhlický et al. 2003). Here we simplify YORP-driven dynamics to a steady variation of ω and ϵ as described by a system of two differential equations:

$$\frac{d\omega}{dt} = f(\epsilon) \,, \tag{36}$$

$$\frac{d\epsilon}{dt} = \frac{g(\epsilon)}{\omega} \,, \tag{37}$$

where the functions f and g have been obtained by Čapek & Vokrouhlický (2004) for a large sample of objects with irregular shapes. Here we use their effective values obtained as medians over this sample. To recall a fundamental property of the YORP dynamics, we note it secularly drives the obliquity to some asymptotic values (for bodies with non-zero surface thermal conductivity the most likely values are 0° or 180°), where the rotation speed is accelerated or decelerated with approximately the same probability (Čapek & Vokrouhlický 2004).

YORP evolution is expected to be temporarily halted by interactions with secular spin-orbit resonances. For low inclinations, it is a similar situation to Koronis prograde-rotating asteroids (Vokrouhlický et al. 2003). At sizes smaller than $\simeq 10$ km, however, the YORP contribution might dominate. The evolution to asymptotic rotation states by YORP – very-fast or very-slow rotation rate – is still poorly understood, but the conventional wisdom is that (i) the acceleration of the rotation may result in mass loss and (ii) de-spinning triggers non-axial rotation or eventually drains so much rotational angular momentum from the body that collisions can re-orient and spin up the body. We use these assumptions in our simulation. We consider a given asteroid disrupted (and thus eliminated from our simulation) when its rotation period drops below 2 hr (see, e.g., Pravec et al. 2003). On the other hand, as the rotation period grows by YORP to a very large value (1000 hr in our simulations), we assume a collisional re-orientation event is likely to take place (see below).

The Yarkovsky and the YORP effects make our initial source population evolve smoothly toward the boundary of the J2/1 (Eq. (34)). Once the orbit crosses the resonance border, it is recorded as a resonant asteroid in our model. Numerical simulations from Sec. 5.3.1 suggest these test asteroids become members of the unstable population. We use these simulations to estimate the residence time of the objects in the J2/1 (Fig. 62). We assume the body is eliminated from the resonance after some period of time, with a new body injected into the source population to maintain the steady state. The output of our simulation is a time series of asteroid residence times inside the J2/1.

Finally, our simulation also includes a rough treatment of collisional disruptions. We assume these events occur with a time-scale $\tau_{\rm disr}$. Additionally, because of the Yarkovsky effect dependence on the

of the true population becomes shallower above a value of $\simeq 15$ mag; e.g. Ivezić et al. (2001).

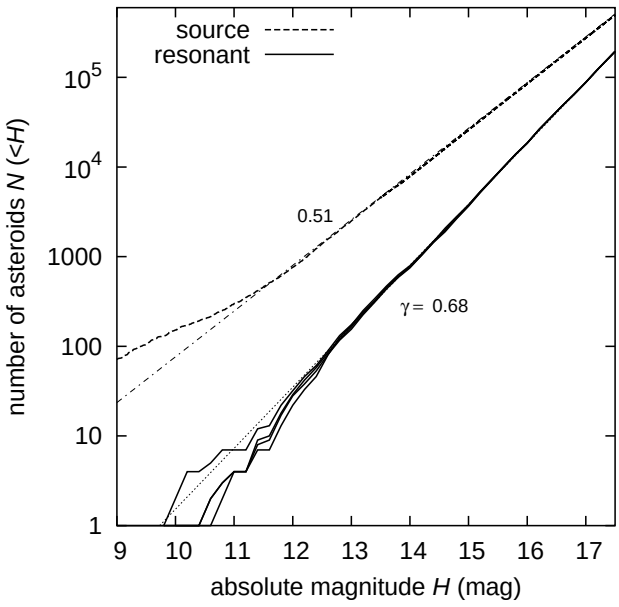

Figure 64: Cumulative H distribution of the simulated unstable population in the J2/1 (solid curves) compared with the source population (dashed curve). All 3 source populations are considered together. Large H values were found by extrapolating from small H values using a power law (compare the dashed curve with the dotted curve in Fig. 52). The 4 solid lines are distributions of resonant population collected during 2 Gy windows: $0.5-2.5$ Gy, $1-3$ Gy, $1.5-3.5$ Gy and $2-4$ Gy. They are nearly identical at small sizes but fluctuate at large sizes because some large asteroids occasionally fall in the resonance. Straight lines are local power-law approximations in the H range $12-14$ (labels are the corresponding exponent value). Here we use our nominal model, $A = A_{\rm nom}$ and $B = B_{\rm nom}$. All asteroids have the same albedo value $p_V = 0.05$.

obliquity and the rotation frequency, we assume non-disruptive collisions can change asteroid's spin state with a time-scale $\tau_{\rm reor}$. Following Farinella et al. (1998), with an update by Farinella & Vokrouhlický (1999), we have

$$\tau_{\rm disr} = A\,(R/R_0)^{\alpha}\,, \tag{38}$$

$$\tau_{\rm reor} = B\,(\omega/\omega_0)^{\beta_1}(R/R_0)^{\beta_2}\,. \tag{39}$$

The coefficients A and B in the equations are somewhat uncertain and depend on assumptions about the internal structure and physical processes associated with large asteroid disruptions and dispersal into fragments. Farinella et al. (1998) give: (i) $A_{\rm nom} = 16.8$ My and $\alpha = 1/2$ for the collisional time-scale ($R_0 = 1$ m is the reference value for the radius), and (ii) $B_{\rm nom} = 84.5$ ky, $\beta_1 = 5/6$ and $\beta_2 = 4/3$ for the reorientation time-scale (with the reference rotation frequency ω_0 corresponding to the rotation period of 5 hr). These estimates were obtained for a projectile population with the equilibrium exponent -2.5 of the cumulative size distribution (different values of this parameter produce different values of the exponents α, β_1 and β_2).

The effective calibration of the time-scale, coefficients A and B, were obtained for the mean material parameters of silicate bodies and mean impact parameters in the main-belt. For this study, we note that $A \propto S^{5/6}$ (Farinella et al. 1998), where S is the impact strength of a target. Since the prevalent C-type objects in the outer part of the main asteroid belt have a strength about an order of magnitude less than basaltic material (e.g. Davis et al. 1985; Marzari et al. 1995, Sec. 4.2), about an order of magnitude smaller value $A \simeq 1.7$ My might be also possible. For that reason we introduce an empirical scaling parameter c_1, so that $A = c_1\,A_{\rm nom}$ and $c_1 \in \langle 0.1, 1\rangle$. Similarly, we introduce a scaling parameter c_2, so that $B = c_2\,B_{\rm nom}$, and $c_2 \in \langle 0.1, 1\rangle$.

Results. Figures 64 and 65 summarize results of our nominal simulation, with $A = A_{\rm nom}$ and $B = B_{\rm nom}$ (thus $c_1 = c_2 = 1$), and a geometric albedo $p_V = 0.05$. Figure 64 shows the size distribution of the resulting unstable population (solid lines). In order to characterize its power-law slope, we do not consider the population at any given time instant but instead we include all asteroids residing in the J2/1 resonance during a given interval of time (i.e., a running window of 2 Gy with initial epochs 0.5 Gy, 1 Gy, 1.5 Gy

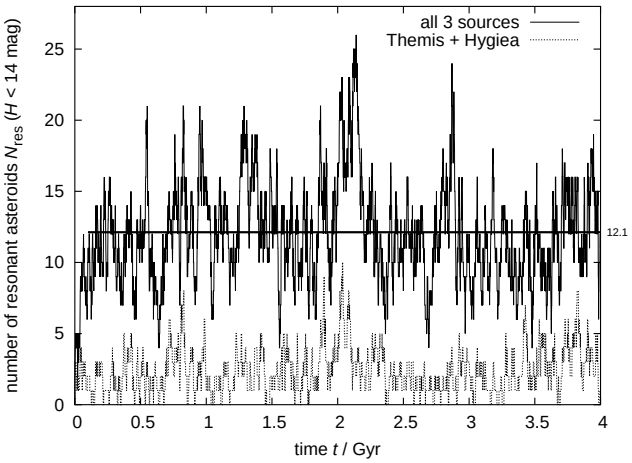

Figure 65: Estimated steady-state population of the unstable asteroids with $H \leq 14$ inside the J2/1 in our nominal simulation where all asteroids are assumed to have $p_V = 0.05$. Fluctuations around the mean value of $\simeq 12$ are due to random injections into the resonance. The bottom dotted curve shows the contribution of the Themis and Hygiea families, $\simeq 15\%$ of the total.

and 2 Gy, with the initial epoch excluded to let the system settle near steady-state equilibrium). Thus, in this plot, the absolute number of J2/1 asteroids is not relevant.[16] The power-law index is found by fitting a line to the mean value of the fluctuating indices during the time window of 2 Gy. In spite of fluctuations produced by large asteroids, we note the distribution function of $12 < H < 14$ is well characterized by a power-law index $\simeq 0.68 \pm 0.05$ (the error bar is dominated by fluctuations over time). This agrees with the observed population (Figs. 51; recall that the observed slope of the $H \leq 14$ asteroids on the unstable orbits becomes 0.66 ± 0.1 when the extremely unstable orbits are excluded) and is significantly steeper than the slope of the main belt source population adjacent to the J2/1 (0.51 ± 0.01). This change in slope is produced by Yarkovsky and YORP forces (e.g. Morbidelli & Vokrouhlický 2003).

Figure 65 shows the simulated number of resonant asteroids with $H \leq 14$ residing in the unstable population during the 4 Gy simulation. After a $\simeq 0.1$ Gy transition phase, the system settles into fluctuations about the stationary value of $\simeq 12$ asteroids. This number comes primarily from a combination of the available source population and strength of the Yarkovsky effect. This result agrees well with the observed 16 asteroids with $H < 14$ on unstable orbits (Sec. 5.2). Note that fluctuations as high as 25 bodies are possible. It is also possible that several of the highly unstable bodies came from a different source (see Sec. 5.3.3).

Using our nominal parameters for collisional effects, $A = A_{\rm nom}$ and $B = B_{\rm nom}$, we tested how varying the albedo – approach (ii) above – would change our results. Using a different seed for our random-number generator, we created 50 possible source populations with different albedo values attributed to the individual asteroids and ran 50 simulations. Each time, we recorded the parameters shown in Figs. 64 and 65, namely the equilibrium number of asteroids with $H \leq 14$ inside the J2/1 and the index γ of the cumulative H-distribution for $12 < H < 14$.

We find the mean value of the expected power-index γ of the resonant population is $\simeq 0.68 \pm 0.05$ (Fig. 66). The expected steady-state number of resonant asteroids on unstable orbits is $\simeq 14 \pm 1$. This is a slight increase from our previous simulation because asteroids with higher albedo values have, for a given H, smaller D values and thus they drift faster via Yarkovsky forces. The albedo distribution shown in Fig. 63 is slightly asymmetric about the mean value 0.05, with a longer tail toward higher albedo values. On the other hand, the observed increase in the steady-state number of resonant asteroids is within the time fluctuations seen in Fig. 67.

We find the results of the nominal simulations do not change much with varying c_1 and c_2 (Fig. 68). For example, for the lowest values of c_1 and c_2, the estimated equilibrium number of $H \leq 14$ unstable resonant asteroids drops to ~ 9. This is because frequent collisions and spin axis re-orientations effectively

[16] We also occasionally obtain very large asteroids – up to 60 km size – injected into unstable population of the J2/1 resonance, but these events are very rare, about $\simeq 0.5\%$ probability. This may be why we currently do not observe them. We obtained our probability estimate by comparing the typical residence lifetime – $\simeq 10$ My (Fig. 62) – with the width of the sampling window (2 Gy). It is also possible that these large asteroids are missing in the resonant population because the assumption of their steady-state production in the source population is violated.

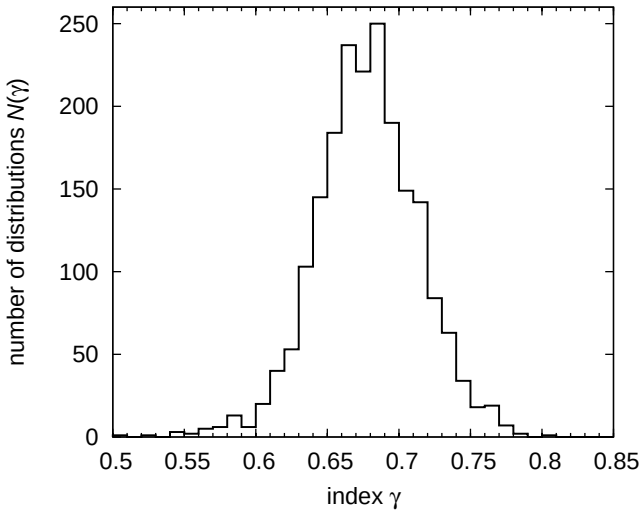

Figure 66: Distribution of the slope parameter γ fit to the simulated population inside the J2/1 on unstable orbits with $12 < H < 14$. Here we use nominal values of the collision and reorientation strength, thus $A = A_{\rm nom}$ and $B = B_{\rm nom}$. We assume asteroid albedo has the same distribution seen in Fig. 63; we ran 50 simulations with different random seed to assign albedoes/sizes to individual asteroids.

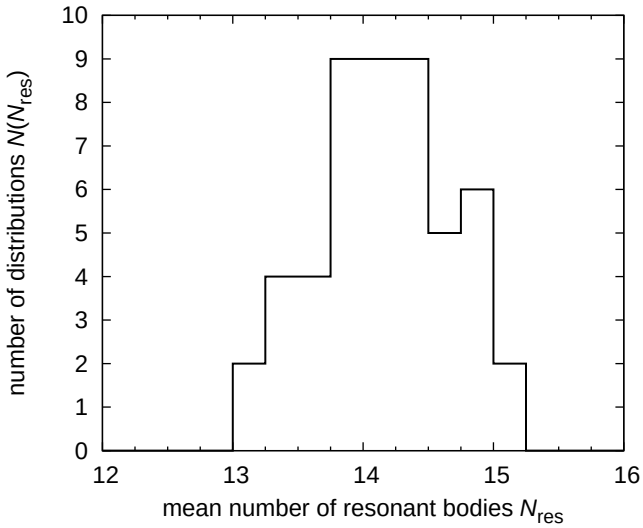

Figure 67: Distribution of the mean value for the number of asteroids with $H \leq 14$ in the J2/1 on unstable orbits. See Fig. 66 for details.

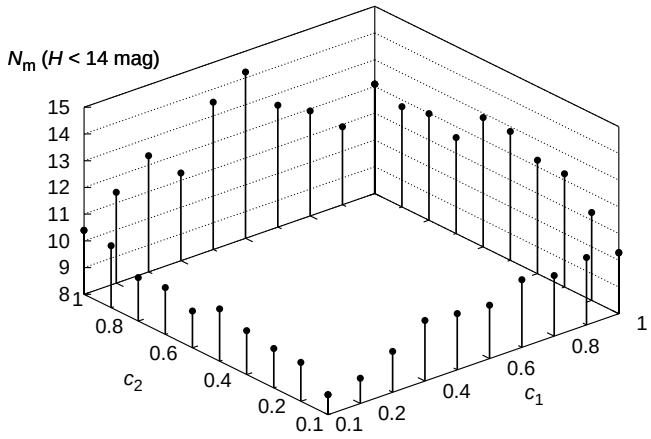

Figure 68: The estimated equilibrium number of $H \leq 14$ asteroids residing on unstable resonant orbits as a function of c_1 and c_2 (i.e. modifications of the collisional lifetime – c_1 – and spin-axis reorientation time-scale – c_2; the nominal result from Fig. 65 corresponds to $c_1 = c_2 = 1$). All bodies have fixed albedo $p_V = 0.05$.

weaken Yarkovsky delivery to the resonance. The work on collisional evolution of the main asteroid belt (Bottke et al. 2004), and hints from anomalous spin axes distribution of asteroids in the Koronis family (Vokrouhlický et al. 2003) suggest that the lowest c_1 and c_2 values are unlikely.

Similar values are found by weakening the YORP effect. For example, dropping the strength of YORP by an order of magnitude produces, with our nominal time-scales (i.e. $c_1 = c_2 = 1$), some 10 unstable asteroids. Only removing the YORP effect entirely from our simulation produces a smaller number – $\simeq 5$ – of large unstable asteroids. This shows how the YORP effect helps deliver asteroids into the J2/1: by preferentially tilting obliquity toward extreme values, YORP increases Yarkovsky drift.

5.3.3 Very unstable objects in the J2/1 resonance

As described previously, the J2/1 objects with very short dynamical lifetimes (≤ 2 My; Fig. 49) do not appear to come from the asteroid populations located along the J2/1 periphery. Instead, we explore in this section whether these very unstable objects are Jupiter family comets (JFCs) or near-Earth asteroids (NEAs) that have become temporarily captured inside the J2/1. Note that such trapping behaviour near separatrix of resonant zones has been observed in many different numerical simulations (e.g. Levison & Duncan 1994; Malyshkin & Tremaine 1999; Efthymiopoulos et al. 1999; Levison & Duncan 1997; Bottke et al. 2000, 2002).

To test our hypothesis, we turn to the results of Bottke et al. (2002), who tracked test bodies from numerous near-Earth object (NEO) sources in order to model the orbital (a, e, i) distribution of the NEO population. As part of their model, Bottke et al. (2002) numerically integrated test bodies from their source regions until they struck a planet, the Sun, or were ejected via a close encounter with Jupiter. Using results from their modelling work, we find that the objects most likely to become temporarily trapped in the J2/1 are active and dormant comets from the transneptunian disk (see also Levison & Duncan 1997, whose numerical integration runs are used in Bottke et al. 2002). We use these results to quantify the number of test bodies in the J2/1.

Bottke et al. (2002) estimated approximately $(6 \pm 4)\,\%$ of all NEOs with $a < 7.4$ AU are dormant JFCs. If there are a steady-state number of $\simeq 1100$ NEOs with $H < 18$, this works out to be roughly $20 - 110$ $H < 18$ NEOs from the dormant JFC population. Using the Bottke et al. (2002) residence time probability distribution computed for Jupiter-family comets, we estimated the number of dormant comets in the J2/1 at any given time. Our residence time distribution was normalized to those objects reaching perihelion $q < 1.3$ AU and $a < 7.4$ AU. We found that the fraction of comets trapped in the J2/1 resonance (i.e., $3.2\,\mathrm{AU} \leq a \leq 3.4\,\mathrm{AU}$ and $q > 1.3\,\mathrm{AU}$) is $\simeq 9\%$ of the JFC/NEO population. Thus, this implies that the dormant comet population in the J2/1 is $2 - 10$ objects with $H < 18$.

To include active comets, we turn to results described in Levison et al. (2002), who estimated that the ratio of dormant comets with $H < 18$ to active comets in the JFC population is roughly 2. Using this ratio, we expect the number of active comets in the J2/1 should be $1 - 5$. The upper limit is consistent with the observed number of $\simeq 5$ active comets currently trapped in the J2/1 (i.e., 83P/Russell 1, 104P/Kowal 2, 124P/Mrkos, P/LINEAR (2000 B3) and P/LINEAR (2000 R2)). Note that these bodies were identified

by numerical integrating comets (without non-gravitational forces) using the orbital elements contained in the Jet Propulsion Laboratory database `http://ssd.jpl.nasa.gov/sb_elem.html`. Our results indicate these comets typically remain trapped in the J2/1 for tens to hundreds of ky, consistent with the dynamical lifetimes of the very unstable objects.

Our results imply the upper limit of the $H < 18$ dormant comet population described above (10 objects) is the most applicable to our estimates. We caution, however, that active JFCs with $q < 1.3$ AU pass closer to the Sun than those with $q > 1.3$ AU and thus may be more prone to thermal-driven splitting and disruption events. Because results from Bottke et al. (2002) have only been calibrated for bodies with $q < 1.3$ AU, we may be somewhat underestimating the number of dormant comets in the J2/1.

Levison et al. (2002) claim that dormant comets are likely to follow a cumulative H distribution with a power-law index of $\gamma = 0.23 - 0.28$, where $N(< H) \propto 10^{\gamma H}$. Using the values above, this suggests that $\simeq 1$ dormant comet with $H < 14$ should reside in the J2/1 at any given time. A check of the available data suggests that 2 such $H < 14$ objects currently reside in the J2/1, and that the power-law index of the 11 objects with $H < 17$ is $\gamma \simeq 0.31$. These values are in reasonable agreement with our results, enough that we predict the very unstable population in the J2/1 is likely to be dominated by dormant JFCs.

5.4 Conclusions

We have shown that the unstable asteroids residing in the 2/1 mean motion resonance with Jupiter have most likely been transported to their current orbits by the Yarkovsky effect; similarly we argued that objects on very unstable orbits are mostly dormant (or active) Jupiter family comets. This model satisfies several constraints: the total number of observed resonant asteroids (larger than some threshold), the slope of their power-law H distribution, and their location in phase space inside the J2/1. To further strengthen our model we need to improve our constraints or find new ones.

To add to our constraints, we need further observations (both recoveries and new discoveries) of faint asteroids in the J2/1. At the present rate of discovery, ground-based surveys may increase the population of multi-opposition resonant asteroids up to $\simeq 500$ by the end of 2005. Advanced survey programs (e.g., Pan-STARRS) or space-borne programs (e.g., GAIA) will further boost the rate of discoveries, such that by the end of this decade the population of known resonant asteroids might very well increase to thousands.

Our model also provides some testable predictions. For instance, we would expect the majority of asteroids on unstable orbits to have prograde rotations because Yarkovsky transport toward larger values of semimajor axis requires obliquities in the range $0^\circ - 90^\circ$. We can check this conclusion by testing what happens when we track the evolution of asteroid spin states (e.g., Vokrouhlický et al. 2003, 2004). This would include numerically integrating spin orientations for asteroids evolving toward the J2/1 along the orbits described in Sec. 5.3.1. Initially, we assume low obliquity values. When an asteroid enters the J2/1, orbital changes and interactions with various secular resonances produce chaotic evolution of the spin axis, in particular forcing the obliquity to span a large interval of values. This effectively erases the "memory" of the pre-resonance state. However, we find the rotation stays prograde in the majority of cases. Unfortunately, photometry and light-curve inversion for faint distant objects is too difficult to allow us to obtain obliquity solutions for most unstable resonant asteroids. New data from large observing programs will be needed (e.g., Kaasalainen 2004).

While the origin of the unstable asteroids in the J2/1 resonance can be partially understood by the model described above, the origin of Zhongguos and Griquas remains puzzling. We know from Sec. 5.2 that both islands A and B are populated, with the former significantly less than the latter. Planetary migration might be responsible for such a differential depletion of primordial populations in both islands (e.g. Ferraz-Mello et al. 1998) or even cause their secondary re-population (see the work of Morbidelli et al. (2005) for Trojan asteroids). However, a steep size distribution of B-Zhongguos make us think of a disruption which occurred recently and dominantly populated with ejecta this island. On contrary, the shallow size distribution of B-Griquas poses a problem for a model explaining them as B-Zhongguos slowly leaking by Yarkovsky effect, because such mechanism should more effectively act on smaller asteroids. We noted in Sec. 5.2 that the island A objects could hardly be ejecta from a disruptive event in the island B, because, for instance, the difference of mean inclination of their orbits would require ejection velocities of several km/s (a possibility is, though, that their inclination values have been later influenced by the near-by ν_{16} secular resonance). This makes the situation even more puzzling, with possibly complex hypotheses such as recently formed population of asteroids in the island B and primordial population of asteroids in the island A.

Acknowledgements

The work of MB and DV has been supported by the Grant Agency of the Czech Republic. We thank the referee, Kleomenis Tsiganis, for valuable comments, that improved the final version of the paper.

6 Yarkovsky footprints in the Eos family

The influence of the Yarkovsky/YORP effect on the evolution of the Eos asteroid family was studied by Vokrouhlický et al. (2006a). Their scenario is supported by several independent observations (the structure of the family in the proper element space, asteroids colour data and new spectroscopic measurements). This chapter is a reprint of the refereed article. The co-authors are D. Vokrouhlický, A. Morbidelli, W.F. Bottke, D. Nesvorný, D. Lazzaro and A.S. Rivkin. MB is responsible namely for the identification of the family in the space of proper elements (Section 6.2.1), N-body simulations of the long-term orbital evolution and their analysis (Secions 6.3, 6.3.1, 6.3.3).

Abstract

The Eos asteroid family is the third most populous, after Themis and Koronis, and one of the largest non-random groups of asteroids in the main belt. It has been known and studied for decades, but its structure and history still presented difficulties to understand. We first revise the Eos family identification as a statistical cluster in the space of proper elements. Using the most to-date catalogue of proper elements we determine a nominal Eos family, defined by us using the hierarchical-clustering method with the cut-off velocity of 55 m/s, contains some 4400 members. This unforeseen increase in known Eos asteroids allows us to perform a much more detailed study than was possible so far. We show, in particular, that most of the previously thought peculiar features are explained within the following model: (i) collisional disruption of the parent body leads to formation of a compact family in the proper element space (with characteristic escape velocities of the observed asteroids of tens of metres per second, compatible with hydrocode simulations), and (ii) as time goes, the family dynamically evolves due to a combination of the thermal effects and planetary perturbations. This model allows us to explain sharp termination of the family at the J7/3 mean motion resonance with Jupiter, uneven distribution of family members about the J9/4 mean motion resonance with Jupiter, semimajor axis distribution of large vs. small members in the family and anomalous residence of Eos members inside the high-order secular resonance z_1. Our dynamical method also allows us to estimate Eos family age to $1.3^{+0.15}_{-0.2}$ Gy. Several formal members of the Eos family are in conflict with our model and these are suspected interlopers. We use spectroscopic observations, whose results are also reported here, and results of 5-color wide-band Sloan Digital Sky Survey photometry to prove some of them are indeed spectrally incompatible with the family.

6.1 Introduction

The study of asteroid families has experienced a renaissance over the last several years from the discovery of several previously unknown, compact asteroid clusters (e.g., Nesvorný et al., 2002b, 2003; Nesvorný and Bottke, 2004). These discoveries can be credited, in part, to automated search programs constantly scan the sky for new near-Earth objects (e.g. Stokes et al., 2002). In the process, they have also found large numbers of main belt asteroids, which has resulted in an unprecedented increase in the catalog of known asteroids over the last decade. These clusters are young enough that their formation ages can be directly determined by integrating their members' orbits backwards in time. Using these data, we have been able to glean new insights into space weathering processes (Jedicke et al., 2004; Nesvorný et al., 2005), the origin of the IRAS/COBE dust bands (e.g. Dermott et al., 2001; Nesvorný et al., 2002b, 2003, 2006a), and the physics of asteroid breakup events (Nesvorný et al., 2006b).

Here, however, we focus our analysis on the Eos family, one of the largest asteroid concentrations in the main belt. This family has been studied by many groups over time; classical early references are Hirayama (1918) and Brouwer (1951), with more work in the 1970's from a variety of authors (see review in Bendjoya and Zappalà, 2002). Brouwer (1951) was the first to discover that the Eos family has some puzzling features that cannot be easily reconciled within a standard model. He noticed that the spread of family members in semimajor axis was anomalously small when compared to their proper eccentricity and inclination (see Table IV in his paper and, e.g., Zappalà et al., 1984). He hypothesized that Eos likely experienced an unusual ejection velocity field or inadequacies of the linear secular theory.[17]

Brouwer (1951) also speculated about the Eos family's age. This issue is important, because a family's age determines how long its members have been subject to post-formation dynamical evolution. Note that the chronology of asteroid families is needed to constrain collisional evolution in the main asteroid belt (e.g. Bottke et al., 2005a,b). Brouwer noticed that within the simplest, linearized secular theory, the sum of proper longitude of pericenter ϖ_p and proper longitude of node Ω_p stays constant because their related proper frequencies are exactly the opposite of one another. He thus proposed to use $(\varpi_p + \Omega_p)$ as an additional parameter to test the properties of asteroid families. In particular, any strong clustering in

[17] As a historical curiosity, we mention that Brouwer (1951) was an opponent of the scenario that families, since their formation, had been subject to unknown perturbations, including *those of non-gravitational origin* (Brown, 1932).

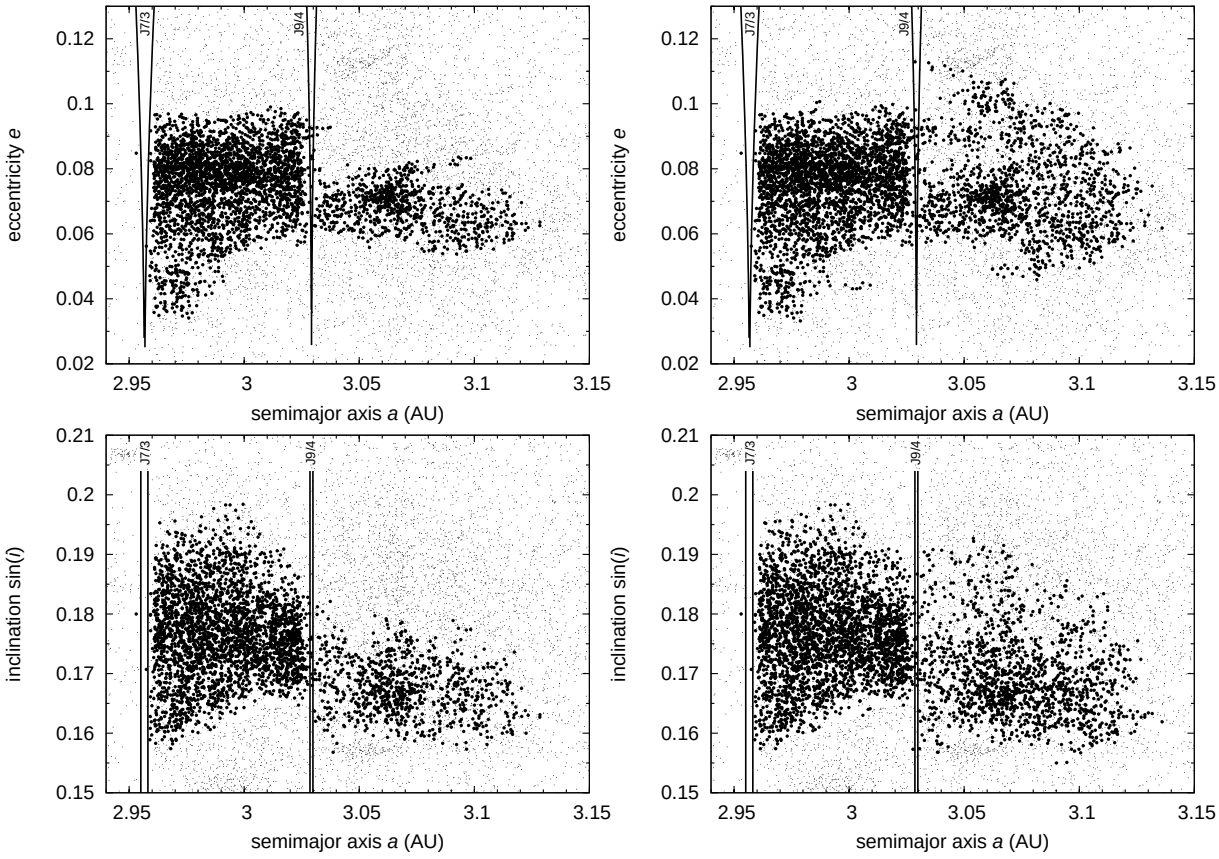

Figure 69: The Eos family determined by the HCM with $V_c = 50$ m/s (left figures) and 55 m/s (right figures) projected onto perpendicular planes in the space of proper elements: (i) semimajor axis a and eccentricity e (upper figures), and (ii) semimajor axis a and sine of inclination $\sin i$ (bottom figures). Family members are shown by thick symbols, while the background asteroids in a surrounding box delimited by the axes range are dots. Position of major mean motion resonances with Jupiter (J7/3 and J9/4) is also shown.

this parameter would suggest the family is $\lesssim 1$ My because more accurate secular theory would inevitably break this property.

An investigation of the limited number of known Eos members by Brouwer (1951; see Table V) indicated that the distribution of $(\varpi_p + \Omega_p)$ was strongly nonuniform, which could be used to argue that the Eos family is young. In spite of Carpino et al.'s (1986) finding that the $(\varpi_p+\Omega_p)$ time variation is anomalously slow in this particular zone of the main asteroid belt, Farinella et al. (1989) critically reassessed Brouwer's argument concluding it might have been fluke. By associating smaller asteroids with the Eos family, these groups showed that $(\varpi_p + \Omega_p)$ is fairly uniform, with some residual non-uniformity stemming from a potentially younger subcluster of asteroids inside the Eos family. Farinella et al. (1989) instead argued for an older age based on fact that large disruption events in the main belt occur very infrequently. They found additional support for their old age argument from the uniform rotation period distribution of the family members, which could have been produced by collisions over long time periods (Binzel, 1988). Hence, they dismissed the usefulness of the $(\varpi_p+\Omega_p)$ parameter for future family studies (except for very young families; Nesvorný et al., 2002b, 2003). We share this point of view; in Sec. 6.3.3, we show that this parameter follows a nearly uniform distribution with deviations compatible with statistical fluctuations and the expected influence of the secular resonance z_1 (compare with Milani and Knežević, 1992, 1994).

Morbidelli et al. (1995) have also pointed out problems in determining the formation history and age of the Eos family. The Eos family is both bracketed by the J7/3 mean motion resonance (MMR) at ~ 2.96 AU and is intersected by the J9/4 MMR at ~ 3.03 AU (Fig. 69). Morbidelli et al. reported that the number of family members with $a > 3.03$ AU appears to be significantly smaller than those with $a < 3.03$ AU. It is unclear how the initial velocity distribution of fragments produced by the parent body break-up could have produced this odd arrangement. One possibility was that there was a cascade of secondary fragmentations inside the original family. No other family, however, shows any evidence for a such a process.

Morbidelli et al. (1995) also noted that 5 asteroids associated with the family were residing inside the J9/4 MMR. By numerically integrating their orbits, they found these objects are ejected from the main belt on a timescale of $100 - 200$ My. Rather than postulate that these fragments were directly injected into the resonance by the family-forming event, Morbidelli et al. instead suggested that they were probably placed on those orbits via a secondary breakup. They also predicted that asteroids in the J9/4 MMR at higher (or lower) eccentricities and inclinations may also be former Eos members. Zappalà et al. (2000) confirmed this prediction when they found that 5 of the 7 objects they observed inside the J9/4 MMR (but unrelated to the family with a simple clustering method in orbital element space) had spectra compatible with Eos family members. The interesting problem with this scenario, however, is that the 5 fugitive asteroids are large enough (diameter $14 < D < 30$ km) that collisional injection over the last $100 - 200$ My is highly unlikely.

Another way to estimate the age of the Eos family is to analyze the collisional evolution of its size-frequency distribution (SFD). Using a 1-D self-consistent collisional evolution code, Marzari et al. (1995) considered the SFD evolution of three prominent families: Themis, Koronis and Eos. While partially succeeding in the Themis and Koronis cases, their match to the Eos family SFD was poor, with their best fit indicating that the Eos family was surprisingly young. It is important to note here that while Marzari et al.'s results provided us with many useful insights, their work does have important limitations: (i) the initial family SFDs were unknown, (ii) they used a disruption scaling law that allowed their asteroids to break up far more frequently than suggested by numerical hydrocodes (e.g., Benz and Asphaug, 1999), (iii) their main belt evolution results are discordant with current constraints (Bottke et al., 2005a,b), and (iv) the observed family SFDs used by Marzari et al. had not been debiased and thus were limited to $D \gtrsim 10$ km bodies.

In what follows, we show that most, though not all, of the enigmatic issues about the Eos family are naturally solved within the framework coined by Bottke et al. (2001, 2002b). They argued that the asteroid families are initially more compact clusters in (a, e, i) proper element space than currently observed. The assumed ejection velocities are then compatible with numerical simulations of the asteroid catastrophic disruptions (e.g., Love and Ahrens, 1996; Ryan and Melosh, 1998; Benz and Asphaug, 1999; Michel et al., 2001, 2002), with the observed fragments with diameters larger than few kilometres launched away at relative velocities smaller than $\simeq 100$ m/s. As time proceeds, the family undergoes evolution by two processes: (i) *collisional*, with $D \lesssim 10$ km asteroids suffering catastrophic disruption within a few Gy (and producing secondary fragments), and (ii) *dynamical*, where the thermal (Yarkovsky) forces, as a function of size, thermal parameters and rotation state (the obliquity and rotation rate, in particular; for a review see Bottke et al., 2002b), spread the initial cluster in semimajor axis and allow the bodies to interact with various secular and mean motion resonances (see also Milani and Farinella, 1994, 1995; Morbidelli and Nesvorný, 1998; Farinella and Vokrouhlický, 1999; Bottke et al., 2001; Nesvorný et al., 2002a; Carruba et al., 2003; Tsiganis *et al.*2003; Nesvorný and Bottke, 2004; Brož et al., 2005b; Carruba et al., 2005).

In this paper, we investigate whether the Eos family has experienced substantial evolution via the Yarkovsky effect. In Sec. 6.2, we review what we know about the Eos family (i.e., its structure in proper element space, its size-frequency distribution, the spectral properties of its members). In Sec. 6.3, we discuss anomalous family features and show, using numerical integration techniques, that they are easily understood within the Yarkovsky-dispersion model. Our model also produces some testable predictions, such as whether interloper asteroids exist inside the family. For many of these bodies, we have determined their spectra and have determined whether their spectral types are consistent with predictions (Sec. 6.4).

6.2 Eos family: basic facts

In this section, we describe the known properties of the Eos family. First we applied formal clustering methods on the most updated database of asteroids to identify the Eos family in the orbital element space. Our work significantly increases the number of asteroids associated with the family as compared to previous searches (e.g., Zappalà et al., 1995; Bendjoya and Zappalà, 2002). Second, we have collected spectral information about various family members (e.g. Cellino et al., 2002 and references therein).

6.2.1 Identification in the proper element space

We applied the hierarchical clustering method (HCM; e.g. Bendjoya and Zappalà, 2002 and references therein) to identify clustered Eos family members in proper element space (semimajor axis a, eccentricity e and sine of inclination $\sin i$). Our database included the analytically-determined proper elements of nearly $170,000$ main belt numbered and multi-opposition asteroids from the `AstDyS` database (`http://newton.`

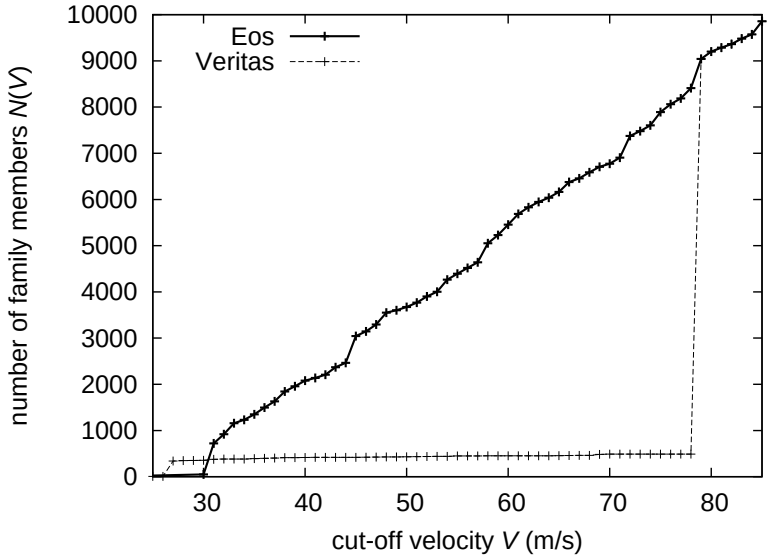

Figure 70: Number of asteroids associated with a family (using the HCM approach) as a function of the cut-off velocity V_c for Eos (thick line) and Veritas (thin line). The large Eos family steadily accumulates asteroids as V_c increases, while identification of the compact Veritas family shows only little dependence on V_c. At a critical value of $V_c = 78$ m/s the two neighboring families coalesce into a single structure.

`dm.unipi.it/`) as of November 2004. We tested different values of the cut-off velocity $30 < V_c < 85$ m/s, the principal free parameter in the HCM method. Lower values were not used to avoid the intrinsic noise of analytical proper elements.

At the largest V_c values, the cluster starts to accumulate a significant portion of the surrounding region in proper element space. This is seen in Fig. 70 where we show the number of HCM identified members of the neighboring Eos and Veritas families as a function of V_c. At the critical value $V_c = 78$ m/s, the two families coalesce into a single cluster of asteroids. This plot also demonstrates the intrinsic difficulty of family identification in case of the large families like Eos. The compact (and young; e.g. Nesvorný *et al.*2003) Veritas family depends very weakly on V_c until it passes a threshold value that allows it to "join" with the background population; this means the family is distinctly defined (see also Fig. 4 of Nesvorný et al. 2005a). Conversely, as V_c is increased for Eos, the family population steadily increases as well. Not surprisingly, we expect this process to accumulate numerous interlopers. Trials and tests are needed to eliminate as many of these objects as possible from the final set.

Figure 69 shows two examples of Eos family identification for $V_c = 50$ m/s (left) and 55 m/s (right; dots are background main belt asteroids inside a orbital-element box defined by the ranges of the axes). The identification of family members for different values of V_c is available at our web-site `http://sirrah.troja.mff.cuni.cz/yarko-site/`. We believe $V_c = 55$ m/s provides a reasonable compromise between completeness and overshooting; at larger V_c values, the family starts to accumulate more distant asteroids with $a > 3.03$ AU, i.e. on the far side of the J9/4 MMR with Jupiter. We use it as our nominal definition of the Eos family. Figure 71 shows the Eos family projected onto the plane of proper a and absolute magnitude H (data are taken consistently from `AstDyS` web-site) again for two V_c values. The structure seen in this figure will be discussed in Sec. 6.3.

Note that 2-D projections of the family (Fig. 69) miss details that can be seen in 3-D proper orbital elements space. In Fig. 72 we show the Eos family as a 3-D cluster (bold symbols) embedded in the background population of asteroids (dots). We have chosen the view to emphasize the low-e and i side in order to bring attention to a stream-like structure radiating out from the family (on our website `http://sirrah.troja.mff.cuni.cz/yarko-site/` we provide a computer animation that allows one to see the Eos family from many different directions in proper element space). The two planes shown in the same figure roughly mark the libration zone of the high-order secular resonance z_1 (e.g. Milani and Knežević 1990, 1992, 1994, and Sec. 6.3.3). We see that the peculiar structure observed in the Eos family tightly adheres to this resonance (see Sec. 6.3.3 for details).

We also investigated cumulative distribution $N(< H)$ of absolute magnitudes H for Eos family asteroids. This can be achieved with high reliability, since even with low V_c values the family contains thousands of members (e.g., the nominal family with $V_c = 55$ m/s has about 4400 asteroids). Fig-

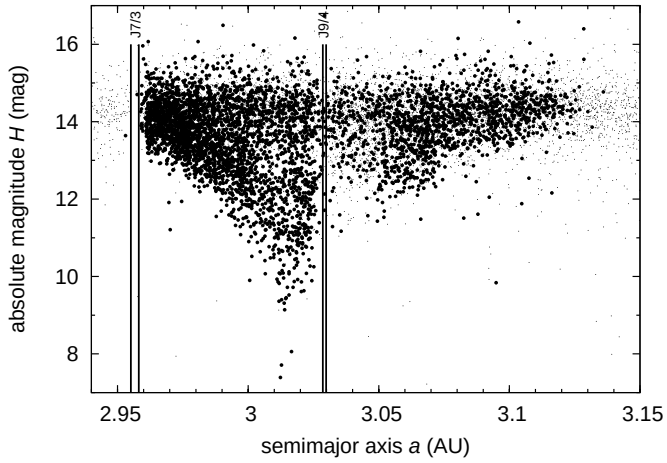

Figure 71: The Eos family determined by the HCM with $V_c = 55$ m/s projected onto a plane of proper semimajor axis a and absolute magnitude H. As in Fig. 69, the family members are thick symbols, surrounding background asteroids are dots. Observation limits prevents detecting asteroids smaller than about $1 - 2$ km in size ($H \simeq 17$). Major mean motion resonances are also shown.

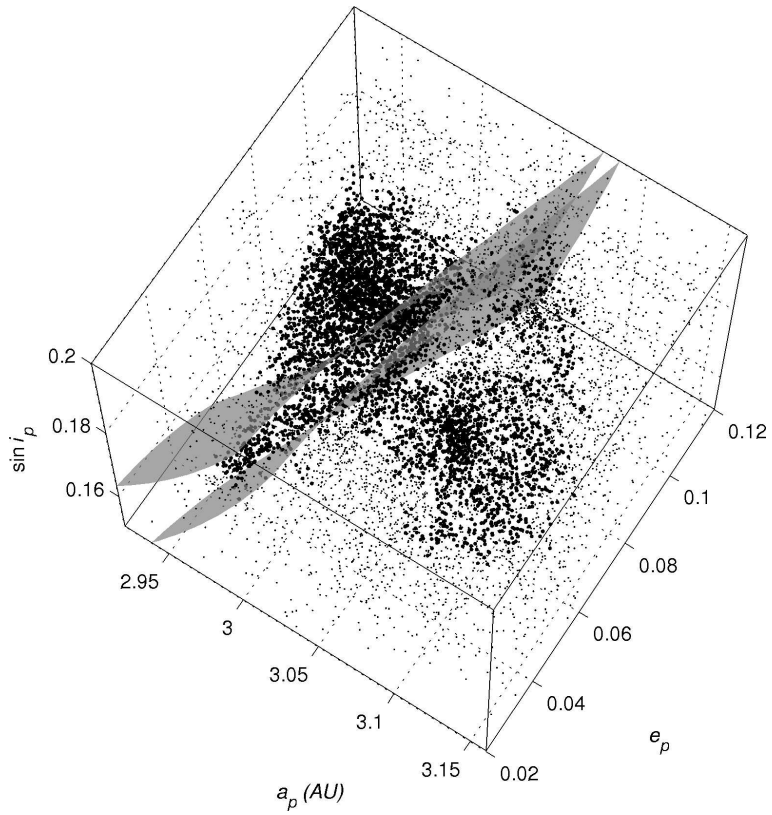

Figure 72: The Eos family (bold symbols) shown in 3-D space of proper orbital elements; dots are background asteroids not associated with the family by the HCM method (here $V_c = 55$ m/s is used). We emphasize existence of an asteroid stream escaping from the family toward low values of the proper eccentricity and inclination. Semi-transparent surfaces indicate approximate borders of the high-order secular resonance z_1 discussed in Sec. 6.3.3. We show ± 0.8 arcsec/yr region about the exact resonance whose location is determined using a semianalytic theory of Milani and Knežević (1990, 1992); this width corresponds to the numerical results from Sec. 6.3.3. Unlike the principal MMRs, the z_1 resonance is a strongly curved 3-D structure in the space of proper elements. The observed anomalous asteroid stream and the position of the z_1 resonance strongly correlate; this suggestive link is investigated in more detail in Sec. 6.3.3.

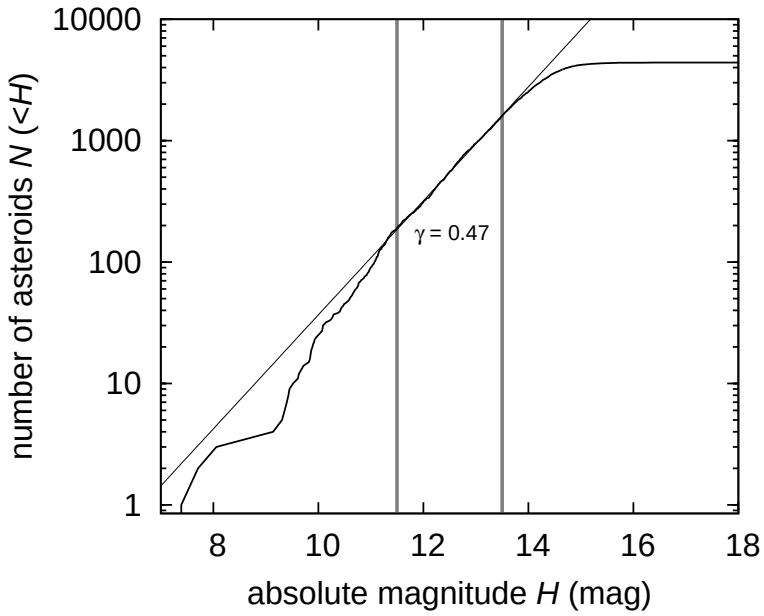

Figure 73: Cumulative distribution $N(< H)$ of absolute magnitude values H for members of the Eos family determined by the HCM with $V_c = 55$ m/s. The straight line is a power-law approximation with index $\gamma = 0.47$ that best fits the family in the magnitude range $H \in (11.5, 13.5)$ (denoted with the two vertical lines); at larger sizes (i.e. smaller values of H) the distribution becomes steeper and dependent on individual objects, while at smaller sizes (larger values of H) the observation bias affects the data.

ure 73 shows this quantity for the nominal cut-off velocity 55 m/s; we used a power-law approximation $N(< H) \propto 10^{\gamma H}$ in the magnitude range $(11.5, 13.5)$ and obtained $\gamma \simeq 0.47 \pm 0.02$. Our value of γ is close to some previously reported values (e.g. Fujiwara, 1982) but discordant with some others who predict a considerably steeper distribution from their method (e.g. Tanga et al. 1999). This value of the power index suggests that the family has undergone significant collisional and dynamical evolution at small asteroid sizes that drove it toward the equilibrium state (e.g. Dohnanyi, 1969; O'Brien and Greenberg, 2003; Bottke et al. 2005c). In particular, Bottke et al. (2005a,b) estimate a $15 - 20$ km size asteroid (roughly $H = 11.5$ for Eos family members) has a collisional lifetime of $\simeq 2$ Gy; thus we would tentatively infer an age for the Eos family of $1 - 2$ Gy from this simple argument. Interestingly, our more quantitative work in Sec. 6.3.2 will provide additional support for this age.

Figure 74 shows the best-fit power-index γ for family members with $11.5 < H < 13.5$ as a function of the cut-off velocity V_c. Except the anomalous "step" at $V_c = 44$ m/s, which is caused by a sudden extension of the family to the region beyond the J9/4 MMR (see also Fig. 70), we find that γ steadily increases. The limiting value $\simeq 0.52$ can be attributed to the overall main-belt population in this particular heliocentric zone; here V_c has become large enough to fill the entire region. The smaller γ values found for small V_c is consistent with Morbidelli et al. (2003), who predicted shallow slopes for most prominent families where their members had $H \gtrsim 15$.

6.2.2 Spectroscopic observations

Information about the physical properties of the Eos family members derives from spectroscopy of large asteroids, completed by numerous observers using a variety of telescopes and instruments, and broad-band photometry of small asteroids taken by the Sloan Digital Sky Survey (SDSS). Here we provide some information about both sources.

We start with results from spectroscopic surveys. Some caution is warranted when comparing data from different sources because: (i) taxonomic systems have significantly evolved over the past two decades and (ii) major surveys have only performed spectroscopy in the visible wavelengths. This later point is important because discriminating the physical properties of asteroids, especially for an object at the outskirts of the broad S-type asteroid color complex, requires additional data in the infrared. For example, asteroid (221) Eos and several other large Eos members have visual spectra that resemble S-type objects (apart from finer details introduced only later on). It was only when an extended spectrum of (221) Eos, covering both visual and infrared bands, was obtained that Bell et al. (1987) and Bell (1989) were able to

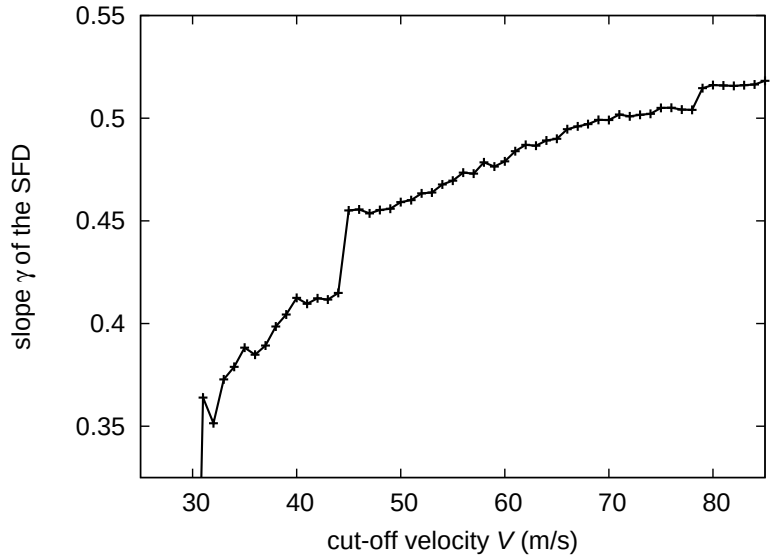

Figure 74: The power-law index γ of the cumulative magnitude distribution $N(< H)$ fitted in the range $H \in (11.5, 13.5)$ as a function of the HCM cut-off velocity V_c. At the largest velocity the system represents basically the whole local main-belt population around the Eos family. At any smaller value of V_c the family is shallower; at our nominal family definition of $V_c = 55$ m/s we have $\gamma = 0.47 \pm 0.02$ (see Fig. 73).

propose that Eos family members comprise a distinct spectral class now called K-type (see Veeder et al. (1995), Doressoundiram et al., (1998) and Zappalà et al., (2000) for reviews of this topic).

Objects that are not related to K-type are assumed to be interlopers. For example, a dedicated visual spectroscopic survey of large Eos members by Doressoundiram et al. (1998) found two asteroids, (1910) Mikkailov and (4455) Ruriko, that were spectrally similar to C-type asteroids (out of a sample of 45 observed family members). Still, there appears to be a modest spectral heterogeneity among Eos members ranging from the K types, such as (221) Eos itself, to T types (see also Xu et al. 1995). Because K- and T-types lie along the edge of the S-type complex, it can be difficult to precisely classify asteroids with these characteristics. Bus and Binzel (2002b), who examined 6 of the 45 asteroids discussed by Doressoundiram et al. (1998) as part of the SMASSII survey, found that 4 were K-types and 2 were S-types (633 Zelima and 1186 Turnera). Doressoundiram et al. (1998) interpreted the spectral differences among these bodies as some kind of weathering process or as perhaps a sign of compositional differences in the Eos parent body (see also Mothé-Diniz and Carvano, 2005). As far as we know, however, there is no general consensus about this interpretation to date.

We also note that the SMASSII survey detected 19 asteroids that are associated with the Eos family at the HCM cut-off velocity $V_c = 55$ m/s (Bus and Binzel, 2002a,b; see also updates at `http://smass.mit.edu/`). Most of them were given K-type classifications, with the exceptions being the two S type asteroids mentioned above and two interloper asteroids classified as Xc-type asteroids: (1604) Tombaugh and (3214) Makarenko.

Another rich and recent source of spectroscopic data is the S^3OS^2 survey by Lazzaro et al. (2004) (see `http://www.daf.on.br/~lazzaro/S3OS2-Pub/s3os2.htm`). They observed 13 asteroids from our nominal Eos family and obtained the following results: Asteroids (1075) Helina (Xc-type), (1605) Milankovitch (X-type), (3328) Interposita (Xc-type), and (4100) Sumiko (B-type) are all spectrally diverse from prevalent K and T types in the Eos family and contribute to the interloper population. Asteroids (251) Sophia (Sl-type) and (4843) Megantic (X-type) are also recognized as interlopers. Moreover, several asteroids were re-classified as D types within the new Bus taxonomy (Bus and Binzel, 2002a,b) from former T types of the Tholen taxonomy (Tholen, 1989), confirming difficulties in spectral classification.

Both datasets, SMASS and S^3OS^2, have been compiled together and applied systematically to asteroid families by Mothé-Diniz et al. (2005). For the Eos family, which was likely identified by these authors at a slightly higher V_c value, they determined that 55 out of 92 asteroids with known spectra belong to the KTD sequence; this sets the classification system for additional Eos family members. The mineralogical interpretation of these data, however, is more uncertain (e.g. D types here often have high albedo values, unlike the well interpreted low-albedo D type objects in the outer part of the asteroid belt and among Trojan asteroids). If we include Xk types in the KTD complex, which are related in the optical band, the

KTD's form 74% of Eos family members. Alien, or more distant spectral types (X, C and B) constitute 26% of asteroids in the Eos family; these values are somewhat higher than expected (Migliorini et al., 1995). Their fraction increases with larger V_c, suggesting the family is embedded in a spectrally alien zone. In spite of the ambiguous compositional implications of the KTD spectral sequence inside the Eos family, the fact that they are surrounded by primitive C-type asteroids may allow us to recognize some interlopers.

As far as broad-band photometry is concerned, we skip in this paper the older observations made for the Johnson UBV system (e.g. Zellner et al., 1985) and instead turn to more recent work of Ivezić et al. (2001, 2002), who analyzed the homogeneity of asteroid families using the broad-band 5-color data of SDSS (see `http://www.astro.princeton.edu/~ivezic/sdssmoc/sdssmoc.html`). Interestingly, in the case of Eos, they find a slight scatter of spectral features. Because the SDSS data are available mostly for small asteroids ($H \geq 12$, say), the result of Ivezić et al. might indicate spectral heterogeneity in the Eos family (e.g., Doressoundiram et al., 1998).

Nesvorný et al. (2005) has investigated this issue using release 2.0 SDSS data. While their main focus was space weathering effects, they were able to identify SDSS colors for 457 members of the Eos family (using a larger V_c value). The average principal component values found for Eos members were $\mathrm{PC}_1 = 0.466 \pm 0.095$ and $\mathrm{PC}_2 = -0.104 \pm 0.083$ (standard deviations), placing this family on the outskirts of the S-complex. While that borderline position complicates interpretations, the unusual colors of some objects may help us identify them as interlopers within the Eos family (see Sec. 6.4).

Additional possible interlopers in the Eos family, suggested by the infrared broad-band photometry reported by Veeder et al. (1995), are (562) Saloma and (1723) Klemola, whose J-H color index is significantly offset from other observed members of the family. Some authors, e.g. Bell (1989), suspect the third largest asteroid associated with Eos family, (639) Latona, might be an interloper based on S-like behavior of in the infrared band.

In Sec. 6.4 we report additional spectral observations of the Eos members made over the past few years by members of our team. We also analyze the most updated SDSS data, release 3.0.

6.3 Eos family: Yarkovsky traces

Hereafter we analyze several outstanding features of the Eos family. We show they can best be explained within a model where the family was formed in a more compact configuration in the proper element space about 1 Gy ago and then experienced dispersion via the Yarkovsky effects and interactions with resonances (Sec. 6.1). To that end, we performed a numerical simulation to determine how an initially compact cluster near the center of the Eos family expands in proper (a, e, i) over time. Note that our initial orbital data was chosen to be consistent with the ejection velocities predicted from laboratory experiments and numerical hydrocode simulations of asteroid disruption events (e.g. Love and Ahrens, 1996; Ryan and Melosh, 1998).

The initial orbital elements of our synthetic family asteroids were chosen according to the procedure described in the Appendix of Carruba et al. (2003). For the Eos family, the estimated mass ratio of the largest fragment and parent body is $\simeq 0.1$ (e.g. Tanga et al., 1999; Campo Bagatin and Petit, 2001). Using this value, we obtain a parent body diameter of $D_{\mathrm{PB}} \simeq 240$ km. To disrupt this object, we assumed a specific energy $Q^{\star}_D \simeq 0.1\,\rho\, D^{1.36}_{\mathrm{PB}}$, where the bulk density $\rho \simeq 2.5$ g/cm^3 (Benz and Asphaug, 1999). We assume that only a small part of this energy is transformed into the kinetic energy of the dispersed fragments, such that their mean quadratic velocity v_{ej} is $v^2_{\mathrm{ej}} = 2\, f_{KE}\, Q^{\star}_D$ (e.g. Davis *et al.*1989; Petit and Farinella, 1993). The fundamental anelasticity parameter $f_{KE} \simeq 0.02$ is intentionally chosen small, such that v_{ej} is on the order of a few tens of m/s.

Following the work of Petit and Farinella (1993), we also adjust our velocities to account for the self-gravity of the parent body, such that the escaping fragments must have a positive binding energy value. We also assumed v_{ej} had a Maxwellian distribution. For simplicity, no mass/size dependence of v_{ej} was assumed. The initial velocity field was set to be isotropic in space, although below we shall argue that the properties of the family indicate this may be an unrealistic assumption. Finally, we transformed the initial velocity field into orbital elements using Gauss equations and estimates of the parent body's true anomaly f and argument of pericenter ω: $f = 90^\circ$ and $\omega + f = 45^\circ$ (see e.g. Morbidelli et al., 1995). This latter choice is somewhat arbitrary, but it produces an initial family which has a characteristic, but not extreme, extent in the proper element space for the given ejection velocities.

We use a Swift-RMVS3 integrator (e.g. Levison and Duncan, 1994) modified to account for the Yarkovsky forces (see `http://sirrah.troja.mff.cuni.cz/yarko-site/` for details of its implementation, speed and accuracy tests). We also complemented the original version of the integrator with computations of synthetic proper elements in a manner compatible with definition laid out in Knežević

and Milani (2000, 2003). This means that we first apply a Fourier filter to the (non-singular) orbital elements in a moving window of $\simeq 0.7$ My (with steps of 0.1 My) to eliminate all periods smaller than some threshold (1.5 ky in our case; we use a standard sequence of Kaiser windows as in Quinn et al., 1991, a procedure equivalent to what is used by Knežević and Milani, 2000). The filtered signal, mean orbital elements, is then output from the simulation for further checks and passed through a frequency analysis code adapted from Šidlichovský and Nesvorný (1997) to obtain (planetary) forced and free terms in Fourier representation of the orbital elements. The isolated free terms are what we use as the proper orbital elements.

The 4 Jovian planets are included in our simulation with their masses, initial positions and velocities taken from the `JPL DE405` ephemeris. The effect of the terrestrial planets are accounted for as a barycentric correction of the initial conditions only, which we believe is justified in this distant zone of the asteroid belt. A timestep of 20 days is used. We used 210 test particles (asteroids) in our runs. Their diameters range from $D = 2$ km to 60 km. Smaller bodies dominate our integrated sample such that we have 10 bodies with $D = 60$ km in our sample and there are $\propto 1/D$ bodies in different size bins.

Their rotation rate distribution is set to be a Maxwellian with a peak value corresponding to a period of 8 hr (though we prevent shorter/longer periods than 4/12 hr; e.g. Binzel, 1988). The orientation of their spin axes is assumed to be uniform in space.[18] The rotation parameters of the asteroids are assumed to be constant for these runs. We acknowledge this is an over-simplification; thermal and gravitational torques produce large variations of asteroid spin vectors on Gy timescales (see e.g. Sec. 6.3.2). Here, however, we trade complexity for simplicity. The thermal parameters of the asteroids, necessary for modeling Yarkovsky forces, are: thermal conductivity $K = 0.005$ W/m/K, specific heat capacity $C_p = 680$ J/kg/K, and surface/bulk densities 1.5 and 2.5 g/cm^3, respectively. We assume that multi-km asteroids in the Eos region have an insulating surface layer of dust or at least a significant porosity which makes K small. We use analytic formulæ from Vokrouhlický (1998, 1999) and Vokrouhlický and Farinella (1999; Appendix) to compute the diurnal and seasonal variants of the Yarkovsky effect. With our chosen thermal parameters, the diurnal effect is about an order of magnitude larger than the seasonal effect, allowing asteroids with retrograde spins to spiral toward the Sun and those with prograde rotations to spiral away from the Sun.

After setting the initial conditions and thermal parameters for our test asteroids, we let our synthetic family evolve for 1 Gy (this end-time was chosen to be in rough accordance with our estimate of the family age in Sec. 6.3.2). Figures 75 and 76 show the dynamical evolution of their proper (a, e, i) over time (solid lines), superimposed onto positions of the currently observed Eos family members (dots). The former figure tracks evolution of asteroids with size $D \geq 7$ km, while the latter is for asteroids with $D \leq 7$ km. In both figures, we show the position of major MMRs –J7/3, J9/4 and J11/5– as well as numerous weaker MMRs such as high-order resonances (e.g. J16/7 or J23/10) and three-body resonances with Jupiter and Saturn (e.g. 8J−3S−3, 6J+2S−1, 5J−1S−2 or 3J−2S−1[19]; Nesvorný and Morbidelli, 1998; Morbidelli and Nesvorný 1999; Morbidelli 2002).

The effect of resonances on orbits migrating in a is twofold, depending of the strength of the resonance and the drift rate (da/dt). Weak resonances can temporarily capture an orbit and change its proper e and/or i by a small amount upon leaving the resonance (Fig. 77; see also Bottke et al. 2000; Vokrouhlický and Brož, 2002). This effect, while small enough to keep asteroids in the family, increases the mean dispersion of e and i over time. Our simulations suggest that this effect allows our test asteroids to match the full extent of the observed family in e but not in i, where it misses about a factor of two. Our integrations, however, assume fixed orientation of the spin axis in space for our test asteroids; in reality, thermal and gravitational torques, together with collisional effects, may produce more complicated evolutionary paths. For example, da/dt can change, or even reverse sign, in time in response to spin axis evolution, allowing them to cross back and forth across weak resonances at variable speeds. This could help increase their dispersal in e and i. It is also possible that our initial velocity field was unrealistic; perhaps a more accurate velocity field would help eliminate the "inclination problem" (Sec. 6.5). We note, however, that effect of dispersion in e and i is size-dependent since smaller asteroids have chance to meet more tiny resonances as they migrate faster than large asteroids. This effect helps explaining "triangular" shape of the families in the $e - H$ and $i - H$ planes discussed by Cellino et al. (2002).

Powerful MMRs, namely the J7/3, J9/4 and even the J11/5, can remove Eos asteroids from the family by significantly increasing (or decreasing) their e and/or i values. The strength of this effect is proportional to the order of the resonance (e.g. Morbidelli, 2002), but it also depends on the Yarkovsky da/dt rate. In

[18] A semi-empirical model of Paolicchi et al. (1996) suggests a size-rotation relation with smaller fragments rotating faster than the large ones. Given other uncertainties in our simulation, we stay with our simple formulation.

[19] We adopt the notation of Nesvorný and Morbidelli (1998) and Morbidelli (2002) who characterize a three-body MMR $(+m_J\mathrm{J} + m_S\mathrm{S} + m)$ with a condition $m_J\dot{\lambda}_J + m_S\dot{\lambda}_S + m\dot{\lambda} \simeq 0$, where λ_J, λ_S and λ are mean longitudes of Jupiter, Saturn and the asteroid.

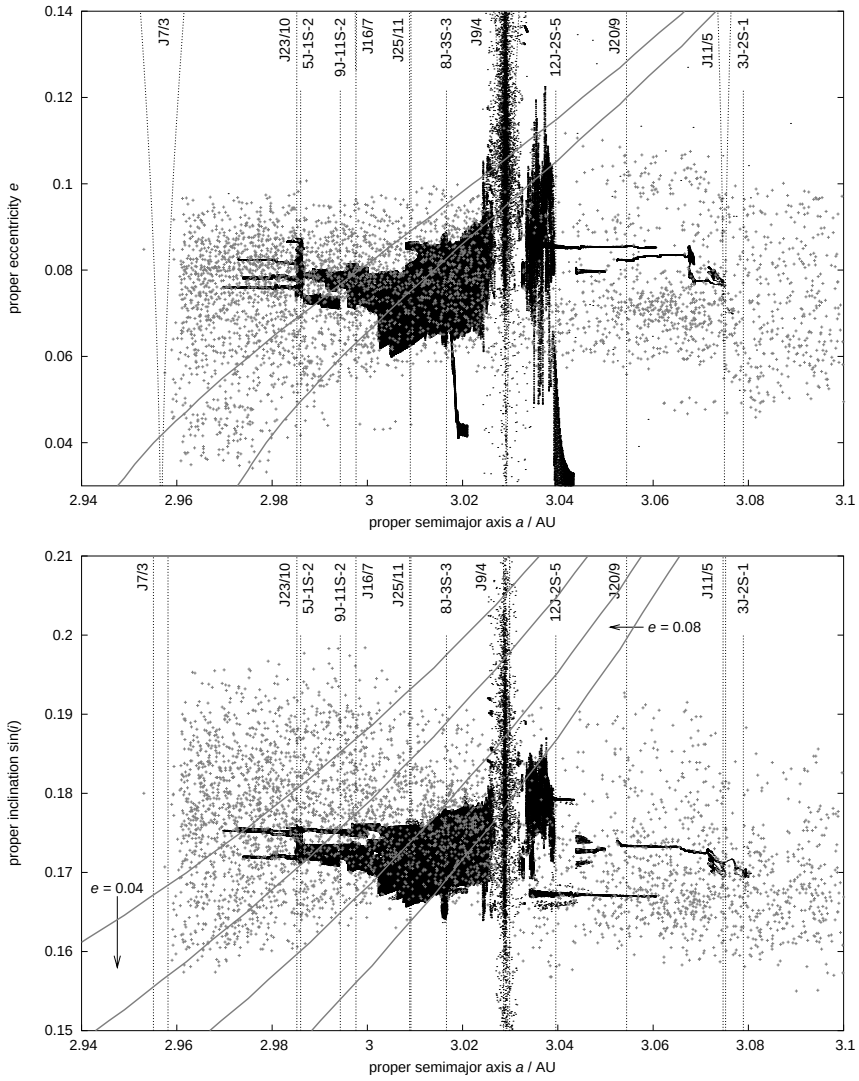

Figure 75: Evolution tracks of our synthetic Eos asteroids with size ≥ 7 km during 1 Gy in our simulation; dots are ≥ 7 km members of the currently observed family with the HCM threshold velocity $V_c = 55$ m/s. Top: proper eccentricity vs. proper semimajor axis; bottom: proper sine of inclination vs. proper semimajor axis. The initially compact family extends in course of time due to a combination of the (i) Yarkovsky forces that produce diffusion in the semimajor axis, and (ii) interaction with MMRs that, upon capture, cause eccentricity and inclination to change. The latter effect is proportional to the resonance strength scaling with its order. Thus the principal resonances –here J9/4– make many of the captured asteroids eliminated from the family. Weaker MMRs, such as 16/7 or the three body resonances (shown in the figure), do not have a capability to eliminate asteroids from the family, yet they can make the family to extend in eccentricity and inclination. A special effect is produced by the high-order secular z_1 resonance (Sec. 6.3.3) that make the Yarkovsky drifting orbits frequently captured and driven along it for a long period of time. This is because this resonance varies along all proper elements, approximately diagonally across the family. The grey curves show nominal location of the resonance ± 0.8 "/y zone for: (i) $\sin i = 0.17$ (top), and (ii) $e = 0.04$ and $e = 0.08$ (bottom). The particle moving toward small proper eccentricity value at ~ 3.02 AU shows a rare temporarily capture in a weak secular resonance $g - 3g_6 + 2g_7$.

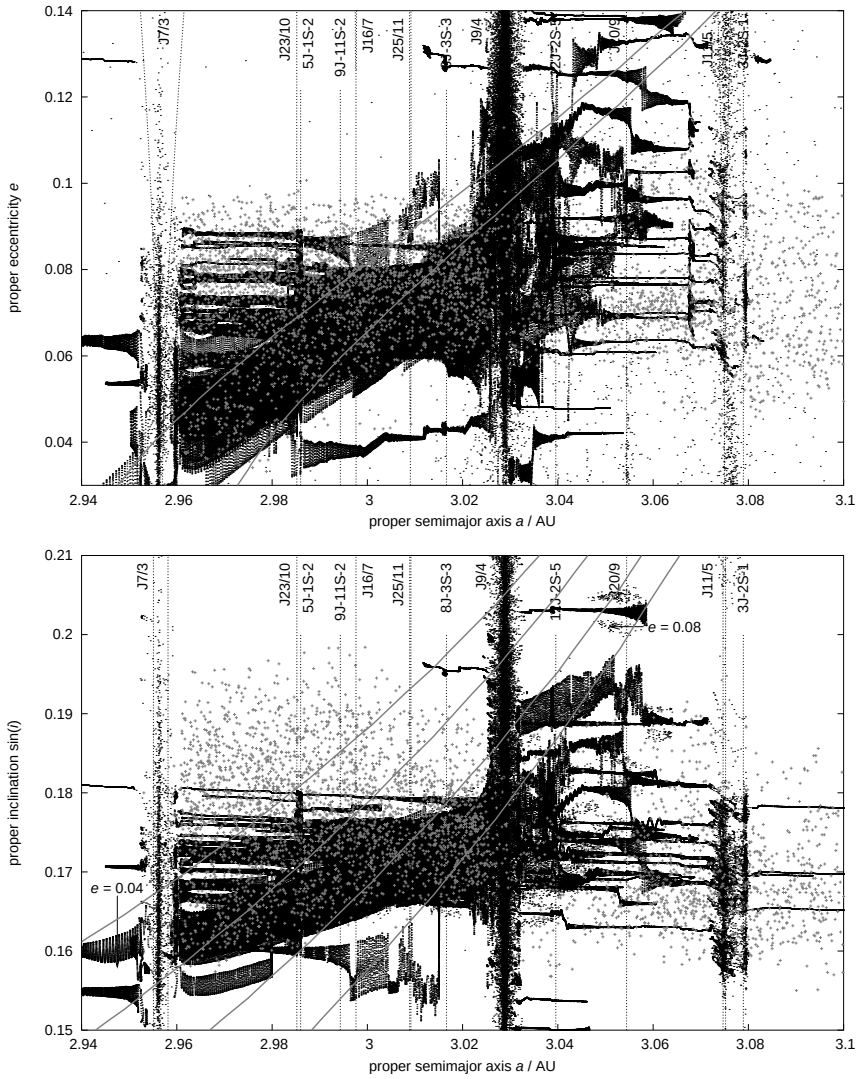

Figure 76: The same as in Fig. 75 but here for asteroids with size $\leq$ 7 km (view dominated by 2 km size bodies). These objects have a faster semimajor axis drift due to the Yarkovsky forces and some manage to cross the whole extend of the family in semimajor axis. As in Fig. 75 we note both interaction with the weak MMRs and significant role of the z_1 secular by trapping the migrating objects and transporting them to smaller values of proper inclination and eccentricity. With that process, nearly the complete eccentricity extend of the family is achieved, though effect on inclination is still small. Transparency of the J9/4 MMR for the migrating objects is higher now, yet many asteroids still get ejected from the Eos family via this route. The J7/3 MMR may eventually be also crossed by few of these smaller asteroids, but upon this crossing the eccentricity and inclination get largely changed. The black sections of the evolutionary tracks indicate the particle is still associated with the Eos family at the nominal HCM cut-off velocity $V_c = 55$ m/s; the dark-gray section indicate the particle escaped too far from the family and ceases to be associated with it. Note, that the few objects that crossed the J7/3 resonance became unrelated to the Eos family at the adopted nominal HCM cut-off velocity.

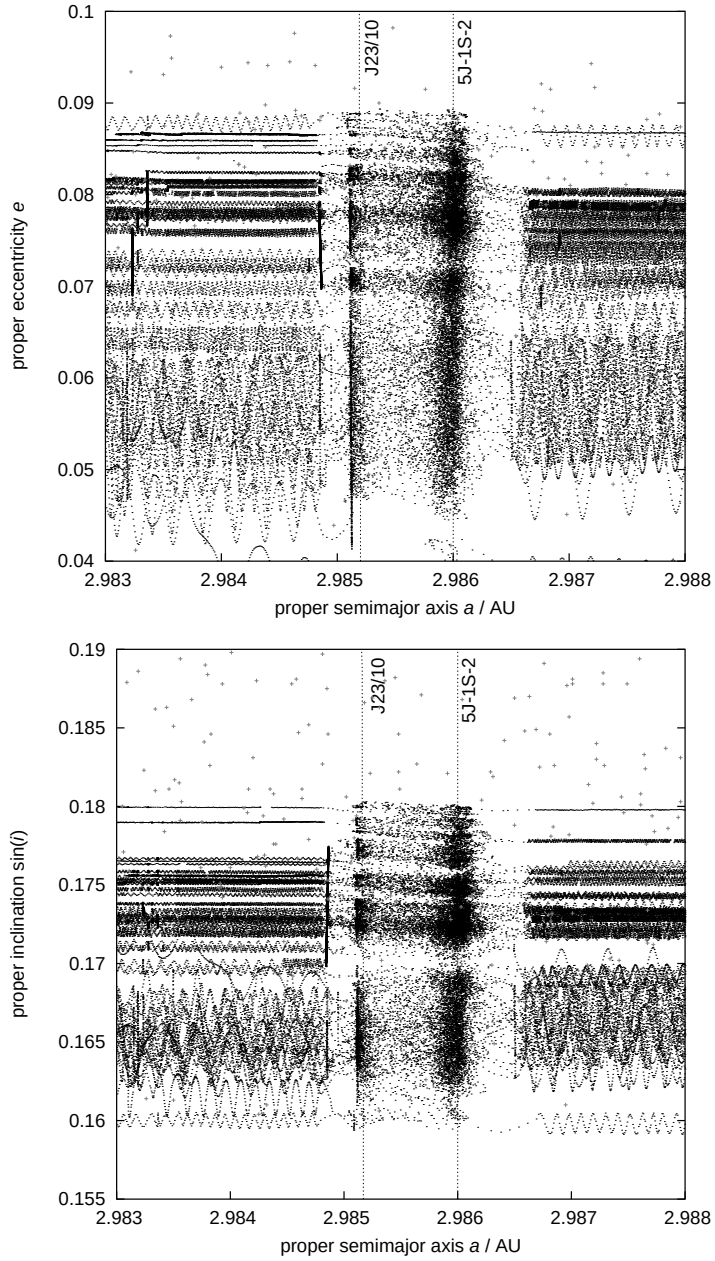

Figure 77: A zoom of the Fig. 75 showing tracks of particles in our simulation near a pair of weak mean motion resonances J23/10 and 5J-1S-2 (see the text for nomenclature); dots are the currently observed asteroids. Upper panel is a projection onto the proper eccentricity vs. proper semimajor axis values, lower panel gives a projection onto the proper sine of inclination vs. proper semimajor axis values. Because of the Yarkovsky forces the orbits migrate toward smaller semimajor axis values. Upon encounter the mean motion resonances, the proper eccentricity might be significantly changed; the inclination effect is quite less for these resonances. The bottommost migrating particles are trapped in the z_1 secular resonance and stay so even after a period of interaction with the mean motion resonances.

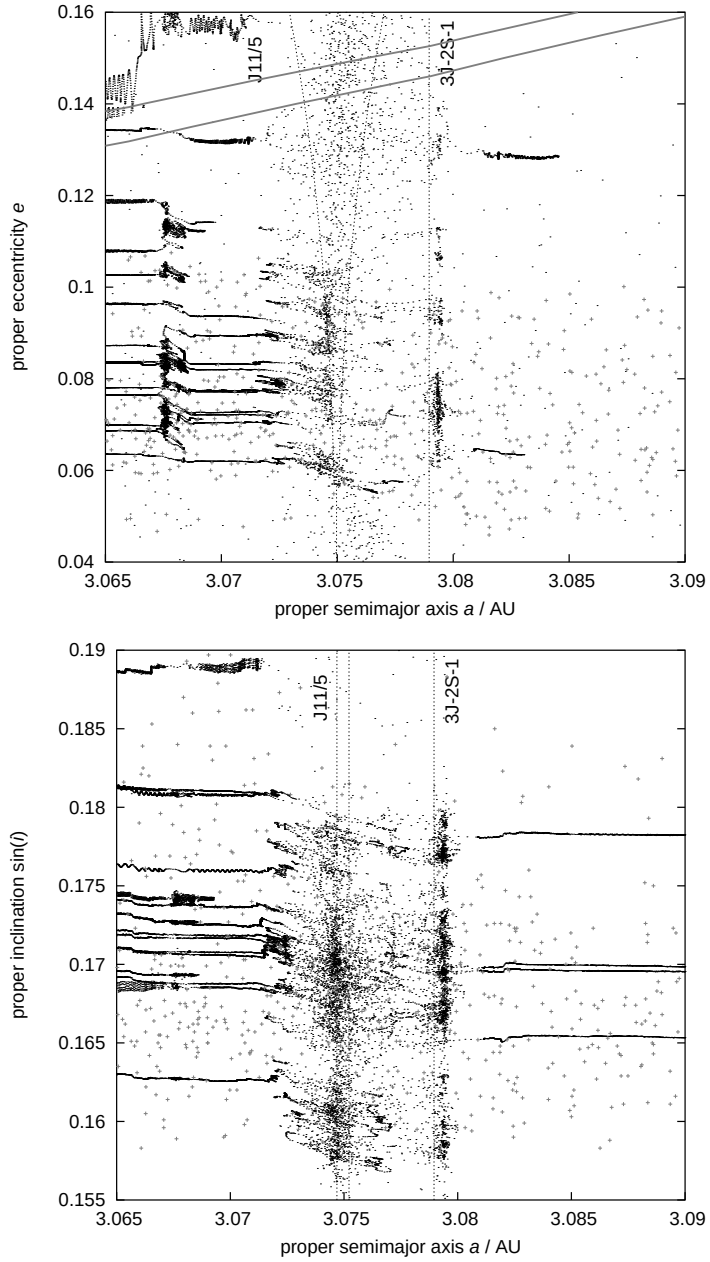

Figure 78: A zoom of the evolutionary paths of the Eos members in our simulation near the J11/5 and 3J-2S-1 resonances. This doublet causes a non-negligible elimination rate and only orbits at sufficiently low initial e value have a good chance to continue populating the family at $a \geq 3.08$ AU.

the Eos family, we have a wide range of possible outcomes, from the near total elimination of observable asteroids (J7/3 MMR) to their partial elimination (J9/4 MMR). Both produce quantitatively testable effects: termination of the family in the former case and a rate-dependent drop in the semimajor axis density of asteroids after passage of the latter. We devote Sec. 6.3.1 to a careful study of this effect.

Figure 78 shows a close up of asteroids drifting into the J11/5 and 3J−2S−1 resonances. This doublet may cause the partial elimination of bodies from the family, mainly because the bodies reaching this resonance may have had their eccentricities "pumped up" by a previous interaction with the J9/4 resonance. The probability of crossing this doublet is higher at low eccentricity. For example, Fig. 69 shows the family at $V_c = 55$ m/s first extends beyond the J11/5 and 3J−2S−1 resonances at e values.

The last resonant effect, very specific to the Eos family, is the influence of the high-order secular resonance z_1 (e.g. Milani and Knežević, 1990, 1992, 1994). While it will be described it more detail in Sec. 6.3.3, we note that many asteroids in our simulation adhere to this resonance and follow a "diagonal route" toward smaller values of proper e and i. At the same time, their location in this resonance makes

their proper e and i values oscillate with large amplitudes and a period of several My. Asteroids migrating toward large a values can also follow this secular resonance, but they are frequently blocked and removed from the family by the J9/4 MMR.

Using these simulations to set the stage for our work, we are now ready to discuss some of the more interesting features of the Eos family in greater detail.

6.3.1 J7/3 and J9/4 MMR tests

The fact that the Eos family is terminated by the J7/3 MMR (Figs. 69 and 71) is one of its most important and interesting properties. Examples of other prominent families terminated by resonances include the Koronis family (terminated by the J5/2 and J7/3 MMRs; Bottke et al., 2001) and Eunomia families (terminated by the J3/1 MMR; Morbidelli and Vokrouhlický, 2003). We note that the width of J7/3 MMR, at the mean eccentricity value of the Eos orbits, is $(\Delta a)_{7/3} \simeq 7 \times 10^{-3}$ AU. This value can be approximately interpreted in terms of a HCM velocity distance $(\Delta v)_{7/3}$ as $(\Delta a)_{7/3}/a_{7/3} \simeq (\Delta v)_{7/3}/v_{7/3}$; here $a_{7/3}$ is the position of the resonance and $v_{7/3}$ is the characteristic orbital velocity at the resonance. With this relation (that assumes no difference in eccentricity and inclination), we estimate the J7/3 MMR presents an "obstacle" of $(\Delta v)_{7/3} \simeq 10$ m/s in the HCM scheme. This estimate was obtained using the circular three-body problem. The true width of the J7/3 MMR might be little larger, but using $V_c = 55$ m/s should allow us to pick up any missing components of the Eos family that happen to reside beyond the J7/3 MMR. Even at $V_c = 70$ m/s, however, very few asteroids are found, and these objects most likely represent the background population.

We thus conclude that the Eos family does not extend beyond the J7/3 MMR, even though it tightly adheres to it along a significant range of e and i values. This configuration is inconsistent with its emplacement from the initial velocity field (e.g., Zappalà et al., 1996; Cellino et al., 1999). Instead, we conclude the initial family dynamically evolved to meet the J7/3 MMR border over time via the Yarkovsky effect. Asteroids reaching the resonance were presumably eliminated by becoming trapped in the resonance and then having their e values pumped up to planet-crossing values (Bottke et al., 2001).

To verify our claim, we placed 102 test asteroids of a given size along the outside border of the J7/3 MMR ($a > 2.96$ AU) and then used numerical integration to track the evolution of these bodies into the resonance by the Yarkovsky effect. As initial data, we used the osculating orbital elements of real Eos members located close to the J7/3 MMR. the obliquities of the objects were set to 135° for each test asteroid. The thermal parameters and rotation rates were chosen to be the same as in the numerical simulation described above. We investigated five characteristic sizes corresponding to the absolute magnitudes $H = 13, 14, 15$ and 16 (we use the mean albedo $p_V = 0.13$ for the size-magnitude conversion). Note that $H = 13$ is the approximate limiting value at which the family members adhere to the J7/3 MMR (see Fig. 71). We also note that $H = 13 - 14$ is about a current completeness limit at the location of the Eos family (R. Jedicke, personal communication). The observation incompleteness beyond this limit is, however, uncorrelated with processes we study below and thus should not affect our conclusions.

Table 20 summarizes the results of our experiment. In general, only the smallest asteroids with low e and i crossed the J7/3 MMR. For $H = 16$ bodies ($D \simeq 2.4$ km), we recorded 13 such cases (out of 102). We conclude that (i) most Eos family members cannot cross this resonance and (ii) a few km-sized asteroids with $a < 2.96$ AU might be Eos escapees. These putative objects would originate from the low e, i tail of the Eos family that is not densely populated (see below for explanation); most family members have $e \geq 0.07$. Finally, we point out that $H > 16$ bodies are hard to detect with current survey capabilities and the first populated magnitude bin is centered about $H = 15$ with lower crossing probability.

The case of the J9/4 MMR is even more interesting than the J7/3 MMR because it allows us to quantitatively test our Yarkovsky-drift model. This is because the J9/4 MMR is weak enough that many observable asteroid can jump the resonance (Bottke et al., 2000b). On the other hand, the J9/4 MMR is powerful enough to trap and eliminate some fraction of asteroids trying to cross it. Thus, the J9/4 MMR is analogous to a river with a strong current; weak swimmers are swept downstream while strong swimmers can reach the opposite bank.

The ratio of eliminated/crossing test asteroids for a given size can be compared to observations of Eos family members on both sides of the J9/4 MMR. To make this comparison, we again integrated a large number of test asteroids and let them drift into the J9/4 MMR. Here we chose the osculating orbital elements of 106 real Eos members with proper $a \in (3.023, 3.027)$ AU and gave them $H = 10 - 16$. The obliquity was set to 45°, allowing the asteroids to drift outward to encounter the J9/4 MMR.

Table 21 gives our results. As expected, significantly more asteroids, as compared to the J7/3 case,

Table 20: Statistics of Yarkovsky-drifting orbits crossing the J7/3 MMR.

H (mag)	D (km)	N	N_c
13	9.4	102	0
14	5.9	102	6
15	3.7	102	7
16	2.4	102	13

†H and D are the absolute magnitude and size of the particles (assuming $p_V = 0.13$), N is the number of integrated orbits, N_c is the number of orbits that crossed the J7/3 MMR without being scattered enough in the inclination and eccentricity to remain approximately in the appropriate range of Eos members.

Table 21: Statistics of Yarkovsky-drifting orbits crossing the J9/4 MMR.

H (mag)	D (km)	N	N_c
10	37.4	102	2
11	23.6	106	6
12	14.9	102	12
13	9.4	106	15
14	5.9	106	21
15	3.7	106	30
16	2.4	106	35

†The first three columns as in Table 20 except here for the J9/4 MMR; N_c is the number of particles that were still associated with the nominal Eos family after the passage through J9/4 MMR during their further evolution.

crossed this higher-order resonance. To compare this data with observations, however, we need to make additional assumptions. This is because of two reasons. First, the J9/4 MMR is miscentered in the family, for its position at $a_{9/4} \simeq 3.03$ AU is to be compared with the family center at $a_c \simeq 3.02$ AU. Thus, there is a priori bias to have more Eos members below the J9/4 than above and we have to correct for this effect. Second, the left side of the family is cut by the J7/3 resonance. As a result, distribution of asteroids with $a \leq a_c$ gives us only a limited information not extending below $a_{7/3} \simeq 2.957$ AU. Our procedure is as follows.

We first concentrate on the Eos region that corresponds to $a \leq a_c$, where the family's center $a_c \simeq 3.02$ AU. We denote the density distribution of members with a given H by $\mathcal{B}(a; H)$. Thus

$$\mathcal{B}(a; H) = \frac{dN}{da} \,, \tag{40}$$

where dN is number of Eos members in the semimajor axis interval $(a, a + da)$ with $a \leq a_c$ and having an absolute magnitude near H. Assuming that the initial distribution of Eos members is symmetric about a_c, we expect

$$N^{<}_{\rm exp}(H) = \int_{a_{7/3}}^{a_{9/4}} \mathcal{B}(a; H)\, da \tag{41}$$

asteroids of absolute magnitude H to reside in the Eos family on the left hand side of J9/4 MMR, thus with $a_{7/3} < a < a_{9/4}$ where $a_{7/3} \simeq 2.9757$ AU and $a_{9/4} \simeq 3.03$ AU. We also define

$$N^{>}_{\rm exp}(H) = \int_{a_{9/4}}^{2a_c - a_{7/3}} \mathcal{B}(a; H)\, da \tag{42}$$

as the number of asteroids with a given H to reside in the Eos family with $a > a_{9/4}$ (we also assume here $\mathcal{B}(a; H) = \mathcal{B}(2a_c - a; H)$ which expresses symmetry of the $\mathcal{B}$-function about a_c). Denoting $N^{<}_{\rm obs}(H)$ and $N^{>}_{\rm obs}(H)$ the numbers of truly observed family members on either size of the J9/4 MMR, and with semimajor axis value specified by limits in Eqs. (41) and (42), we finally define

$$r(H) = \frac{N^{>}_{\rm obs}(H)/N^{>}_{\rm exp}(H)}{N^{<}_{\rm obs}(H)/N^{<}_{\rm exp}(H)} \,. \tag{43}$$

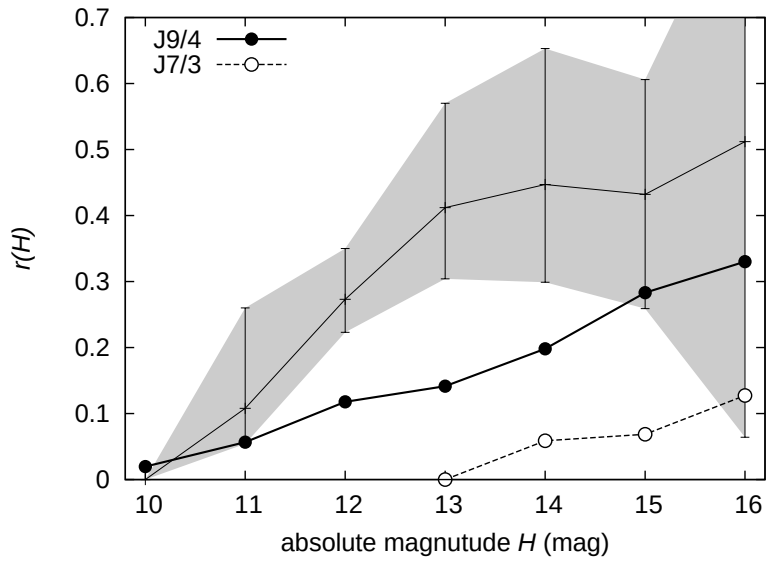

Figure 79: The thin line shows ratio $r(H)$, from Eq. (43), of the observed vs expected Eos members on the right over left hand sides of the J9/4 MMR as a function of the absolute magnitude H; we consider bodies binned in 0.5 zones of H about $H = 10 - 16$ with the last value, however, having large uncertainty due to few known objects only (see Fig. 71). The shaded uncertainty interval is based on computed $r(H)$ values for Eos family identifications with V_c in the range $50 - 60$ m/s (lower values for smaller V_c). Values $r < 1$ indicate a relative paucity of Eos members above the J9/4 MMR as regards to the population below the J9/4 MMR. The solid line shows probability to cross the J9/4 MMR for orbits migrating toward larger semimajor axis values by the Yarkovsky forces (symbols are data in Table 21). The lowest dashed line is the same for the J7/3 MMR.

The value of $r(H)$ is a measure of how the true Eos population disperses/evolves toward smaller/larger a values. In particular, if $r \simeq 1$, the family dispersion is equal on both sides of J9/4 MMR.

Figure 79 shows the ratio $r(H)$ for the Eos family identified with three HCM velocity cut-offs: 50 m/s, 55 m/s (nominal value; thin line) and 60 m/s. The fact that $r(H)$ is always smaller then unity quantitatively confirms that there is a net depletion of the observed members in the Eos family on the right side of the J9/4 MMR. We also note, that $r(H)$ is strongly size dependent, such that there is a paucity of large family members beyond the J9/4 MMR with $a > a_{9/4}$.

This observation is inconsistent with a static model where Eos family members remain in the same orbits (see the discussion in Morbidelli *et al.*1995). In our scenario, however, the $r(H)$ values are a natural outcome of Yarkovsky evolution, with larger Eos members eliminated as they try to cross the resonance. In fact, if we had an ideal model, the $r(H)$ values should equal the probability that our integrated test asteroids cross the J9/4 MMR ($c(H)$) (Table 21). For his reason, Fig. 79 shows the crossing probability $c(H)$ together with $r(H)$.

Overall, we find a rough agreement between $r(H)$ and $c(H)$. In particular, both indicate very few bodies with $H \leq 10$ should be able to cross the J9/4 MMR. The principal difference is in the crossing probabilities for $H = 12 - 14$ asteroids, where $r(H) > c(H)$. We find several possible reasons for this mismatch:

- For $r(H)$ to match $c(H)$, all asteroids must cross the resonance. Our model in Sec. 6.3.2, however, indicates that some asteroids might be initially thrown to orbits with $a > a_{9/4}$. If true, we need to modify our model assumptions. The best fit solution from Sec. 6.3.2 predicts this happens for $H \geq 13$ and it may help increasing the local population of the Eos members with $a \geq a_{9/4}$.

- Asteroids below some size threshold might reach the J9/4 MMR with smaller obliquity values and thus would migrate faster than the model asteroids in our simulation. Such a result might be produced by the YORP effect, which would have perhaps 1 Gy to work (Sec. 6.3.2). The work of Vokrouhlický et al. (2003), and previous theoretical studies, suggest $D \simeq (30 - 40)$ km Koronis asteroids complete the YORP cycle (i.e., approach an asymptotic obliquity value) in ~ 2.5 Gy. Scaling from this result, and using the mean albedo value $p_V \simeq 0.13$ for Eos family members, we estimate that $H \geq 12$ asteroids are small enough ($D \leq 15$ km) to reach near asymptotic YORP obliquity states within 1 Gy. This would efficiently shift data points corresponding to $H \geq 12$ in Fig. 79 by -0.75 while helping bring $c(H)$ and $r(H)$ closer together.

Thus, while model and observation are not in perfect agreement, we consider the results of our test satisfactory.

6.3.2 $a - H$ projection analysis

Like other families, the Eos family shows an inverted triangular pattern when its members are projected onto the plane defined by a and H: the largest asteroid resides near the mean value of a for the family, while extreme values of a are occupied by small asteroids (Fig. 71). Because it appears natural that smaller fragments received larger relative velocities with respect to the parent body during the initial ejection phase, Cellino et al. (1999) attempted to use this distribution to calibrate the unknown size-velocity distribution for the fragments. It turns out, however, that a significant portion, though not 100%, of this plot is produced by Yarkovsky evolution (Bottke et al., 2001, and below). Thus, we can only reconstruct the initial size-velocity distribution by first accounting for evolutionary processes.

As we will describe below, we used the methods described in Vokrouhlický et al. (2005) to determine the initial velocity distribution of the Eos family. Our results indicate that ejection velocities gave the Eos family an extension in a equivalent to $\sim 30-50\%$ of the spread of the observed family. The remainder was produced by Yarkovsky drift/dynamical dispersion produced by resonances. These results are in good agreement with an independent analysis of Dell'Oro et al. (2004), who suggest that the initial families were statistically smaller than the observed families by a factor of two. Our work is quantitative enough to allow us to estimate the age of the Eos family, and it complements and improves upon the results described in Nesvorný et al. (2005a).

Method. Here we briefly describe the method of Vokrouhlický et al. (2005) used to analyze the semimajor axis dispersion on an asteroid family. Consider family members plotted in the 2-D space (a, H). In order to transform this data into a 1-D space, Vokrouhlický et al. (2005) introduced the parametric relation

$$0.2\, H = \log\, (\Delta a / C) \tag{44}$$

between H and Δa. Here $\Delta a = a - a_{\rm c}$, where $a_{\rm c}$ is the center of the family and C is a free parameter that can be positive or negative. The family can then be characterized by a distribution of C values. We define the distribution function as:

$$\mathcal{D}(C) = \frac{dN}{dC}\ , \tag{45}$$

where dN is the number of family asteroids in a strip of (a, H) generated by changing C in the range $(C, C + dC)$. This approach allows the function $\mathcal{D}(C)$ to contain all of the family's data. We can then test various family configuration models in (a, H) space by comparing them with the observed $\mathcal{D}(C)$ distribution (using a pseudo-χ^2 methods).

The choice of the template function (44), and the related distribution (45), instead of the simple distribution $\mathcal{B}(a; H)$ of semimajor axis values has been motivated by simple models involving purely either Yarkovsky dispersion or fragment ejection with velocity strictly inversely proportional to their size. Both would yield $\mathcal{D}(C)$ constant. So any deviation from a uniform $\mathcal{D}(C)$ distribution could be translated into a deviation from these "toy models". Luckily, these go in a rather opposite way. A static model, with no dynamical evolution of the family, but velocity field either anisotropic and/or with a velocity dispersion for fragments of a given size, give typically $\mathcal{D}(C)$ concentrated near the origin or with a single maximum, asymmetric to the origin. Conversely, the model where combined Yarkovsky and YORP dynamical evolution of the family plays an important role results in $\mathcal{D}(C)$ that has two maximum values symmetrically offset from the origin $C = 0$.

Yarkovsky/YORP Family Evolution Model. Figure 80 shows $\mathcal{D}(C)$ for the Eos family identified using the $V_{\rm c} = 55$ m/s with $a \le a_{\rm c}$ (to avoid problems with the J9/4 MMR). The ordinate is the number $N_{\rm obs}(C)$ of Eos members in the interval $(C, C + \Delta C)$, with $\Delta C = 4 \times 10^{-6}$ AU (there are 41 contributing bins/data points in this distribution). To match up the features in the plot as best as possible, we assumed $a_{\rm c}$ was uniformly distributed between 3.015 AU and 3.025 AU. These values are close to (221) Eos.

We find that $\mathcal{D}(C)$ has a maximum at $C \simeq -7.5 \times 10^{-5}$ AU. The value $\mathcal{D}(0)$ is roughly half of the maximum value. The error bars defined using $\sqrt{N_{\rm obs}(C)}$ in each C bin. We discarded 3 objects, (1845) Helewalda, (8340) Mumma, (9711) Zeletava, from our analysis that had their $|C|$ value larger than 1.6×10^{-4} AU. In Fig. 71, they form a "triangle" of bodies with $a \le 2.98$ AU and $H \le 12$ that are separated from the bulk of the family. We suspect these objects are objects interlopers in the family.

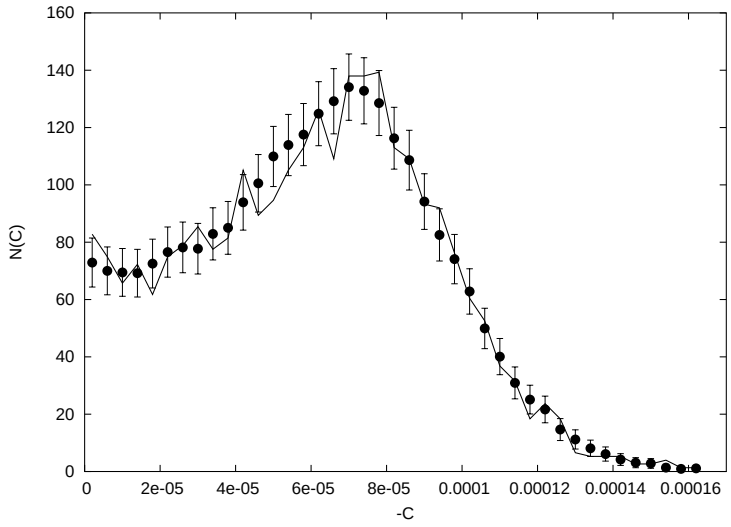

Figure 80: Comparison of the observed and modeled distribution $\mathcal{D}(C)$ for the Eos family; here we use model with size-independent velocity $V_{\rm SD}$ that charaterizes dispersal of the initial fragments along all directions. We actually show directly number $N_{\rm obs}(C)$, and $N(C)$, of asteroids within a strip $(C, C+\Delta C)$ for $\Delta C = 4\times10^{-6}$ AU used in the target function $\Psi_{\Delta C}$ in Eq. (50). Symbols are the observed bodies $N_{\rm obs}(C)$ with the assigned formal uncertainty $\sqrt{N_{\rm obs}(C)}$; only the left branch of the family with asteroids having $a \leq a_{\rm c}$ is used here. This is an averaged result where $a_{\rm c}$ is assumed to be uniformly distributed in the range $(3.015, 3.025)$ AU. Broken solid line is our modeled family that minimizes the target function $\Psi_{\Delta C}$.

Indeed, in Sec. 6.4 we show that the first 2 are spectrally alien to the KTD-types common among Eos family members.

The $\mathcal{D}(C)$ maximum in Fig. 80 is produced by the unusual (a, H) distribution of the Eos family (Fig. 71), where small asteroids populate regions near the outskirts of the family and leave the the center underpopulated. This distribution is unlikely to have been created by any reasonable ejection velocity field. Instead, we believe this artifact was produced by Yarkovsky/YORP evolution. Recall that the Yarkovsky-O'Keefe-Radzievskii-Paddack (YORP) effect (e.g. Rubincam, 2000; Vokrouhlický and Čapek, 2002; Bottke et al., 2002b) is a variant of the Yarkovsky effect that can modify the rotation rates and obliquities of irregularly-shaped bodies. In the Eos family, YORP preferentially tilts the obliquities of family members toward extreme values (Čapek and Vokrouhlický, 2004) that, in turn, help increase Yarkovsky da/dt rates. Hence, Yarkovsky/YORP should move small asteroids from the center of the family to more distant a values.

To test this hypothesis, we constructed a simple numerical model that tracked the evolution of test Eos family asteroids. Our goal was to quantitatively match the observed distribution $\mathcal{D}(C)$. Its main features and parameters are as follows:

- The initial orbits for our Eos family members were based on a test velocity distribution. The velocity components V_R, V_T and V_N along the radial, transverse, and normal directions with respect to the parent body's orbit were given the same Gaussian distribution with standard deviation $V_{\rm SD}$. We consider two models for $V_{\rm SD}$: (i) It is a size-independent free parameter with values of the order $\simeq 0-100$ m/s, or (ii) $V_{\rm SD} = V\,(5\,{\rm km}/D)$, where V is a free parameter of the model. The number of fragments used in our simulations is the same as number of observed asteroids in the family. They were assigned the same H as the observed objects, with H converted to D using two methods (Tedesco et al., 2002): (i) all asteroids were given albedo $p_V = 0.13$ corresponding to the mean value of the Tedesco et al. Eos sample, and (ii) we assign random p_V to individual asteroids that follow the observed distribution of p_V (Fig. 81). In the latter case, we ran several simulations because the size of each asteroid is a statistical quantity. The results were then averaged over several simulations.

- The test asteroids are assigned initial diameters, orbital elements, obliquity (ϵ), and angular velocity of rotation (ω). The initial orientation of the spin axes is random in space. We assume ω follows a Gaussian distribution peaked at period $P = 8$ h (e.g. Binzel, 1988).

- The orbital evolution of each of the fragments is tracked individually, with Yarkovsky drift rates

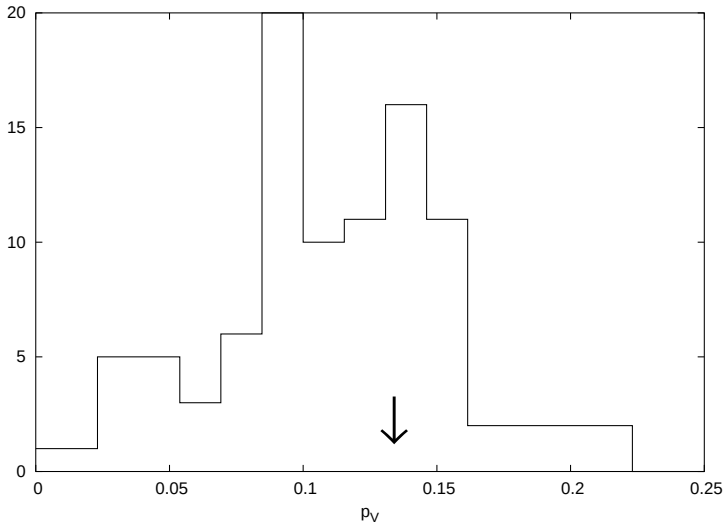

Figure 81: Distribution of the geometric albedo values p_V for Eos members determined by Tedesco et al. (2002); abscissa is p_V, ordinate is number of asteroids with p_V in a given bin. The arrow indicates the mean value.

(e.g. Vokrouhlický, 1998, 1999):

$$\frac{da}{dt} = \kappa_1 \cos\epsilon + \kappa_2 \sin^2\epsilon \ . \tag{46}$$

Here κ_1 and κ_2 are functions depending on surface thermal parameters and asteroid size. In accord with the numerical simulation above, we used the following set of thermal constants: thermal conductivity $K = 0.005$ W/m/K, specific heat capacity $C_p = 680$ J/kg/K, and surface/bulk densities of 1.5 and 2.5 g/cm^3, respectively. Eq. (46) assumes (i) our model asteroids reside on a circular orbit and (ii) that we can use a restricted, linearized analysis to describe heat diffusion in the asteroid's surface layers. Our tests indicates that Eq. (46) is within a 2 of more sophisticated treatments of Yarkovsky/YORP.

- The two rotation state parameters, ϵ and ω, undergo YORP evolution according to:

$$\frac{d\omega}{dt} = c_{\rm YORP}\, f(\epsilon) \ , \tag{47}$$

$$\frac{d\epsilon}{dt} = c_{\rm YORP}\, \frac{g(\epsilon)}{\omega} \tag{48}$$

(e.g. Vokrouhlický and Čapek, 2002; Čapek and Vokrouhlický, 2004). The f- and g-functions here are the median strength of the YORP torques derived by Čapek and Vokrouhlický (2004) for asteroids with the surface thermal conductivities described above. We also introduce a free parameter $c_{\rm YORP}$ by which we can multiply the f- and g-functions in Eqs. (47) and (48); this "fudge" factor helps account for the uncertainties in modeling the YORP effect.

- We assume that non-catastrophic collisions can reorient the spin vectors of the test asteroids with a timescale:

$$\tau_{\rm reor} = B\,(\omega/\omega_0)^{\beta_1} (D/D_0)^{\beta_2} \ . \tag{49}$$

Here $B = 84.5$ ky, $\beta_1 = 5/6$, $\beta_2 = 4/3$, the reference size $D_0 = 2$ m, and the rotation frequency ω_0 corresponding to a rotation period of 5 hr. This basic approach was pioneered by Farinella et al. (1998). We ignore for now the effects of disruptive collisions.

With a given initial configuration of the family, we run our code for a time T, ranging from 0.5 to 2 Gy, and we let the family evolve by the Yarkovsky/YORP effects. Our solutions are a function of three parameters: T, V, and $c_{\rm YORP}$. To determine the quality of the fit between the simulation and the observed Eos family, we define a pseudo-χ^2 target function

$$\Psi_{\Delta C} = \sum_{\Delta C} \frac{\left(N(C) - N_{\rm obs}(C)\right)^2}{N_{\rm obs}(C)} \ . \tag{50}$$

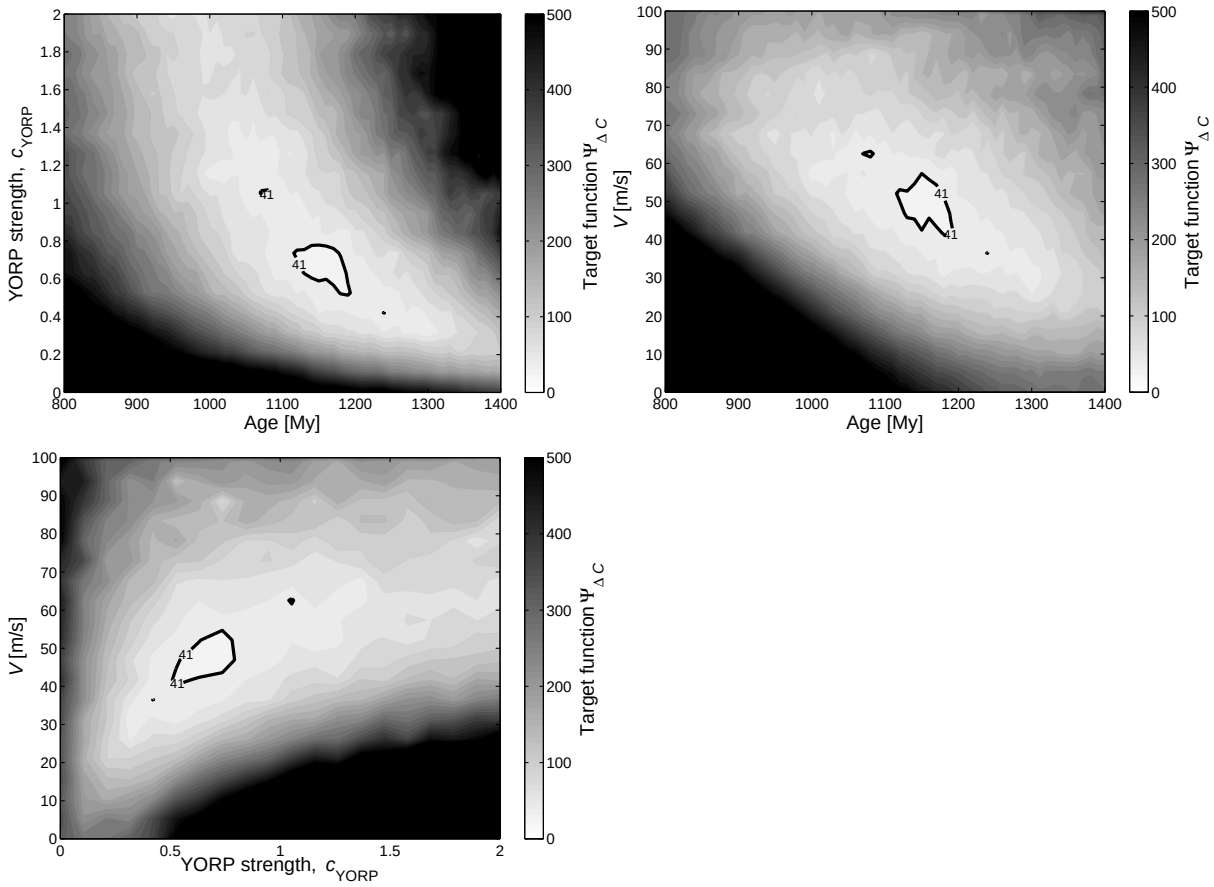

Figure 82: Projection of the target function $\Psi_{\Delta C}$ onto planes defined by the model parameters: (a) T vs. $c_{\rm YORP}$, (b) T vs. V, and (c) $c_{\rm YORP}$ vs. V (as in the previous figure $V_{\rm SD} = V$ is size-independent). Each time we plot the smallest $\Psi_{\Delta C}$ value along the ray of the third parameter (i.e. in the first case we fix T and $c_{\rm YORP}$ values of seek the minimum value for all tested values of V). We show shaded contours of $\Psi_{\Delta C}$ with the value indicated by a bar on the right; the best fit value is $\Psi_{\Delta C} = 27.8$. This compares to 41 bins in ΔC, which set the formal $1\,\sigma$ uncertainty level (shown in bold curve).

The errors assigned to the number $N_{\rm obs}(C)$ in a given bin $(C, C+\Delta C)$ is $\sqrt{N_{\rm obs}(C)}$. $N(C)$ is the simulated number of asteroids in the appropriate C-bin. Our procedure seeks to minimize $\Psi_{\Delta C}(T, V, c_{\rm YORP})$ by varying the 3 parameters over a large range of values. Admissible solutions are characterized by $\Psi_{\Delta C}$ values of the order equal to the number of bins in C (41 in our case), while solutions giving much larger $\Psi_{\Delta C}$ are incompatible with the observed family.

Results. For simplicity, our first simulations assumed the test asteroids had a single albedo value $p_V = 0.13$ and that $V_{\rm SD} = V$ is size-independent. Figure 82 shows contour plots of $\Psi_{\Delta C}$ projected onto several 2-D parameter planes: T vs. $c_{\rm YORP}$, T vs. V and $c_{\rm YORP}$ vs. V. The best-fit solution for $N(C)$, together with the observed data $N_{\rm obs}(C)$ and their formal error-bars, is shown in Fig. 80. Each time we picked the best $\Psi_{\Delta C}$-value along the suppressed dimension. The "critical" isoline value of 41 is plotted in bold; recall this value formally corresponds to solutions that barely match the observed family at the chosen 1σ-interval from all data points.

The best-fit solution is: $T = 1160^{+40}_{-100}$ My, $c_{\rm YORP} = 0.7^{+0.3}_{-0.2}$ and $V = 52^{+10}_{-14}$ m/s. Note that the 3 parameters are not uncorrelated in our solution, such that stronger YORP (i.e. larger $c_{\rm YORP}$) pushes the family age T to smaller values. The least correlated are $c_{\rm YORP}$ and V. The best-fit V is compatible with values expected from the hydrocode modeling. The initial family thus had about half of its current a spread.

The $c_{\rm YORP} \simeq 0$ value is strongly incompatible with observations; this means that YORP is needed to match observations. Its strength, however, is poorly constrained. The best-fit value of the target function (50) is $\Psi_{\Delta C} = 27.8$, smaller than 41 and statistically significant (assuming our approximations

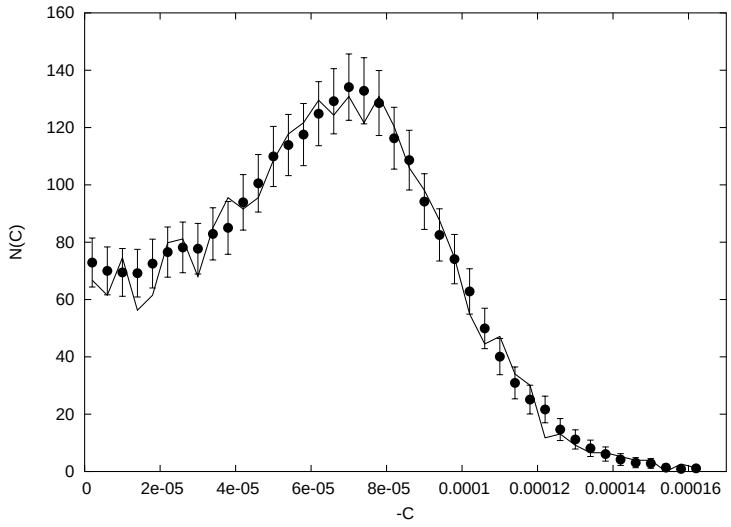

Figure 83: The same as in Fig. 80 but here for the model where $V_{\rm SD} = V\,(5\,{\rm km}/D)$ is size-dependent.

are reasonable; note the value of the standard goodnes-of-fit parameter $Q = 0.89$ for our solution, see, e.g., Press et al., 2001).

Figures 83 and 84 show the best fit solution for $N(C)$ and 2-D contour plots of the target function $\Psi_{\Delta C}$ in case of our more refined model where $V_{\rm SD} = V\,(5\,{\rm km}/D)$. Now V is a solved-for parameter with the ejection velocity set for $D = 5$ km fragments. Our best-fit solution is: $T = 1150^{+150}_{-100}$ My, $c_{\rm YORP} = 1.1^{+0.9}_{-0.7}$ and $V = 93^{+25}_{-20}$ m/s. The uncertainty limits are derived from the $\Psi_{\Delta C} = 41$ contour plot. The minimum target function, $\Psi_{\Delta C} = 26.2$, is below the admissible limit of 41; hence we consider it statistically significant and slightly better than the previous solution. The general features of the solution are similar to the previous one. In our opinion, two results are of particular interest: (i) the estimated age of the Eos family consistently spans the same interval of values, and (ii) the estimated YORP strength is within a factor $0.5 - 1$ of the modeled value by Čapek and Vokrouhlický (2004).

In the previous tests we assumed the luminosity of the Sun was constant. Evolutionary models of the solar interior, however, suggest the Sun was $\sim 25\%$ fainter some 4 Gy ago (e.g. Bahcall et al., 2001; Table II). A smaller radiation flux in the past should produce weaker thermal Yarkovsky/YORP effects and thus may modify our conclusions. For that reason, we have rerun our previous simulations to account for a time-variable solar luminosity ($L(t)$):

$$L(t) \simeq L_0 \left[1 + 0.3 \left(1 - \frac{t}{t_0}\right)\right]^{-1} , \qquad (51)$$

where L_0 is the current current solar luminosity, $t_0 \simeq 4.57$ Gy is the age of the Sun, and t is time (in Gy) measured from the origin of the Solar system (e.g. Bertotti et al., 2003; Chap. 7). Our results indicate that while the best-fit values for $c_{\rm YORP}$ and V are comparable to our previous results, the estimated age T of the family is slightly increased: $T = 1200^{+120}_{-100}$ My. Note that according to Eq. (51), the mean solar luminosity over the past Gy was about 4% lower than today, which corresponds to a $\simeq 4\%$ increase in the Eos family's age. Thus, for a moderately young family like Eos, the effect of a fainter Sun in the past appears to be smaller than other model uncertainties.

Finally, we tested how our results change as a function of asteroid geometric albedo p_V. To do so, we used a p_V distribution determined for 98 Eos members (selected from our nominal family at HCM $V_{\rm cut} = 55$ m/s) by Tedesco et al. (2002) - Fig. 81. Note that the data show a considerable spread about the mean value of $p_V = 0.13$, with some skew toward values that are smaller than the median value. We ran 10 simulations similar to those above using the mean ejection velocities of fragments inversely proportional to their D (our second model above). Our asteroid diameters were determined by randomly assigning p_V values.

We found that our best fit values of $\Psi_{\Delta C}$ ranged from 17 to 26, which means our solutions were a reasonable fit with observations. Considering the mean value of the best-fit solution for each of the free parameters (weighted by the best-fit value of the target function), and an envelope of the $\Psi_{\Delta C} = 41$ region in the parametric space, we obtain $T = 1300^{+150}_{-200}$ My, $c_{\rm YORP} = 0.7^{+1}_{-0.5}$ and $V = 70^{+20}_{-20}$ m/s. In

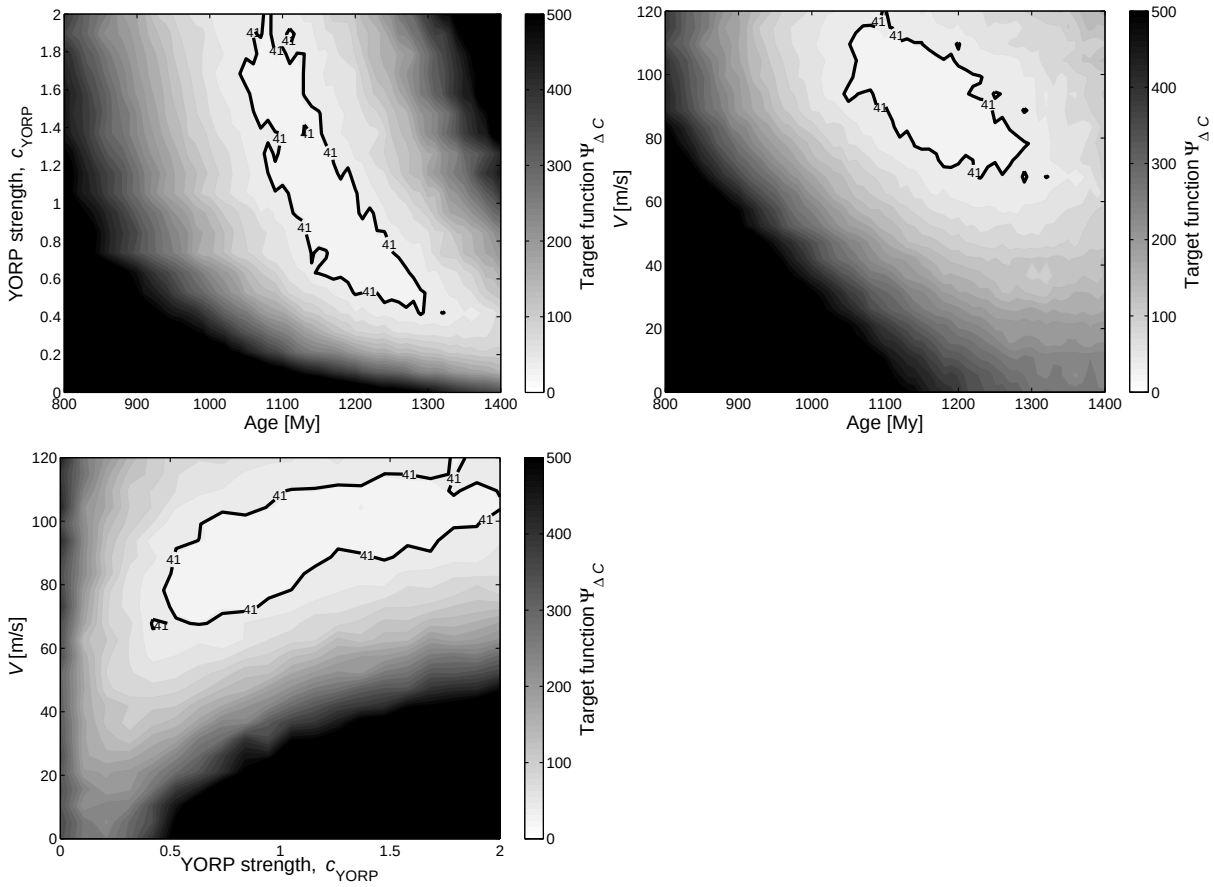

Figure 84: The same as in Fig. 82 but here for the model where $V_{\rm SD} = V\,(5\,{\rm km}/D)$ is size-dependent. The best-fit value is $\Psi_{\Delta C} = 26.2$.

comparison with the fixed albedo $p_V = 0.13$ model, we find that our family's age T slightly increased. This is because lower albedo values imply larger asteroid sizes and thus slower Yarkovsky da/dt rates (and slower YORP torques).

6.3.3 Asteroids in the z_1 secular resonance

So far, there has been little work on how high-order secular resonances affect the long-term fast of asteroid families. In part, this is because the topic is analytically and numerical challenging from the orbital dynamics point of view. Milani and Knežević (1990, 1992, 1994) and Knežević and Milani (2003) have been pioneers in the investigation of high-order secular resonances. They found that the Eos family is intercepted by the $z_1 = g + s - g_6 - s_6$ resonance.[20] While no significant effects on family evolution are expected on My timescales, Milani and Knežević (1990, 1992) speculated that they might affect the structure of the Eos family over longer timescales. Note that this hypothesis has been cited several times over the last 15 years (e.g. Zappalà et al., 1990; Marzari et al., 1995) but no one has yet tested it.

The second reason why the high-order secular resonances received a little attention so far is that the asteroid families were assumed by many to deviate from simple models for other, more obvious reasons such as uncertain geometry of the initial velocity field. These were expected to mask any noticeable trace of the dynamics in weak secular resonances. New results, however, suggest the asteroids drifting by Yarkovsky effect into these resonances can follow unusual orbital paths. For example, Bottke et al. (2001) showed that Koronis family asteroids experience a significant jump in proper eccentricity ($\simeq 0.025$) when

[20] This resonance causes the secular angle $\varpi + \Omega - \varpi_6 - \Omega_6$ to librate rather than circulate on a typical timescale of 3−5 My; here ϖ is longitude of pericenter and Ω is longitude of node of the asteroid, while ϖ_6 and Ω_6 are the same parameters for Jupiter. In an analytical theory, such as Milani and Knežević (1990, 1992), the $g + s - g_6 - s_6$ frequency appears as a small divisor associated with this resonance. More in general, a z_k resonance corresponds to a divisor $k\,(g - g_6) + s - s_6$ with an integer k. All z_k resonances are secondary modes of the $g - g_6$ secular resonance and thus have larger width than other nonlinear secular resonances of the same order (e.g., Milani and Knežević, 1994; Carruba et al., 2005).

they drift into (and interact with) the $g + 2g_5 - 3g_6$ secular resonance.

Below we will show that the shape of the Eos family has also been affected by secular resonances. As asteroids migrate in the proper element space by the Yarkovsky effect, they become captured by the z_1 secular resonance and are driven to a specific region at the outskirts of the family (Fig. 72).

Theoretical basis. A fundamental model used to track a perturbed asteroid's motion is the restricted three-body problem of Sun-Jupiter-asteroid (e.g. Morbidelli, 2002). Many aspects of asteroid motion, including fine perturbations, can be studied within this framework. Each of the various problems, such as motion in/near mean motion or secular resonances, is best understood if properly chosen variables are used. We thus start with a brief review of the variables tailored to understand the z_1 resonance.

The restricted three-body problem is a 4-degree of freedom autonomous system with the first 3-degrees describing 3-D motion of the test body (asteroid) and the last degree being Jupiter's orbital longitude (removing time-dependence due to Jupiter's motion). In a Hamiltonian approach, the asteroid-related degrees of freedom can be described using Delaunay variables $(L, G, H; l, g, h)$ or variables derived from them by canonical transformations (e.g. Morbidelli, 2002). For instance, we can choose

$$\begin{pmatrix} L & l \\ G & g \\ H & h \end{pmatrix} \rightarrow \begin{pmatrix} \Lambda = L & \lambda = l + g + h \\ \Sigma = L - G & \sigma = -g - 2h \\ \Theta = 2G - H - L & \theta = -h \end{pmatrix} , \tag{52}$$

where the new canonical variables $(\Lambda, \Sigma, \Theta; \lambda, \sigma, \theta)$ replace the original Delaunay set.

Representations of Jupiter's motion become more involved when we include perturbations with Saturn; these produce secular variations of its orbital elements. This extends the problem by at least 3 degrees of freedom (e.g. Moons et al., 1998; Morbidelli, 2002); notably nonsingular elements $(e' \cos \varpi', e' \sin \varpi'$; $\sin(I'/2) \cos \Omega', \sin(I'/2) \sin \Omega')$ of Jupiter are going to be expressed as harmonic functions of the secular angles $\lambda_5 = g_5 t$, $\lambda_6 = g_6 t$ and $\lambda_{16} = s_6 t$ (here g_5, g_6 and g_{16} are the corresponding fundamental frequencies of the planetary system; e.g. Morbidelli, 2002). The conjugated momenta to these angular variables are Λ_5, Λ_6 and Λ_{16}. Using another canonical transformation

$$\begin{pmatrix} \Sigma & \sigma \\ \Lambda_6 & \lambda_6 \\ \Lambda_{16} & \lambda_{16} \\ \cdots & \cdots \end{pmatrix} \rightarrow \begin{pmatrix} -\Sigma & -\sigma - \lambda_6 - \lambda_{16} \\ \Sigma - \Lambda_6 & -\lambda_6 - \lambda_{16} \\ \Lambda_6 - \Lambda_{16} & -\lambda_{16} \\ \cdots & \cdots \end{pmatrix} , \tag{53}$$

we obtain variables suitable to analyze orbital motions in the z_1 resonance because $\Sigma' = -\Sigma$ and $\sigma' = -\sigma - \lambda_6 - \lambda_{16}$ appear to be resonant momentum and critical argument of this secular resonance.

In a simplified model where all other degrees of freedom are eliminated by averaging, the resonance becomes represented by a 1-D model in resonant variables (Σ', σ'). In particular, σ' circulates outside the resonance with secular frequency $-\dot{\sigma} - g_6 - s_6$ (overdot is a time derivative), while σ' librates inside the resonance, i.e. near the hypersurface $\mathcal{Z}_1 : -\dot{\sigma} - g_6 - s_6 \simeq 0$. Because $\Sigma' = \sqrt{a}\,(1 - \sqrt{1 - e^2})$, and a is constant due to the eliminated variable λ, the resonance produces long-term variations in eccentricity e. Moreover, because Θ is also constant, due to the elimination of θ, we have a quasi-integral $\sqrt{a(1 - e^2)}\,(2 - \cos I)$. Thus the long-term variations of orbital eccentricity e and inclination I are resonantly coupled and the inclination is given long-term variations.

Difficulties arise when non-gravitational forces like the Yarkovsky effect are included in the model. In the simplest representation, we can only retain the major secular effect, namely a steady a change. Because the characteristic timescale for this perturbation is long, even when compared to secular dynamics timescales in the weak z_1 resonance, one must still assume a is constant during one resonant cycle of σ' and investigate the evolution of the system under slowly (adiabatically) changing parameter a. This approach could, in principle, yield capture probabilities in the z_1 resonance for bodies with different da/dt rates. Once in the resonance, however, the asteroids show coupled oscillations in e and I superposed over a slow migration along the $\mathcal{Z}_1$ hypersurface. This takes place until the asteroid reaches conditions that allow it to jump out of the resonance.

z_1 resonance in the Eos family. To examine evolution inside the z_1-resonance, we first need to identify those Eos family asteroids currently inside the resonance. This was accomplished by taking our nominal family with 4394 members and numerically integrating their orbits for 10 My. Our goal was to compute the behavior of the critical angle σ'. To do this accurately, we excluded Yarkovsky forces from our integrations. We output the mean orbital elements of the asteroids every 1.5 ky using Fourier

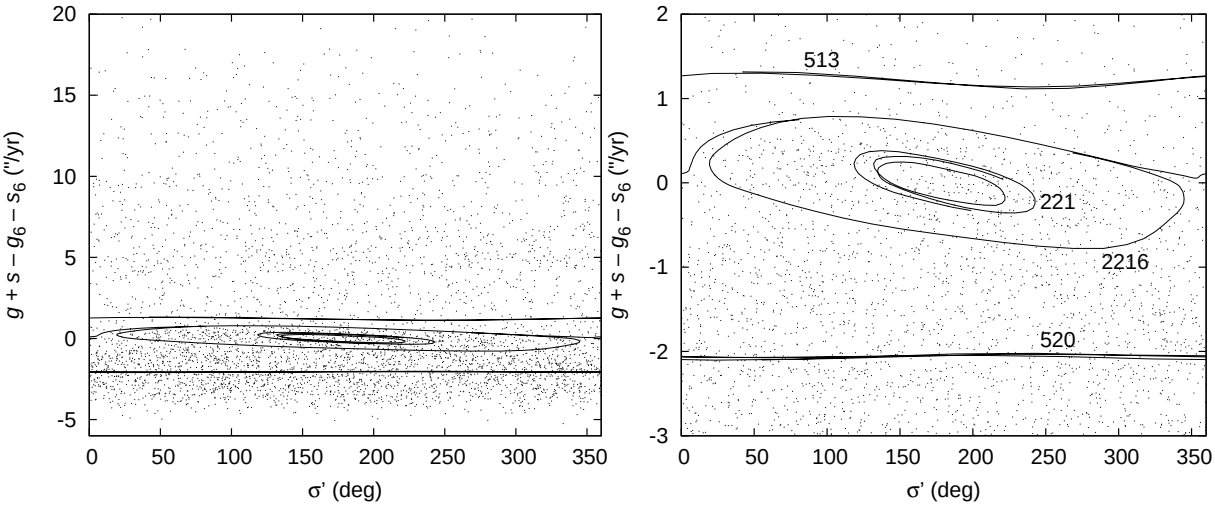

Figure 85: Configuration space of the z_1 secular resonance: critical angle σ' at the abscissa and secular frequency $g + s - g_6 - s_6$ on the ordinate. Left: all family asteroids included; right: zoom of the previous figure near z_1 resonance zone. Solid curves show evolution tracks of several Eos-family asteroids during our 10 My orbital integration (high-frequencies have been eliminated). The innermost librating orbit is (221) Eos itself, while other asteroids show and example of transitions between libration and circulation –(2216) Kerch– and circulations – (513) Centesima and (520) Franziska. Dots are current position of Eos asteroids (HCM family with $V_c = 55$ m/s). The negative value of $g + s - g_6 - s_6$ frequency occurs when orbital semimajor axis is smaller than the z_1 libration centre for given value of the eccentricity and inclination; thus the bulk of the family (adhering eventually to the J7/3 MMR; see Fig. 72) projects to this part of our plot.

filtering of high-frequencies taken from the osculating orbital elements. The mean orbital elements were then processed to identify asteroids residing in the z_1 resonance. In particular, we used a running window filter that was 750 ky wide and had steps of 100 ky.

In each interval, we Fourier-analyzed the time series of the non-singular orbital elements and determined the frequency and phase of the proper and forced terms. Among the forced terms, we were principally interested in isolating the g_6 and s_6 frequencies and their associated phases. The phases were used to construct the critical angle σ' of the resonance, where ϖ and Ω are substituted by the phases of the corresponding proper terms in non-singular orbital elements, and ϖ_6 and Ω_6 are the phases of the corresponding forced terms. We replaced the momentum Σ' with the frequency combination $g+s-g_6-s_6$ and plotted asteroid tracks in the configuration space of these two variables.

Figure 85 shows several examples including asteroid (221) Eos that is currently trapped in the z_1 resonance (e.g. Milani and Knežević, 1990, 1992). We show the motion of asteroids whose (i) σ' librates at small amplitudes, which allows them to residing near the center of the resonance, (ii) σ' alternates between libration and circulation, which allows them to reside near the separatrix of the resonance, and (iii) σ' circulates. Typical libration periods of σ' inside the resonance are $3 - 5$ My, with the resonance width ~ 0.8 arcsec/yr.

Figure 72 helps to translate this information into a portion of the proper element space affected by the z_1 resonance. Interestingly, we find that it stretches over a non-negligible fraction of the Eos family. We find that 13% (575 out of 4394) of all Eos family members are captured inside this resonance. (As an aside, we also found that $\simeq 1.5\%$ of Eos family members both reside and librate in the $g + s - g_5 - s_7$ secular resonance. This is because this resonance is much weaker than the z_1; Milani and Knežević, 1990, 1992). Figure 86 shows the distribution of the critical angle σ' of all 4394 asteroids associated with the family. Unlike previous studies, we show the distribution of σ' separately for Eos members residing inside (top) and outside (bottom) the z_1 resonance. The first is non-uniform because σ' values are naturally confined near the stable resonant point at 180°. However, when non-resonant Eos members are considered, we find that σ' distribution is uniform up to random fluctuations.

For sake of completeness, we also show a σ' histogram for the 58 Eos family asteroids known to Brouwer (1951): dashed histogram in both panels of Fig. 86. Like Brouwer, we also find they show some degree of non-uniformity. The reason is that large asteroids near (221) Eos are preferentially located inside the z_1 resonance (the same applies, to a lesser degree, to data reported by Milani and Knežević, 1992). Hence the previously-reported non-uniform distribution of σ' is a selection effect unrelated to the age of the

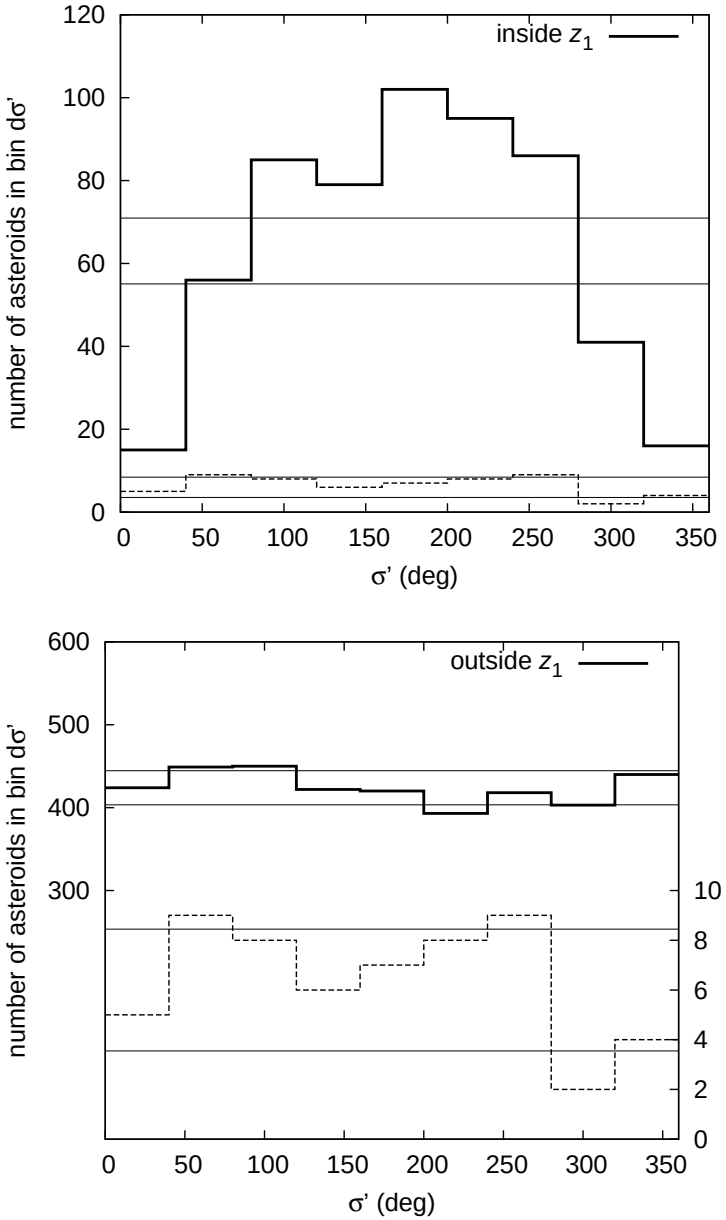

Figure 86: Distribution of the critical angle σ' values determined for members of our nominal Eos family (solid line and left ordinate). Previous analyses, e.g. Brouwer (1951) or Milani and Knežević (1992), found it non-uniform and suspected a young age of the family; the dashed curve (and right ordinate in the bottom panel) in both figures reconstructs the similar quantity for the 58 Eos members known to Brouwer (1951). Here, we show that (i) with modern data, many more asteroids added in the family, the distribution is fairly uniform, and (ii) the anomaly reported by the previous studies is due to selecting asteroids preferentially inside the z_1 resonance, for which σ' is limited to their libration interval (and the σ' values are preferentially found near extremes of the libration cycle). This is proved by showing the σ' distribution separatelyfor asteroids which were found to librate in the z_1 resonance (top), and for those which are outside the resonance (bottom). In each case the horizontal lines show the $\sqrt{N_m}$-uncertainty strip about the mean value N_m of the uniform distribution. In the bottom panel, where asteroids residing in the z_1 were eliminated, the fluctuations of N_m fall in this uncertainty strip.

family.

We found that the z_1 produced no significant instability among Eos family members over our 10 My integration. Nevertheless, as shown in Fig. 87, it produces a non-negligible spread of the family in eccentricity and inclination, likely contributing to solve the old problem of the Eos family (see Sec. 1). This is partly surprising given the weakness of the resonance: for a near-separatrix case, such as (2216) Kerch, the synthetic proper eccentricity, determined from an integration spanning $\simeq 1$ My, may oscillate in time by nearly 0.02, about a half of the total eccentricity extension of the family. The same applies to the inclination.

The role of the z_1 resonance changes and strengthens, however, when Yarkovsky forces are taken into account. As demonstrated by our numerical integration above (see also Vokrouhlický and Brož, 2002), migrating asteroids encountering the z_1 resonance can become captured for several tens to hundreds of My. During this time, its orbital parameters slide along the z_1 resonance while its semimajor axis changes. Hence, Eos family members moving toward the Sun experience a decrease in their mean a, e, I values. This populates the anomalous tail of the Eos family (Sec. 6.2). Investigating Eos family members whose proper elements satisfy $a \leq 3.01$ AU, $e \leq 0.065$ and $\sin i \leq 0.17$, we found that 67% (246 out of 366) reside in the z_1 resonance. This high fraction, when compared to the rest of the Eos family, suggests they reached their current orbits via an interaction between the resonance and Yarkovsky-induced drift.

6.4 Additional data and observations

In order to check our results, we conducted spectroscopic observations of about a dozen asteroids in the Eos zone. Our objective was to determine whether particular asteroids were related to the KTD-types seen among the majority of Eos family members or whether they were more likely to be interlopers in the family. In one case, we investigated asteroids located inside the z_1 secular resonance with anomalously small values of proper e, i as compared to the other Eos family members (Sec. 6.3.3). In a second case, we examined suspected interlopers in the Eos family that were far from from the family members plotted in Fig. 3. We start by describing our own observations in Sec. 6.4.1. We then add to this database using an updated SDSS color information in Sec. 6.4.2.

6.4.1 Spectroscopy

Asteroids inside the z_1 resonance. Table 22 summarizes our target asteroids and the observational circumstances. The asteroids inside the z_1 stream are generally small, so their spectroscopy is challenging even with moderately large instruments. Our sample of the observed asteroids is random, mainly derived from observational possibilities from available instruments and times. The Kitt Peak National Observatory (KPNO) and Palomar observations reported here were acquired both through a dedicated program for this work and also as targets of opportunity during the ongoing Small Main-Belt Asteroid Spectroscopic Survey (SMASS). The KPNO observations used the RCSP spectrometer on the Mayall 4-m telescope, generally covering the spectral range $500 - 920$ nm, and the Palomar observations used the Double Spectrograph on the Hale 5-m telescope and generally covered the spectral range $320 - 950$ nm. Details of the observations and reductions can be found in Binzel et al. (2004), which used the same telescopes and instruments and had identical data reduction and analysis techniques. To summarize, well-known solar-type stars were observed frequently during the night interspersed with target objects in order to account for the influence of the solar spectrum and the terrestrial atmosphere on the target asteroids. Commonly used IRAF routines and packages[21] were used to extract the spectra of the asteroids and stars, and a set of mean extinction coefficients appropriate for each observing site was used for additional corrections. The resulting asteroid/star ratios were then tied into the spectral taxonomy of Bus and Binzel (2002a,b).

Figure 88 shows the collected reflectance spectra for our 4 objects, indicating three are T-class and one –(62948) 2000 VE32– is an X-type. As discussed in Sec. 6.2.2, the T-types are compatible with the bulk Eos family and thus we interpret these 3 objects as potential Eos members that were pushed to their present orbits by Yarkovsky forces. The X-type asteroid in the same zone appears to be an interloper object caught in the z_1 resonance. The $\sim 25\%$ fraction of alien asteroids in our observing sample, though not statistically significant, may correspond to the overall $\sim 25 - 30\%$ interloper fraction inside the Eos family inferred from spectroscopic observation of large members (see Sec. 6.2.2). In fact, we might even expect higher interloper fraction among small Eos members because of shallower exponent of the families' size distribution as compared to the background population (Morbidelli et al., 2003).

[21] See Tody (1986) and `http://iraf.noao.edu/iraf-homepage.html` for details.

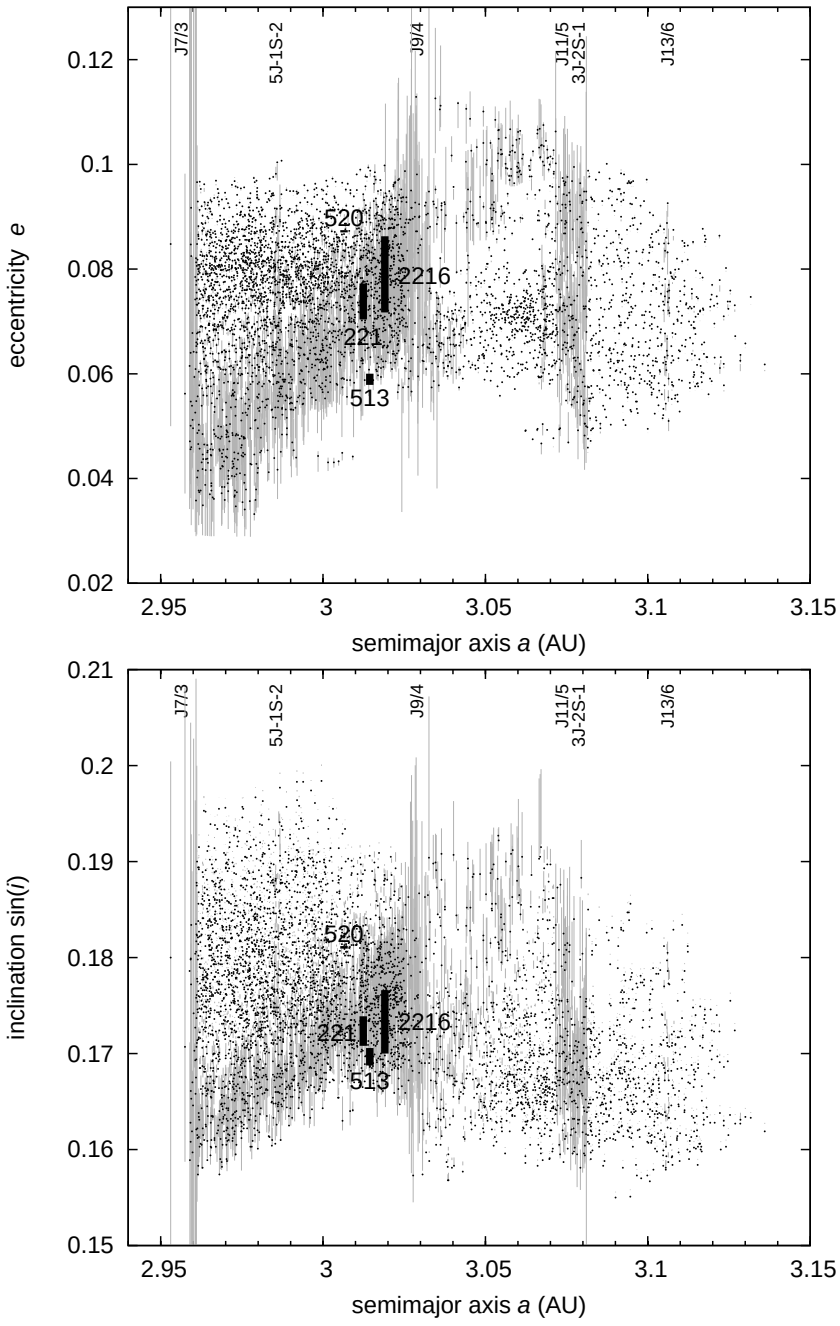

Figure 87: Stability of the proper elements for the nominal Eos family. In black dots we show the nominal family from proper elements of the `AstDyS` catalogue, used also in previous parts of this paper. In grey lines we show variation of the synthetic proper elements determined from our 10 My integration for all 4394 members. In particular, the grey intervals delimit minimum and maximum values of the proper elements (eccentricity e and inclination $\sin i$) determined by Fourier filtering on a running 700 ky wide window in our integration. The principal diagonal grey strip in both plots is the effect of the z_1 secular resonance. In this case, the period of e and $\sin i$ oscillation is several My (e.g. Fig. 85). Note the amplitude of the z_1 driven variation of the proper orbital elements is surprisingly large (as opposed to the resonance weakness) and it amounts to a fair fraction of the whole dispersion of the family in the appropriate elements. The thick bars are the four asteroids from Fig. 85; obviously, the largest amplitude of the oscillation occurs for (2216) Kerch, which resides near separatrix of the z_1 resonance. We also indicate effects of several MMRs, whose nomenclature is indicated at top. The most significant are effects of J7/3 and J9/4, but we can notice also J11/5 and the three-body resonance 3J-2S-1.

Table 22: Observations of the asteroids in the z_1 resonance zone (Fig. 88).

Asteroid	a (AU)	H	V_c (m/s)	ST	Date	Site
(20845) 2000 UY102	2.979	12.3	48	T	20-Jan-02	KPNO
(21211) 1994 PP36	2.976	13.41	48	T	20-Jan-02	KPNO
(33780) 1999 RU171	2.973	13.05	48	T	06-Mar-02	KPNO
(62948) 2000 VE32	2.960	13.73	58	X	22-May-03	KPNO

†Orbital data and family association (2nd through 4th columns): a is the proper semimajor axis, H absolute magnitude (AstOrb source), V_c is the critical HCM velocity cutoff at which the asteroid associates with the family.

‡ST stands for the inferred spectral type from our observation (5th column).

⋆Observational circumstances (6th through 7th columns): UT date, observatory (KPNO stands for the 4-m Kitt Peak National Observatory telescope).

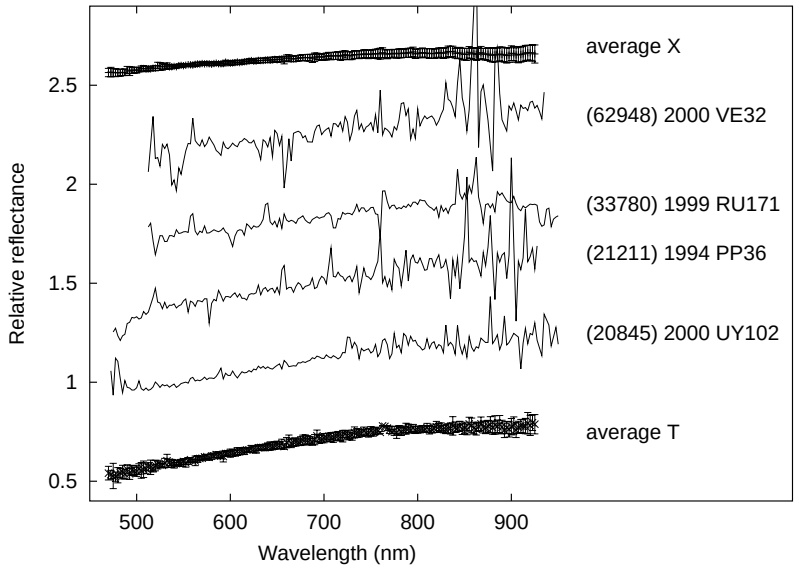

Figure 88: Relative reflectance spectra, normalized to unity at 550 nm, of asteroids in Table III. For (20845) UY102 the ordinate is in order, while for the other objects we arbitrarily shifted the data each time by 0.4 for visibility. For sake of comparison, we also show average reflectance spectra of T-type and X-type asteroids from the SMASS dataset (Bus and Binzel, 2002a,b, and `http://smass.mit.edu/`).

Suspected interlopers. Next we comment on observations of suspected interlopers in the Eos family (Table 23). In this case we used three sites and instruments to collect the data: (i) the 1.52-m European Southern Observatory (ESO) telescope at La Silla, (ii) 4-m telescope at KPNO, and (iii) 5-m telescope at Palomar.

The observations carried out at La Silla were an extension of the S^3OS^2 survey (Lazzaro et al., 2004) during two observational runs in March and November 2002. The ESO 1.52-m telescope was equipped with a Boller and Chivens spectrograph and a 2048×2048 pixels CCD detector with a readout noise of $7[e^-$ rms] and square pixels of $15\,\mu$m. A grating of 225 gr/mm with a dispersion of 33 nm/mm in the first order was used. This configuration resulted in an useful spectral range of $490 - 920$ nm with a FWHM of 1 nm. The spectra were taken through a 5 arcsec slit oriented in the East-West direction. The spectral data reduction was performed using the IRAF package and the classical procedure with averaged bias and dome flat-fields. Wavelength calibration was performed using a He-Ar lamp, which spectrum was obtained several times during each night. The spectra were corrected for airmass by using the mean extinction curve of La Silla (Tüg, 1977). Different solar analogs (Hardorp, 1978) were observed in each observational run in order to compute reflectivities. Tests made using different solar analogs produced differences in the reflectance spectra smaller than 1%/100 nm. The solar analogs HD44594 and

Table 23: Observations of the suspected interlopers in the Eos family (Fig. 89); data as in the Table 22.

Asteroid	a (AU)	H	V_c (m/s)	ST	Date	Site
(251) Sophia	3.095	9.84	55	L	22-May-03	KPNO
(1755) Lorbach	3.092	10.74	58	T	21-Jan-02	KPNO
(2193) Jackson	3.108	10.31	60	X	23-Mar-02	La Silla
(3937) Bretagnon	3.066	11.45	55	X	22-Mar-02	La Silla
(4431) Holeungholee	3.060	11.4	65	X	20,21-Mar-02	La Silla
(8340) Mumma[a]	2.970	11.9	48	D	23-Nov-01	Palomar
(11993) 1999 XX	3.086	12.86	49	Xk	22-May-03	KPNO
(27789) 1993 BB7	3.072	12.18	45	K	08,11-Nov-02	La Silla
(36151) 1999 RG193	3.087	12.45	52	Xk	22-May-03	KPNO

[a](8340) Mumma is also the largest asteroid in the z_1 stream from the Eos family.

⋆Additional sites: Palomar (60-inch Palomar telescope), La Silla (1.52-m ESO telescope located at La Silla, Chile, operated under the agreement with the CNPq/Observatório Nacional, Rio de Janeiro).

HD20630 were used in the March and November run, respectively. The obtained asteroid spectra have been normalized around 550 nm by convention.

Figure 89 folds all acquired spectra into a common frame with a necessary shift in the reflectance scale for visibility. The lowest shown are three X-type objects, certainly spectrally alien to the Eos family. The same holds for (251) Sophia, a large target seemingly offset in semimajor axis from the family members of comparable sizes (Fig. 90). Our data make us classify this target as L-type, dissimilar to the main KTD sequence in the family. All these four objects are our searched, high-C interlopers. Further objects require closer discussion.

Asteroid (8340) Mumma is the only object we observed with semimajor axis smaller than $a_c = 3.02$ AU and a high value of the C parameter (see Fig. 90 where we summarize positions of our observed targets in the (a, H) projection; an X-type asteroid (1845) Helewalda was added here for sake of interest, Mothé-Diniz et al., 2005). We note that this is the largest object located inside the z_1 secular resonance. With $a = 2.97$ AU, it is largely offset from the family center, so that the Yarkovsky forces could not have transported it to its location from the family center in $\simeq 1$ Gy. For these reasons, we believe it is an interloper. We find (8340) Mumma a possibly D-type object, though its spectral steepness sets it apart from other D-type asteroids embedded inside the Eos family. In the next section, we use SDSS data to show that (8340) Mumma is likely to be an interloper.

Asteroid (27789) 1993 BB7 has a spectrum resembling that of the K-type asteroids, suggesting that it is an Eos family member even though it has a large value of $C = 1.77 \times 10^{-4}$ AU. Figure 90 suggests this object is at the furthest extreme of the family. We speculate that its C value might have been enhanced by a favorable initial orbit and/or jumping through the J9/4 MMR on its way toward larger semimajor axis values. Indeed, the finite width of this resonance, $0.005 - 0.01$ AU (Figs. 75 and 76), helps dispersing family members on far side of the J9/4 MMR.

Of the 2 Xk-type objects, (11993) 1999 XX and (36151) 1999 RG193, the first lies close to the periphery of the family. Its flat spectra, however, makes a match less likely. The most intriguing case is that of (1755) Lorbach, a T-type asteroid well beyond a reasonable association with the family (Fig. 90); note that this asteroid is associated with the Eos family at $V_c = 58$ m/s. T-types are not exclusive members of the Eos family but rather are found throughout the main belt. This suggests that (1755) Lorbach could be an interloper.

Searching two different spectroscopic databases, SMASS and S^3OS^2, we found 49 T-type asteroids. Out of this sample, 5 are members of the Eos family. Note that an additional 22 T-type Eos members are known through dedicated observing programmes (Doressoundiram et al., 1998; Mothé-Diniz et al., 2005), but we restrict our sample to the general purpose databases described above. The zone surrounding the Eos family contains another 12 T-type asteroids.[22] This suggests the background zone near the Eos family contains a non-negligible number of T-type asteroids, of which (1755) Lorbach may be a member.

[22]These are: (96) Aegle, (465) Alekto, (596) Scheila, (717) Wisibada, (979) Ilsewa, (986) Amelia, (987) Wallia, (1006) Lagrangea, (1209) Pumma, (1306) Scythia, (2813) Zappala, (2929) Harris.

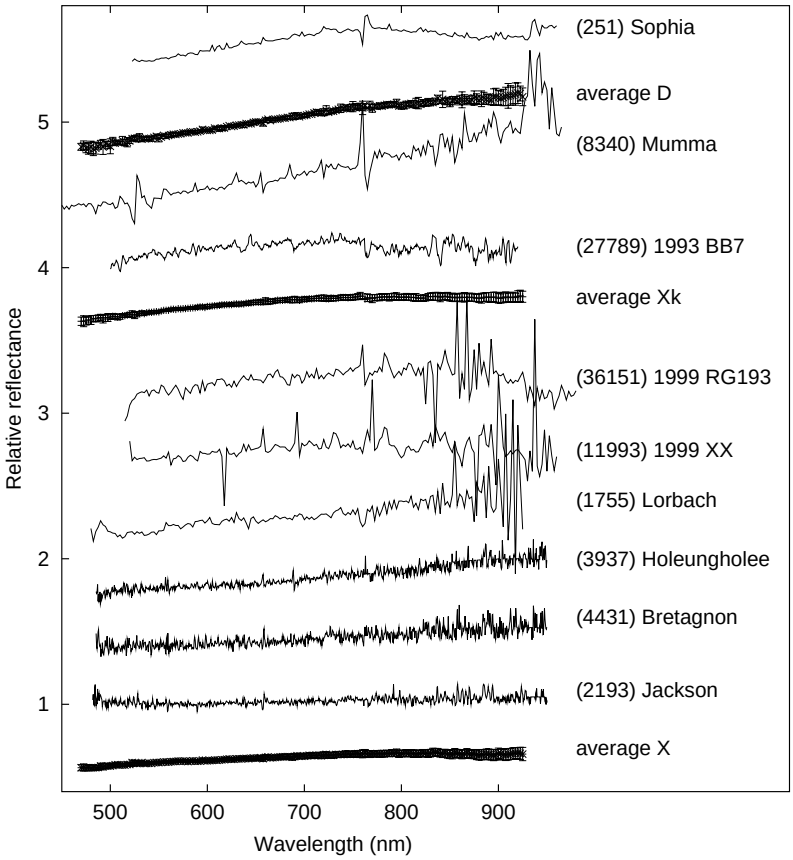

Figure 89: Relative reflectance spectra, normalized to unity at 550 nm, of asteroids in Table IV. For (2193) Jackson the ordinate is in order, while for the other objects we arbitrarily shifted the data each time by 0.4 for visibility. Noisier data for some objects reflect their relative faintness. For sake of comparison, we also show average reflectance spectra of X-type, Xk-type and D-type asteroids from the SMASS dataset (Bus and Binzel, 2002a,b, and `http://smass.mit.edu/`).

6.4.2 SDSS data

In addition to narrow-band spectroscopy, we also examined the SDSS database containing 5 color data in order to characterize smaller asteroids inside the Eos family. We use the same methodology and data analysis as in Nesvorný et al. (2005a), though here we take advantage of the third, updated release of the SDSS data. This source contains five color information about 43424 objects. We found 985 Eos members in this database, which were used to construct normalized reflectance spectra and compute their principal components PC_1 and PC_2 (see Eq. (1) in Nesvorný et al., 2005a). For the final analysis, we choose only 499 asteroids with formal PC_1 and PC_2 errors smaller than 0.1.

Figure 91 shows our results. The left panel gives the mean 5-point spectrum (dashed line) together with a formal standard deviation strip (shaded zone). The overall shape is a good match to the T-type classification. This comparison, however, may be partially flawed because of the unique properties of the SDSS broad-band filters. Namely, the long-wavelength SDSS z filter spans a rather broad wavelength interval centered about 909.7 nm (e.g. Fukugita et al., 1996) and it smears the absorption feature near 0.9 μm that is crucial for the spectral taxonomy in optical bands.

For this reason, we projected the family into the principal component axes (Fig. 91, right panel). Though some scatter is noticeable here, the Eos members appear to constitute a distinct cluster in these variables. Assuming the Eos cluster represents a formal relation of the two principal component parameters PC_1 and PC_2, we may determine confidence levels corresponding to this relationship (see e.g. Bertotti et al., 2003, Sec. 20.5). In Fig. 91 we show the ellipses of 90% and 99% Eos membership based of our analysis. Asteroids close to these limits, or beyond them, are weakly connected with the bulk of the family and likely represent outliers.

We searched for large objects close to or beyond the 90% confidence level which correspond to a large

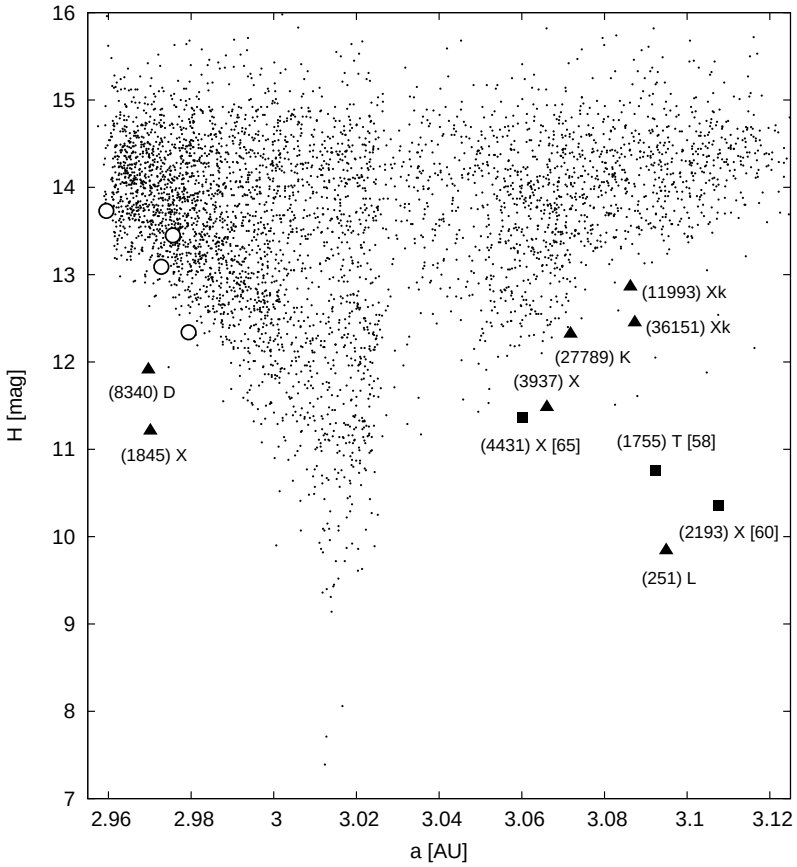

Figure 90: The nominal Eos family, $V_c = 55$ m/s, projected onto the plane of proper semimajor axis a and absolute magnitude H – dots. Symbols indicate position of asteroids whose spectra are reported in the paper: (i) open circles are objects inside the z_1 secular resonance (Table 1 and Fig. 88), all T-types except for (62948) 2000 VE32 which is X-type and resides nearest to the J7/3 MMR; (ii) triangles are objects nominally associated with the family but which correspond to extremal values of C parameter from Eq. (44), such that $|C| \geq 1.6 \times 10^{-4}$ AU, which are suspected interlopers; (iii) squares are the same as blue in (ii) but for asteroids associated with the Eos family at HCM cutoff velocity larger than 55 m/s. In the latter two classes we show the asteroid designation, spectral type and, in the (iii) case, the HCM cutoff velocity at which the body associates with the family (the number in squared brackets in m/s).

$|C|$ from Eq. (44), i.e. objects detached from the family in (a, H). We found 4 cases of interest (shown as crosses in Fig. 91). (4843) Megantic and (4431) Holeungholee, denoted 3 and 4, have both been classified X-types using narrow-band spectroscopy (Lazzaro *et al.*2004; Mothé-Diniz et al., 2005). They are shifted out of the center of the Eos group toward smaller PC_1 values; this indicates they have a flatter spectrum than other objects. These objects are likely interlopers.

The other two are (8340) Mumma, denoted 1, and (1755) Lorbach, denoted 2. They are particularly interesting because our analysis of their narrow-band photometry (Sec. 6.4.1) classified them as D and T, respectively. These classes are generally compatible with the family (Sec. 6.2.2) but they could also be interlopers. For (8340) Mumma, SDSS photometry places it toward the D group (high PC_2 value). In fact its displacement in PC_2 component, relative to the family center, is larger than other D-type Eos members, such that (8340) Mumma occurs beyond the 99% confidence level of the family PC_1-PC_2 identification. Thus, SDSS data suggests that (8340) Mumma is an interloper, in spite its D-type classification. The same analysis rejects (1755) Lorbach as an Eos member in spite of its T-type classification because this asteroid resides at the 90% confidence level line for being associated with the Eos family.

Finding these last two asteroids incompatible with membership to the Eos family is "good news" since their respective values of the C parameter ($C = -2.1 \times 10^{-4}$ AU for (8340) Mumma; $C = 5.1 \times 10^{-4}$ AU for (1755) Lorbach) are far too large to explain them using our Yarkovsky diffusion model (see e.g. Figs. 80, 83 and 90).

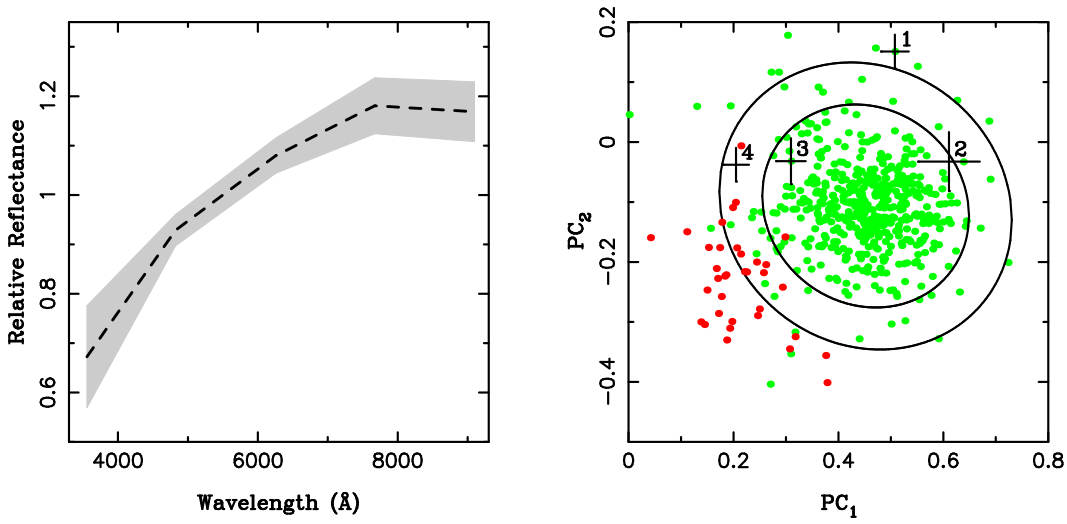

Figure 91: Left: Dashed curve shows a mean 5-color spectrum for 499 small Eos members from the SDSS database (release 3.0; see Jurić *et al.*2002 and `http://www.astro.princeton.edu/~ivezic/sdssmoc/sdssmoc.html`) whose principal spectral components have an error smaller than 0.1 (here we normalized the result to unity at 550 nm as conventional). The shaded zone shows a standard deviation interval about the mean. Right: The Eos family members (light symbols) projected onto the plane of spectral principal components PC_1 and PC_2 (e.g. Nesvorný et al., 2005a); here we use again the sample of 499 asteroids observed with SDSS with small enough errors. The two ellipses show a 90% (inner ellipse), resp. 99% (outer ellipse), confidence level of a formal relation between the two components that define the Eos family as a cluster of data in these variables. Objects outside these limits are likely alien to the family. Here we list large members in this zone: (i) 1 – (8340) Mumma, (ii) 2 – (1755) Lorbach, (iii) 3 – (4843) Megantic, and (iv) 4 – (4431) Holeungholee; the horizontal and vertical intervals show error-bars of the data. The last two were classified X-types by the narrow-band spectroscopy, while (8340) Mumma received D classification and (1755) Lorbach T classification (see Fig. 89). For sake of comparison we also show the neighboring Veritas family (dark symbols), classified as C-type group.

6.5 Conclusions

In this paper, we have attempted to understanding the structure and history of the Eos asteroid family. Using our Yarkovsky diffusion model, we were able to match several outstanding features seen in the proper element space (e.g., the sharp termination of the family at the J7/3 MMR; the the migration of asteroids along the z_1 secular resonance). Our model also predicted the relative fraction of Eos family members on both sides of the J9/4 MMR and it can be used to understand the concentration of small asteroids at extreme semimajor axis values (see also Vokrouhlický et al., 2005). Moreover, by matching the semimajor axis distribution of Eos family members, we were able to estimate that the family is $T = 1.3$ Gy old, some 30% younger than used by Nesvorný et al. (2005a). Interestingly, this brings the Eos "data point" closer to the empirical relation between the average spectral slope PC_1 within the family and its age determined by these authors (see Fig. 11 in Nesvorný *et al.*2005a).

The mineralogy of the Eos parent body is still a puzzle (e.g. Burbine et al., 2001; Mothé-Diniz and Carvano, 2005). For this reason, caution should be used when interpreting the spectra of Eos family members. Nevertheless, we predict that the majority of small asteroids inside the z_1 stream are most likely from the Eos family. Similarly, we ruled out several asteroids as interlopers based on their orbital position, which was inconsistent with Yarkovsky evolution, and their spectral features/taxonomic type (e.g., (8340) Mumma and (1755) Lorbach).

Despite our successes, we cannot yet fully reproduce the large eccentricity and, especially, inclination dispersion of the Eos family (Sec. 1). We believe this problem may have been produced by a projectile striking the Eos parent body from the out-of-plane direction. Bottke et al. (1994) analyzed the impact velocity distribution for main belt projectiles on a putative Eos family progenitor and found that asteroids are a factor $\simeq 4$ more likely to strike from the out-of-plane than in-plane direction. This feature could produce an anisotropic ejecta velocity field, with the highest-velocity fragments having the same trajectory as the projectile. Given the probabilities above, this could produce a larger dispersion of inclinations (and eccentricities) than one might expect.

To examine this issue more closely, we note that our best-fit solution from Sec. 6.3.2 indicates that

$D \simeq 4$ km asteroids, which dominate the observed Eos population, were ejected with an along-track velocity component of $\simeq 100$ m/s (we investigated only the semimajor axis dispersion). If this value were applied used to the other two components, radial and normal, we would expect maximum eccentricity and inclination dispersions of $\simeq 0.024$ and $\simeq 0.012$. The observed dispersion, however, is $\simeq 0.040$ and $\simeq 0.025$, larger than the maximum estimated values. By accounting for the larger characteristic velocities of ejecta in the normal and radial directions as explained above, we believe we can explain this mismatch.[23]

Other than the Koronis family (Bottke et al., 2001), the Eos family is the second main belt family to have received a thorough analysis using the modern dynamical tools. By studying other families, we hope – among other goals – to constrain their ages enough to decipher the overall history of the main belt.

Acknowledgments. This work, David Vokrouhlický and Miroslav Brož, has been supported by the Grant Agency of the Czech Republic, grant 205/05/2737. Research funds for William Bottke and David Nesvorný were provided by NASA's Planetary Geology and Geophysics Program. The work of Daniela Lazzaro has been supported by CNPq through grant No. 306605/2003-1. We thank Andrea Milani and Zoran Knežević for providing us with their numerically computed secular proper frequencies across the whole asteroid belt and a related software allowing to display location of various high-order secular resonances. We also thank Hal Levison for the suggestion to study the role of faint young Sun (Sec. 6.3.2) and Zeljko Ivezić for providing us with the SDSS moving objects catalogue (Data release 3.0). Reviews by Valerio Carruba and Alberto Cellino were much helpful to prepare the final version of the paper. Observations obtained at the Hale Telescope, Palomar Observatory are part of a collaboration between the California Institute of Technology, NASA/JPL, and Cornell University.

[23] The same feature is seen in the young Veritas family (e.g. Nesvorný et al., 2003), whose initial velocity field holds a high degree of anisotropy. For instance, from the relative measure of the inclination and semimajor axis dispersion of Veritas multi-kilometer members we determine that the ratio of the mean normal vs transverse velocity components was $3-5$ in this case. It is tempting to assume a similar explanation as for the Eos.

7 The Agnia family embedded inside the z_1 secular resonance

The Agnia asteroid family is an exceptional case — it is located inside a secular resonance, which causes large oscillations of eccentricity and inclination, nevertheless, it preserves very well the information about the initial spread, just after the disruption event. We determine the upper and lower bounds for the age of the Agnia family by two independent methods. The co-authors are D. Vokrouhlický, W.F. Bottke, D. Nesvorný and A. Morbidelli. MB is responsible mainly for the N-body simulations and their analysis in Sections 7.3.2 and 7.4.1.

Abstract

The Agnia asteroid family, a cluster of asteroids located near semimajor axis $a = 2.79$ AU, has experienced significant dynamical evolution over its lifetime. The family, which was likely created by the breakup of a diameter $D \sim 50$ km parent body, is almost entirely contained within the high-order secular resonance z_1. This means that unlike other families, Agnia's full extent in proper eccentricity and inclination is a byproduct of the large-amplitude resonant oscillations produced by this resonance. Using numerical integration methods, we found that the spread in orbital angles observed among Agnia family members would have taken at least 40 My to create; this sets a lower limit on the family's age. To determine the upper bound on Agnia's age, we used a Monte Carlo model to track how the small members in the family evolve in semimajor axis by Yarkovsky thermal forces. Our results indicate the family is no more than 140 My old, with a best-fit age of 100^{+30}_{-20} My. Using two independent methods, we also determined that the $D \sim 5$ km fragments were ejected from the family-forming event at a velocity near 15 m/s. This velocity is consistent with results from numerical hydrocode simulations of asteroid impacts and observations of other similarly-sized asteroid families. Finally, we found that 57% of known Agnia fragments are prograde rotators. The reason for this limited asymmetry is unknown, though we suspect it is a fluke produced by the stochasic nature of asteroid disruption events.

7.1 Introduction

Asteroid families, which are clusters of asteroids in proper semimajor axis (a), eccentricity (e), and inclination (i) space produced by asteroid collisions, are among the more intriguing features found in the main asteroid belt. Since their discovery early in the past century (e.g., Hirayama, 1918; historical notes in Bendjoya and Zappalà, 2002), considerable effort has gone toward trying to understand these enigmatic formations. Moreover, as the number of known asteroids has increased, we have become increasingly aware that extended families are "witness plates" to a variety of interesting and poorly understood phenomena.

In this paper, we build on the work described in Vokrouhlický et al. (2005a,b; see also Bottke et al. 2002; 2005a,b) to understand the dynamical structure of asteroid families using modern methods and numerical tools. This means studying (i) how cratering and/or catastrophic disruption events on asteroids produce fragments and (ii) how those fragments evolve over time through collisional and dynamical processes. We focus here on the Agnia family, which resides in the central part of the main asteroid belt at $a \approx 2.79$ AU. This places this family on the periphery of the 5/2 mean motion resonance (MMR) located at $a \approx 2.8$ AU. Other than this resonance, the Agnia family is unaffected by any other MMR of significant strength. On the other hand, we find Agnia exceptional among known asteroid families for how it interacts with the high-order secular resonance z_1. Both of these facts will play an important role in story presented below.

7.2 Agnia family: basic facts

We start our work by identifying the members of the Agnia family using the hierarchical clustering method (HCM; e.g., Bendjoya and Zappalà, 2002 and references therein). Our code can detect concentrations of asteroids in (a, e, i) space among analytically-determined proper elements; more than 170,000 main belt numbered and multi-opposition asteroids exist in the `AstDyS` database (`http://newton.dm.unipi.it/`) as of November 2004. We adopt the "standard metric" of Zappalà et al. (1990, 1995) and compute the relative velocity V found between two asteroid orbits. Families are identified when asteroids have V lower than a cut-off velocity value V_c between a neighboring pair of members.

As it is characteristic of compact families, the number of members found by the HCM method increases slowly as a function of V_c until a critical point is reached. At that point, the family members link themselves with the surrounding background population. For the Agnia family, we find this threshold occurs at $V_c = 63$ m/s. Thus a conservative approach for the Agnia family is to keep V_c as low as possible in order to characterize its main features. Hence, our adopted nominal value for the Agnia family is $V_c = 33$ m/s; the interested reader can find data files for this family at different cutoff values on our website `http://sirrah.troja.mff.cuni.cz/yarko-site/` .

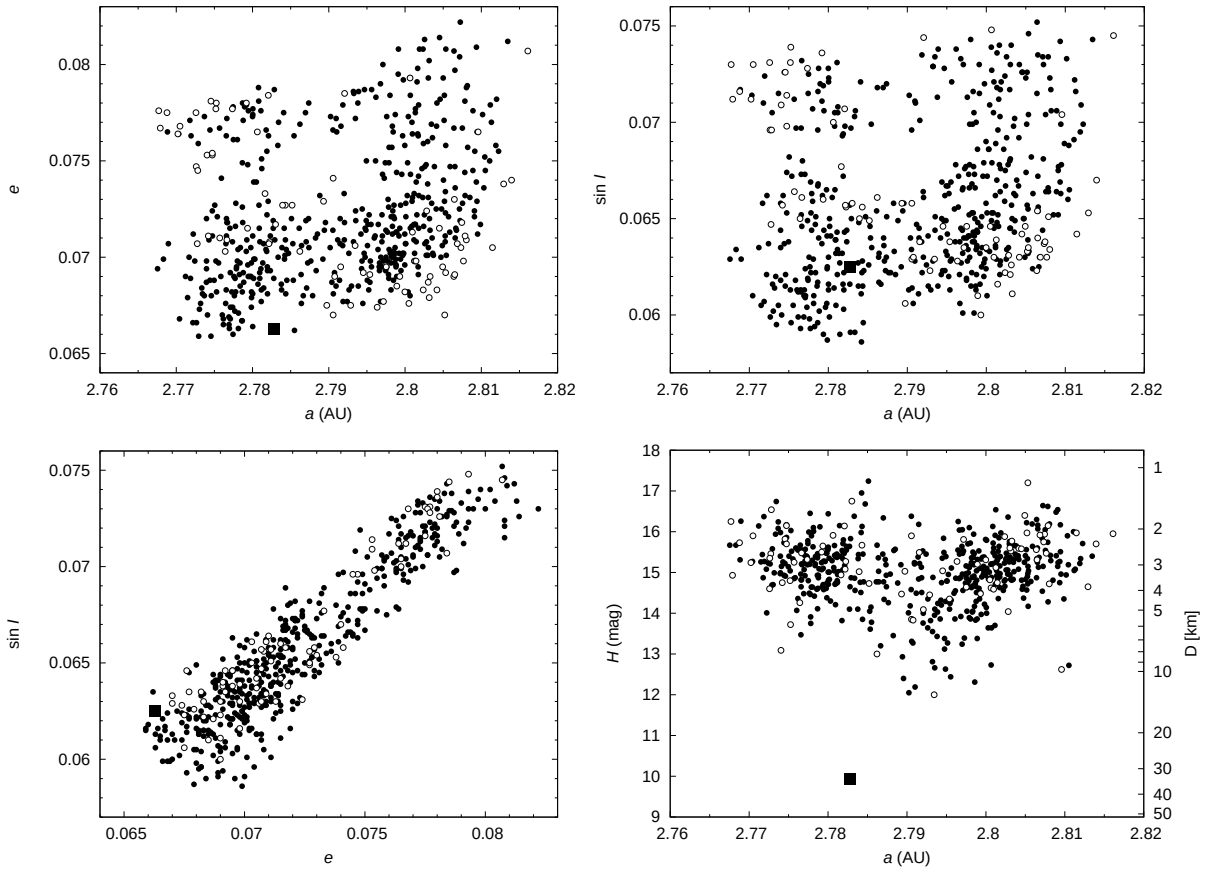

Figure 92: Projection of the Agnia family, as identified by the HCM method with a cut-off velocity $V_c = 33$ m/s, onto different planes of proper element space parameters: semimajor axis a, eccentricity e and inclination i. H is the absolute magnitude. The strong correlation of the e and $\sin i$ values (bottom left) indicates presence of a high-order secular resonance z_1 into which most of the family members are immersed (Fig. 95). The center of $H \geq 14$ asteroids in semimajor axis, approximately 2.79 AU (dashed line), is offset from position of the largest asteroid (847) Agnia (shown as filled square in the bottom right panel). Their difference corresponds to about 30 m/s in terms of along-track velocity. The right ordinate on the bottom right figure indicates the best guess for the size of the members (assumes a geometric albedo $p_V = 0.17$, that of the largest asteroid (847) Agnia). Filled symbols are Agnia members whose critical angle of the z_1 resonance librates, open symbols are those with the critical angle of the z_1 resonance circulating.

Figure 92 shows 2-D projections of our nominal Agnia family distribution in proper a, e, i and in absolute magnitude H. Though each of these projections coincides with some interesting feature which will be analyzed below, the most peculiar and singular one is the strong correlation between proper eccentricity e and inclination i values (Fig. 1c). This almost linear relationship is unlikely to be a consequence of the initial ejection velocity field produced by the parent body's disruption, mainly because the inclination and eccentricity dispersions depend on different velocity components. Note that an exception to this rule would be a velocity field in the shape of a highly collimated jet, which has yet to be observed in real families or in numerical simulations of catastrophic disruption events (e.g., Durda et al., 2004). We therefore postulate that the e-i relationship is a consequence of some dynamical effect that shaped the family after it had been formed. Indeed, in the next section we show that the family has been stretched in a specific direction of the (e, i) plane by the influence of high-order secular resonance $z_1 = g + s - g_6 - s_6$.

Figure 93 shows the cumulative H distribution $N(< H)$ for the Agnia family. It is useful to adopt a power-law approximation $N(< H) \propto 10^{\gamma H}$ to quantitatively express the power law index (or slope) of $N(< H)$ by a single parameter γ. In the range $(13.5, 15.5)$, we find $\gamma \simeq 0.61$. We argue below (see Conclusions) that this exponent is unlikely to be a byproduct of collisional evolution; instead, it most likely corresponds to that of the post-breakup distribution of fragments. Note that the accumulation of additional bodies near Agnia makes the size distribution shallower, ultimately reaching a value $\gamma \sim 0.55$. The slope of $N(< H)$ distribution also becomes shallow for $H > 15$; this either stems from observational incompleteness or from an actual change in slope (see e.g., Morbidelli et al., 2003). In the latter case, the

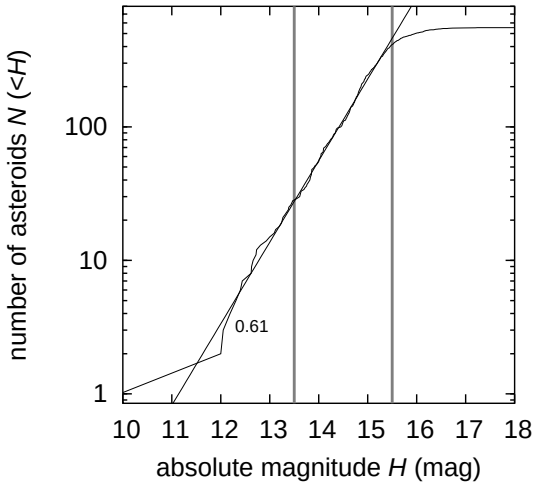

Figure 93: Cumulative distribution $N(< H)$ of the Agnia members absolute magnitudes H for the nominal identification of the family. Using a power-law approximation $N(< H) \propto 10^{\gamma H}$ in the interval $(13.5, 15.5)$, we find $N(< H)$ is best matched with $\gamma \simeq 0.61$ (straight line).

likely cause is collisional evolution between the family members and the background main belt population (Morbidelli et al., 2003; Bottke et al., 2005a,b).

Spectroscopic surveys have determined that (847) Agnia is an S-class asteroid (e.g., Bus and Binzel, 2002a,b; Lazzaro et al., 2004). SMASS II survey also identified (3491) Fridolin, (4051) Hatanaka, (4261) Gekko, (5242) Kenreimonin, (6077) Messner, (7056) Kierkegaard and (7728) Giblin to be Sq-type asteroids and (1020) Arcadia and (3701) Purkyne to be S-type asteroids. Mothé-Diniz et al. (2004) claim that another five S-type asteroids are associated with the Agnia family, but they lie at $V_c \sim 50$ m/s, which is beyond our nominal identification at $V_c = 33$ m/s. These authors also point out that the dominant spectral classes of the background asteroids in the Agnia vicinity are C or X, very different from family dominating Sq-type asteroids.

Sunshine et al. (2004) claim that Agnia family members, which have a high-calcium pyroxene component in their spectra (and possibly minor amounts of olivine), may have experienced igneous differentiation. A close examination of the family, shows that the members have nearly identical spectra. Sunshine et al. (2004) claim this homogeneity may mean that Agnia is a secondary family produced by the breakup of a basaltic fragment from a primary asteroid parent body. Note that the Agnia parent body is only thought to have had a diameter $D \sim 50$ km (Durda et al., 2006, in preparation), which would be consistent with such a scenario. The source and fate of the asteroid that Agnia is derived from is unknown. Bottke et al. (2005c) hypothesize that Agnia may be linked to large M-type asteroids like (16) Psyche and (216) Kleopatra, which are generally thought to be iron cores from disrupted differentiated bodies.

IRAS observations of (847) Agnia suggest its albedo is $p_V = 0.172 \pm 0.022$ (Tedesco et al., 2002). This value is consistent with typical S-type asteroids. Little is known about Agnia family members with $H \geq 13$ (approximately $D \leq 8$ km). In particular, their albedo value has not been determined yet.

We have also attempted to characterize the reflectance spectra of Agnia family members using five color photometry data from the Sloan Digital Sky Survey's (SDSS) (e.g., Ivezić et al., 2001; Jurić et al., 2002). We adopted the same methodology and data anlysis as in Nesvorný et al. (2005). Searching the SDSS database, we found information on 99 Agnia family asteroids. For each of them, we constructed normalized reflectance spectra and computed their principal components PC_1 and PC_2 (see Eq. (1) in Nesvorný et al., 2005). We then winnowed this down to 26 objects with formal PC_1 and PC_2 errors smaller than 0.1.

Figure 94 shows these data (filled circles) together with other family members whose PC_1 and PC_2 errors exceed the chosen threshold 0.1 but still fall within the limits of the axes (open circles; there are more asteroids falling even outside). Assuming the bodies have a common mineralogy and hence a parametric relation between PC_1 and PC_2, we identify the Agnia family as a distinct cluster in spectral parameter space in much the same manner as families are identified as clusters in proper element space. From the available high-quality data (filled circles) we can construct a 90% confidence level zone showing family membership (see e.g. Bertotti et al., 2003, Sec. 20.5). This is shown with the ellipse on Fig. 94.

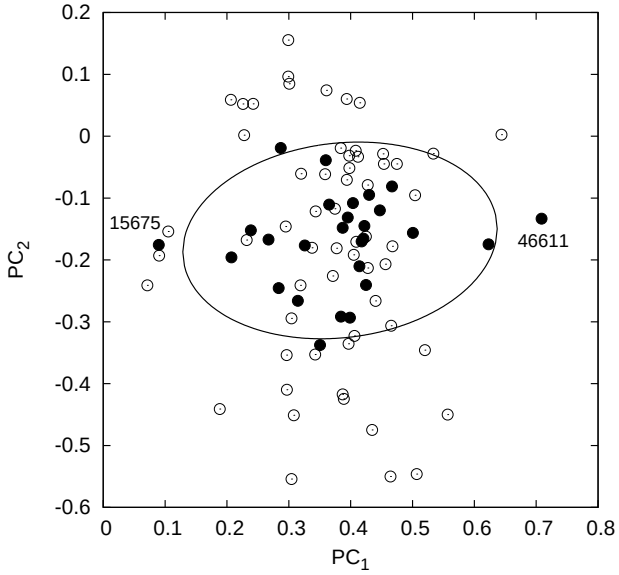

Figure 94: Principal spectral components PC_1 and PC_2 of the Agnia members from the SDSS five color photometry: (i) full circles are asteroids for which the formal PC_1 and PC_2 errors are smaller than 0.1, (ii) open circles are asteroids for which either of the formal PC_1 and PC_2 errors exceed 0.1. The 90% confidence level region of the family cluster from the good data is shown by the ellipse. Only two members with reliably determined PC_1 and PC_2 values fall outside this limit: (i) (15675) Goloseevo, and (ii) (46611) 1993 TH4.

Two asteroids, (15675) Goloseevo and (46611) 1993 TH4, fall outside this 90% confidence level threshold, indicating they are only marginally linked to the family. These bodies could be outliers or instead may support a possible larger spectral diversity in the family (see Sunshine et al. 2004); in the $a - H$ plane, these two asteroids lie at the border of the family with $a \simeq 2.773$ AU. Note the $PC_1 = 0.3$ spectral slope is the dividing line between the S-complex (for which $PC_1 > 0.3$) and C-complex (for which $PC_1 < 0.3$; e.g. Bus and Binzel, 2002a; Nesvorný et al., 2005). The Agnia family members fall on both sides of this limit, consistent with more precise spectroscopic data that suggests the family contains numerous asteroids with taxonomic type Sq (Bus and Binzel, 2002a). The mean values for the spectral components from SDSS data are $PC_1 = 0.38$ and $PC_2 = -0.17$.

7.3 Agnia family: relation to the z_1 resonance

As described above, the most interesting dynamical aspect of the Agnia family, unique among the known families, is the fact that it is nearly entirely embedded within the high-order secular resonance z_1. In this section, we describe the major features of this peculiar resonance and then discuss our proof that the resonance contains most of the known Agnia family members. The long-term evolution of the Agnia family is described in Sec. 7.4.

7.3.1 z_1 resonance main features in brief

A resonance occurs when a combination of angular variables of the asteroid and planets, called a resonant (critical) angle σ, becomes stationary over long time periods, such that it librates about a fixed center. When the constituting variables do not involve mean anomalies, but only longitudes of node and pericenter of the asteroid and planets, we speak about a secular resonance (e.g., Morbidelli, 2002). This is because σ, as well as the angles on which it depends, is stationary in the two-body problem and changes only as a result of planet-asteroid interactions. Thus, their evolution, as well as that of the resonance angle σ, is slow. Consequently, this coherent influence allows even a weak secular resonance to produce significant orbital perturbations over time. Developing a theory describing secular resonances therefore requires to delve into perturbation theory. This can be complicated, particularly when σ comprises more than two secular angles. In that and our case, we are dealing with a high-order secular resonance.

Methods that allow one to systematically analyze high-order secular resonances in the motion of asteroids were pioneered by the work of Milani and Knežević (1990, 1992, 1994). At present, however, no complete analytic or semi-analytic theory is yet available for use. Milani and Knežević were principally

interested about the degree of instability that high-order secular resonances can produce in the definition of proper orbital elements (e.g., Knežević and Milani, 2000, 2003; Knežević et al., 2002).

However, the high-order secular resonances are important for yet another reason. As demonstrated by several groups (Bottke et al. 2001; Vokrouhlický et al. 2002, 2005a; see also Vokrouhlický and Brož 2002 and Carruba et al. 2005), high-order secular resonances may also serve as pathways for small asteroids drifting in semimajor axis due to the Yarkovsky effect. This process is most clearly identified when it affects the dynamical evolution of asteroids in some well-defined, localized structure such as an asteroid family. For instance, Koronis family asteroids drifting outward (away from the Sun) by the Yarkovsky effect have their proper eccentricities significantly increased when they interact with the $g + 2g_5 - 3g_6$ secular resonance at $a \sim 2.92$ AU (Bottke et al., 2001). A second example includes the small asteroids in the Eos family, which form a stream spreading toward small eccentricity and inclination values along the z_1 resonance (Vokrouhlický et al., 2002, 2005a). Finally, some V-type asteroids appear to have escaped from the Vesta family by migrating along the $z_2 = 2\,(g - g_6) + s - s_6$ resonance (Carruba et al., 2005).

A fundamental aspect to understanding the Agnia family structure is the $z_1 = g + s - g_6 - s_6$ resonance with resonant angle $\sigma = \varpi + \Omega - \varpi_6 - \Omega_6$. Here ϖ and Ω are the longitude of perihelion and node of the asteroid orbit, while ϖ_6 and Ω_6 are angles that change linearly with time and have frequency g_6 and s_6 from planetary theory (e.g., Morbidelli, 2002). The proper frequencies g and s taken from the time series of the ϖ and Ω angles are relevant for the critical angle σ. We thus have $d\sigma/dt = g + s - g_6 - s_6$, which is where the nomenclature $z_1 = g + s - g_6 - s_6$ arises. It can be easily shown (e.g., Vokrouhlický et al., 2005a) that the conjugated resonant momentum is $\Sigma = G - L = \sqrt{a}\,(\sqrt{1-e^2} - 1)$, given here in terms of the Delaunay variables L and G or the Keplerian orbital elements a and e. At the simplest level of perturbation theory, the resonant variables are assumed "active", while angles related to the additional dimensions are eliminated from the problem by the averaging principle (e.g., Morbidelli, 2002). Their conjugated momenta are therefore conserved. These are $K_1 = L = \sqrt{a}$ and $K_2 = 2G - H = \sqrt{a\,(1-e^2)}\,(2 - \cos i)$. As (Σ, σ) periodically change due to the resonance, e oscillates (note the a is conserved by K_1). Due to conservation of K_2, i is forced to change in a correlated way with e.

Obviously, K_1 and K_2 are conserved only when the sole resonant gravitational perturbations are taken into account. Non-resonant effects will then oscillate with small amplitudes and short periods. More importantly, when non-gravitational effects such as the Yarkovsky forces are active, they slowly change and allow asteroids to enter, follow, or leave the z_1 resonance. For the sake of discussion below, we also introduce a modified quantity $K_2' = \sqrt{1-e^2}\,(2 - \cos i)$; that is, by virtue of integrals K_1 and K_2, also conserved in the resonant motion. Below we show by direct numerical integration that it stays approximately constant even when Yarkovsky forces modify the semimajor axis a.

7.3.2 Agnia members inside the z_1 resonance

Here we show that the orbits of most Agnia members are located inside the z_1 resonance. To do so, we numerically integrated the orbits of all 553 known members of the family for 10 My using a SWIFT-RMVS integrator (e.g., Levison and Duncan, 1994). Modifications to this code were made to include the second-order symplectic map from Laskar and Robutel (2001) and to account for Yarkovsky forces (see `http://sirrah.troja.mff.cuni.cz/yarko-site/` for details of its implementation, speed and accuracy tests). We computed synthetic proper elements from the code's results in a way compatible with the definitions provided by Knežević and Milani (2000, 2003). This means that we first apply a Fourier filter to the (non-singular) orbital elements in a moving window of $\simeq 0.75$ My (with steps of 0.1 My) to eliminate all periods smaller than some threshold value (in our case, 1.5 ky). The filtered signal, in the form of mean orbital elements, is then output from the simulation for further checks and passed through a frequency analysis code adapted from Šidlichovský and Nesvorný (1997) to obtain (planetary) forced and free terms in the Fourier representation of orbital elements. The isolated free terms are identified as the proper orbital elements.

The giant planets are included in our simulation with their masses, initial positions and velocities taken from the `JPL DE405` ephemeris. We do not include terrestrial planets in the simulation, but we do account for a barycentric correction of the initial conditions; this approximation is justified in the zone of the asteroid belt where Agnia is located (for the problem at hand). The initial orbital elements of the asteroids are taken from the `AstOrb` database.

Figure 95 shows the current position of the Agnia members in the plane defined by the critical angle σ of the z_1 resonance and the conjugated frequency $\dot{\sigma} = g + s - g_6 - s_6$ (that replaces here the conjugated momentum Σ). In this test we do not include Yarkovsky forces. Our procedure to compute the quantities in Fig. 95 is as follows. The mean orbital elements of asteroids, computed each 0.1 My as described above, are Fourier filtered to identify the forced g_6 and s_6 frequencies and their associated phases. The same

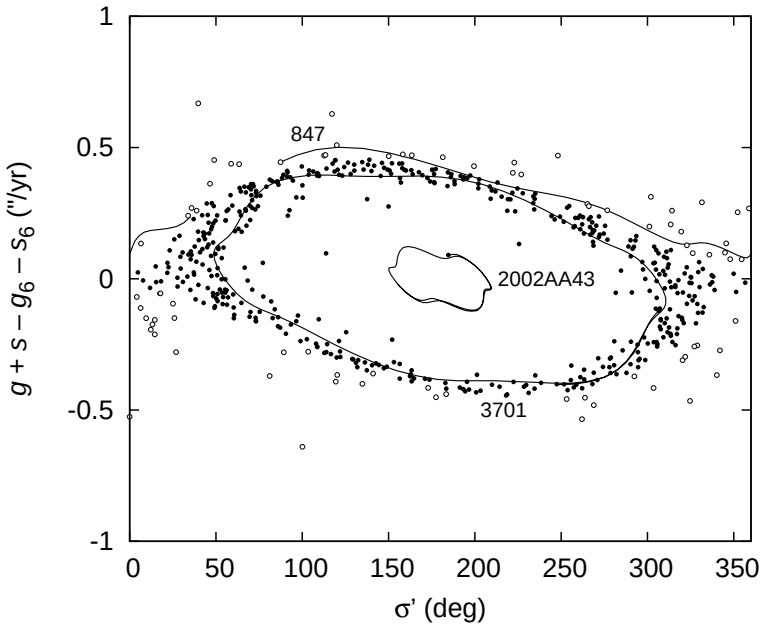

Figure 95: Agnia family members (symbols) projected onto the plane of critical angle σ of the z_1 resonance vs. the associated frequency $\dot{\sigma} = g + s - g_6 - s_6$. Bulk of the family asteroids reside inside this resonance and close to its separatrix. Filled symbols for librating orbits, open symbols for circulating orbits. The solid lines show evolution paths as determined from 10 My numerical integration for three characteristic cases: (i) asteroid (3701) Purkyne is the most typical evolutionary track in the family (large-amplitude libration), (ii) asteroid 2002 AA43 is a rare case of small-amplitude libration in the resonance, and (iii) asteroid (847) Agnia is located right outside the resonance, but very near to its separatrix. Libration period for (3701) Purkyne is about 8 My, circulation of (847) Agnia, very close to the separatrix, is even slower. Dispersion of the family members along all values of the resonance angle σ shows the age of the family to be at least several times the characteristic libration period.

procedure is followed to get the free frequencies g and s. The frequencies are then plotted on the ordinate and their phases are used to construct the resonant angle σ.

The symbols in Fig. 95, which are given as full or open circles, tell us whether during the 10 My timespan the resonant angle σ (i) librates over some restricted interval of values (indicating that the orbit is inside the z_1 resonance) or (ii) circulates and spans all values. Three examples, low-amplitude libration, large-amplitude libration (the most typical for the family), and circulation, are shown by the lines and are identified by the asteroid's name. We found that 478 asteroids (thus 86%) are currently located inside the z_1 resonance. We find this to be an exceptional situation; we are not aware of any other asteroid family that is similarly embedded inside a high-order secular resonance. In other families that have been investigated to date (e.g., Eos, Vesta or Erigone), the secular resonance only affects a small percentage of its members.

What are the implications of this unique feature of the Agnia family? Figure 96 shows the evolutionary tracks over 10 My for our Agnia asteroids, which are now projected onto the plane of synthetic proper elements e and $\sin i$. The effect of this secular resonance forces the proper elements to oscillate in a correlated way, such that $K_2' = \sqrt{1-e^2}\,(2-\cos i)$ stays constant. It is important to note that the amplitude of these oscillations covers the full extent of the family. This means that the computed values of proper e and i, as given e.g. in the `AstDyS` database used above, only have limited meaning and they change in time along the direction shown in this figure. Because there is a strong sensitivity in this calculation on initial orbital conditions, the relative configuration of the family in the e-i projection, as seen today, does not conserve information about its initial state.

If K_2' is conserved, however, there may be ways to make use of this information. For the sake of simplicity, let us neglect for the moment the effect of Yarkovsky dispersion of the family (to be analyzed in the next Section). We would conclude, in absence of other perturbations (such as weak mean motion resonances; Nesvorný and Morbidelli, 1998; Morbidelli and Nesvorný, 1999), that motion in the z_1 resonance is sufficiently stable to conserve the K_2' value for each asteroid over an extremely long timescale (hundreds of My; this value was verified for asteroids in the Eos and Erigone families for both z_1 and z_2 resonances, Vokrouhlický et al., 2005a,b). Thus, the distribution of K_2' values, rather than e and i

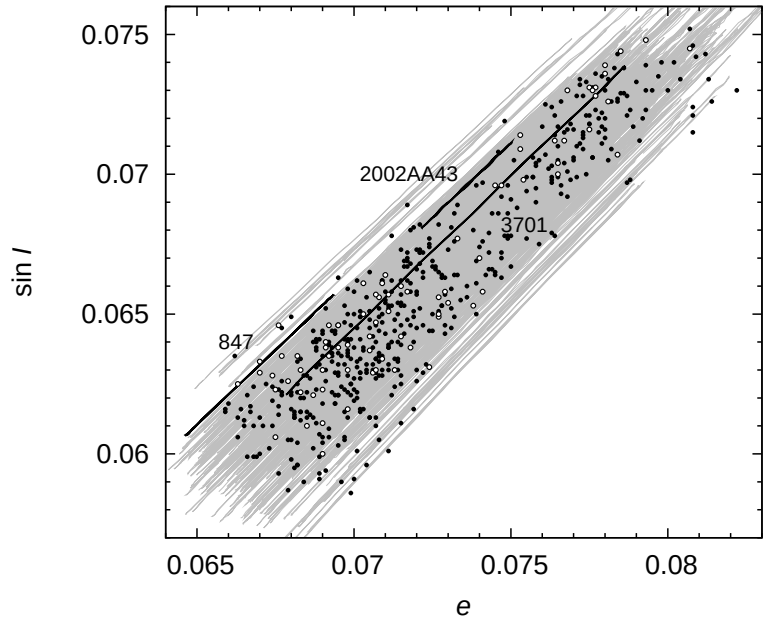

Figure 96: Agnia family members (symbols) projected onto the plane of proper eccentricity e and sine of inclination $\sin i$. The thick solid lines indicate evolutionary tracks of the three asteroids from Fig. 95. The largest variations correspond to (3701) Purkyne, the large-amplitude libration case. The grey lines are similar 10 My evolutionary tracks for all family members. The family is thus stretched along the direction of quasi-integral $K_2' = \sqrt{1-e^2}\,(2-\cos i)$ and its extension fully determined by the z_1 resonance dynamics.

themselves, stays constant over long time spans, during which it conserves information about the initial state of the family.

Figure 97 shows the distribution of K_2' for all 553 Agnia members. It is a tight, near Gaussian distribution with a standard deviation (dispersion) of $\sim 1.5 \times 10^{-4}$. In a simple experiment, we tried to transform this information into a characteristic velocity dispersion produced by the breakup of the Agnia parent body (i.e., its initial, post-breakup velocity field). Considering an isotropic velocity field, and assuming that the fragments are dispersed with a Gaussian distribution with a standard deviation V (such as in Petit and Farinella, 1993), our best fit case for the observed Agnia distribution yields $V \sim 15$ m/s. This low-velocity dispersion value is compatible with results from hydrocode simulations (e.g., Love and Ahrens, 1996; Ryan and Melosh, 1998; Benz and Asphaug, 1999). A similar velocity dispersion was also observed for the Karin family, whose parent body was only slightly smaller than Agnia ($D = 32$ km for Karin vs. 50 km for Agnia) (e.g., Nesvorný et al., 2002, 2006b; Durda et al., 2006, in preparation).

7.4 Agnia family: evolutionary model

Up to this point, we have focused on how the z_1 secular resonance affects proper e and i. Fig. 92, however, shows other interesting features related to the a distribution of Agnia members. It is well-known that the semimajor axis values of small asteroids affected by Yarkovsky forces disperse families over time (e.g., Bottke et al., 2002 and references therein). In this section we investigate how this process can be used to constrain the age of the Agnia family.

7.4.1 Simple numerical model

We first performed a numerical simulation to determine how a synthetic realization of the Agnia family evolves over a timespan of 150 My. This final time was not chosen arbitrarily. Rather, it is in agreement with an upper estimate of this family's age from our analysis in Sec. 7.4.2. Our primary goal here is to find a lower bound of the family's age based on observations of a nearly-uniform distribution of its members along the separatrix of the z_1 resonance (Fig. 95). For that task, we do not include the Yarkovsky forces into our simulation. We also perform a second simulation containing Yarkovsky forces to verify that the K_2' distribution discussed above is conserved (and thus can be used to infer information about the initial state of the family).

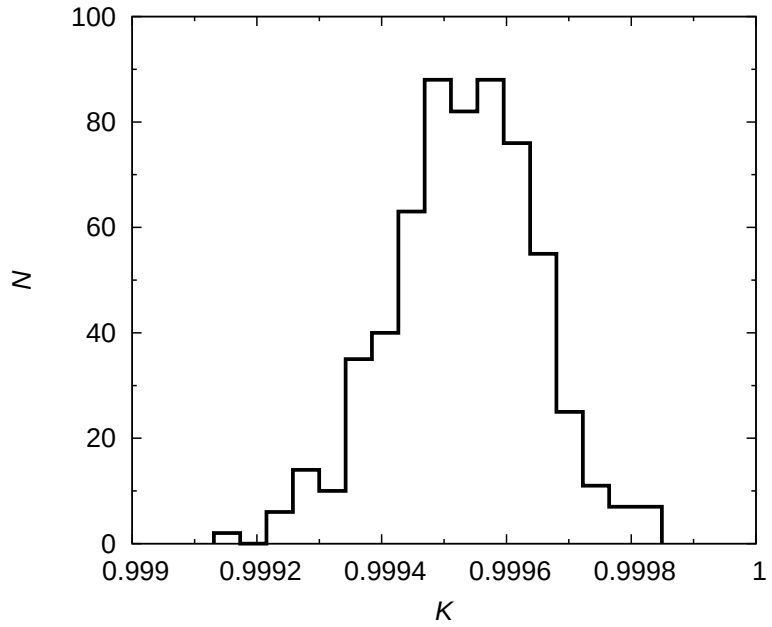

Figure 97: Distribution of the quasi-integral $K_2' = \sqrt{1-e^2}\,(2-\cos i)$ values for Agnia members. The characteristic dispersion of $\delta K_2' \simeq \pm 10^{-4}$ in this quantity agrees very well with an initial ejecta dispersion with a typical velocity of $\simeq 15$ m/s. This is also a value found below by an independent method of semimajor axis dispersion. Unlike the proper orbital elements, the K_2' variable undergoes little dynamical evolution (Fig. 100) and thus in this way the true initial velocity field is imprinted in K_2'-distribution.

First we note that Agnia members are nearly-uniformly distributed along the separatrix of the z_1 resonance (Fig. 95). This implies that the Agnia family cannot be very young. Note that reasonable ejection velocity fields produced by collisional breakup events yield longitudes of perihelion and node dispersed by $\lesssim 10^\circ$. For a typical velocity of ~ 15 m/s, suggested above from the K_2' dispersion, it would be even less. Hence, the "uniformity" of Agnia family members in σ does not necessarily require Yarkovsky forces. It can be fully understood from the differential rate of circulation/libration of the angle σ for different asteroids. The time it takes this to happen can be used to infer a lower limit on the age of the Agnia family.

For this purpose, we conducted the following numerical experiment. We started with a synthetic Agnia family as a tightly compact cluster in a, e, i and σ. Within the z_1 resonance, this fake family is initially a compact cloud as shown in the first panel of Fig. 98. To better define the circulation time, our fake family is composed of a subgroup of 23 observed Agnia family members and 3 sets of "clones" produced by adding small values to the eccentricities and inclinations of the real objects. Thus, we integrated 92 bodies in total.

Figure 98 shows the evolution of our synthetic family as tracked in the space of z_1-resonance variables $(\sigma, \dot\sigma)$. We note that the initially tight cluster of objects spreads in time. After ~ 40 My, it becomes uniformly dispersed along the separatrix of the z_1 resonance. This result confirms that the Agnia family is more than 40 My old. To describe the dispersal quantitavely (instead of a trivial observation in $(\sigma, \dot\sigma)$ plots), we can use one of the following techniques:

1. We define an auxiliary polar angle ϕ in the $(\sigma, \dot\sigma)$-plane (see Figure 98), with a scaling that maps a $(0^\circ, 360^\circ)$ interval of σ and $(-1, 1)''$/yr interval in $\dot\sigma = g + s - g_6 - s_6$ into common intervals $(-1, 1)$. At each timestep of our numerical simulation, we compute a dispersion D_ϕ in the polar angle ϕ as

$$D_\phi^2 = \frac{1}{N(N-1)} \sum_{i \neq j} (\phi_i - \phi_j)^2 \ , \tag{54}$$

   where $N = 92$ is the number of integrated bodies and ϕ_i is the polar angle of the i-th body (Figure 99). Since we start with a compact cluster, D_ϕ is small at the beginning ($\sim 7^\circ$) but grows with time due to the differential libration of the bodies in the resonance. After ~ 40 My it saturates at $\sim 103.5^\circ$, the value corresponding to a uniform distribution of bodies along a circle.

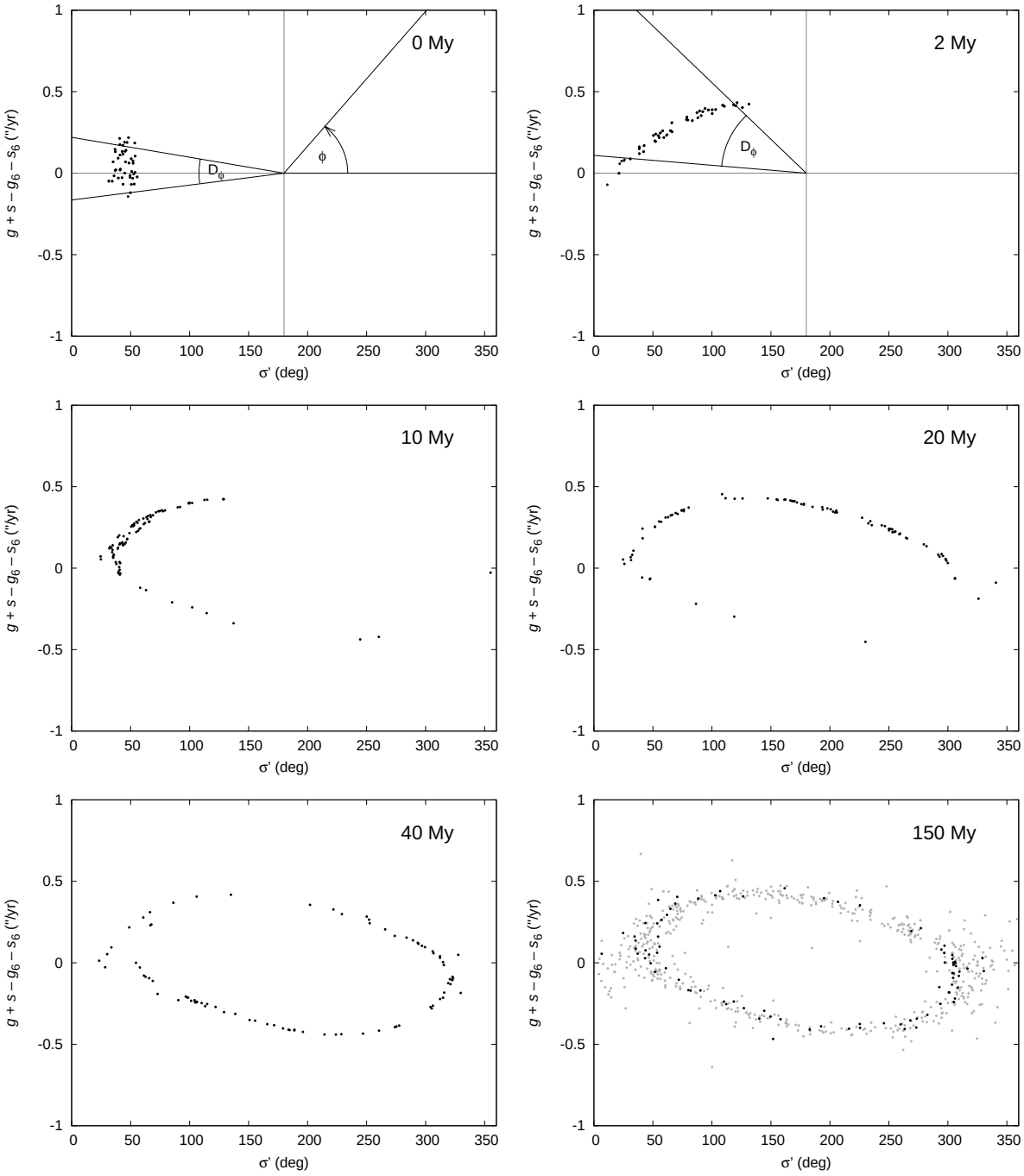

Figure 98: Snapshots of the numerically integrated evolution of the Agnia family projected onto the z_1 resonance variables: initial state of 92 tightly clustered bodies (top left), 2 My (top right), 10 My (middle left), 20 My (middle right), 40 My (bottom left), 150 My (bottom right). After about 40 My the clump becomes entirely dispersed near separatrix of the resonance with no memory of the initial state; the last frame (at 150 My) shows both the numerically integrated particles (bold symbols) and the true Agnia family (light symbols). The auxiliary angle ϕ, whose origin and sense is shown on the top left panel, is used to better describe dispersion of the clump (see Fig. 99 and the text). An animation of our complete simulation can be found at `http://sirrah.troja.mff.cuni.cz/yarko-site/` .

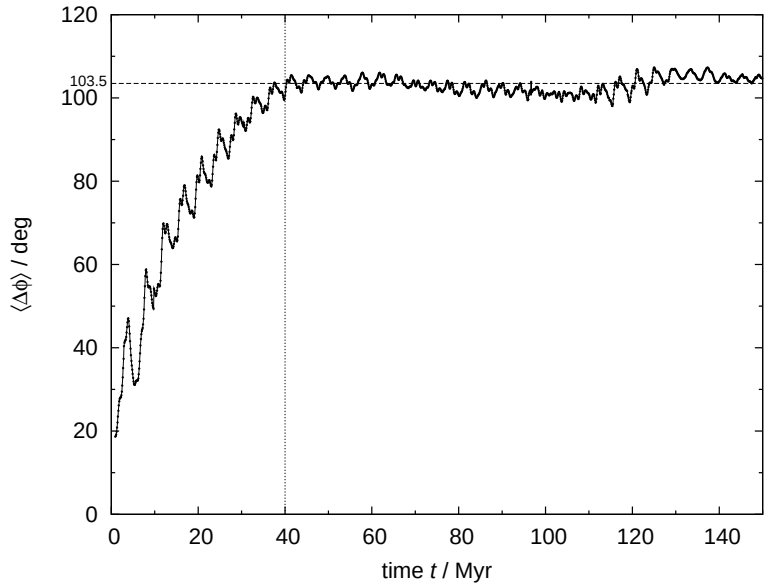

Figure 99: Temporal evolution of D_ϕ from Eq. (54) issued to measure dispersion of the synthetic Agnia family along the separatrix of the z_1 resonance. Initially, the family starts very compact, but after $\simeq 40$ My D_ϕ attains the value of $\simeq 103^\circ$ with no further evolution. This value corresponds to a uniformly distributed bodies along the separatrix and also to the currently observed Agnia family members. The oscillations, especially near the initial epoch, are due to slower change in ϕ near the unstable stationary foci of the z_1 resonance (i.e., near $\sigma = 0^\circ$ and 360°).

2. We calculate the dispersions D_e and $D_{\sin i}$ of the proper eccentricity and the sine of the proper inclination (defined similarly as D_ϕ). They exhibit the same pattern and reach an equilibrium state after ~ 40 My, but with larger oscillations (Figure 100). Moreover, the proper e and $\sin i$ distributions of the observed asteroids exhibit a depletion in the family centre. (Actually, there is a 'hole' in the 3-D space of (a, e, i) visible at Figure 92; see Section 7.4.2 for the discussion of the semimajor axis.) This is a natural consequence of the fact, that the asteroids spend more time near the unstable loci of the z_1 resonance at $\sigma = 0^\circ$ and 360° (similarly to the well-known pendulum case).

3. We use a standard 2-dimensional Kolmogorov-Smirnov test (Press *et al.* (2001)): we calculate a time series of probabilities $p(>D)$, that the two 2-D distributions in the $(e, \sin i)$ plane of the observed family members and of the dispersing cluster are identical (i.e., the Kolmogorov-Smirnov difference D between the two distributions might be a product of statistical fluctuations). We show the probability $p(>D)$ vs. time t plot in Figure 101 and an example of the $(e, \sin i)$ plot at the particular time $t = 92.4$ My, when the probability is high.

Next, we repeat our numerical simulation above with Yarkovsky forces included. The goal here is to verify the near-conservation of the K_2' variable even in this generalized case. We start with the same initial data as before. The sizes of the our integrated bodies (23 asteroids and clones) are computed from their H values and a geometric albedo of 0.17. Most of these bodies are $3 < D < 8$ km in diameter. We assign them low-surface conductivity values of $K = 0.002$ W/m/K, surface and bulk densities of 1.5 and 2.5 g/cm^3 and specific heat capacity 680 J/kg/K (values expected for regolith-covered multi-kilometer main belt asteroids). Rotation periods are given a Gaussian distribution peaked at 6 hr, but values smaller than 3 hr and larger than 12 hr are excluded. Spin axis obliquities are set to represent a random distribution of spin axes in space. Because these initial data are unconstrained, we do not attempt in this simulation to fit the observed a distribution among the Agnia family members. This will be tackled in the next section using a Monte Carlo technique.

All our previous results are similar to the new runs, except now 4 bodies out of 92 managed to escape from the resonance due to Yarkovsky drift. We focus our attention on the behavior of the dispersion D_K of the K_2' quantity defined above (shown as a bold lower curve in Fig. 100). Interestingly, D_K is nearly constant over the entire integration timespan of 150 My; major perturbations only occur when some of the bodies leave the z_1 resonance. This result is important because it confirms that we can use

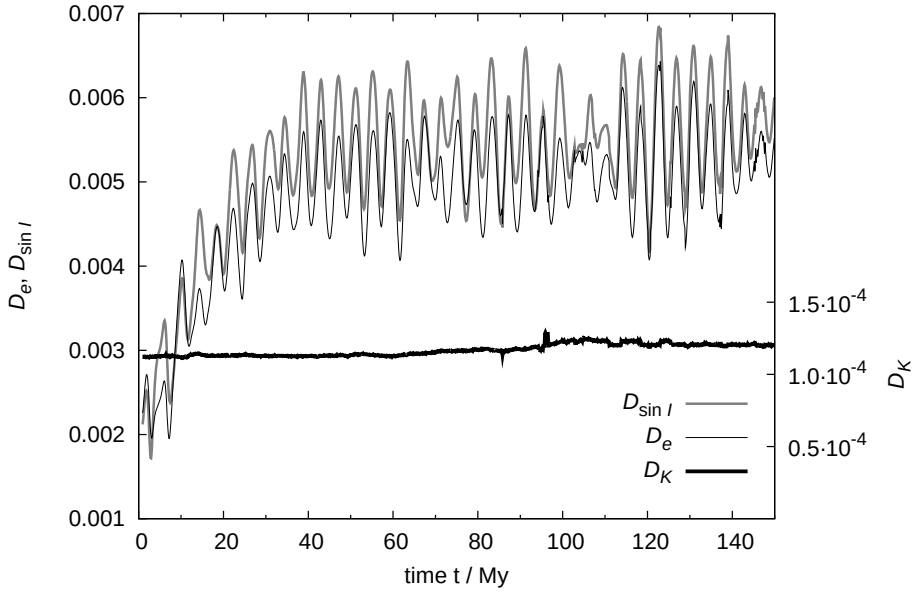

Figure 100: Temporal evolution of D_e and $D_{\sin i}$ (left ordinate) which undergo both: (i) long-term increase with saturation at $\simeq 40$ My (compare with D_ϕ at Fig. 99), and (ii) large oscillations with a period of near-separatrix libration. The right ordinate and bold lower curve shows temporal evolution of D_K, dispersion of the K_2' variable, now determined in the simulation that contains the Yarkovsky forces. D_K is quasi-constant with only very small change due to a few particles that escaped from the z_1 resonance.

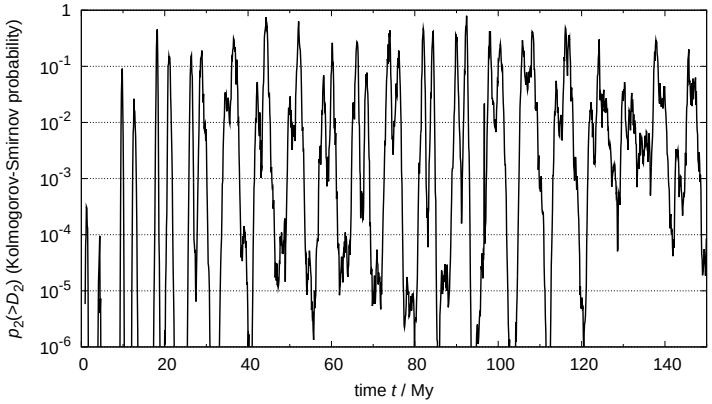

Figure 101: Kolmogorov-Smirnov test of difference D between the combined 2-D eccentricity and inclination distribution of the observed Agnia family and in our simulation. We show probability $p(>D)$ of such a difference arises just as a statistical fluke and the two distributions are identical (log-scale). Since we start with a compact cluster, $p(>D)$ is initially very small, but then it periodically attains values very close to unity (with a period of large-amplitude librations in the z_1, of course). A maximum of more than 80% coincidence is attained at time ~ 92 My.

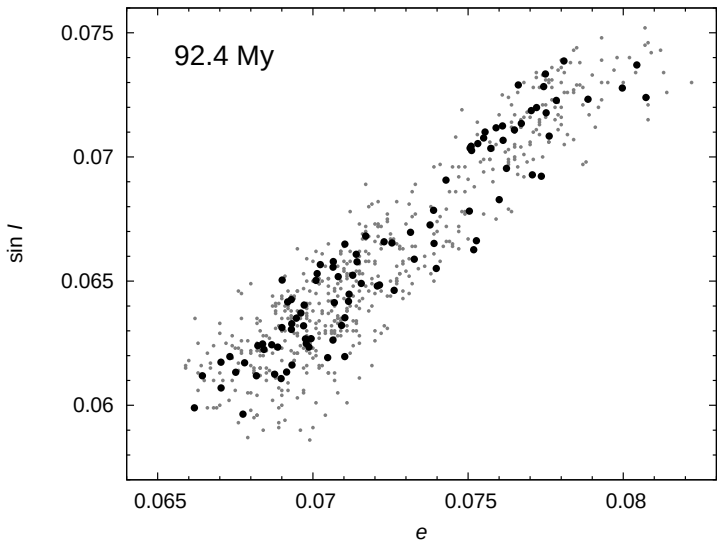

Figure 102: The nominal Agnia family members projected onto the plane of proper eccentricity e and inclination $\sin i$ (light symbols) and the configuration of of numerically integrated sample of bodies at time 92.4 My when the Kolmogorov-Smirnov probability of their coincidence shows a maximum. Both distributions indicate concentration toward extreme values of the proper elements and depletion near their mean values for the family. This effect occurs periodically due to libration cycle in the z_1 resonance.

the currently-observed K_2' distribution to infer quantitative information about the initial velocity field (Sec. 7.3.2 and Fig. 97).

7.4.2 Semimajor axis distribution fitted

We are now finally in a position to explore the semimajor axis evolution of Agnia family members. We find that the observed a distribution is characterized by those small members that have achieved extreme a values (Fig. 92). Our method here closely follows the work of Vokrouhlický et al. (2005b), who showed that such a skewed distribution is a consequence of the Yarkovsky-O'Keefe-Radzievskii-Paddack (YORP) effect. Objects have their spin axes evolve to alignments perpendicular to the orbital plane, which in turn accelerates the Yarkovsky migration of asteroids and depletes the family center. In what follows, we apply the method of Vokrouhlický et al. (2005b) to the Agnia case.

Consider family members projected onto the plane of proper semimajor axis a and absolute magnitude H. By choosing a center a_c of the family, typically (but not necessarily) close to the largest body, we assign a parameter C to each asteroid according to: $0.2\,H = \log(\Delta a/C)$, with $\Delta a = a - a_c$. We characterize the distribution of these family members using a one-dimensional array $N_{\rm obs}(C)$ that indicates the number of asteroids occupying a bin $(C, C + \Delta C)$ for some suitable value of ΔC. An effort is then made to match the observed distribution $N_{\rm obs}(C)$ with a model prediction of $N(C)$ objects in the $(C, C + \Delta C)$ bin. To that end, Vokrouhlický et al. (2005b) search to minimize a "target (χ^2-like) function" (see also Press et al., 2001)

$$\Psi_{\Delta C} = \sum_{\Delta C} \frac{\left[N\left(C\right) - N_{\rm obs}\left(C\right)\right]^2}{N_{\rm obs}\left(C\right)} \tag{55}$$

by varying the free parameters in the model. Note the occurrence of $N_{\rm obs}(C)$ in the denominator of (55) which may be formally interpreted as assigning $\sqrt{N_{\rm obs}(C)}$ errors to the observed number of asteroids in the appropriate bin. Admissible solutions are characterized by $\Psi_{\Delta C}$ of the order equal to the number of used bins in C, while solutions giving much larger $\Psi_{\Delta C}$ are incompatible with the observed family. We use the incomplete gamma function $Q(a, \Psi^\star_{\Delta C})$ as a goodness-of-fit parameter (see, e.g., Press et al., 2001), where a is the number of ΔC-bins minus three (number of free parameters) and $\Psi^\star_{\Delta C}$ is the minimum value of the target function (55). Since our best solution yields a high-quality fit ($Q = 0.97$), we simplify the parameter-error analysis by deriving them from the level curve of $\Psi_{\Delta C} = a + 3$, i.e. level curve of the target function equal to the number of ΔC-bins ("observations"). Solution of this $\Psi_{\Delta C}$ level-curve correspond to $Q \sim 0.2 - 0.3$ according to number of degrees.

As far as our theoretical model is concerned, we use the same Monte Carlo approach as described in Vokrouhlický et al. (2005b). Namely, we start with an initial, post-breakup a distribution for the family asteroids using a simple model with an isotropic velocity field. Fragments of a characteristic size, 5 km in our case, are assumed to be dispersed with a Gaussian distribution of velocity components having a standard deviation value of V. V is one of the free parameters to be solved for in minimalization of $\Psi_{\Delta C}$. After defining the initial conditions, each asteroid evolves in a from Yarkovsky forces over a time interval defined as the age of the family T. The strength of the Yarkovsky forces depends on some assumed thermal parameters and also on the spin state of the asteroid.[24] The latter quantity is folded into a dependence on the obliquity ϵ and rotation period P. While these parameters are set at the initial time, they are assumed to evolve over the long-term due to the YORP effect (Rubincam, 2000; Vokrouhlický and Čapek 2002). We use a characteristic strength of the YORP effect computed by Čapek and Vokrouhlický (2004) for a large sample of objects with different random shapes and surface conductivities. The uncertainties in modeling of the YORP effect are adjusted by including a third free parameter $c_{\rm YORP}$ that linearly multiplies the YORP influence on ϵ and P. Finally, we run numerous simulations over a matrix of different values for the free parameters $(T, V, c_{\rm YORP})$. Then, for each run, we compute the target function $\Psi_{\Delta C}$ and search for parameters that lead to its minimum value.

Figure 103 (symbols in the upper left part) shows the distribution of $N_{\rm obs}(C)$ values for the Agnia family and $\Delta C = 1.5 \times 10^{-6}$ AU. The computed distribution was derived as a mean over central values $a_{\rm c}$ in $(2.788, 2.792)$ AU (i.e., near the center of small members in the family). If we were using only a single $a_{\rm c}$ value from this interval, some of the bin occupancies would show random fluctuations that would affect our fit. We eliminated this potential problem by computing the $N_{\rm obs}(C)$ distribution using an average over results for which $a_{\rm c}$ spans a small interval near the unknown center of the family. The concentration of small Agnia members toward extreme values of a is seen in $N_{\rm obs}(C)$ as two significant maxima that are offset from the center at $C \sim \pm 10^{-5}$ AU. They are slightly asymmetric to express little more Agnia asteroids with $a \geq a_{\rm c}$ (see also Fig. 92).

The largest asteroid, (847) Agnia, is offset by $\simeq 0.005$ AU from the center of the smaller members in the family (Fig. 92). Though unusual, this feature may mean the fragments were ejected with an anisotropic velocity field (see, e.g., examples in Marzari et al., 1996). The a displacement described above corresponds to ~ 30 m/s in the transverse velocity component, comparable with the characteristic velocity dispersion of smaller family members that are discussed below.

Figure 103 shows results from our simulation where we considered the surface conductivity K of Agnia members as a random variable in the range $0.001-0.01$ W/m/K. More precisely, we distribute the quantity $\log K$ uniformly in the interval $(-3, -2)$. We assumed surface and bulk densities of 1.7 and 2.5 g/cm^3 and specific thermal heat $C = 680$ J/kg/K. In addition to the three solved-for parameters $(T, V, c_{\rm YORP})$, we introduced a fourth parameter ξ which yields the fraction of prograde rotating asteroids. Each set of matrix runs assumed a different value of ξ. The goal was to better describe the asymmetry of the $N_{\rm obs}(C)$ distribution. Figure 103 suggests $\xi \geq 0.5$. Thus, we tested values in the interval $(0.5, 0.75)$.

The minimum value of the target function $\Psi_{\Delta C}$ obtained with our model was 22, significantly less than the number of C-bins (39). For this reason, we consider our result statistically sound; this is also confirmed by the quality-factor value $Q = 0.97$. If, for simplicity, we thus used the threshold $\Psi_{\Delta C} = 39$ to define the standard error of the solved-for parameters, our best fit solution would read: $T = 100^{+30}_{-20}$ My, $V = 16^{+4}_{-6}$ m/s and $c_{\rm YORP} = 0.9^{+1.1}_{-0.3}$. These values correspond to $\xi = 0.57$, which may indicate a slight asymmetry between the number of prograde and retrograde rotating asteroids produced by the initial breakup of the family. Figure 104 shows how the minimum-acquired $\Psi^{\star}_{\Delta C}$ depends on different choices of ξ, indicating even an equal partition ($\xi = 0.5$) could still offer a statistically reasonable though less satisfying solution. Conversely, ξ must be smaller than 0.68, a value that would lead to an unjustified asymmetry between the initially prograde and retrograde rotators.

Interestingly, our best fit value of $\xi = 0.57$ is similar to that found by Nesvorný and Bottke (2004) for the members of the young Karin cluster. The source of this asymmetry is unknown. One possibility is that there is something intrinsic in the breakup process that produces more prograde than retrograde objects (e.g., La Spina et al., 2005). A second possibility is that the value of ξ produced in different breakup events follows a Gaussian distribution centered around $\xi = 0.5$. If true, the similarities between Agnia and Karin families may be a statistical fluke. Finally, a third possibility is that immediately after a family-forming event, fragments take some time to generate regolith. In the interim, their higher K values, which may be closer to bare rock than a regolith-covered surface, may allow the seasonal Yarkovsky effect to dominate the diurnal variant, such that all asteroids drift inward. This effect would create an offset

[24] We use a linearized approximation by Vokrouhlický (1998, 1999) and Vokrouhlický and Farinella (1999) to obtain the diurnal and seasonal components of the semimajor axis secular change da/dt.

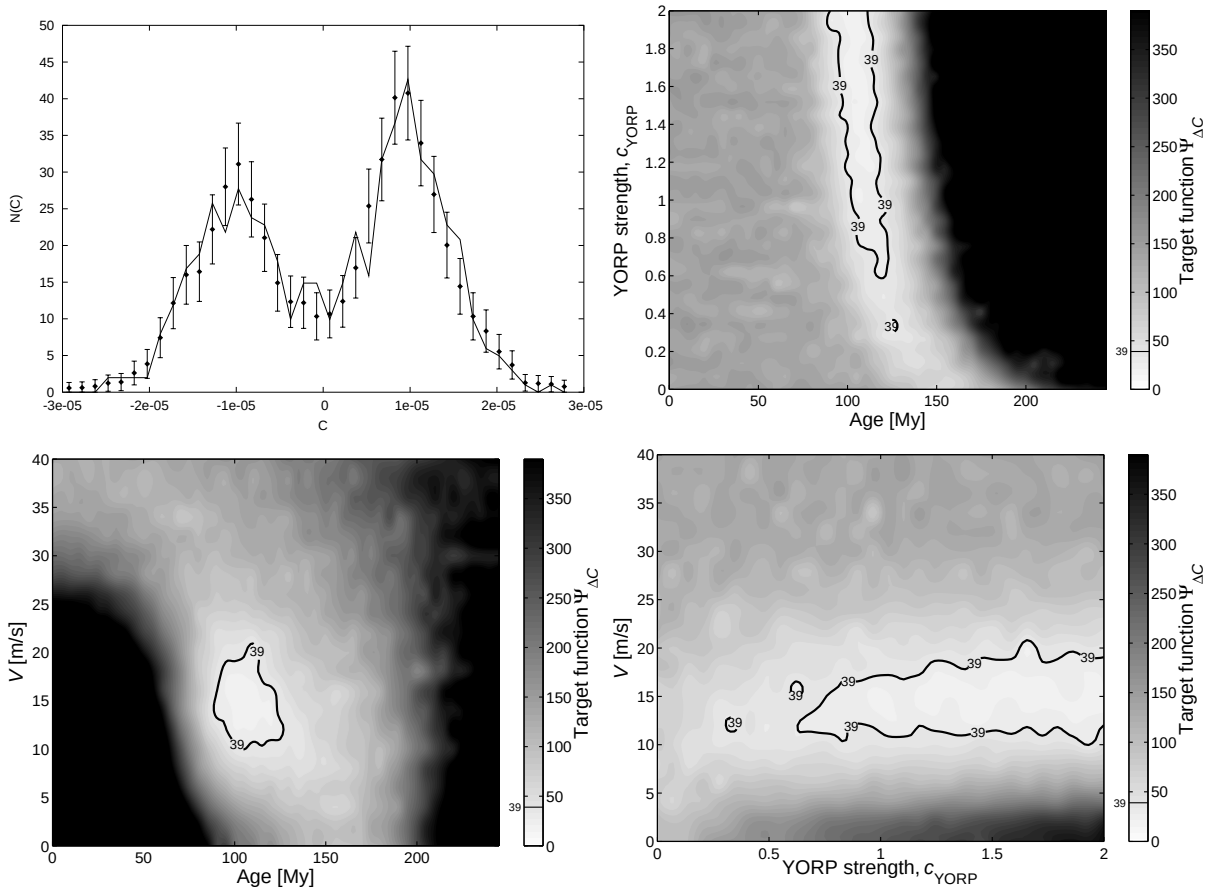

Figure 103: Results of our simulation for the Agnia family with mean albedo $p_V = 0.17$ and surface thermal conductivity randomly spanning $K = 0.001 - 0.01$ W/m/K. The best-fit solution $N(C)$ (solid line in the top left panel) is shown with the observed data $N_{\rm obs}(C)$. These were obtained by $(C, C + \Delta C)$ binning with $\Delta C = 1.5\times10^{-6}$ AU and $a_{\rm c}$ uniformly averaged in the range (2.788, 2.792) AU. We assign a formal error-bars of $\sqrt{N_{\rm obs}(C)}$ to $N_{\rm obs}(C)$. Note a slight asymmetry of the data about $C = 0$ with significant maxima at $C = \pm10^{-5}$ AU. The other three panels show projection of the best value of the target function $\Psi_{\Delta C}$ for various pairs of the solved-for parameters: (i) age T vs. YORP strength parameter $c_{\rm YORP}$, (ii) age T vs. characteristic velocity V of initial ejection of $D = 5$ km fragments, and (iii) $c_{\rm YORP}$ vs. V. Formal 1σ contour, defined by $\Psi_{\Delta C} = 39$ (number of bins in C; see the text), is shown in bold; contours for other values of the target function are shown in light (their increment is $\Delta\Psi_{\Delta C} = 10$).

in the family's semimajor axis distribution that would be skewed toward smaller a values. Eventually, the family asteroids would develop regolith and return to a state where their migration was dominated by the diurnal Yarkovsky effect (which allows asteroids to evolve both inward toward and outward away from the Sun). Of these three possibilities, we can rule out the last one for Agnia because it appears to have more members further from the Sun than closer to the Sun.

According to Vokrouhlický et al. (2005b) the best-fit value of T roughly scales with $\sqrt{p_V}$, such that a smaller mean albedo value for Agnia family members (in the multi-km range) would make the family older. An albedo value smaller than ~ 0.1, however, is unlikely. For this reason, we consider the upper age of the Agnia family to be ~ 140 My. If small family members have higher albedo values than predicted here (e.g., Tedesco et al., 2002), the Agnia family's age might be smaller than 100 My, with the lower bound set at 40 My (Sec. 7.4.1). We also find it interesting that the best-fit value of the characteristic dispersion velocity V of $D = 5$ km Agnia members is compatible with our estimate from an analysis of the K_2' function distribution (Fig. 97). As in Vokrouhlický et al. (2005b) the strength of the YORP effect is loosely constrained with only the no-YORP solution ($c_{\rm YORP} = 0$) statistically excluded.

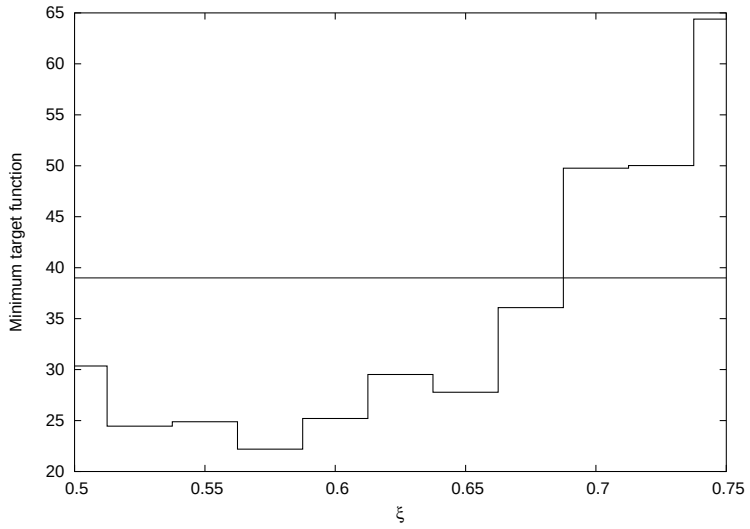

Figure 104: Minimum values of the target function $\Psi^{\star}_{\Delta C}$ for different values of the asymmetry parameter ξ characterizing initial proportion of the prograde vs retrograde rotating fragments. The best-fit solution slightly prefers more prograde rotators among initial collision ejecta (57% vs 43%). Statistically admissible solutions are, however, obtained also for symmetric partition of prograde/retrograde rotators.

7.5 Conclusions

The unique relation of the Agnia asteroid family to the high-order resonance z_1 allows a deeper insight into its evolution and initial state than is possible with other families of comparable size and age. We have shown this by placing independent, and consistent, constraints on the age of this family. We have also derived a characteristic velocity for multi-kilometer family members that is consistent with estimates from other small families.

Interestingly, Bottke et al. (2005a,b) find that the mean disruption lifetime of a $D \sim 2$ km asteroid in the main belt is ~ 700 My. If this estimate is true, most observed Agnia members are original fragments that have not yet experienced secondary fragmentations. The Agnia family, together with other even younger families (Nesvorný et al., 2002, 2003), might be thus a good laboratory to study outcome of the collisional fragmentation of large main belt asteroids (see e.g., Nesvorný et al., 2006b).

We note that a relatively young age found for this family is in agreement with the dominant Sq spectral type of its members, and a related small mean value of PC_1 found from the SDSS data. Nesvorný et al. (2005) interpret both in the frame of a space weathering scenario.

A preliminary analysis indicates that the Agnia family is unlikely to be a significant contributor to the dust and micrometeorite population produced by main belt collisions. Using the code described in Bottke et al. (2005d), we examined dust population from the present-day Agnia family. Our results suggest that Agnia-derived dust is likely to be $2-3$ orders of magnitude smaller than that produced by the background main belt population. This is because the family is both small (parent body $D \sim 50$ km) and modestly old (~ 100 My); the combination means that its dust/micrometeorite population has likely reached quasi-collisional equilibrium with the background population. Thus, unless the tight (a, e, i) clustering of the Agnia family can overcome its putative low dust production rate, the Agnia family is unlikely to be a source of some of the weak dust bands proposed by Sykes (1988).

Finding smaller asteroid families in the main belt, studying their structure, and linking this analysis to the physics of collisional processes, origin of interplanetary dust and meteorite science is an interesting long-term project. Our study of the Agnia family is a piece of mosaic indicating our current ability to fulfill this task.

Acknowledgments. This work has been supported by the Grant Agency of the Czech Republic (grant 205/05/2737) and NASA's Planetary Geology & Geophysics program (WFB and DN).

8 Conclusions

We studied the influence of non-gravitational forces on the long-term evolution of small asteroids. The major results presented in this thesis can be summarized as follows:

1. We reviewed the applications of the Yarkovsky/YORP effect and its mathematical formulation.

2. We described major aspects of the orbital evolution of meteoroids and small asteroid fragments under the influence of gravitational resonances and the Yarkovsky effect. We computed several statistics (e.g., the crossing probability of the J3/1 resonance) which may be used in future to improve Monte-Carlo models of meteoroid transport.

3. The short-lived orbits of (2953) Vysheslavia, and several other asteroids located just above 5/2 mean motion resonance with Jupiter, can be explained as a consequence of the Yarkovsky effect, which pushes the asteroids from stable regions into the current unstable positions. We supported this conclusion by photometric observations of (2953) Vysheslavia — they reveal the retrograde spin-axis orientation, which is in concert with negative Yarkovsky semimajor axis drift.

4. The unstable asteroids inside 2/1 mean motion resonance with Jupiter have been most probably transported from the neigbouring Main Asteroid Belt; the Yarkovsky/YORP effect is efficient enough to keep this transient population in steady-state. Unfortunately, we were not able to unveil the origin of the long-lived Zhongguos and Griquas yet.

5. We studied the Eos asteroid family, namely the three dynamical procesess, how the Yarkovsky drifting orbits interact with resonances: "bracketing" by strong mean motion resonances, "crossing" of weaker resonances, and "trapping" in secular resonances. The Yarkovsky effect seems to be essential to understand the current observed shape of the family in the space of proper orbital elements. We were also able to determine the family age to be 1.3 Gy.

6. The Agnia family is located almost entirely inside the z_1 secular resonance, a lucky coincidence, which allowed us to disclose the family age (surely more than 40 My and less then 140 My) and the magnitude of the mutual velocities (15 m/s for 5 km fragments) gained due to the original disruption event.

7. We implemented computation of proper and resonant orbital elements into the commonly used SWIFT integration package.

9 Appendices

9.1 A catalogue of synthetic proper elements

In order to study fine details of orbital dynamics and small structures in the (a, e, I) elements space, we have to apply a suitable digital averaging to the osculating elements produced by numerical integrators. We use the following approach for regular (non-resonant) orbits:

1. We sample *osculating orbital elements* with a typical sampling period 1 y and store the non-singular elements: a, $h = e\cos\varpi$, $k = e\sin\varpi$, $p = \sin\frac{I}{2}\cos\Omega$ and $q = \sin\frac{I}{2}\sin\Omega$ in a running window array (typically, it holds data for all planets and test particles and for the last 80 timesteps in the memory).

2. We apply a multi-level convolution filter (the so called Kaiser windows), similarly as Quinn *et al.* (1991). One have to carefully select the sequence of filter functions (denoted A and B) and the corresponding decimation factors, to avoid aliasing. For example, we use filters A, A, A, B and factors 10, 10, 5, 3 and the resulting *mean elements* then have an output timestep 1500 y.

3. The mean elements are stored in another running window array (with 2^N elements) and a frequency modified Fourier transform (FMFT) is calculated for the (h, k) and (p, q) pairs (Šidlichovský & Nesvorný (1997); the FMFT C-function was kindly provided by N. Nesvorný). We obtain g and s frequencies, corresponding amplitudes and phases for the 10 terms with the 10 largest amplitudes.

4. Now, we have to drop terms with planetary frequencies (because the amplitudes of these *forced terms* are proportional to e or I of the planets; they are not proper elements of the asteroid).

5. The $e_{\rm p}$ or $I_{\rm p}$ proper elements are the amplitudes of the largest remaining g or s terms. Proper semimajor axis $a_{\rm p}$ is a simple running average. The width of the running window is usually $2^9 = 512$ elements (i.e., 0.768 My) and the output time-step 0.1 My.

We implemented the filtering outlined above in the framework of the SWIFT integrator (*SWIFT*); the routines can be used both on-line during the numerical integration (to reduce the output storage) and off-line. See *Yarko-site* for download.

As a particular test of our algorithms, we prepared a catalogue of proper elements (`prop_fmft.dat`; presented at *Yarko-site*). The system allows a fully automated calculation of proper elements for all numbered asteroids, listed the Bowell's AstOrb catalogue (*AstOrb*)[25] of osculating elements, a comparison with the already existing AstDyS proper elements catalogue (*AstDyS*) by Milani and Knežević, and possibly an update on a regular basis. (The computation of 10^5 orbits takes approximately 2 weeks of CPU time on a 4 CPU MOSIX cluster.)

A comparison between the AstDyS catalogue and our `prop_fmft.dat` (one example is at Figure 105) shows that both methods mostly produce equivalent results (with a relative difference between the eccentricities or the inclinations smaller than 10 %). The differences are larger for 10 % of orbits, which can be attributed to: i) the shorter integration time span in our case, ii) the better spectral resolution of the FMFT method (especially, when the integration spans longer time, a single spectral line splits-up to a multiplet with different amplitudes and phases), iii) proximity of chaotic mean motion resonances, or iv) secular resonances with very long libration periods (we do not remove $\simeq$ My oscillations).

[25] There is a *WWW interface to the* `astorb.dat` *catalogue* at the *Yarko-site* also. It allows to search asteroids by their designations (regular expressions), grep the most important orbital and physical data, calculate ephemerides and plot sky maps (either generated from the GSC catalogue or downloaded from the Palomar Digitized Sky Survey). The Earth's ephemeris is calculated according to the VSOP82 theory, the orbital motion of the asteroid around the Sun is approximated by a two-body ephemeris. Because the up-to-date versions of the `astorb.dat` catalogue have the osculation epoch always close to the present, the precision of the ephemeris is of the order 1 arcsec. This is sufficient to predict the position of an asteroid on the sky at the time of an intended observation and to pin-point a telescope, which has a field of view 10 arcmin. We use this tool during photometric observations at the Hradec Králové Observatory. The long-term observational program is partly devoted to the photometry of the Eos family asteroids; the lightcurves obtained so far can be downloaded from *HPHK Observer services* (see also Figure 106).

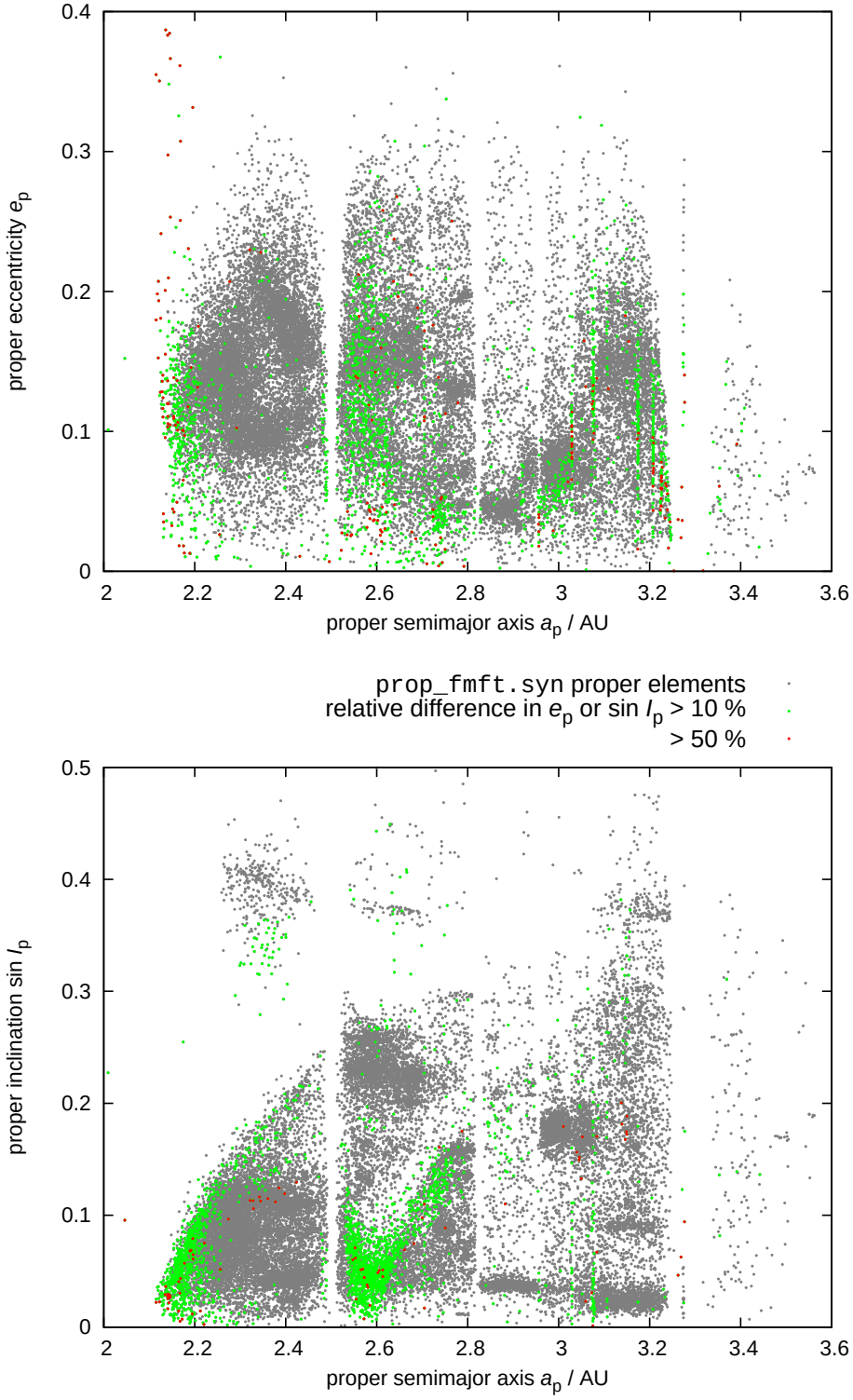

Figure 105: The proper semimajor axis vs. eccentricity (top) and vs. proper sine of inclination (bottom) calculated for the first ≃30,000 orbits from the AstOrb catalogue of osculating elements, version Mar 2$^{\mathrm{nd}}$ 2003. The comparison with the AstDyS catalogue of proper elements is provided: the orbits, which differ by more then 10 % (or 50 %) in inclinations are plotted green (red). The principal differences are caused by the secular resonances: z_2, z_3 (near 2.2 AU) and $g + g_5 - 2g_6$ (near 2.6 AU). The differences in g and s frequencies are smaller (only 0.5 % of orbits is offset by more than 10 %). The proper semimajor axis is practically the same in both catalogues (the relative differences are smaller than 10^{-4}).

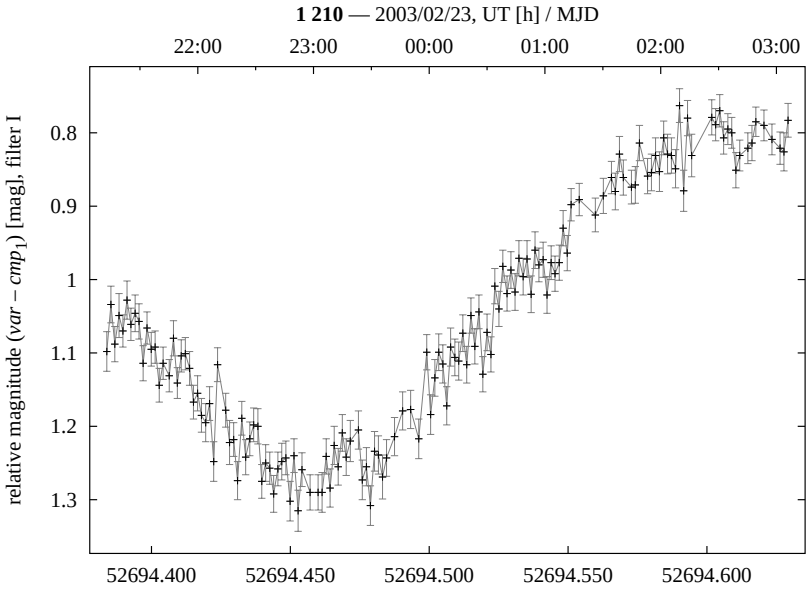

Figure 106: An example of the photometric observations acquired at the Hradec Králové Observatory: the Eos family asteroid (1210) Morosovia on Feb 23$^{\mathrm{rd}}$ 2003. A 40-cm $f/5$ reflector (Jan Šindel Telescope) equipped with a SBIG ST-7 CCD camera and an photometric I filter was used. Instrumental relative magnitudes are plotted here. This observation was perfomed by Martin Lehký. We usually exploit the WWW facilities at the *Yarko-site* during these observartions.

9.2 The SWIFT-MVS2 integrator, a faster variant of the MVS

The package SWIFT (Levison & Duncan (1994), *SWIFT*) is a well known and commonly used tool for solar system studies. It allows to integrate a set of massive, mutually interacting bodies, and massless "test particles". SWIFT includes 4 integration methods: Wisdom-Holman Mapping (WHM or MVS), Regularised Mixed Variable Symplectic (RMVS), a fourth order T+U Symplectic (TU4) and Bulirsch-Stoer (BS).

We have modified the original code in the following manner: i) We have incorporated Yarkovsky (hereinafter such an integrator is referred with the suffix -Y) and Poynting-Robertson (-PR) dissipative accelerations into the integrators and checked their results against analytic predictions (see Section 2.3.3). ii) We have implemented on-line digital filters based on the Kaiser windows (-F) (see Section 9.1). iii) We have implemented the 2^{nd} order symplectic integration scheme (MVS2) by Laskar & Robutel (2001), which seems to be at least 2 times faster than MVS, while keeping the same relative energy error. However, the algorithm is not "regularised", i.e., no close encounters are allowed. iv) We have parallelised integrators (namely the calculation of the TP accelerations) according to the OpenMP standard (*OpenMP*), which allows to run SWIFT on multiprocessor machines. We will present results of tests involving the new integrators, the parallelisation, the filter and the Yarkovsky acceleration implementation.

The `swift_rmvsy` package is available for download on our web *Yarko-site*. It can be compiled, together with the original SWIFT package, for various Unix-like systems and Windows.

The Yarkovsky and Poynting-Robertson accelerations. The theory of the Yarkovsky effect was published in Vokrouhlický (1998), Vokrouhlický & Farinella (1999). We have modified original SWIFT subroutines and added several new ones to incorporate the Yarkovsky acceleration (and later also the Poynting-Robertson force to study dust particle dynamics). Our method corresponds to Cordeiro *et al.* (1997), i.e., the thermal acceleration is applied during a 'kick' phase of the symplectic integrator, similarly as the conservative perturbation.

The addition of a weak dissipative force to the symplectic integrator does not affect its stability — it was proven by the comparison of secular changes of semimajor axis $\mathrm{d}a/\mathrm{d}t$ with the analytic estimates from Gauss equations (Figure 107).

A comparison of BS, MVS, RMVS and -FY integrators. A typical test run setup (unless specified otherwise) is: $4 + 50$ particles, timestep 20 days, stop time 0.2 My. (Initial orbital elements of the TPs

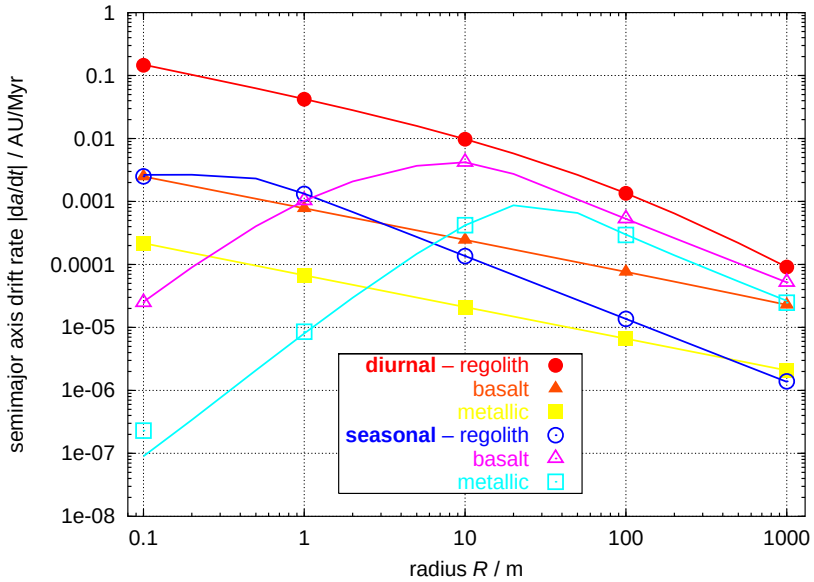

Figure 107: The absolute values of the semimajor axis drift rates $\mathrm{d}a/\mathrm{d}t$ (in AU/My) for particles with several values of radii (from 0.1 m to 1 km) and three different types of thermal parameters: regolith, basalt and metallic-like. The initial orbits of test particles were $a = 2\,\mathrm{AU}$, $e = 0$, $i = 0^\circ$. The two variants of the Yarkovsky acceleration (diurnal and seasonal) are plotted separately. The lines correspond to the analytic estimates, the points are computed numerically by a LSM fit of the output $a(t)$.

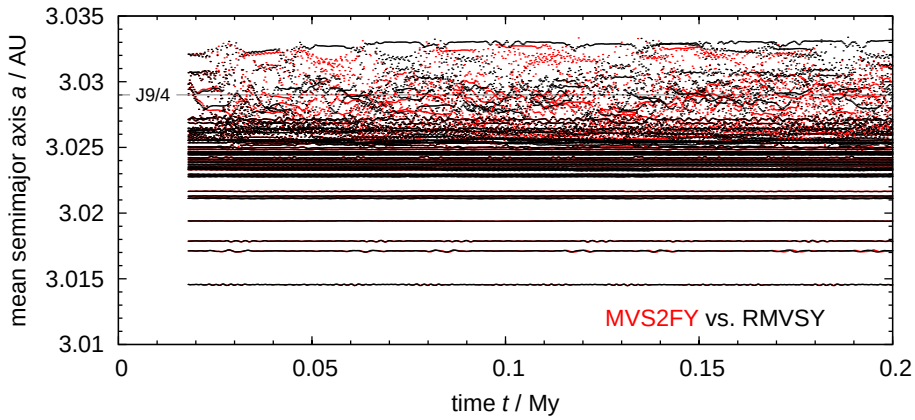

Figure 108: An example of a single test run in the mean semimajor axis vs. time plot. The integrators MVS2FY (red dots in the background) and RMVSY (black dots in the foreground) are used here. The results differ substantially only for chaotic orbits in the neighbourhood of the 9/4 mean motion resonance with Jupiter (the red dots are visible), while the results are equivalent in the stable regions (only the black dots are visible). The output of mean orbital elements starts at $\simeq 0.02$ My due to the initialisation of the digital filter.

are randomly distributed in the region of the Eos family, just below the J9/4 mean motion resonance.) The integrators BS, BSFY, MVS, RMVS3, RMVSF and RMVSFY have been tested. All $a(t)$ plots for individual runs look very similar, as they should; only chaotic orbits differ significantly (Figure 108). The summary of the CPU running times is presented in Table 24. We conclude, the on-line digital filter slows down the RMVS3 integrator by 30 %. Subroutines for the Yarkovsky effect calculation slow integrator further by a factor 1.8. The Bulirsch-Stoer integrator (with Yarkovsky subroutines) is approximately 10 times slower than RMVSFY.

Table 24: A comparison of the CPU times for several integrators (see text for the explanation of the abbreviations). The computation was performed on an Athlon 1.4 GHz processor; 'omf77' refers to the *Omni compiler*.

integrator (compiler)	time/sec	notices
BS (omf77)	4092	local error 10^{-8}
BSFY (omf77)	12200	
MVS (omf77)	273	
RMVS3 (omf77)	356	
RMVSF (omf77)	480	
RMVSFY (omf77)	874	

A comparison of g77, omf77 and other compilers. The comparison of different compilers has been performed for the RMVSFY integrator (see Table 25). The compiler omf77 seems to be faster than g77 by approximately 10 %. The commercial Fujitsu/Lahey and Portland group compilers 'beat' g77 by 30 %.

Table 25: A comparison of 5 different compilers available for the Linux operating system; computed on a Celeron 1 GHz processor.

RMVSFY (g77)	1652	g77–0.5.24
RMVSFY (omf77)	1496	Omni–1.3 (*Omni compiler*)
RMVSFY (fujitsu)	1371	Fujitsu F95
RMVSFY (lf95)	1147	Fujitsu/Lahey F95 Express 6.0
RMVSFY (pgf90)	1133	Portland group Fortran90
	1164	(with `-mp` on 1 CPU)

A Parallel version of SWIFT. The parallel program RMVSFY have been started on a two-processor machine. However, the RMVSFY is only 1.5 faster on two processors than on a single one (Table 26).

Table 26: A test of the parallelised RMVSFY integrator on a dual Pentium III 800 MHz machine. (The *Omni compiler* is able to compile it for SMP machines; see also *OpenMP*.)

RMVSFY (omf77)	1857	run only on 1 CPU
	1263	2 CPUs (SMP architecture)

A similar test has been performed for the MVSFY integrator (which allows no close encounters) and also for an integration involving one half of test particles (Table 27). The MVSFY turns out only 1.2 times faster than RMVSFY due to the delay caused by the filter and Yarkovsky subroutines (as compared to the factor 1.3 between the pure MVS and RMVS3). On 2 CPUs the integration by MVSFY takes 1.55 times shorter time span. (In case of 10 times larger number of TPs, i.e. 500, the ratio is even slightly better: 1.62.) When we manually split the job into two pieces and run two separate jobs, it will take 1.9 shorter time than the single run on 1 CPU. (It means: we loose 20 % of the computation speed on 2 CPUs, compared with 2 single runs, but we gain a simple manipulation with the output data files — there is no need to merge 2 output binary files.)

Table 27: A test of the MVSFY integrator. The setup is the same as in Table 26.

MVSFY (omf77)	1613	run only on 1 CPU (50 TPs)
	1044	2 CPUs (SMP architecture)
	846	1/2 of TPs
MVSFY (omf77)	1537	1 CPU, NTP = 500, $t_{\rm stop} = 0.02$ My
	945	2 CPUs

Tests of a MOSIX cluster. We have tested the MVSFY integrator on a heterogeneous MOSIX cluster (*Mosix*) with 8 CPUs and slow 10 Mb network (Table 28) The speed of the migrated process is almost the same (98 %), but only for low I/O. (Luckily, it is a typical case for our runs). Of course, on a 100 Mb or 1 Gb LAN the difference is not that substantial.

It is not yet possible to use the parallel version of SWIFT on Mosix, because Mosix does not support distributed shared memory. A usual surrogate is to split the calculation to several separate runs (e.g., using the automated `swiftsplit` script, included in the `swift_rmvsy` package). Nevertheless, the Mosix cluster is now still very useful for a comfortable job management.

Table 28: Running times for a single job migrating over a Mosix cluster to a Celeron 850 MHz machine and for 2 threads on a single CPU.

MVSFY (omf77)	1624	run on the home node, migration forbidden
	2030	started elsewhere, migrated to the same node
	1654	the same run, but with low I/O operations
MVSFY (omf77)	5078	2 threads on a single CPU

A new symplectic integrator SWIFT-MVS2FY(PR) ($\tau^4\epsilon + \tau^2\epsilon^2$). The SWIFT-MVS2FY is a new implementation of the integrator $\mathcal{SBAB}_2$ by Laskar & Robutel (2001), which is of the order $\tau^4\epsilon+\tau^2\epsilon^2$ and of index 2 (i.e., the number of evaluations of Hamiltonian parts $\mathcal{A}$ and $\mathcal{B}$). This integrator is yet without regularisation, i.e., it does not handle close encounters correctly. We use larger timestep 80 days (i.e., *4 times larger* than before) for tests in Table 29, but the precision of the integration remains comparable to the MVS. The MVS2FY integrator is approximately 1.7 times faster than MVSFY and 2 times faster than RMVSFY at the same level of precision. One can still enlarge the timestep.

Table 29: Running times for MVS2FY integrator with the timestep 80 days. (Nevertheless, the integration is still more precise than the MVS one.)

MVS2FY (omf77)	940	1 CPU
	588	2 CPUs
	945	1 CPU, `-omp` (without OpenMP pragma)

The energy and momentum errors do not accumulate, when we use the symplectic integrators. Nevertheless, the energy and momentum integrals oscillate and we can measure the precision of the integrator as the dispersion of the energy values over a sufficiently long time interval.

Both *the total energy error and the CPU time* depend on the integration timestep (Figures 109 and 110). The MVS2F is more precise by two orders of magnitude in a wide range of timesteps — from 2 up to 200 days. On the other hand, for a given timestep, it is usually 1.8 times slower than the MVSF. We usually use the timestep 20 days for the MVSF (or RMVS3F) integrators in our studies of the Main Belt Asteroids. So, if we want to keep the total energy error the same with the MVS2F, we can safely use 100 days timestep. In this case, however, the MVS2F is more than two times faster the MVSF.

To conclude, the SWIFT-MVS2FY integrator seems to be more efficient than the original MVS.

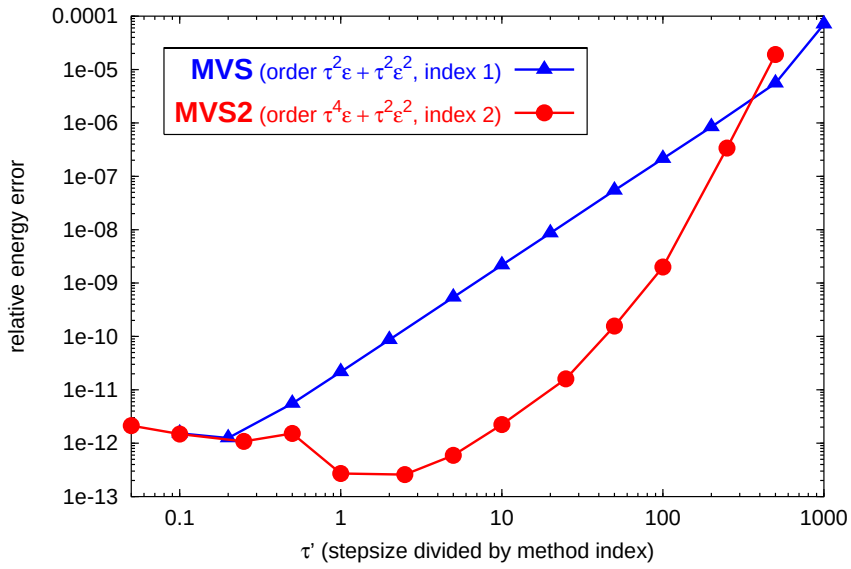

Figure 109: The relative timestep τ' vs. the relative energy error, computed for the Sun-Jupiter-Saturn system evolving for 0.1 My. τ' is the timestep dt divided by the method index, i.e., 1 for the classical leap-frog MVS and 2 for the new MVS2. The relative energy error is computed as the standard deviation σ_E of the total energy $E(t)$, in course of the integration, divided by the mean total energy $\langle E \rangle$.

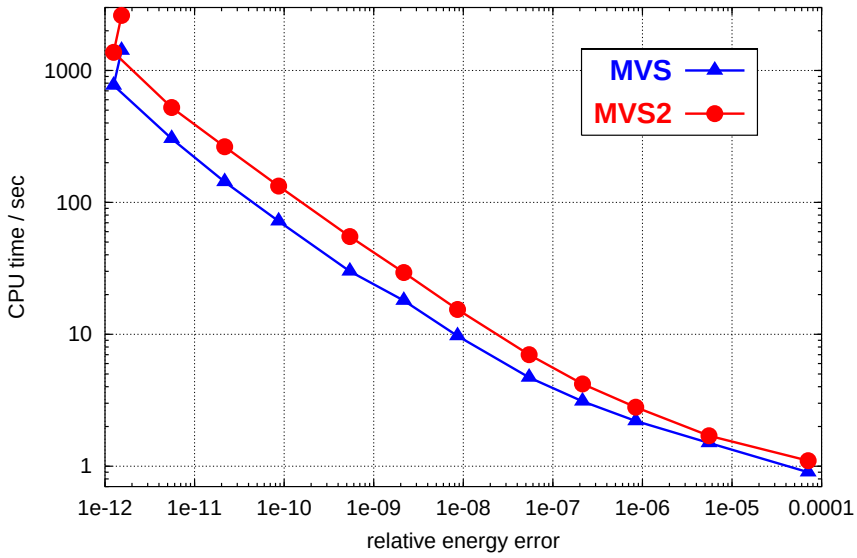

Figure 110: The dependence of the CPU time on the relative energy error for both integrators MVS2F and MVSF. The MVS2F timestep is selected 4 times larger than the MVSF one to keep a comparable precision (the total energy error). The computation has been performed on an Athlon 1.4 GHz processor.

9.3 A reprint of Yarkovsky's 'lost' pamphlet

We reprint here the work of Ivan Osipovich Yarkovsky, which he privately published in 1901 and where he describes the phenomenon, now called the Yarkovsky effect. (Even thought, the very first note on the Yarkovsky effect was later discovered in his *Hypothése cinetique*, published in French in 1888.) The booklet is called *Плотность свѣтового ефира и оказываемое имъ сопротивление движению* (*The density of luminiferous ether and the resistance it offers to motion*); it was printed in Bryansk. This is the Yarkovsky's 'lost' pamphlet quoted by Öpik (1951). We decided to include the reprint here, because of the historical interest and because the original publication is not easily accessible (while this thesis can be downloaded from the *Yarko-site*).

All credit goes to George Beekman (`@???`). His outstanding effort led to the rediscovery of Yarkovsky's 'lost' publication. After several travels to Russia, he found it in the library of the Sternberg Astronomical Institute in Moscow in 2002 (see Beekman (2006)). English translation is being prepared under the custody of D.P. Rubincam and V. Slabinski.

ПЛОТНОСТЬ СВѢТОВОГО ЭѲИРА

И ОКАЗЫВАЕМОЕ ИМЪ

СОПРОТИВЛЕНІЕ ДВИЖЕНІЮ.

И. О. ЯРКОВСКАГО

Инженеръ-Технолога.

БРЯНСКЪ.
Типографія Юдина.
1901.

Плотность свѣтового эѳира и оказываемое имъ сопротивленіе движенію.

Планеты нашей солнечной системы, двигаясь въ міровомъ пространствѣ вокругъ солнца, удерживаются на своихъ орбитахъ силою притяженія солнца, не позволяющею имъ удалиться отъ него, и центробѣжною силою, не позволяющею имъ приблизиться къ нему. Равновѣсіе между центробѣжною силою и силою притяженія опредѣляетъ орбиту и скорость движенія по ней. Но если сила притяженія солнца способна удержать планету на ея орбитѣ, она не даетъ намъ никакого понятія о томъ, откуда могла появиться первоначальная скорость по орбитѣ. Подъ вліяніемъ одной только силы притяженія планета могла бы начать двигаться только по направленію линіи, соединяющей ее съ центромъ солнца и, слѣдовательно, по прошествіи извѣстнаго времени, должна была бы упасть на солнце.

Откуда же взялось движеніе планетъ кругомъ солнца по элипсамъ, близкимъ къ кругамъ? Для этого долженъ былъ быть сообщенъ планетамъ какой либо импульсъ въ направленіи перпендикулярномъ къ линіи, соединяющей центры солнца и планеты, или же должна дѣйствовать въ томъ же направленіи какая либо постоянная сила, побуждающая планету къ движенію по касательной къ ея орбитѣ.

Космогоническая гипотеза Канта-Лапласа находитъ подобный импульсъ во вращеніи первоначальной туманности; теорія Декарта—во вращательномъ движеніи вихрей, но ни та, ни другая не даетъ намъ объясненія причины возникновенія этого вращенія. Ньютонъ отказывается отъ объясненія этого движенія, находя, что „оно не имѣетъ механической причины“. Его преемники говорятъ объ импульсахъ, сообщенныхъ планетамъ, но умалчиваютъ о томъ, какимъ образомъ сообщились эти импульсы.

Какъ я сказалъ, движеніе по касательной къ орбитѣ могло произойти или отъ разъ сообщеннаго планетѣ импульса, который вслѣдъ затѣмъ

пересталъ дѣйствовать, или же отъ нѣкоторой силы, дѣйствовавшей на планету въ продолженіи извѣстнаго времени, а можетъ быть дѣйствующей на нее и до сихъ поръ. Какая въ этомъ разница?

Если планеты на своемъ пути не встрѣчаютъ никакого сопротивленія, то тогда необходимо допустить воздѣйствіе импульса; въ этомъ случаѣ дѣйствіе постоянной силы невозможно, потому что оно давало бы планетѣ постоянное ускореніе въ ея движеніи по орбитѣ, чего въ дѣйствительности не замѣчается. Если, напротивъ, планеты преодолѣваютъ при своемъ движеніи въ міровомъ пространствѣ какое либо сопротивленіе, напримѣръ сопротивленіе среды мірового пространства, то тогда импульсъ невозможенъ, потому что, сообщивъ разъ планетѣ извѣстный запасъ энергіи, онъ не могъ бы восполнять ту ея часть, которая обязательно терялась бы на преодолѣніе сопротивленія движенію планеты; въ этомъ случаѣ для поддержанія той правильности движенія, которую мы видимъ въ движеніи планетъ, необходима сила, дѣйствующая постоянно и соразмѣренная такимъ образомъ, чтобы производимая ею работа была бы соотвѣтственна работѣ того сопротивленія, которое встрѣчаетъ планета на своемъ пути.

Такимъ образомъ вопросъ о томъ, сообщенъ ли планетамъ импульсъ, или на нихъ дѣйствуетъ постоянно какая то сила, самъ собою сводится къ тому: встрѣчаютъ ли планеты при своемъ движеніи какое либо сопротивленіе, или же, напротивъ, такого сопротивленія совершенно не существуетъ.

Какое же изъ этихъ двухъ предположеній имѣетъ мѣсто въ дѣйствительности?

Современная наука, не имѣя подъ руками какой либо силы, которая могла бы исполнять эту роль, останавливается на импульсѣ, а такъ какъ она не замѣчаетъ ни малѣйшаго замедленія въ движеніи планетъ, то для того, чтобы быть послѣдовательною, отвергаетъ существованіе сопротивленія; но міровое пространство, безспорно, наполнено все эѳиромъ, который, къ тому же, признается въ настоящее время матеріальнымъ. Для согласованія одного съ другимъ приходится признать этотъ эѳиръ безконечно разрѣженнымъ; такъ какъ и это не можетъ вполнѣ уничтожить его сопротивленія, то нѣкоторые упорно отрицаютъ матеріальность эѳира, а другіе— и вполнѣ его существованіе.

Я не могу не упомянуть здѣсь объ одномъ фактѣ, на который я уже указывалъ въ моей кинетической гипотезѣ *), и который приводится нѣкоторыми, какъ фактъ, рѣшающій безповоротно вопросъ о сопротивленіи среды мірового пространства и рѣшающій его въ отрицательномъ смыс-

*) Всемірное тяготѣніе какъ слѣдствіе образованія вѣсомой матеріи внутри небесныхъ тѣлъ. Москва 1889 г. стр. 260.

лѣ, тогда какъ онъ какъ-разъ свидѣтельствуетъ неопровержимымъ образомъ о томъ, что это сопротивленіе существуетъ.

Въ 1882 году появилась комета, идущая по тому же пути, по которому проходили кометы 1843 и 1880 годовъ. Путь этой кометы представлялъ собою сильно растянутый элипсисъ, такъ что комета подходила очень близко къ солнцу и имѣла громадную скорость.

Астрономы Финлей (Finlay) и Элькинъ (Dr. Elkin) замѣтили ее за недѣлю до перигелія и имѣли возможность наблюдать нѣсколько мѣсяцевъ послѣ него.

Сопоставленіе положеній и скоростей одной и другой вѣтви орбиты этой кометы давало возможность вывести вполнѣ точное заключеніе о томъ, уклонилась ли комета хоть сколько нибудь отъ математически вычисленной кривой, по которой она должна была слѣдовать. Сопоставленіе это дало вполнѣ точный отвѣтъ, что въ движеніи кометы не было замѣчено никакого уклоненія, а отсюда казалось бы ясное слѣдствіе, что сопротивленія эѳирной среды не существовало.

Это наглядное доказательство дало поводъ нѣкоторымъ утверждать, что съ этихъ поръ вопросъ о сопротивленіи эѳира долженъ быть похороненъ навсегда. А между тѣмъ ничто лучше этого наблюденія не можетъ служить доказательствомъ существованія сопротивленія и, слѣдовательно, связанной съ нимъ, постоянно дѣйствующей на планеты силы по касательной къ ихъ орбитѣ.

Противники сопротивленія эѳирной среды упустили изъ виду одно, что комета эта прошла на разстояніи менѣе 65 000 миль отъ поверхности солнца. Такъ какъ хромосфера солнца, которая безспорно состоитъ изъ водорода, простирается на разстояніи 400 000 миль *), то очевидно комета вошла въ среду водорода, уже не эѳира, а матеріальнаго газа. Комета двигалась приблизительно со скоростью 500 000 метровъ въ секунду. Неужели же возможно допустить, чтобы водородъ хромосферы не оказалъ на комету никакого сопротивленія? Но было бы ошибкою думать, что на этомъ разстояніи комета встрѣчала только одинъ водородъ: нѣкоторые протуберанцы достигаютъ высоты 200 000 миль **), а протуберанцы состоятъ изъ паровъ желѣза и др., слѣдовательно весьма вѣроятно, что комета на своемъ пути встрѣчалась и съ этими парами.

Возможно ли послѣ этого говорить, что комета не встрѣтила сопротивленія? Тутъ уже вопросъ идетъ не объ эѳирѣ, а о вѣсомой, хорошо намъ знакомой матеріи; отрицать сопротивленіе подобной среды невозможно, а принявъ во вниманіе громадную скорость кометы

*) Young. Le Soleil. Paris. 1883. p. 143.
**) Тамъ же стр. 167.

и то обстоятельство, что сопротивленіе пропорціонально если не кубу, то во всякомъ случаѣ квадрату скорости, приходится прійти къ заключенію, что величина его была громадна. А между тѣмъ сопротивленіе это астрономами, наблюдавшими движеніе кометы, не было замѣчено. Примирить эти противорѣчія можно только, признавъ, что сопротивленіе дѣйствительно существовало, но что оно въ то же время преодолѣвалось какою то силою, которой мы пока не знаемъ.

Но если эта сила дѣйствовала при прохожденіи кометы черезъ хромосферу солнца, не могла же она исчезнуть послѣ того, какъ комета вышла изъ нея. Если эта сила продолжала дѣйствовать послѣ того, какъ сопротивленіе исчезло, то она должна была заявить о своемъ существованіи сообщеніемъ ускоренія кометѣ. Между тѣмъ этого не случилось. Если сила эта не могла исчезнуть, и вмѣстѣ съ тѣмъ ускоренія не замѣчалось, слѣдовательно очевидно, сопротивленіе тоже не исчезло и по выходѣ кометы изъ хромосферы солнца, т. е. и внѣ хромосферы солнца, гдѣ уже существованія вѣсомой матеріи предполагать нельзя, и гдѣ допускается существованіе только одного эѳира, и тамъ сопротивленіе существуетъ, т. е. эѳиръ оказываетъ сопротивленіе движенію небесныхъ тѣлъ.

Какъ ни логично подобнаго рода разсужденіе, противъ него можно возразить слѣдующее: мы говоримъ, что по выходѣ кометы изъ фотосферы „сила не могла исчезнуть“; это только допущеніе, которое нужно еще подтвердить. Дѣйствительно можно сдѣлать предположеніе, что движущая сила дѣйствовала только во время прохожденія кометы черезъ фотосферу, а затѣмъ перестала дѣйствовать.—Какова можетъ быть эта сила: внѣшняя, т. е. зараждающаяся внѣ кометы, или внутренняя? Если мы допустимъ сперва это послѣднее предположеніе, то мы должны признать, что появленіе сопротивленія движенію кометы съ передней ея стороны возбуждаетъ какую то силу, толкающую ее впередъ, то есть дѣйствующую въ обратномъ направленіи этого сопротивленія, при томъ съ увеличеніемъ сопротивленія и движущая сила увеличивается, съ уменьшеніемъ его она уменьшается и, наконецъ, съ исчезновеніемъ его она тоже исчезаетъ.

Такое нарожденіе силы въ зависимости отъ сопротивленія незможно потому, что представляетъ собою ничто иное, какъ perpetuum mobile. Основаніе perpetuum mobile состоитъ, какъ извѣстно, не въ томъ, чтобы заставить какой либо механизмъ двигаться вѣчно, а въ томъ, чтобы, расходуя нѣкоторое количество энергіи, получить въ механизмѣ запасъ энергіи большій или, по крайней мѣрѣ, равный израсходованному. Комета въ этомъ случаѣ представляла бы именно такой механизмъ: расходуя извѣстную часть энергіи на преодолѣніе сопротивленія, она вмѣстѣ съ тѣмъ внутри себя порождала бы равное

израсходованному количество энергіи и, такимъ образомъ, представляла бы собою perpetuum mobile.

Воздерживаясь здѣсь отъ доказательства давно уже доказанной невозможности существованія въ природѣ perpetuum mobile, я полагаю, что имѣю право сказать, что эта сила не можетъ быть силою внутренней и должна исходить извнѣ. Но если эта сила внѣшняя, то, исходя изъ какого либо центра, правдоподобнѣе всего изъ солнца, она распространяется во всѣ стороны и ея напряженіе обратно пропорціонально квадратамъ разстояній; такая сила, очевидно, хотя уменьшается съ увеличеніемъ разстоянія, но все же дѣйствуетъ и исчезнуть не можетъ ни на какомъ разстояніи, другими словами, распространяется до безконечности. Поэтому приходится признать, что выходъ кометы изъ фотосферы солнца не могъ оказать на эту силу, какъ внѣшнюю, никакого дѣйствія; она осталась все тою же и продолжала оказывать свое вліяніе на комету, и въ такомъ случаѣ все наше разсужденіе, приведенное выше, остается вѣрнымъ и справедливымъ, а слѣдовательно и сопротивленіе эѳира существовать должно.

Итакъ на всякое движущееся въ міровомъ пространствѣ тѣло, будь это комета или планета, дѣйствуютъ двѣ силы: одна движущая, а другая сила сопротивленія; если при этомъ не замѣчается ни постояннаго ускоренія, ни замедленія, то первое, что приходится признать,—что эти двѣ силы постоянно взаимно уравновѣшиваются. Если движущая сила исходитъ изъ какого либо центра, то скорости планетъ должны зависѣть отъ разстоянія до этого центра, потому что сила должна уменьшаться съ увеличеніемъ разстоянія.

Скорости планетъ находятся дѣйствительно между собою въ нѣкоторой зависимости, вытекающей изъ 3-го закона Кеплера.

Если мы обозначимъ черезъ T и T_1 времена обращенія двухъ планетъ около солнца, а черезъ ρ и ρ_1 ихъ разстояніе отъ солнца, то по закону Кеплера квадраты временъ обращеній относятся, какъ кубы разстояній планетъ отъ солнца, т. е. $\frac{T^2}{T_1^2} = \frac{\rho^3}{\rho_1^3}$ или $\frac{\rho^3}{T^2} = \frac{\rho_1^3}{T_1^2} = K$ постоянному числу.

Но такъ какъ орбиты планетъ близки къ кругамъ, то мы можемъ допустить $T = \frac{2\pi\rho}{V}$, гдѣ V есть скорость планеты по орбитѣ.

Подставляя въ предыдущее равенство вмѣсто T его величину, получимъ $\frac{\rho^3 V^2}{(2\pi)^2 \rho^2} = K$ или $\rho V^2 = K\ (2\pi)^2 = C$, постоянному числу.

Дѣйствительно, если мы выразимъ скорости планетъ по орбитѣ V въ километрахъ въ секунду, а ρ въ разстояніи земли отъ солнца, принятомъ за 10, то получимъ слѣдующую таблицу:

	V	V^2	ρ	$C=V^2\rho$
Меркурій	46,81	2191	3,871	8482
Венера	34,6	1197	7,233	8658
Земля	29,79	887,4	10,00	8875
Марсъ	23,85	568,8	15,237	8667
Юпитеръ	12,9	166,4	52,028	8658
Сатурнъ	9,5	90,25	95,389	8609
Уранъ	6,7	44,89	191,833	8611
Нептунъ	5,4	29,16	300,551	8764
			Среднее. . .	8665,5

И такъ $V^2\rho=C$ постоянному числу; въ принятыхъ нами единицахъ это $C=8665,5$.

Какъ мы видимъ, скорость зависитъ исключительно отъ разстоянія планеты отъ солнца, она не зависитъ ни отъ ея массы, ни отъ ея размѣровъ: если бы на мѣстѣ малой планеты была громадная, она двигалась бы съ тою же самою скоростью, съ какою движется и малая; величина скорости опредѣляется исключительно только однимъ разстояніемъ отъ солнца, слѣдовательно, мы должны заключить, что солнце есть тотъ центръ, изъ котораго исходитъ сила, движущая планеты по орбитѣ.

Но какимъ же образомъ сила, исходящая изъ солнца, можетъ заставить планеты двигаться въ направленіи перпендикулярномъ къ направленію самой силы.

Если мы разсмотримъ ближе вращеніе планетъ около ихъ оси при передвиженіи ихъ по орбитѣ, то замѣтимъ, что всѣ планеты поворачиваются около своей оси такимъ образомъ, что передняя часть планеты, воспринимающая на себя сопротивленіе, поворачивается къ солнцу, а затѣмъ поворачивается далѣе, такъ что становится заднею стороною по отношеніи къ направленію движенія планеты. Если сопротивленіе оказываетъ на планету извѣстное давленіе, если эѳиръ—газъ, то очевидно, что на передней части

подъ давленіемъ эѳиръ углубляется въ поры, такъ сказать, нагнетается, и въ такомъ состояніи планета поворачивается къ солнцу, а ея поверхность подъ дѣйствіемъ его лучей подвергается нагрѣванію. Пріобрѣтаемая такимъ образомъ теплота передается эѳиру и производитъ увеличеніе энергіи его атомовъ. Въ такомъ видѣ поверхность, нагрѣтая солнечными лучами, переходитъ на заднюю сторону, гдѣ сопротивленія нѣтъ. Очевидно, эѳиръ, пріобрѣтшій бо́льшую энергію при посредствѣ лучей солнца, стремится расшириться и, выходя изъ поръ поверхности планеты, своею реакціею толкаетъ ее впередъ. Сумма всѣхъ этихъ весьма малыхъ толчковъ чрезвычайно большого количества атомовъ эѳира даетъ нѣкоторую равнодѣйствующую, которая и преодолѣваетъ сопротивленіе эѳира съ передней стороны.

Такимъ образомъ мы видимъ, что лучи солнца, передавая поверхности земли, а черезъ нее и эѳиру теплоту, имѣютъ возможность оказать на планету нѣкоторое давленіе съ задней ея стороны, которое и можетъ представить собою силу, преодолѣвающую сопротивленіе среды, дѣйствующей на планету съ передней стороны. Изложенное здѣсь можетъ намъ дать понятіе о томъ механизмѣ, который превращаетъ лучи солнца въ движущую силу, дѣйствующую перпендикулярно къ направленію луча, что на первый взглядъ могло бы казаться невозможнымъ.

Такимъ образомъ, еще разъ повторяю, мы имѣемъ двѣ силы, дѣйствующія на планету: одну движущую, другую силу сопротивленія.

Относительно силы сопротивленія мы можемъ составить себѣ нѣкоторое представленіе: она должна быть въ зависимости отъ плотности сопротивляющейся среды, она должна зависѣть отъ площади поперечнаго сѣченія движущагося тѣла, т. е. планеты, и наконецъ она должна представлять собою нѣкоторую функцію скорости движенія планеты, какую—мы пока сказать не можемъ.

Что касается силы движущей, то какъ мы видѣли, она должна зависѣть отъ разстоянія отъ солнца и кромѣ того, подобно равному ей сопротивленію, должна быть пропорціональна поперечному сѣченію планеты.

Постараемся опредѣлить величину обѣихъ этихъ силъ и для этого попробуемъ допустить, что сила, движущая планету, порождается тою энергіей, которую эта планета получаетъ отъ солнца.

Если черезъ a назовемъ количество энергіи, получаемой однимъ квадратнымъ метромъ земной поверхности отъ солнца, то количество энергіи, получаемое квадратнымъ метромъ другой какой либо планеты, находящейся на разстояніи ρ отъ солнца, выразится отношеніемъ $\frac{X}{a} = \frac{(10)^2}{\rho^2}$, гдѣ раз-

стояніе земли отъ солнца принято равнымъ 10, или $X = \frac{100a}{\rho^2}$, а количество энергіи, воспринимаемое всею поверхностью планеты при діаметрѣ D, будетъ $X = \frac{100a}{\rho^2} \frac{\pi D^2}{4}$.

Чтобы получить количество работы, которое способна воспроизвести эта энергія (предполагая ее теплотою), умножаемъ X на механическій эквивалентъ теплоты A, получаемъ $T = \frac{100a}{\rho^2} \frac{\pi D^2}{4} . A.$

Таково выраженіе работы, развиваемой при движеніи любой планеты. Сопротивленіе R, встрѣчаемое планетою, какъ мы видѣли, пропорціонально $\frac{\pi D^2}{4}$ и представляетъ собою какую то $f(V)$ и зависитъ отъ плотности среды, а потому $R = \Delta \frac{\pi D^2}{4} f(V)$.

Работа же этого сопротивленія T_1 получится, если помножимъ R на V, т. е. $T_1 = \Delta \frac{\pi D^2}{4} f(V) V$.

Мы сказали, что въ каждый данный моментъ $T = T_1$, поэтому $\frac{100a}{\rho^2} \frac{\pi D^2}{4} A = \Delta \frac{\pi D^2}{4} f(V) V$ или $\frac{100Aa}{\rho^2 \Delta} = f(V) V$.

Но какъ мы видѣли выше $V^2 \rho = C$ или $\rho = \frac{C}{V^2}$, то, подставляя вмѣсто ρ его величину въ первую часть равенства, получимъ:

$$\frac{100AaV^4}{C^2 \Delta} = f(V) V.$$

Откуда $f(V) = \frac{100Aa}{C^2 \Delta} V^3$.

Коэфиціентъ есть постоянное число, слѣдовательно та функція, которую мы предположили неизвѣстною, представляетъ собою кубъ скорости съ нѣкоторымъ постояннымъ коэфиціентомъ.

Чтобы опредѣлить величину сопротивленія T_1 мы воспользуемся тѣмъ, что она всегда равна T, величину котораго мы можемъ опредѣлить всегда, такъ какъ въ выраженіе $T = \frac{100a}{\rho^2} \frac{\pi D^2}{4} A$, входятъ величины ρ, A, D, намъ вполнѣ извѣстныя, и величина a, которая опредѣлена въ настоящее время съ нѣкоторымъ приближеніемъ, достаточнымъ для того, чтобы мы не сдѣлали крупной ошибки. Величина a, т. е. количество энергіи, получаемой однимъ квадратнымъ метромъ земной поверхности отъ

солнца, по всему вѣроятію слагается изъ суммы различныхъ энергій: свѣтовой, тепловой, электрической. Изъ этихъ энергій тепловая въ настоящее время опредѣлена довольно тщательно и называется солнечной постоянной; она была измѣрена различными учеными и заключалась между цифрою, данною Пулье (Pouillet)—0,293 и цифрою Форба (Forbes)—0,47. Въ настоящее время Ланглей (Langley) признаетъ необходимымъ принять ее равною 0,5 единицъ теплоты на квадратный метръ въ одну секунду, что мы и примемъ при дальнѣйшихъ нашихъ вычисленіяхъ.

Такимъ образомъ, если принять, что солнце передаетъ землѣ только тепловую энергію, оставивъ пока остальное безъ вниманія, то формула $T=\frac{100a}{\rho^2}\frac{\pi D^2}{4}A$, при $a=0{,}5$ и $A=424$, представится въ слѣдующемъ видѣ $T=\frac{21200}{\rho^2}\frac{\pi D^2}{4}$.

Вычисляя T для различныхъ планетъ, получимъ слѣдующую таблицу:

	ρ	ρ^2	$\frac{21200}{\rho^2}$	$\frac{\pi D^2}{4}$ въ метрахъ.	$T=\frac{21200}{\rho^2}\frac{\pi D^2}{4}$ работа въ килограммометрахъ.	Работа въ лошадиныхъ силахъ.
Меркурій.	3,87	14,98	1415	$18{,}096\times10^6$	25 605 340 000	3424×10^6
Венера. .	7,23	52,28	405,6	$113{,}1\times10^6$	45 873 360 000	6116×10^6
Земля . .	10,00	100,00	212	$127{,}28\times10^6$	26 983 360 000	3598×10^6
Марсъ . .	15,24	232,25	91,28	$36{,}85\times10^6$	3 363 668 000	448×10^6
Юпитеръ.	52,03	2735	7,75	15837×10^6	122736750000	1636×10^6
Сатурнъ .	95,39	9099	2,33	11690×10^6	27 237 700 000	$361{,}1\times10^6$
Уранъ . .	191,8	36787	0,576	$2256{,}4\times10^6$	1 299 686 000	$17{,}3\times10^6$
Нептунъ .	300,5	90300	0,234	2463×10^6	576 342 000	$7{,}7\times10^6$

Такъ какъ полученная работа $T=RV$, гдѣ R представляетъ сопротивленіе, то это послѣднее получить нетрудно, раздѣляя T на V; желая же получить давленіе, производимое сопротивленіемъ на одинъ квадратный метръ, мы должны раздѣлить еще R на $\frac{\pi D^2}{4}$, или проще, раздѣлить имѣющуюся

у насъ величину $\frac{21200}{\rho^2}$ на V, тогда получимъ слѣдующую таблицу:

	$\frac{21200}{\rho^2}$	V въ метрахъ	Давленіе на 1 кв. метръ $\frac{21200}{\rho^2 V}$ въ килограммахъ.	Полное давл. на всю поверхность $\frac{21200}{\rho^2 V} \cdot \frac{\pi D^2}{4}$ въ килограммахъ.
Меркурій. .	1415	46 810	0,03022	545 487
Венера. . .	405,6	34 600	0,01172	1 323 270
Земля . . .	112	29 790	0,007116	921 236
Марсъ. . .	91,28	23 850	0,003827	144 821
Юпитеръ. .	7,75	12 900	0,0005868	9 628 896
Сатурнъ . .	2,33	9 500	0,0002452	284 067
Ураиъ. . .	0,576	6 700	0,00008597	195 404
Нептунъ. .	0,234	5 400	0,00004333	104 924

Если принять во вниманіе, что давленіе нашей атмосферы дастъ на одинъ квадратный метръ 10 350 кил., то сопротивленіе эѳира движенію планеты, дающее для нашей земли 0,007116 килограмма, представляется совершенно ничтожной величиной. Отношеніе давленія атмосферы къ давленію, производимому сопротивленіемъ эѳирной среды, будетъ $\frac{10\,350}{0{,}007116} = 1\,454\,469.$

Меня заинтересовалъ вопросъ, какое сопротивленіе преодолѣвали бы планеты, если бы движеніе ихъ происходило въ воздухѣ? Скорости, какія существуютъ на землѣ, далеко меньше скоростей движенія планетъ, однако и на землѣ случаются скорости нѣсколько тысячъ футъ въ секунду. Съ такими скоростями движутся артиллерійскіе снаряды; движенія ихъ достаточно изслѣдованы и сопротивленіе воздуха хорошо опредѣлено. Задавшись цѣлью сравнить сопротивленіе эѳира съ сопротивленіемъ воздуха, я взялъ одну изъ формулъ, именно Піобера, выражающую сопротивленіе воздуха для круглыхъ артиллерійскихъ снарядовъ, которая имѣетъ слѣдующій видъ: $P = 0{,}022932\ A_1\ V^2\ (1 + 0{,}023\ V)$, гдѣ P

есть сопротивленіе въ килограммахъ, A_1 площадь большого круга въ квадратныхъ метрахъ и V скорость въ метрахъ, и вычисливъ значеніе $\frac{P}{A_1}$ т. е. давленіе на одинъ квадратный метръ, происходящее отъ сопротивленія воздуха, принимая скорость V равною скорости движенія всѣхъ планетъ поочередно, получилъ слѣдующее:

	Сопротивленіе въ килограммахъ на одинъ квадр. метръ площади большого круга при предположеніи движенія планеты въ воздухѣ.		Сопротивленіе въ килограммахъ на одинъ квадр. метръ площади большого круга при предположеніи движенія планеты въ воздухѣ.
Меркурій	54 144 441 720	Юпитеръ	1 135 990 453
Венера	21 871 363 200	Сатурнъ	454 279 395
Земля	13 963 422 266	Уранъ	159 663 042
Марсъ	7 169 429 300	Нептунъ	83 719 988

Желая узнать отношеніе сопротивленія воздуха къ сопротивленію эѳира, я раздѣлилъ соотвѣтственно одно на другое и получилъ слѣдующую таблицу.

	Сопротивленіе воздуха.	Сопротивленіе эѳира.	Отношеніе перваго ко второму.	Корень квадратный изъ послѣдняго столбца.
Меркурій	54 144 441 720	0,03022	1 791 670 920 000	1 338 000
Венера	21 871 368 200	0,01172	1 866 440 000 000	1 366 000
Земля	13 963 422 266	0,007116	1 962 250 000 000	1 401 000
Марсъ	7 169 429 300	0,003827	1 873 380 000 000	1 369 000
Юпитеръ	1 135 990 453	0,0005868	1 935 900 000 000	1 391 000
Сатурнъ	454 279 395	0,0002452	1 852 690 000 000	1 361 000
Уранъ	159 663 042	0,00008597	1 857 190 000 000	1 363 000
Нептунъ	83 719 988	0,00004333	1 932 001 000 000	1 390 000
		Среднее	1 883 940 240 000	1 372 587

Такъ какъ сопротивленіе движенію тѣла при прочихъ одинаковыхъ условіяхъ пропорціонально плотностямъ тѣхъ газовъ, въ которыхъ движутся тѣла, то мы можемъ сказать, что 4-ая графа (или средняя величина изъ цифръ этой графы) представляетъ собою отношеніе между плотностями воздуха и эѳира, или мы можемъ сказать, что плотность эѳира составляетъ $\frac{1}{1\,883\,940\,240\,000} = 0{,}000\,000\,000\,000\,53$ или $= 53 \times 10^{-14}$ плотности воздуха.

Какое бы не было строеніе эѳира, мы все же знаемъ, что онъ способенъ передавать колебанія. Я полагаю, что эѳиръ подобенъ газу. Попробуемъ опредѣлить скорость, съ которою должны въ немъ распространяться эти колебанія.

Мы знаемъ, что звукъ въ воздухѣ распространяется со скоростью около 333 метровъ. Мы знаемъ также, что скорость распространенія звука въ различныхъ газахъ обратно пропорціональна корню квадратному изъ плотностей этихъ газовъ.

Въ предыдущей таблицѣ 4-ая графа, какъ мы видѣли, представляетъ отношеніе плотностей, а пятая корень квадратный изъ этого отношенія, средняя величина котораго опредѣляется 1 372 500. Поэтому мы можемъ сказать, что звукъ или другое ему подобное волнообразное движеніе въ эѳирѣ, если онъ подобенъ газу, должно распространяться со скоростью $333 \times 1\,372\,500 = 457\,042\,500$ метровъ.

Намъ извѣстны колебанія эѳира свѣтовыя, электрическія, распространяющіяся со скоростью 300 000 000 метровъ. Хотя величины эти одного порядка, но все же относятся, какъ 3 къ 2.

Мы должны однако принять во вниманіе, что наше вычисленіе не совсѣмъ точно. Не говоря уже о томъ, что примѣненіе формулы, выведенной для сопротивленія движенію артиллерійскихъ снарядовъ, можетъ оказаться недостаточно точнымъ для планетъ, скорость которыхъ въ 30—40 разъ больше, мы завѣдомо дѣлаемъ еще одну ошибку и дѣлаемъ ее по неволѣ. Мы принимаемъ во вниманіе только тепловую энергію солнца, ту энергію, которую принято называть солнечною постоянною, между тѣмъ солнце посылаетъ къ намъ безспорно энергію и другого рода, какъ напримѣръ свѣтовую, электрическую, а можетъ быть и иныя. Этихъ видовъ энергіи мы не принимаемъ во вниманіе, потому что она не измѣрена, а между тѣмъ увеличеніе того количества a, которое мы приняли, какъ количество энергіи, посылаемой солнцемъ нашей землѣ, необходимо измѣнило бы вычисленную нами скорость распространенія волнъ въ эѳирѣ; оно бы уменьшило величину этой скорости и слѣдовательно приблизило бы эту скорость къ скорости свѣта, т. е. 300 000 000 метровъ. Очевидно, что сумма всѣхъ этихъ энергій, вмѣстѣ взятыхъ, необходимо дастъ величину бо́льшую, чѣмъ взятая нами

солнечная постоянная 0,5. Нельзя отрицать, что вся эта энергія способна воспроизводить то же дѣйствіе, какъ и тепловая, въ смыслѣ сообщенія планетѣ движущей силы, а слѣдовательно и должна быть обязательно принята во вниманіе.

Такъ какъ количество всей этой энергіи опытнымъ путемъ не опредѣлено, то попробуемъ опредѣлить ее обратнымъ путемъ, т. е. исходя изъ того, что плотность эѳира должна быть такова, что въ ней колебанія должны распространяться со скоростью 300 000 000 метровъ. Тогда, называя плотность эѳира черезъ δ, а плотность воздуха принимая за единицу, получимъ:

$$\frac{\sqrt{1}}{\sqrt{\delta}} = \frac{300\,000\,000}{333} = 900901.$$

Откуда $\frac{1}{\delta} = 811\,622\,611\,801$. (Въ этомъ случаѣ плотность эѳира $\delta = 123 \times 10^{-14}$.)

Это будетъ отношеніе плотностей, пропорціонально которому должно быть сопротивленіе въ эѳирѣ и воздухѣ, а какъ сопротивленіе движенія земли въ воздухѣ вычислено нами 13 963 422 266, то сопротивленіе земли въ эѳирѣ должно быть равно:

$\frac{13\,963\,422\,266}{811\,622\,611\,801} = 0{,}0172043$ килограмма на квадратный метръ поверхности.

Сопротивленіе это, какъ мы знаемъ, для нашей планеты равно $\frac{a.\ A.\ 10^2}{\rho^2 V} = 0{,}0172043$, гдѣ a есть количество энергіи, воспринимаемой квадратнымъ метромъ земной поверхности въ одну секунду (полагая что вся эта энергія превращена въ тепловую), A—механическій эквивалентъ теплоты, ρ разстояніе земли отъ солнца, принятое равнымъ 10, а V скорость по орбитѣ. Такъ какъ $\rho = 10$, то сокращая и опредѣляя a, получимъ:

$a = \frac{0{,}0172043 V}{A}$, подставляя величину A и V, получимъ:

$$a = \frac{0{,}0172043 \times 29790}{424} \text{ или } \frac{512{,}516097}{424} \text{ или } a = 1{,}2087.$$

Какъ мы видимъ, количество энергіи, получаемой квадратнымъ метромъ земной поверхности отъ солнца въ одну секунду, опредѣлилось: $a = 1{,}2087$.

Если именно это количество теплоты (въ видѣ разнаго рода энергій) воспринимается квадратнымъ метромъ поверхности земли въ 1 секунду, то вычисляя плотность эѳира по сопротивленію, а это послѣднее по движущей силѣ, и принимая, что колебательныя движенія распространяются обратно пропорціонально квадратнымъ корнямъ изъ плотностей газовъ, мы получимъ

скорость колебательнаго движенія въ эѳирѣ равною 300 000 000 метрамъ.

Въ первоначальномъ нашемъ вычисленіи мы приняли только солнечную постоянную, опредѣленную Ланглеемъ 0,5, тогда какъ настоящее наше вычисленіе показываетъ, что этой энергіи должно получаться гораздо больше. Что ея получается больше,—это безспорно, такъ какъ въ солнечную постоянную входитъ исключительно тепловая энергія. Принимая во вниманіе, что солнце сообщаетъ землѣ свѣтовую, электрическую энергію, а можетъ быть еще и въ иной формѣ, нельзя назвать абсурдомъ то предположеніе, что остающіяся 0,7087 калоріи можетъ объясниться этимъ путемъ. Допустивъ же это предположеніе, мы видимъ, что свѣтъ представляетъ собою совершенно подобныя колебанія въ эѳирѣ, какъ звукъ въ воздухѣ.

До сихъ поръ явленія, происходящія въ міровомъ пространствѣ или, лучше сказать, въ эѳирѣ, не могли быть согласованы между собою. Въ то время, какъ свѣтовыя явленія требовали обязательно матеріальнаго эѳира, явленія астрономическія,—движеніе небесныхъ тѣлъ безъ видимаго сопротивленія,—какъ бы противорѣчили этой матеріальности. Въ настоящей замѣткѣ я попробовалъ примирить между собою эти явленія и, при помощи вычисленій, показать, что подобнаго рода примиреніе возможно.

Исходя изъ того, что сопротивленіе планетъ преодолѣвается энергіей, посылаемой планетамъ отъ солнца, я вычислилъ эту энергію и такимъ образомъ получилъ величину самого сопротивленія; при этомъ оказалось, что сопротивленіе это пропорціонально кубу скорости, что должно считать весьма правдоподобнымъ. Имѣя сопротивленіе, я попробовалъ сравнить его съ сопротивленіемъ воздуха, для чего я примѣнилъ формулу, выведенную изъ наблюденій надъ движеніемъ круглыхъ артиллерійскихъ снарядовъ, движеніемъ, обладающимъ самою большею скоростью, создаваемою нами. Какъ я замѣтилъ выше, подобное примѣненіе нельзя считать абсолютно точнымъ, тутъ можетъ быть ошибка, такъ какъ разница въ скоростяхъ артиллерійскихъ снарядовъ и планетъ довольно велика.

Вычисленіе это дало мнѣ возможность составить себѣ понятіе о плотности эѳира, а имѣя таковую, я попробовалъ сравнить скорость колебаній, происходящихъ въ воздухѣ, съ таковыми, происходящими въ эѳирѣ. Полученный результатъ, принимая во вниманіе тѣ громадныя цифры, съ которыми приходилось имѣть дѣло, настолько близокъ, что мнѣ кажется отвергать то, что свѣтъ есть колебаніе, происходящее въ эѳирѣ, совершенно подобное тому, какое производятъ звуки въ воздухѣ, почти невозможно.

Мнѣ скажутъ, что свойства свѣтовыхъ и звуковыхъ колебаній совершенно различны. Это вѣрно. Но и частицы, принимающія участіе въ этихъ колебаніяхъ, тоже совершенно различны: въ то время, какъ въ воздухѣ колеблятся частицы сложныя, имѣющія возможность деформироваться, слѣдовательно обладающія нѣкоторою упругостью, въ эѳирѣ напротивъ атомы, его составляющіе, какъ я давно утверждаю, абсолютно тверды, упругостью не обладаютъ. Въ этомъ состоитъ разница, которая, какъ мнѣ кажется, и способна объяснить различіе свойствъ этихъ двухъ родовъ колебаній.

Въ заключеніе я не могу не обратить вниманія на то, что вычисленная нами плотность эѳира, заключающаяся во всякомъ случаѣ между 53×10^{-14} и 123×10^{-14} относительно плотности воздуха, далеко разнится отъ вычисленія плотности эѳира, сдѣланнаго В. Томсономъ (Лордомъ Кельвиномъ), который получилъ эту плотность ровною 2×10^{-25}. Эти два вычисленія разнятся между собою очень значительно.

Плотность эѳира, вычисленная В. Томсономъ, въ 6 250 000 000 000 разъ менѣе той, которая получена мною.

Въ двухъ моихъ предыдущихъ брошюрахъ *) я показалъ ошибочность вычисленія В. Томсона и въ настоящее время могу только подтвердить справедливость моихъ тогдашнихъ умозаключеній.

К. Ярковскій.

26 сентября 1900 года
с. Дятьково
Орловской губ. Брянскаго уѣз.

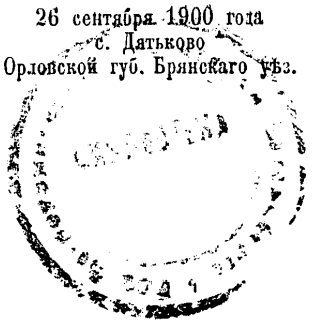

*) «Увлеченіе математическими теоріями въ современной наукѣ» и «Новыя доказательства увлеченія математическими теоріями и т. д.».

9.4 Publications and citations

We list refereed papers, proceedings contributions, abstracts and popular articles of MB, together with relevant citations we recorded in the literature.

Thesis

1 **M. Brož**, 1999, Orbitální vývoj asteroidálních fragmentů způsobený vlivem gravitace planet a tepelnými efekty, Diploma Thesis, Charles University.

1 D. Vokrouhlický, P. Farinella, The Yarkovsky Seasonal Effect on Asteroidal Fragments: A Nonlinearized Theory for Spherical Bodies, *Astrophys. J.* **118**, 3049, 1999.
2 V. Carruba, J.A. Burns, W. Bottke, D. Nesvorný, Orbital evolution of the Gefion and Adeona asteroid families: close encounters with massive asteroids and the Yarkovsky effect, *Icarus* **162**, 308, 2003.
3 V. Carruba, Dynamics of asteroid families and irregular satellites of jovian planets, PhD Dissertation, Cornell University, 2004.
4 V. Carruba, T.A. Michtchenko, F. Roig, S. Ferraz-Mello, D. Nesvorný, On the V-type asteroids outside the Vesta family. I. Interplay of nonlinear secular resonances and the Yarkovsky effect: the cases of 956 Elisa and 809 Lundia, *Astron. Astrophys.* **441**, 819, 2005.

Refereed papers

1 D. Vokrouhlický and **M. Brož**, 1999, An improved model of the seasonal Yarkovsky force for the regolith–covered asteroid fragments, *Astron. Astrophys.* **350**, 1079.

1 J.N. Spitale and R. Greenberg, The Yarkovsky effect on regolith-covered bodies, *BAAS* **32**, 2000.
2 E.J. Lyytinen and J. Van Flandern, *Earth Moon Planets* **82-3**, 149, 2000.
3 J.N. Spitale and R. Greenberg, Numerical evaluation of the general Yarkovsky effect: Effects on semimajor axis, *Icarus*, **149**, 222, 2001.
4 J.N. Spitale and R. Greenberg, Numerical evaluation of the general Yarkovsky effect: Effects on eccentricity and longitude of periapse, *Icarus*, **156**, 211, 2001.
5 J.N. Spitale and R. Greenberg, Numerical evaluation of the Yarkovsky effect on orbital elements of asteroids, *LPSC* **32**, 1346, 2001.
6 A.A. Guillens, R. Vieira Martins and R.S. Gomes, A global study of the 3/1 resonance neighborhood: A search for unstable asteroids, *Astron. J.* **124**, 2322, 2002.
7 J.N. Spitale, *Detailed study of the Yarkovsky effect on asteroids and solar system implications*, PhD Dissertation, University of Arizona, 2002.
8 E. Skoglov, The influence on the spin vectors of asteroids from the Yarkovsky effect, *Astron. Astrophys.* **393**, 673, 2002.
9 D.P. O'Brien, *The Collisional and Dynamical Evolution of the Main-Belt, NEA, and TNO Populations*, PhD Dissertation, University of Arizona, 2004.

2 D. Vokrouhlický, **M. Brož**, P. Farinella and Z. Knežević, 2001, Yarkovsky–driven leakage of Koronis family members: I. The case of 2953 Vysheslavia, *Icarus* **150**, 78.

1 V. Zappalá, A. Cellino and A. Dell'Oro, A search for the collisional parent bodies of large NEAs, *Icarus* **157**, 280, 2002.
2 A.A. Guillens, R. Vieira Martins and R.S. Gomes, A global study of the 3/1 resonance neighborhood: A search for unstable asteroids, *Astron. J.* **124**, 2322, 2002.
3 D. Nesvorný and W.F. Bottke, Direct detection of the Yarkovsky effect for main-belt asteroids, *Icarus* **170**, 324, 2004.
4 A. Dell'Oro, G. Bigongiari, P. Paolicchi and A. Cellino, Asteroid families: evidence of ageing of the proper elements, *Icarus* **169**, 341, 2004.
5 A. Lemaitre, Asteroid family classification from very large catalogs, in: *Dynamics of Populations of Planetary Systems*, IAU Colloquium 197, Cambridge University Press, 2005, p. 135.
6 T. Monthé-Diniz, F. Roig and J.M. Carvano, Reanalysis of asteroid families structure through visible spectroscopy, *Icarus* **174**, 54, 2005.

3 W.F. Bottke, D. Vokrouhlický, **M. Brož**, D. Nesvorný and A. Morbidelli, 2001, Dynamical spreading of asteroid families by the Yarkovsky effect, *Science* **294**, 1693.

1 M. Guzzo, Z. Knežević and A. Milani, Probing the Nekhoroshev statbility of asteroid orbits, *Celest. Mech. Dyn. Astr.*, **83**, 121, 2002.
2 J.R. Minkel, New studies sharpen picture of near-Earth asteroids, *Scientific American*, Nov 27, 2001.
3 P. Michel, W. Benz, P. Tanga and D. Richardson, Collisions and gravitational reaccumulation: Forming asteroid families and satellites, *Science* **294**, 1696, 2001.
4 D.C. Richardson, Rocks that go bump in the night, *Nature* **417**, 697, 2002.
5 V. Zappalá, A. Cellino and A. Dell'Oro, A search for the collisional parent bodies of large NEAs, *Icarus* **157**, 280, 2002.
6 T.A. Michtchenko, D. Lazzaro, S. Ferraz-Mello and F. Roig, Origin of the basaltic asteroid 1459 Magnya. A dynamical and mineralogical study of the outer main belt, *Icarus* **158**, 343, 2002.
7 A.A. Guillens, R. Vieira Martins and R.S. Gomes, A global study of the 3/1 resonance neighborhood: A search for unstable asteroids, *Astron. J.* **124**, 2322, 2002.
8 E.I. Chiang, A collisional family in the classical Kuiper belt, *Astrophys. J.* **573**, L65, 2002.

9 P. Michel *et al.*, Formation of asteroid families by catastrophic disruption: Simulations with fragmentation and gravitational reaccumulation, *Icarus* **160**, 10, 2002.
10 C. Schreiber, Kann der Yarkovsky-Effekt die Asteroiden neu gruppieren?, *Telepolis*, `http://www.heise.de/tp/r4/artikel/16/16261/1.html`
11 P. Michel, W. Benz and D.C. Richardson, Disruption of fragmented parent bodies as the origin of asteroid families, *Nature* **421**, 608, 2003.
12 V. Trimble and M. Aschwanden, Astrophysics in 2002, *Publ. Astron. Soc. Pac.* **115**, 514, 2003.
13 Z. Knežević and A. Milani, Proper element catalogues and asteroid families, *Astron. Astrophys.* **403**, 1165, 2003.
14 K. Tsiganis, *Chaotic motion of asteroids*, PhD Thesis, University of Thessaloniky, 2002.
15 R.D. Lorentz and J.N. Spitale, The Yarkovsky effect as a heat engine, *Icarus* **170**, 229, 2004.
16 P. Michel, W. Benz and D.C. Richardson, Catastrophic disruption of pre-shattered parent bodies, *Icarus* **168**, 420, 2004.
17 U. Penco, A. Dell'Oro, P. Paolicchi *et al.*, Yarkovsky depletion and asteroid collisional evolution, *Planet. Sp. Science* **52**, 1087, 2004.
18 A. Dell'Oro, G. Bigongiari, P. Paolicchi and A. Cellino, Asteroid families: evidence of ageing of the proper elements, *Icarus* **169**, 341, 2004.
19 A. Lemaitre, Asteroid family classification from very large catalogs, in: *Dynamics of Populations of Planetary Systems*, IAU Colloquium 197, Cambridge University Press, 2005, p. 135.
20 S. Foglia and G. Masi, New clusters for highly inclined main-belt asteroids, *Minor Planet Bulletin* **31**, 100, 2004.
21 A. Cellino, A. Dell'Oro and V. Zappalà, Asteroid families: open problems, *Planet. Sp. Sci.* **52**, 1075, 2004.
22 W.S. Koon, J.E. Marsden, S.D. Ross, *et al.*, Geometric mechanics and the dynamics of asteroid pairs, *Ann. New York Acad. Sci.* **1017**, 11, 2004.
23 P. Michel, W. Benz and D.C. Richardson, Catastrophic disruption of asteroids and family formation: a review of numerical simulations including both fragmentation and gravitational reaccumulations, *Planet. Sp. Sci.* **52**, 1109, 2004.
24 D.P. O'Brien, *The Collisional and Dynamical Evolution of the Main-Belt, NEA, and TNO Populations*, PhD Dissertation, University of Arizona, 2004.
25 A.A. Christou, Gravitational scattering within the Himalia group of jovian prograde irregular satellites, *Icarus* **174**, 215, 2005.
26 T. Monthé-Diniz, F. Roig and J.M. Carvano, Reanalysis of asteroid families structure through visible spectroscopy, *Icarus* **174**, 54, 2005.
27 P. Tanga, Impact of Gaia on dynamics and evolution of the Solar System, in *The Three-Dimensional Universe with Gaia*, C. Turon, K.S. O'Flaherty, M.A.C. Perryman (Eds.), p. 243, 2005.
28 M. Ćuk and J.A. Burns, Effects of thermal radiation on the dynamics of binary NEAs, *Icarus* **176**, 418, 2005.

4 D. Nesvorný, A. Morbidelli, D. Vokrouhlický, W.F. Bottke and **M. Brož**, 2002, The Flora family: a case of the dynamically dispersed collisional swarm?, *Icarus* **157**, 155.

1 T.A. Michtchenko, D. Lazzaro, S. Ferraz-Mello and F. Roig, Origin of the basaltic asteroid 1459 Magnya. A dynamical and mineralogical study of the outer main belt, *Icarus* **158**, 343, 2002.
2 P. Michel *et al.*, Formation of asteroid families by catastrophic disruption: Simulations with fragmentation and gravitational reaccumulation, *Icarus* **160**, 10, 2002.
3 A. Cellino, V. Zappalà and E.F. Tedesco, Near-Earth objects: Origins and need of physical characterization, *Meteorit. Planet. Sci.* **37**, 1965, 2002.
4 B. Schmitz, T. Haggstrom and M. Tassinari, Sediment-dispersed extraterrestrial chromite traces a major asteroid disruption event, *Science* **300**, 961, 2003.
5 Z. Knežević and A. Milani, Proper element catalogues and asteroid families, *Astron. Astrophys.* **403**, 1165, 2003.
6 K. Tsiganis, *Chaotic motion of asteroids*, PhD Thesis, University of Thessaloniky, 2002.
7 A. Dell'Oro, G. Bigongiari, P. Paolicchi and A. Cellino, Asteroid families: evidence of ageing of the proper elements, *Icarus* **169**, 341, 2004.
8 A. Cellino, A. Dell'Oro and V. Zappalà, Asteroid families: open problems, *Planet. Sp. Sci.* **52**, 1075, 2004.
9 P.R. Heck, B. Schmitz, H. Baur, *et al.*, Fast delivery of meteorites to Earth after a major asteroid collision, *Nature* **430**, 323, 2004.
10 A. Lemaitre, Asteroid family classification from very large catalogs, in: *Dynamics of Populations of Planetary Systems*, IAU Colloquium 197, Cambridge University Press, 2005, p. 135.
11 E.R.D. Scott and L. Wilson, Meteoritic and other constraints on the internal structure and impact history of small asteroids, *Icarus* **174**, 46, 2005.
12 H. Scholl, F. Marzari and P. Tricarico, Dynamics of Mars Trojans, *Icarus* **175**, 397, 2005.
13 E.F. Tedesco, A. Cellino and V. Zappalà, The statistical asteroid model I. The main-bel population for diameters greater than 1 km, *Astron. J.* **129**, 2869, 2005.
14 S.J. Kenyon and B.C. Bromley, Prospects for detection of catastrophic collisions in debris disks, *Astron. J.* **130**, 269, 2005.
15 S.J. Kenyon and B.C. Bromley, Terrestrial planet formation I. The transition from oligarchic growth to chaotic growth, *Astron. J.*, in press, 2005.
16 A.A. Christou, Gravitational scattering within the Himalia group of jovian prograde irregular satellites, *Icarus* **174**, 215, 2005.
17 D.P. O'Brien and R. Greenberg, Collisional and dynamical evolution of the main-belt and NEA size distributions, *Icarus* **178**, 179, 2005.
18 T. Monthé-Diniz, F. Roig and J.M. Carvano, Reanalysis of asteroid families structure through visible spectroscopy, *Icarus* **174**, 54, 2005.
19 A. Bishoff, E.R.D.Scott, K. Metzler and C.A. Goodrich, Nature and origin of meteoritic breccias, in: *Meteorites and the Early Solar System II*, Eds. ???, Univ. of Arizona Press, Tucson, in press, 2006.
20 R. Gil-Hutton, Identification of families among highly inclined asteroids, *Icarus*, in press, 2006.

5 **M. Brož**, D. Vokrouhlický, F. Roig, D. Nesvorný, W.F. Bottke and A. Morbidelli, 2005, Yarkovsky origin of the unstable asteroids in the 2/1 mean motion resonance with Jupiter, *Mon. Not. R. Astr. Soc.* **359**, 1437.

6 D. Vokrouhlický, **M. Brož**, T. Michałowski, S.M. Slivan, F. Colas, L. Šarounová and F.P. Velichko, 2006, Spin axis of (2953) Vysheslavia and its implications, *Icarus* **180**, 217.

7 D. Vokrouhlický, **M. Brož**, A. Morbidelli, W.F. Bottke, D. Nesvorný, D. Lazzaro and A.S. Rivkin, 2006, Yarkovsky footprints in the Eos family, *Icarus*, in press.

1 T. Mothé-Diniz and J.M. Carvano, 221 Eos: A remnant of a partially differentiated parent body? *Astron. Astrophys.* **442**, 727, 2005.

8 D. Vokrouhlický, **M. Brož**, W.F. Bottke, D. Nesvorný and A. Morbidelli, 2006, Yarkovsky/YORP chronology of asteroid families, *Icarus*, in press.

9 D. Vokrouhlický, **M. Brož**, W.F. Bottke, D. Nesvorný and A. Morbidelli, 2006, The peculiar case of the Agnia asteroid family, *Icarus*, in press.

Book chapters

1 W.F. Bottke, D. Vokrouhlický, D.P. Rubincam and **M. Brož**, Dynamical evolution of asteroids and meteoroids using the Yarkovsky effect, in: *Asteroids III*, Eds. W.F. Bottke, A. Cellino. P. Paolicchi and R. Binzel, (Arizona Univ. Press, Tucson 2003), p. 395.

1 A. Dell'Oro *et al.*, Evidences of ageing of orbital elements (a,e) from the observed structure of asteroid families, *Asteroids, Comets and Meteors*, abstract 05-11, p. 53 (2002).
2 A. Morbidelli *et al.*, Origin and evolution of near-Earth objects, in: *Asteroids III*, Eds. W.F. Bottke, A. Cellino. P. Paolicchi and R. Binzel, (Arizona Univ. Press, 2003), p. 409.
3 V. Zappalá *et al.*, Physical and dynamical properties of asteroid families, in: *Asteroids III*, Eds. W.F. Bottke, A. Cellino. P. Paolicchi and R. Binzel, (Arizona Univ. Press, 2003), p. 619.
4 D. Nesvorný *et al.*, Regular and chaotic dynamics in the mean-motion resonances, in: *Asteroids III*, Eds. W.F. Bottke, A. Cellino. P. Paolicchi and R. Binzel, (Arizona Univ. Press, 2003), p. 379.
5 R.P. Binzel *et al.*, Physical properties of Near-Earth Asteroids, in: *Asteroids III*, Eds. W.F. Bottke, A. Cellino. P. Paolicchi and R. Binzel, (Arizona Univ. Press, 2003), p. 255.
6 P. Pravec, A.W. Harris and T. Michalowski, Asteroid rotation, in: *Asteroids III*, Eds. W.F. Bottke, A. Cellino. P. Paolicchi and R. Binzel, (Arizona Univ. Press, 2003), p. 113.
7 E. Asphaug, E. Ryan and M. Zuber, Asteroid Interiors, in: *Asteroids III*, Eds. W.F. Bottke, A. Cellino. P. Paolicchi and R. Binzel, (Arizona Univ. Press, 2003), p. 463.
8 D. Scheeres, D.D. Durda and P.E. Geissler, The fate of asteroid ejecta, in: *Asteroids III*, Eds. W.F. Bottke, A. Cellino. P. Paolicchi and R. Binzel, (Arizona Univ. Press, 2003), p. 527.
9 A.W. Harris and J.S.V. Lagerros, Asteroids in the thermal infrared, in: *Asteroids III*, Eds. W.F. Bottke, A. Cellino. P. Paolicchi and R. Binzel, (Arizona Univ. Press, 2003), p. 205.
10 T. Burbine *et al.*, Meteoritic parent bodies: Their number and identification, in: *Asteroids III*, Eds. W.F. Bottke, A. Cellino. P. Paolicchi and R. Binzel, (Arizona Univ. Press, 2003), p. 669.
11 R.P. Binzel, Spin control for asteroids, *Nature* **425**, 131, 2003.
12 U. Penco, A. Dell'Oro, P. Paolicchi *et al.*, Numerical modelling of main belt collisional evolution: depletion effects, in: it Proceedings of the ACM04 Conference, ESA SP-500, p. 363, 2003.
13 R.D. Lorentz and J.N. Spitale, The Yarkovsky effect as a heat engine, *Icarus* **170**, 229, 2004.
14 U. Penco, A. Dell'Oro, P. Paolicchi *et al.*, Yarkovsky depletion and asteroid collisional evolution, *Planet. Sp. Science* **52**, 1087, 2004.
15 R. Michelsen, Near-Earth Asteroids from discovery to characterization, *PhD Thesis*, N. Bohr Institute for Astronomy, Physics and Geophysics, University of Copenhagen, 2004.
16 A.F. Cheng, Collisional evolution of the asteroid belt, *Icarus* **169**, 357.
17 A. Dell'Oro, G. Bigongiari, P. Paolicchi and A. Cellino, Asteroid families: evidence of ageing of the proper elements, *Icarus* **169**, 341, 2004.
18 D.J. Sheeres, F. Marzari and A. Rossi, Evolution of NEO rotation rates due to close encounters with Earth and Venus, *Icarus* **170**, 312, 2004.
19 A. Cellino, A. Dell'Oro and V. Zappalà, Asteroid families: open problems, *Planet. Sp. Sci.* **52**, 1075, 2004.
20 M. Delbó, *The nature of near-earth asteroids from the study of their thermal infrared emission*, PhD Dissertation, Freie Universität Berlin, 2004.
21 P.R. Heck, B. Schmitz, H. Baur, *et al.*, Fast delivery of meteorites to Earth after a major asteroid collision, *Nature* **430**, 323, 2004.
22 C.R. Chapman, The hazard of near-Earth asteroid impacts on Earth, *Earth. Planet. Sci. Lett.* **222**, 1, 2004.
23 T. Monthé-Diniz, F. Roig and J.M. Carvano, Reanalysis of asteroid families structure through visible spectroscopy, *Icarus* **174**, 54, 2005.
24 M. Ćuk and J.A. Burns, Effects of thermal radiation on the dynamics of binary NEAs, *Icarus* **176**, 418, 2005.
25 E.F. Tedesco, A. Cellino and V. Zappalà, The statistical asteroid model I. The main-belt population for diameters greater than 1 km, *Astron. J.* **129**, 2869, 2005.
26 H. Scholl, F. Marzari and P. Tricarico, Dynamics of Mars Trojans, *Icarus* **175**, 397, 2005.
27 H. Michałska, *Dynamika podwójnych planetoid pod wplywem efektu Jarkowskiego*, Master Thesis, A. Mickiewicz University, 2005.
28 D.C. Richardson, P. Elankumaran and R.E. Sanderson, Numerical experiments with rubble piles: equilibrium shapes and spins, *Icarus* **173**, 349, 2005.

29 T. Monthé-Diniz and J.M. Carvano, 221 Eos: A remnant of a partially differentiated parent body? *Astron. Astrophys.*, submitted.
30 H. Fu, R. Jedicke, D. Durda, R. Fevig and J.V. Scotti, Identifying near-Earth objects families, *Icarus*, in press, 2005.
31 G. Beekman, I.O. Yarkovsky and the discovery of his effect, *J. Hist. Astron.* **37**, ???, 2006.
32 P. Pravec, Photometric survey of asynchronous binary asteroids, in: *Symposium on Telescope Science*, Eds. B.D. Warner *et al.*, Society for Astronomical Science, p. 61, 2005.
33 P. Pravec *et al.*, Photometric survey of binary near-Earth asteroids, *Icarus*, in press, 2006.
34 J. Virtanen, Asteroid orbital inversion using statistical methods, PhD Thesis, University of Helsinki, 2005 (`http://e-thesis.helsinki.fi/julkaisut/mat/tahti/vk/virtanen/asteroid.pdf`).
35 P. Michel and M. Yoshikawa, Earth impact probability of the asteroid (25143) Itokawa to be sampled by the spacecraft Hayabusha, *Icarus*, in press, 2005.
36 V. Carruba, T.A. Michtchenko, F. Roig, S. Ferraz-Mello and D. Nesvorný, On the V-type asteroids outside the Vesta family. I. Interplay ..., *Astron. Astrophys.* **441**, 819, 2005.
37 P. Tanga, Impact of Gaia on dynamics and evolution of the Solar System, in *The Three-Dimensional Universe with Gaia*, C. Turon, K.S. O'Flaherty, M.A.C. Perryman (Eds.), p. 243, 2005.
38 A.W. Harris, M. Mueller, M. Delbó and S.J. Bus, The surface properties of small asteroids: Peculiar Betulia, a case study, *Icarus*, in press, 2005.
39 H.H. Hsieh and D. Jewitt, Active asteroids: Mystery in the Main Belt, in: *Asteroids, Comets and Meteors*, Eds. J.A. Fernandez and S. Ferraz-Mello, Cambridge University Press, 2006, in press.
40 F. Roig and R. Gil-Hutton, Selecting candidate V type asteroids from the analysis of the Sloan Digital Sky Survey colors, *Icarus*, submitted, 2006.
41 A. La Spina, P. Paolicchi and U. Penco, Yarkovsky-evolved asteroid dynamical families: a correlation between their present properties and the impact geometry?, preprint, 2005.
42 D.C. Richardson and K.J. Walsh, Binary minor planets, *Ann. Rev. Earth Planet. Sci.* **34**, 2006.
43 R. Gil-Hutton, Identification of families among highly inclined asteroids, *Icarus*, in press, 2006.
44 L.A.M. Benner, M.C. Nolan, S.J. Ostro, J.D. Giorgini, D.P. Pray, A.W. Harris, C. Magri and J.L. Margot, Near-Earth Asteroid 2005 CR37: Radar images and photometry of a candidate contact binary, *Icarus*, in press, 2006.
45 P. Michel and M. Yoshikawa, Dynamical origin of the asteroid (25143) Itokawa: the target of the sample return Hayabusa space mission, *Astron. Astrophys.*, in press, 2006.
46 M. Delbó, A. dell'Oro, A.W. Harris, S. Mottola and M. Mueller, Thermal inertia of near-Earth asteroids and magnitude of the Yarkovsky effect, *Nature*, in press, 2006.

Proceedings contributions

1 **M. Brož** and D. Vokrouhlický, 2002, The peculiar orbit of Vysheslavia: further hints for its Yarkovsky driven origin, in: *Dynamics of Natural and Artificial Celestial Bodies*, Eds. H. Pretka-Ziomek, E. Wnuk, P.K. Seidelmann, D. Richardson. Kluwer Academic Publishers, Dordrecht, p. 307.

2 D. Vokrouhlický and **M. Brož**, 2002, Interaction of the Yarkovsky-drifting orbits with weak resonances: Numerical evidence and challenges, in: *Modern Celestial Mechanics: from Theory to Applications*, Eds. A. Celletti, S. Ferraz-Mello and J. Henrard, Kluwer Academic Publishers, Dordrecht, p. 467.

3 **M. Brož**, D. Vokrouhlický, F. Roig, D. Nesvorný, W.F. Bottke and A. Morbidelli, 2005, The population of asteroids in the 2:1 mean motion resonance with Jupiter revised, in: *Dynamics of Populations of Planetary Systems*, Eds. Z. Knežević and A. Milani, Cambridge Academic Press, p. 179.

4 D. Vokrouhlický, **M. Brož**, W.F. Bottke, D. Nesvorný and A. Morbidelli, 2005, Non-gravitational perturbations and the evolution of the asteroid main belt, in: *Dynamics of Populations of Planetary Systems*, Eds. Z. Knežević and A. Milani, Cambridge Academic Press, p. 145.

5 **M. Brož**, D. Vokrouhlický, A. Morbidelli, D. Nesvorný, W.F. Bottke, F. Roig and D. Čapek, 2005, Non-gravitational forces acting on small bodies, in: *Asteroids, Comets and Meteors*, Eds. D. Lazzaro, Cambridge Academic Press, submitted.

Abstracts of talks and posters

1 **M. Brož** and D. Vokrouhlický, 1998(Aug), Yarkovsky effects as a source of mobility for the asteroid fragments, presented at IAU Colloquium 173, *Evolution and source regions of asteroids and comets*, Tatranská Lomnica.

2 **M. Brož**, D. Vokrouhlický, P. Farinella and W.F. Bottke, 1999(Oct), Capture of Yarkovsky-driven asteroid orbits into higher-order main-belt resonances, *BAAS* **31**, 1111.

3 D. Vokrouhlický, **M. Brož**, P. Farinella and Z. Knežević, 1999(Oct), Yarkovsky-driven leakage of Koronis family members and the case of 2953 Vysheslavia, *BAAS* **31**, 1111.

1 P. Michel, W. Benz, P. Tanga and D. Richardson, Collisions and gravitational reaccumulation: Forming asteroid families and satellites, *Science* **294**, 1696, 2001.

4 **M. Brož** and D. Vokrouhlický, 2000(Jul), Evolution of the Yarkovsky-driven orbits of meteoroids, in: *The Restless Universe*, presented at the NATO Advanced Study Institute, Blair Atholl.

5 D. Vokrouhlický, **M. Brož**, A. Morbidelli, W.F. Bottke and D. Nesvorný, 2001(Jun), Long-term dynamical diffusion in asteroid families via Yarkovsky effect, poster presented at *Asteroids 2001* conference, Palermo.

1 P. Michel, W. Benz, P. Tanga and D. Richardson, Collisions and gravitational reaccumulation: Forming asteroid families and satellites, *Science* **294**, 1696, 2001.

2 S.F. Dermott *et al.*, Asteroidal dust, in: *Asteroids III*, Eds. W.F. Bottke, A. Cellino. P. Paolicchi and R. Binzel, (Arizona Univ. Press, 2003), p. 423.

6 W.F. Bottke, D. Vokrouhlický, **M. Brož**, D. Nesvorný and A. Morbidelli, 2001(Oct), Dynamical Spreading of the Koronis Family via the Yarkovsky Effect, *BAAS* **33**, 1136.

7 W.F. Bottke, D. Vokrouhlický, A. Morbidelli, D. Nesvorný and **M. Brož**, 2002(Aug), The consequences of the Yarkovsky effect: The legacy of Paolo Farinella, invited talk at *Asteroids, Comets and Meteors*, Berlin.

8 D. Vokrouhlický, **M. Brož**, A. Morbidelli, W.F. Bottke, D. Nesvorný, D. Lazzaro and A. Rivkin, 2002(Aug), Yarkovsky footprints in the Eos family, presented at *Asteroids, Comets and Meteors*, Berlin.

9 **M. Brož**, D. Vokrouhlický, A. Morbidelli, D. Nesvorný and F. Roig, 2002(Aug), A connection of the 2:1 resonance asteroids with the Themis family?, poster at *Asteroids, Comets and Meteors*, Berlin.

10 **M. Brož**, 2002(Aug), A faster version of the SWIFT-MVS integrator and implementation of the Yarkovsky force, poster at *Asteroids, Comets and Meteors*, Berlin.

11 **M. Brož**, D. Vokrouhlický, F. Roig, A. Morbidelli and D. Nesvorný, 2004(Apr), The Yarkovsky delivery of unstable asteroids inside the 2/1 mean motion resonance with Jupiter, *BAAS* **36**, 857.

12 **M. Brož**, D. Vokrouhlický, A. Morbidelli, D. Nesvorný, W.F. Bottke, F. Roig and D. Čapek, 2005 (Aug), Non-gravitational forces acting on small bodies, invited talk at *Asteroids, Comets and Meteors* (IAU Symposium 229), Búzios.

13 **M. Brož**, D. Vokrouhlický, F. Roig, D. Nesvorný, W.F. Bottke and A. Morbidelli, 2005(Aug), Elusive Zhongguos and Griquas — long-lived asteroids inside the J2/1 resonance, poster at *Asteroids, Comets and Meteors* (IAU Symposium 229), Búzios.

Popular articles and books

1 **M. Brož**, 2000, Yarkovského efekt a dynamika sluneční soustavy, *Astropis* 1/2000.

2 **M. Brož**, 2000, Impaktní krátery (1) — Morasko, *Povětroň* 4/2000, p. 7.[26]

3 **M. Brož**, 2000, Impaktní krátery (2) — Ries, *Povětroň* 5/2000, p. 6.

4 **M. Brož**, 2001, NEAR phones home (o přistání na Erosu), *Povětroň* 3/2001, p. 4.

5 **M. Brož**, 2001, Asteroidy na začátku 3. tisíciletí (1), *Povětroň* 5/2001, p. 4.

6 **M. Brož**, 2001, (253) Mathilde a (433) Eros pod lupou NEARu, *Povětroň* 2/2001, p. 3.

7 **M. Brož**, 2002, 10 otázek a odpovědí (2), *Povětroň* 1/2002, p. 22.

8 **M. Brož**, P. Scheirich, 2002, Asteroidy na počátku 3. tisíciletí (2), *Povětroň* 2/2002, p. 8.

9 J. Ďurech, **M. Brož**, 2002, Určení průměrů planet prostým okem?!, *Povětroň* 3/2002, p. 6.

10 **M. Brož**, 2002, 10 otázek a odpovědí (3), *Povětroň* 4/2002, p. 4.

11 **M. Brož**, 2002, Technické řešení dalekohledu JST, *Povětroň* 5/2002, p. 8.

12 **M. Brož**, M. Lehký, 2002, Pozorovací program JST, *Povětroň* 5/2002, p. 7.

13 **M. Brož**, 2003, Meteority v Museum für Naturkunde, Berlin, *Povětroň* 1/2003, p. 7.

14 **M. Brož**, 2003, 10 otázek a odpovědí (4), *Povětroň* 3/2003, p. 14.

15 **M. Brož**, 2003, Impaktní kráter Steinheim, *Povětroň* S1/2003, p. 3.

16 **M. Brož**, 2004, Dynamická astronomie v roce 2004, *Povětroň* 3/2004, p 4.

17 **M. Brož**, 2004, Astronomický kurz (1) — Protoplanetární disk, *Povětroň* 4/2004, p. 4.

18 **M. Brož**, 2004, Film Sluneční soustava 2003, *Povětroň* 4/2004, p. 16.[27]

19 **M. Brož**, 2004, Astronomický kurz (2) — Vznik planet, *Povětroň* 5/2004, p. 12.

20 **M. Brož**, M. Nosek, J. Trebichavský, D. Pecinová (Eds.), 2004, Sluneční hodiny na pevných stanovištích. Čechy, Morava Slezsko a Slovensko, Academia, Prague (403pp).[28]

[26] `http://www.astrohk.cz/ashk/povetron/`
[27] `http://www.astrohk.cz/ss2003/`
[28] `http://www.astrohk.cz/slunecni_hodiny.html`

21 **M. Brož**, M. Cholasta, J. Kujal, R. Lacko, 2005, Planetární stezka, *Povětroň* S2/2004.[29]
22 **M. Brož**, 2005, Co na planetární stezce nenajdete?, *Povětroň* 3/2005, p. 4.
23 **M. Brož**, 2006, Astronomický kurz (3) — Planetesimály a embrya, *Povětroň* 1/2006, p. 4.

[29] `http://www.astrohk.cz/planetarni_stezka/`

References

A'Hearn, M.F., Belton, M.J.S., Delamere, W.A. & 30 coauthors 2005. Deep Impact: Excavating comet Tempel 1. *Science* **310**, 258–264.

AstDyS — Asteroids Dynamic Site, `http://hamilton.dm.unipi.it/`.

AstOrb — The Asteroid Orbital Elements Database, `ftp://ftp.lowell.edu/pub/elgb/astorb.html`.

Bahcall, J.N., Pinsonneault, M.H., Basu, S., 2001. Solar models: Current epoch and time dependences, neutrinos, and helioseismological properties. *Astrophys. J.* **555**, 990–1012.

Beekman, G., 2006. I.O. Yarkovsky and the discovery of 'his effect'. *J. Hist. Astron.* in press.

Bell, J.F., 1989. Mineralogical clues to the origin of asteroid dynamical families. *Icarus* **78**, 426–440.

Bell, J.F., Hawke, B.R., Owensby, P.D., 1987. Carbonaceous chondrites from S-type asteroids? *Bull. Am. Astron. Soc.* **19**, 841.

Bendjoya, P., Zappalà, V., 2002. Asteroid family identification. in: *Asteroids III* (W.F. Bottke, A. Cellino., P. Paolicchi & R.P. Binzel, Eds.), pp. 613–618. Arizona University Press, Tucson.

Benz, W., Asphaug, E., 1999. Catastrophic disruptions revisited. *Icarus* **142**, 5–20.

Bertotti, B., Farinella, P., Vokrouhlický, D., 2003. *Physics of the Solar System*. Kluwer Academic Publishers, Dordrecht.

Binzel, R.P., 1988. Collisional evolution in the Eos and Koronis asteroid families: Observational and numerical results. *Icarus* **73**, 303–313.

Binzel, R.P., Rivkin, A.S., Stuart, J.S., Harris, A.W., Bus, S.J., Burbine, T.H., 2004. Observed spectral properties of near-Earth objects: Results for population distribution, source regions, and space weathering processes. *Icarus* **170**, 259–294.

Bland, P.A., Conway, A., Smith, T.B., Berry, F.J., Pillinger, C.T., 1998. in: *Meteorites: Flux with Time and Impact Effects*, pp. 43. Geological Society, London, Special Publications 140.

Bottke, W.F., Nolan, M.C., Greenberg, R., Kolvoord, R.A., 1994. Velocity distributions among colliding asteroids. *Icarus* **107**, 255–268.

Bottke, W.F., Jedicke, R., Morbidelli, A., Petit, J.-M., Gladman, B., 2000a. Understanding the distribution of near-Earth asteroids. *Science* **288**, 2190–2194.

Bottke, W.F., Rubincam, D.P., Burns, J.A., 2000b. Dynamical evolution of main belt meteoroids: Numerical simulations incorporating planetary perturbations and Yarkovsky thermal forces. *Icarus* **145**, 301–331.

Bottke, W.F., Vokrouhlický, D., Brož, M., Nesvorný, D., Morbidelli, A., 2001. Dynamical Spreading of Asteroid Families by the Yarkovsky Effect. *Science* **294**, 1693–1695.

Bottke, W.F., Morbidelli, A., Jedicke, R., Petit, J.-M., Levison, H.F., Michel, P., Metcalfe, T.S., 2002a. Debiased orbital and absolute magnitude distribution of the near-Earth objects. *Icarus* **156**, 399–433.

Bottke, W.F., Vokrouhlický, D., Rubincam, D.P., Brož, M. 2002b. Dynamical evolution of asteroids and meteoroids using the Yarkovsky effect. in: *Asteroids III* (W.F. Bottke, A. Cellino. P. Paolicchi & R.P. Binzel, Eds.), pp. 395–408. Arizona University Press, Tucson.

Bottke, W.F., Durda, D.D., Nesvorný, D., Jedicke, R., Morbidelli, A., Vokrouhlický, D., Levison, H.F., 2005a. The fossilized size distribution of the main asteroid belt. *Icarus* **175**, 111–140.

Bottke, W.F., Durda, D.D., Nesvorný, D., Jedicke, R., Morbidelli, A., Vokrouhlický, D., Levison, H.F., 2005b. Linking the collisional history of the main asteroid belt to its dynamical excitation and depletion. *Icarus* **179**, 63–94.

Bottke, W.F., Durda, D.D., Nesvorný, D., Jedicke, R., Morbidelli, A., Vokrouhlický D., Levison, H.F., 2005c. The origin and evolution of stony meteorites. in: *Dynamics of Populations of Planetary Systems* (Z. Knežević & A. Milani, Eds.), pp. 357–374. Cambridge University Press, Cambridge.

Bottke, W.F., Nesvorný, D., Grimm, R.E., Morbidelli, A., O'Brien, D.P., 2006. Iron meteorites are remnants of planetesimals formed in the terrestrial planet region. *Nature* **439**, 821–824.

Bowell, E.K., Muinonen, K., Wasserman, L.H., 1994. A public-domain asteroid orbit database. in: *Asteroids, Comets and Meteors 1993* (A. Milani, M. Di Martino & A. Cellino, Eds.), pp. 477–481. Kluwer Academic Publishers, Dordrecht.

Brouwer, D., 1951. Secular variations of the orbital elements of minor planets. *Astron. J.* **56**, 9–32.

Brown, E.W., 1932. Observation and gravitational theory in the Solar System. *Publ. Astron. Soc. Pacific* **44**, 21–40.

Brož, M., 1999. Orbital evolution of the asteroid fragments due to planetary perturbations and Yarkovsky effects. diploma thesis, Charles Univ., Prague.

Brož, M. 2002, A faster version of the SWIFT-MVS integrator and implementation of the Yarkovsky Force. Poster No. 05.19p presented at the *Asteroids, Comets and Meteors* meeting, Berlin.

Brož, M., Vokrouhlický, D., 2001. The peculiar orbit of Vysheslavia: further hints for its Yarkovsky driven origin? in: *Dynamics of Natural and Artificial Celestial Bodies* (H. Pretka-Ziomek, E. Wnuk, P.K. Seidelmann & D. Richardson, Eds.), pp. 307–312. Kluwer Academic Press, Dordrecht.

Brož, M., Vokrouhlický, D., Roig, F., Nesvorný, D., Bottke, W.F., Morbidelli, A., 2005a. The population of

asteroids in the 2:1 mean motion resonance with Jupiter revised. in: *Dynamics of Populations of Planetary Systems* (Z. Knežević & A. Milani, Eds.), pp. 179–186. The Cambridge University Press, Cambridge.

Brož, M., Vokrouhlický, D., Roig, F., Nesvorný, D., Bottke, W.F., Morbidelli, A., 2005b. Yarkovsky origin of the unstable asteroids in the 2/1 mean motion resonance with Jupiter. *Mon. Not. R. Astron. Soc.* **359**, 1437–1455.

Brož, M., Vokrouhlický, D., Bottke, W. F., Nesvorný, D., Morbidelli, A., & Čapek, D., 2006. Non-gravitational forces acting on small bodies. in: *Asteroids, Comets, Meteros 2005. Proceedings IAU Symposium No. 229* (S. Ferraz-Mello, J. Fernández & D. Lazzaro, Eds.), submitted.

Burbine, T.H., Binzel, R.P., Bus, S.J., Clark, B.E., 2001. K asteroids and CO3/CV3 chondrites. *Meteorit. Planet. Sci.* **36**, 245–253.

Burbine, T.H., McCoy, T.J., Meibom, A., Gladman, B., Keil, K., 2002. Meteoritic parent bodies: their number and identification. in: *Asteroids III* (W.F. Bottke, A. Cellino. P. Paolicchi & R.P. Binzel, Eds.), pp. 653–667. Arizona University Press, Tucson.

Burns, J.,A., Lamy, P.L., Soter, S., 1979. Radiation forces on small particles in the solar system. *Icarus* **40**, 1–48.

Bus, S.J., Binzel, R.P., 2002a. Phase II of the small main-belt asteroid spectroscopic survey. The observations. *Icarus* **158**, 106–145.

Bus, S.J., Binzel, R.P., 2002b. Phase II of the small main-belt asteroid spectroscopic survey. A feature-based taxonomy. *Icarus* **158**, 146–177.

Campo Bagatin, A., Petit, J.-M., 2001. Effects of the geometric constraints on the size distributions of debris in asteroidal fragmentation. *Icarus* **149**, 210–221.

Čapek, D., Vokrouhlický, D., 2004. The YORP effect with finite thermal conductivity. *Icarus* **172**, 526–536.

Čapek, D., Vokrouhlický, D.. 2006. Accurate vs efficient methods of the Yarkovsky/YORP effect computation. *Icarus*, to be submitted.

Carpino, M., Gonczi, R., Farinella, P., Froeschlé, Ch., Froeschlé, C., Paolicchi, P., Zappalà, V., 1986. The accuracy of proper orbital elements and the properties of asteroid families: Comparison with the linear theory. *Icarus* **68**, 55–76.

Carruba, V., Burns, J.A., Bottke, W.F., Nesvorný, D., 2003. Orbital evolution of the Gefion and Adeona asteroid families: close encounters with massive asteroids and the Yarkovsky effect. *Icarus* **162**, 308–327.

Carruba, V., Ferraz-Mello, S., Michtchenko, T.A., Roig, F., Nesvorný, D., 2005. On the V-Type asteroids outside the Vesta family. I: Interplay of non-linear secular resonances and the Yarkovsky effect. The cases of 956 Elisa and 809 Lundia. *Astron. Astrophys.* **441**, 819–830.

Cellino, A., Michel, P., Tanga, P., Zappalà, V., Paolicchi, P., Dell'Oro, A., 1999. The velocity-size relationship for members of asteroid families and implications for the physics of catastrophic collisions. *Icarus* **141**, 79–95.

Cellino, A., Bus, S.J., Doressoundiram, A., Lazzaro, D., 2002. Spectroscopic properties of asteroid families. in: *Asteroids III* (W.F. Bottke, A. Cellino. P. Paolicchi & R.P. Binzel, Eds.), pp. 633–643. Arizona University Press, Tucson.

Chapman, C.R., 2002. Cratering on asteroids from Galileo and NEAR Shoemaker. in: *Asteroids III* (W.F. Bottke, A. Cellino, P. Paolicchi & R. Binzel, Eds.), pp. 315–330. University of Arizona Press, Tucson.

Chapman, C.R., Paolicchi, P., Zappalà, V., Binzel, R.P., Bell, J.F., 1989. Asteroid families: Physical properties and evolution. in: *Asteroids II* (R.P. Binzel, T. Gehrels & M.S. Matthews, Eds.), pp. 386–415. University of Arizona Press, Tucson.

Chesley, S.R., Ostro, S.J., Vokrouhlický, D., Čapek, D., Giorgini, J.D., Nolan, M.C., Margot, J.-L., Hine, A.A., Benner, L.A.M., Chamberlin, A.B., 2003. Direct detection of the Yarkovsky effect by radar ranging to asteroid 6489 Golevka. *Science* **302**, 1739–1742.

Chesley, S.R., Yeomans, D.K., 2005. Nongravitational accelerations on comets. in: *Dynamics of Populations of Planetary Systems* (Z. Knežević & A. Milani, Eds.), pp. 289–302. Cambridge University Press, Cambridge.

Cordeiro, R.R., Gomes, R.S., Vieira Martins, R. 1997, A Mapping for Nonconservative Systems. *Celest. Mech. Dyn. Astr.*, **65**, 407–419.

Dahlgren, M., 1998. A study of Hilda asteroids. III. Collision velocities and collision frequencies of Hilda asteroids. *Astron. Astrophys.* **336**, 1056–1064.

Davidsson, B.J.R., Gutiérrez, P.J., 2005. Nucleus properties of Comet 67P/Churyumov Gerasimenko estimated from non-gravitational force modeling. *Icarus* **176**, 453–477.

Davis, D.R., Chapman, C.R., Weidenschilling, S.J., Greenberg, R., 1985. Collisional history of asteroids: Evidence from Vesta and the Hirayama families. *Icarus* **63**, 30–53.

Davis, D.R., Farinella, P., Paolicchi, P., Weidenschilling, S.J., Binzel, R.P., 1989. Asteroid collisional history: Effects on sizes and spins. in: *Asteroids II* (R.P. Binzel, T. Gehrels & M.S. Matthews, Eds.), pp. 805–826. Arizona University Press, Tucson.

DE405 — JPL Planetary and Lunar Ephemerides, `ftp://ssd.jpl.nasa.gov/pub/eph/export/`

Delbó, M., Harris, A.W., Binzel, R.P., Pravec, P., Davies, J.K., 2003. Keck observations of near-Earth asteroids in the thermal infrared. *Icarus* **166**, 116–130.

Dell'Oro, A., Bigongiari, G., Paolicchi, P., Cellino, A., 2004. Asteroid families: evidence of ageing of the proper elements. *Icarus* **169**, 341–356.

Dermott, S.F., Grogan, K., Durda, D.D., Jayaraman, S., Kehoe, T.J.J., Kortenkamp, S.J., Wyatt, M.C., 2001. Orbital evolution of interplanetary dust. in: *Interplanetary Dust* (E. Grün, B.A.S. Gustafson, S.F. Dermott & H. Fechtig, Eds.), pp. 569–639. Springer, Berlin.

Dohnanyi, J.W., 1969. Collisional models of asteroids and their debris. *J. Geophys. Res.* **74**, 2531–2554.

Doressoundiram, A., Barucci, M.A., Fulchignoni, M., Florczak, M., 1998. Eos family: A spectroscopic study. *Icarus* **131**, 15–31.

Drummond, J.D., Weidenschilling, S.J., Chapman, C.R., Davis, D.R., 1988. Photometric geodesy of main-belt asteroids. II. Analysis of lightcurves for poles, periods, and shapes. *Icarus* **76**, 19–77.

Durda, D.D., Greenberg, R., Jedicke, R., 1998. Collisional models and scaling laws: A new interpretation of the shape of the main-belt asteroid size distribution. *Icarus* **135**, 431–440.

Durda, D.D., Bottke, W.F., Enke, B.L., Merline, W.J., Asphaug, E., Richardson, D.C., Leinhardt, Z.M., 2004. The formation of asteroid satellites in large impacts: results from numerical simulations. *Icarus* **170**, 243–257.

Durda, D.D., Bottke, W.F., Nesvorný, D., Asphaug, E., Richardson, D.C., 2006. Size-frequency distributions of fragments from SPH/N-body simulations: Comparison with observed asteroid families. *Icarus*, submitted.

Efthymiopoulos, C., Contopoulos, G., Voglis, N., 1999. Cantori, islands and asymptotic curves in the stickiness region. *Celest. Mech. Dyn. Astr.* **73**, 221–230.

Farinella, P., Carpino, M., Froeschlé, Ch., Froeschlé, C., Gonczi, R., Knežević, Z., Zappalà, V., 1989. The ages of asteroid families. *Astron. Astrophys.* **217**, 298–306.

Farinella, P., Froeschle, C., Gonczi, R., 1994. Meteorite delivery and transport. in: *Asteroids, Comets, Meteors 1993* (A. Milani, M. Di Martino & A. Cellino, Eds.) p. 205. Kluwer Academic Publishers, Dordrecht.

Farinella, P., Vokrouhlický, D., 1999. Semimajor axis mobility of asteroidal fragments. *Science* **283**, 1507–1510.

Farinella, P., Vokrouhlický, D., Hartmann, W.K., 1998. Meteorite delivery via Yarkovsky orbital drift. *Icarus* **132**, 378–387.

Farley, K.A., Vokrouhlický, D., Bottke, W.F., Nesvorný, D. 2006, A late Miocene dust shower from the break-up of an asteroid in the main belt. *Nature* **439**, 295–297.

Ferraz-Mello, S., 1994. Dynamics of the asteroidal 2/1 resonance. *Astron. J.* **108**, 2330–2337.

Ferraz-Mello, S., Michtchenko, T.A., Roig, F., 1998. The determinant role of Jupiter's Great Inequality in the depletion of the Hecuba gap. *Astron. J.* **116**, 1491–1500.

Fujiwara, A., 1982. Complete fragmentation of the parent bodies of Themis, Eos, and Koronis families. *Icarus* **52**, 434–443.

Fukugita, M., Ichikawa, T., Gunn, J.E., Doi, M., Shimasaku, K., Schneider, D.P., 1996. The Sloan Digital Sky Survey photometric system. *Astron. J.* **111**, 1748–1756.

Giorgini, J.D., Ostro, S.J., Benner, L.A.M., Chodas, P.W., Chesley, S.R., Hudson, R.S., Nolan, M.C., Klemola, A.R., Standish, E.M., Jurgens, R.F., Rose, R., Chamberlin, A.B., Yeomans, D.K., Margot, J.-L., 2002. Asteroid 1950 DA's encounter with Earth in 2880: Physical limits of collision probability prediction. *Science* **296**, 132–136.

Gladman, B.J., Migliorini, F., Morbidelli, A., Zappala, V., Michel, P., Cellino, A., Froeschle, C., Levison, H.F., Bailey, M., Duncan, M. 1997. Dynamical lifetimes of objects injected into asteroid belt resonances. *Science* **277**, 197–201.

Grady, M.M., 2000. *Catalogue of Meteorites*, Cambridge University Press, Cambridge.

Guillens, S.A., Vieira Martins, R., Gomes, R.S., 2002. A global study of the 3:1 resonance neighborhood: a search for unstable asteroids. *Astron. J.* **124**, 2322–2331.

Hagihara, Y., 1975. *Celestial Mechanics. Volume IV — Periodic and quasi-periodic solutions*. Japan Society for the promotion of Science, Tokyo.

Hardorp, J., 1978. The Sun among the stars. *Astron. Astrophys.* **63**, 383–390.

Henrard, J., Lemaître, A., 1983. A second fundamental model for resonance. *Celest. Mech. Dyn. Astr.* **30**, 197–218.

Henrard, J., Lemaître, A., 1987. A perturbative treatment of the 2/1 Jovian resonance. *Icarus* **69**, 266–279.

Henrard, J., Watanabe, N., Moons, M., 1995. A bridge between secondary and secular resonances inside the Hecuba gap. *Icarus* **115**, 336–346.

Hirayama, K., 1918. Groups of asteroids probably of common origin. *Astron. J.* **31**, 185–188.

HPHK Observer services, `http://www.astrohk.cz/observer.html`.

Ivezić, Z., & 32 collaborators, 2001. Solar system objects observed in the Sloan Digital Sky Survey commissioning data. *Astron. J.* **122**, 2749–2784.

Ivezić, Z., Lupton, R.H., Jurić, M., Tabachnik, S., Quinn, T., Gunn, J.E., Knapp, G.R., Rockosi, C.M., Brinkmann, J., 2002. Color confirmation of asteroid families. *Astron. J.* **124**, 2943–2948.

Jedicke, R., Larsen, J., Spahr, T., 2003. Observational selection effects in asteroid surveys. in: *Asteroids III* (W.F. Bottke, A. Cellino. P. Paolicchi & R.P. Binzel, Eds.), pp. 71–87. Arizona University Press, Tucson.

Jedicke, R., Nesvorný, D., Whiteley, R., Ivezić, Z., Jurić, M., 2004. An age-colour relationship for main-belt S-complex asteroids. *Nature* **429**, 275–277.

Jurić, M. & 12 collaborators, 2002. Comparison of positions and magnitudes of asteroids observed in the Sloan Digital Sky Survey with those predicted for known asteroids. *Astron. J.* **124**, 1776–1787.

Kaasalainen, M., Torppa, J., Muinonen, K., 2001. Optimization methods for asteroid lightcurve inversion. II. The complete inverse problem. *Icarus* **153**, 37–51.

Kaasalainen, M., 2004. Physical models of large number of asteroids from calibrated photometry sparse in time. *Astron. Astrophys.* **422**, L39–L42.

Knežević, Z., Milani, A., Farinella, P., 1997. The dangerous border of the 5:2 mean motion resonance. *Planet. Sp. Sci.* **45**, 1581–1585.

Knežević, Z., Milani, A., 2000. Synthetic proper elements for outer main belt asteroids. *Celest. Mech. Dyn. Astr.* **78**, 17–46.

Knežević, Z., Milani, A., 2003. Proper element catalogs and asteroid families. *Astron. Astrophys.* **403**, 1165–1173.

Knežević, Z., Lemaître, A., Milani, A., 2002. The determination of asteroid proper elements. in: *Asteroids III* (W.F. Bottke, A. Cellino. P. Paolicchi & R.P. Binzel, Eds.), pp. 603–612. Arizona University Press, Tucson.

La Spina, A., Paolicchi, P., Kryszczyńska, A., Pravec, P., 2004. Retrograde spins of near-Earth asteroids from the Yarkovsky effect. *Nature* **428**, 400–401.

La Spina, A., Paolicchi. P., Penco, U., 2005. Yarkovsky-evolved asteroid dynamical families: a correlation between their present properties and the impact geometry? *Bull. Am. Astron. Soc.* **37**, 1514.

Laskar, J., Robutel, P., 2001. High order symplectic integrators for perturbed Hamiltonian systems. *Celest. Mech. Dyn. Astr.* **80**, 39–62.

Lazzaro, D., Angelia, C.A., Carvanoa, J.M., Mothé-Diniz, T., Duffard, R., Florczak, M., 2004. S^3OS^2: the visible spectroscopic survey of 820 asteroids. *Icarus* **172**, 179–220.

Lemaître, A., Henrard, J., 1990. On the origin of chaotic behavior in the 2/1 Kirkwood gap. *Icarus* **83**, 391–409.

Levison, H., Duncan, M., 1994. The long-term dynamical behavior of short-period comets. *Icarus*, **108**, 18–36.

Levison, H., Duncan, M., 1997. From the Kuiper belt to Jupiter-family comets: The spatial distribution of ecliptic comets. *Icarus* **127**, 13–32.

Levison, H., Morbidelli, A., Dones, L., Jedicke, R., Wiegert, P.A., Bottke, W.F., 2002. The mass disruption of Oort cloud comets. *Science* **296**, 2212–2215.

Love, S.G., Ahrens, T.J., 1996. Catastrophic impacts on gravity dominated asteroids. *Icarus* **124**, 141–155.

Luther, R., 1869. Beobachtungen des Planeten (108) Hecuba af der Bilk-Düsseldorfer Sternwarte. *Astron. Nach.* **74**, 31–32.

Magnusson, P., 1986. Distribution of spin axes and senses of rotation for 20 large asteroids. *Icarus* **68**, 1–39.

Malyshkin, L., Tremaine, S., 1999. The keplerian map for the planar restricted three-body problem as a model of comet evolution. *Icarus* **141**, 341–353.

Marzari, F., Davis, D.R., Vanzani, V., 1995. Collisional evolution of asteroid families. *Icarus* **113**, 168–187.

Marzari, F., Cellino, A., Davis, D.R., Farinella, P., Zappalà, V., Vanzani, V., 1996. Origin and evolution of the Vesta asteroid family. *Astron. Astrophys.* **316**, 248–262.

Michałowski, T., 1993. Poles, shapes, senses of rotation, and sidereal periods of asteroids. *Icarus* **106**, 563–572.

Michałowski, T., Pych, W., Berthier, J., Kryszczyńska, A., Kwiatkowski, T., Boussuge, J., Fauvaud, S., Denchev, P., Baranowski, R., 2000. CCD photometry, spin and shape models of five asteroids: 225, 360, 416, 516, and 1223. *Astron. Astrophys. Suppl. Ser.* **146**, 471–479.

Michałowski, T., Kwiatkowski, T., Kaasalainen, M., Pych, W., Kryszczyńska, A., Dybczyński, P.A., Velichko, F.P., Erikson, A., Denchev, P., Fauvaud, S., Szabó, G.M., 2004. Photometry and models of selected main belt asteroids I. 52 Europa, 115 Thyra, and 382 Dodona. *Astron. Astrophys.* **416**, 353–366.

Michel, P., Benz, W., Tanga, P., Richardson, D.C., 2001. Collisions and gravitational reaccumulation: Forming asteroid families and satellites. *Science* **294**, 1696–1700.

Michel, P., Tanga, P., Benz, W., Richardson, D.C., 2002. Formation of asteroid families by catastrophic disruption: Simulations with fragmentation and gravitational reaccumulation. *Icarus* **160**, 10–23.

Michtchenko, T.A., Ferraz-Mello, S., 1997. Escape of asteroids from the Hecuba gap. *Planet. Sp. Sci.* **45**, 1587–1593.

Migliorini, F., Zappalà, V., Vio, R., Cellino, A., 1995. Interlopers within asteroid families. *Icarus* **118**, 271–291.

Milani, A., Farinella, P., 1994. The age of Veritas asteroid family deduced by chaotic chronology. *Nature* **370**, 40–42.

Milani, A., Farinella, P., 1995. An asteroid on the brink. *Icarus* **115**, 209–212.

Milani, A., Knežević, Z., 1990. Secular perturbation theory and computation of asteroid proper elements. *Celest. Mech. Dyn. Astr.* **49**, 347–411.

Milani, A., Knežević, Z., 1992. Asteroid proper elements and secular resonances. *Icarus* **98**, 211–232.

Milani, A., Knežević, Z., 1994. Asteroid proper elements and the dynamical structure of the asteroid main belt. *Icarus* **107**, 219–254.

Milani, A., Sansaturio, M.E., Chesley, S.R., 2001. The asteroid identification problem iv: Attributions. *Icarus* **151**, 150–159.

Moons, M., Morbidelli, A., Migliorini, F., 1998. Dynamical structure of the 2/1 commensurability with Jupiter and the origin of the resonant asteroids. *Icarus* **135**, 458–468.

Morbidelli, A., 1996. The Kirkwood gap at the 2/1 commensurability with Jupiter: New numerical results. *Astron. J.* **111**, 2453–2461.

Morbidelli, A., 2002. *Modern celestial mechanics: Aspects of Solar System dynamics*. Taylor & Francis, London.

Morbidelli, A., Moons, M., 1993. Secular resonances in mean motion commensurabilities — The 2/1 and 3/2 cases. *Icarus* **102**, 316–332.

Morbidelli, A., Nesvorný, D., 1999. Numerous weak resonances drive asteroids toward terrestrial planets orbits. *Icarus* **139**, 295–308.

Morbidelli, A., Vokrouhlický, D., 2003. The Yarkovsky-driven origin of Near Earth Asteroids. *Icarus* **163**, 120–134.

Morbidelli, A., Zappalà, V., Moons, M., Cellino, A., Gonczi, R., 1995. Asteroid families close to mean motion resonances: Dynamical effects and physical implications. *Icarus* **118**, 132–154.

Morbidelli, A., Nesvorný, D., Bottke, W.F., Michel, P., Vokrouhlický, D., Tanga, P., 2003. The shallow magnitude distribution of asteroid families. *Icarus* **162**, 328–336.

Morbidelli, A., Levison, H.F., Tsiganis, K., Gomes, R.S., 2005. Chaotic capture of Jupiter's Trojan asteroids in the early Solar System. *Nature* **435**, 462–465.

Murray, C.A., 1986. Structure of the 2:1 and 3:2 Jovian resonances. *Icarus* **65**, 70–82.

Mosix cluster, `http://www.mosix.org`.

Mothé-Diniz, T., Carvano, J.M., 2005a. 221 Eos: A remnant of a partially differentiated parent body? *Astron. Astrophys.* **442**, 727–729.

Mothé-Diniz, T., Roig, F., Carvano, J.M., 2005. Reanalysis of asteroid families structure through visible spectroscopy. *Icarus* **174**, 54–80.

Mottola, S., de Angelis, G., di Martino, M., Erikson, A., Hahn, G., Neukum, G., 1995. The near-earth objects follow-up program: First results. *Icarus* **117**, 62–70.

Nesvorný, D., Bottke, W.F., 2004. Detection of the Yarkovsky effect for main-belt asteroids. *Icarus* **170**, 324–342.

Nesvorný, D., Ferraz-Mello, S., 1997. On the asteroidal population of the first-order Jovian resonances. *Icarus* **130**, 247–258.

Nesvorný, D., Morbidelli, A., 1998. Three-body mean motion resonances and the chaotic structure of the asteroid belt. *Astron. J.* **116**, 3029–3037.

Nesvorný, D., Vokrouhlický, D., 2006. New candidates for recent asteroid breakups. *Astron. J.*, submitted.

Nesvorný, D., Morbidelli, A., Vokrouhlický, D., Bottke, W.F., Brož, M., 2002a. The Flora family: a case of the dynamically dispersed collisional swarm? *Icarus* **157**, 155–172.

Nesvorný, D., Bottke, W.F., Dones, L., Levison, H.F., 2002b. The recent breakup of an asteroid in the main-belt region. *Nature* **417**, 720–722.

Nesvorný, D., Bottke, W.F., Levison, H.F., Dones, L., 2002. Recent origin of the Solar System dust bands. *Astrophys. J.* **591**, 486–497.

Nesvorný, D., Jedicke, R., Whiteley, R.J., Ivezić, Ž., 2005. Evidence for asteroid space weathering from the Sloan Digital Sky Survey. *Icarus* **173**, 132–152.

Nesvorný, D., Vokrouhlický, D., Bottke, W.F., Sykes, M.V., 2006a. Properties of asteroid dust bands and their sources. *Icarus* **181**, 107–144.

Nesvorný, D., Enke, B.L., Bottke, W.F., Durda, D.D., Asphaug, E., Richardson, D.C., 2006b. Karin cluster formation via asteroid impact. *Icarus*, in press.

Nesvorný, D., Vokrouhlický, D., Bottke, W.F., 2006c. The breakup of a main belt asteroid 450 ± 50 ky ago. *Science*, submitted.

O'Brien, D.P., Greenberg, R., 2003. Steady-state size distributions for collisional populations: analytical solution with size-dependent strength. *Icarus* **164**, 334–345.

Omni OpenMP compiler project, `http://phase.hpcc.jp/Omni/`

OpenMP specification, `http://www.openmp.org`

Öpik, E.J., 1951. Collision probability with the planets and the distribution of planetary matter. *Proc. R. Irish Acad.* **54**, 165–199.

Paolicchi, P., 2005. Rotational properties of asteroids: a tool to understand their evolution? *Mem. Soc. Astron. Italiana Suppl.* **6**, 110–115.

Paolicchi, P., Verlicchi, A., Cellino, A., 1996. An improved semi-empirical model of catastrophic impact processes. I. Theory and laboratory experiments. *Icarus* **121**, 126–157.

Paolicchi, P., Burns, J.A., Weidenschilling, S.J., 2002. Side effects of collisions: Spin rate changes, tumbling rotations, and binary asteroids. in: *Asteroids III* (W.F. Bottke, A. Cellino, P. Paolicchi & R. Binzel, Eds.), pp. 517-526. University of Arizona Press, Tucson.

Peterson, C., 1976. A source mechanism for meteorites controlled by the Yarkovsky effect. *Icarus* **29**, 91–111.

Petit, J.-M., Farinella, P., 1993. Modelling the outcomes of high-velocity impacts between small solar system bodies. *Celest. Mech. Dyn. Astr.* **57**, 1–28.

Pravec, P., Harris, A.W., 2000. Fast and slow rotation of asteroids. *Icarus* **148**, 12–20.

Pravec, P., Šarounová, L., Wolf, M., 1996. Lightcurves of 7 near–Earth asteroids. *Icarus* **124**, 471–482.

Pravec, P., Harris, A.W., Michałowski T., 2002. Asteroid rotations. in: *Asteroids III* (W.F. Bottke, A. Cellino. P. Paolicchi & R.P. Binzel, Eds.), pp. 113–122. Arizona University Press, Tucson.

Press, V.H., Teukolsky, S.A., Vetterlink, W.T., Flannery, B.P., 2001. *Numerical recipes in Fortran 77*. Cambridge University Press, Cambridge.

Quinn, T.R., Tremaine, S., Duncan, M., 1991. A three million year integration of the earth's orbit. *Astron. J.*, **101**, 2287–2305.

Robutel, P., Laskar, J., 2001. Frequency map and global dynamics in the Solar System. Short period dynamics of massless particles. *Icarus* **152**, 4–28.

Roig, F., Nesvorný, D., Ferraz-Mello, S., 2002. Asteroids in the 2:1 resonance with Jupiter: dynamics and size distribution. *Mon. Not. R. Astron. Soc.* **335**, 417–431.

Rubincam, D.P., 1987. LAGEOS orbit decay due to infrared radiation from Earth. *J. Geophys. Res.* **92**, 1287–1294.

Rubincam, D.P., 1995. Asteroid orbit evolution due to thermal drag. *J. Geophys. Res.* **100**, 1585–1594.

Rubincam, D.P., 2000. Radiative spin-up and spin-down of small asteroids. *Icarus* **148**, 2–11.

Ryan, E.V., Melosh, H.J., 1998. Impact fragmentation: From the laboratory to asteroids. *Icarus* **133**, 1–24.

SDSS MOC — Sloan Digital Sky Survey Moving Object Catalog, `http://www.astro.washington.edu/ivezic/sdssmoc/sdssmoc.html`

Sekanina, Z., Brownlee, D.E., Economou, T.E., Tuzzolino, A.J., Green, S.F., 2004. Modeling the nucleus and jets of comet 81P/Wild 2 based on the Stardust encounter data. *Science* **304**, 1769–1774.

Šidlichovský, M., Nesvorný, D., 1997. Frequency modified Fourier transform and its applications to asteroids. *Celest. Mech. Dyn. Astr.* **65**, 137–148.

Slivan, S.M., 2002. Spin vector alignment of Koronis family asteroids. *Nature* **419**, 49–51.

Slivan, S.M., Binzel, R.P., Crespo da Silva, L.D., Kaasalainen, M., Lyndaker, M.M., Krčo, M., 2003. Spin vectors in the Koronis family: Comprehensive results from two independent analyses of 213 rotation lightcurves. *Icarus* **162**, 285–307.

SMASS — Small Main-Belt Asteroid Spectroscopic Survey, `http://smass.mit.edu`

Soderblom, L.A., Becker, T.L., Bennett, G. & 19 coauthors, 2002. Observations of comet 19P/Borrelly by the Miniature Integrated Camera and Spectrometer aboard Deep Space 1. *Science* **296**, 1087–1091.

Stardust, JPL, NASA, `http://stardust.jpl.nasa.gov`

Stokes, G.H., Evans, J.B., Larson, S.M., 2002. Near-Earth asteroid search programs. in: *Asteroids III* (W.F. Bottke, A. Cellino. P. Paolicchi & R.P. Binzel, Eds.), pp. 45–54. Arizona University Press, Tucson.

Sunshine, J.M., Bus, S.J., McCoy, T.J., Burbine, T.H., Corrigan, C.M., Binzel, R.P., 2004. High-calcium pyroxene as an indicator of igneous differentiation in asteroids and meteorites. *Meteor. Planet. Sci.* **39**, 1343–1357.

SWIFT, `http://www.boulder.swri.edu/~hal/swift.html`

Sykes, M.V., 1988. IRAS observations of extended zodiacal structures. *Astrophys. J.* **334**, L55–L58.

Tanga, P., Cellino, A., Michel, P., Zappalà, V., Paolicchi, P., Dell'Oro, A., 1999. On the size distribution of asteroid families: The role of geometry. *Icarus* **141**, 65–78.

Tedesco, E.F., Noah, P.V., Noah, M., Price S.D., 2002. The supplemental IRAS minor planet survey. *Astron. J.* **123**, 1056–1085.

Tholen, D.J., 1989. Asteroid taxonomic classifcations. in: *Asteroids II* (R.P. Binzel, T. Gehrels & M.S. Matthews, Eds.), pp. 1139–1150. Arizona University Press, Tucson.

Tietjen, F., 1869. Elemente und Ephemeride der Hecuba (108). *Astron. Nach.* **74**, 47–48.

Tody, D., 1986. The IRAF data reduction and analysis system. in: *Instrumentation in Astronomy VI* (D.L. Drawford, Ed.), Society of Photo-Optical Instrumentation Engineers, Bellingham, 733.

Tsiganis, K., Varvoglis, H., Morbidelli, A., 2003. Short-lived asteroids in the 7/3 Kirkwood gap and their relationship to the Koronis and Eos families. *Icarus* **166**, 131–140.

Tüg, H., 1977. Vertical extinction on La Silla. *Messenger* **11**, 7–8.

Veeder, G.J., Matson, D.L., Owensby, P.D., Gradie, J.C., Bell, J.F., Tedesco, E.F., 1995. Eos, Koronis, and Maria family asteroids: Infrared (JHK) photometry. *Icarus* **114**, 186–196.

Vokrouhlický, D., 1998. Diurnal Yarkovsky effect as a source of mobility of meter-sized asteroidal fragments. I. Linear theory. *Astron. Astrophys.* **335**, 1093–1100.

Vokrouhlický, D., 1999. A complete linear model for the Yarkovsky thermal force on spherical asteroid fragments. *Astron. Astrophys.* **344**, 362–366.

Vokrouhlický, D., Brož, M., 2002. Interaction of the Yarkovsky-drifting orbits with weak resonances: Numerical evidence and challenges. in: *Modern Celestial Mechanics: from Theory to Applications* (A. Celletti, S. Ferraz-Mello & J. Henrard, Eds.) pp. 467–472. Kluwer Academic Publishers, Dordrecht.

Vokrouhlický, D., Čapek, D., 2002. YORP–induced long–term evolution of the spin state of small asteroids and meteoroids. Rubincam's approximation. *Icarus* **159**, 449–467.

Vokrouhlický, D., Farinella, P., 1999. The Yarkovsky seasonal effect on asteroidal fragments: A nonlinearized theory for spherical bodies. *Astron. J.* **118**, 3049–3060.

Vokrouhlický, D., Farinella, P., 2000. Efficient delivery of meteorites to the Earth from a wide range of asteroid parent bodies. *Nature* **407**, 606–608.

Vokrouhlický, D., Milani, A., Chesley, S.R., 2000. Yarkovsky effect on small near-Earth asteroids: Mathematical formulation and examples. *Icarus* **148**, 118–138.

Vokrouhlický, D., Brož, M., Farinella, P., Knežević, Z., 2001. Yarkovsky-driven leakage of Koronis family members. I. The case of 2953 Vysheslavia. *Icarus* **150**, 78–93.

Vokrouhlický, D., Brož, M., Morbidelli, A., Bottke, W.F., Nesvorný, D., Lazzaro, D., Rivkin, A.S., 2002. Yarkovsky footprints in the Eos family. Abstract No. 12.01 presented at the *Asteroids, Comets and Meteors* meeting, Berlin.

Vokrouhlický, D., Nesvorný, D., Bottke, W.F., 2003. The vector alignments of asteroid spins by thermal torques. *Nature* **425**, 147–151.

Vokrouhlický, D., Čapek, D., Kaasalainen, M., Ostro, S.J., 2004. Detectability of YORP rotational slowing of asteroid 25143 Itokawa. *Astron. Astrophys.* **414**, L21–L24.

Vokrouhlický, D., Čapek, D., Chesley, S.R., Ostro, S.J., 2005c. Yarkovsky detection opportunities. I. Solitary asteroids. *Icarus* **173**, 166–184.

Vokrouhlický, D., Čapek, D., Chesley, S.R., Ostro, S.J., 2005d. Yarkovsky detection opportunities. II. Binary systems *Icarus* **179**, 128–138.

Vokrouhlický, D., Brož, M., Michałowski, T., Slivan, S.M., Colas F., Šarounová, L., Velichko, F., 2005e. Spin axis of (2953) Vysheslavia and its implications. *Icarus* **180**, 217–223.

Vokrouhlický, D., Brož, M., Morbidelli, A., Bottke, W.F., Nesvorný, D., Lazzaro, D., Rivkin, A.S., 2006a. Yarkovsky footprints in the Eos family. *Icarus*, in press.

Vokrouhlický, D., Brož, M., Bottke, W.F., Nesvorný, D., Morbidelli, A., 2006b. Yarkovsky/YORP chronology of asteroid families. *Icarus*, in press.

Wikipedia, the Free Encyclopedia, `http://www.wikipedia.org`

Xu, S., Binzel, R.P., Burbine, T.H., Bus, S.J., 1995. Small main belt asteroid spectroscopic survey: Initial results. *Icarus* **115**, 1–35.

Yarko-site, `http://sirrah.troja.mff.cuni.cz/yarko-site/`

Yarkovsky, I.O., 1888. Hypothése cinetique de la gravitation universelle en connection avec la formation des élémentes chimiques. Moscow.

Yarkovsky, I.O., 1901. The density of luminiferous ether and the resistance it offers to motion. Bryansk.

Yeomans, D.K., Chodas, P.W., Sitarski, G., Szutowicz, S., Królikowska, M., 2004. Cometary orbit determination and nongravitational forces. in: *Comets II* (M.C. Festou, H.U. Keller & H.A. Weaver, Eds.), pp. 137–151. Arizona University Press, Tucson.

Zappalà, V., Farinella, P., Knežević, Z., Paolicchi, P., 1984. Collisional origin of the asteroid families: Mass and velocity distributions. *Icarus* **59**, 261–285.

Zappalà, V., Cellino, A., Farinella, P., Knežević, Z., 1990. Asteroid families. I – Identification by hierarchical clustering and reliability assessment. *Astron. J.* **100**, 2030–2046.

Zappalà, V., Bendjoya, P., Cellino, A., Farinella, P., Froeschlé, C., 1995. Asteroid families: Search of a 12,487-asteroid sample using two different clustering techniques. *Icarus* **116**, 291–314.

Zappalà, V., Cellino, A., Dell'Oro, A., Migliorini, F., Paolicchi, P., 1996. Reconstructing the original velocity fields of asteroid families. *Icarus* **124**, 156–180.

Zappalà, V., Bendjoya, P., Cellino, A., Di Martino, M., Doressoundiram, A., Manara, A., Migliorini, F., 2000. Fugitives from the Eos family: First spectroscopic confirmation. *Icarus* **145**, 4–11.

Zellner, B., Tholen, D.J., Tedesco, E.F., 1985. The eight-color asteroid survey: Results for 589 minor planets. *Icarus* **61**, 355–416.

Index